Development of Nanostructured 8 mol% Yttria Stabilized Zirconia (8YSZ) Electrolytes with Enhanced Ionic Conductivity for Solid Oxide Fuel Cell (SOFC) Applications

A thesis
submitted for the degree of

DOCTOR OF PHILOSOPHY
in
MATERIALS ENGINEERING

by

Kotikalapudi Rajeswari

School of Engineering Sciences and Technology
University of Hyderabad
Hyderabad- 500 046
India
2011

Dedicated to my

Husband

Nagesh Kumar

DECLARATION

I hereby declare that the matter embodied in this thesis entitled, "**Development of Nanostructured 8 mol% Yttria Stabilized Zirconia (8YSZ) Electrolytes with enhanced Ionic Conductivity for Solid Oxide Fuel Cell (SOFC) Applications**" submitted to University of Hyderabad for the award of **Doctor of Philosophy** in **Materials Engineering** is a record of original research work carried out by me under the supervision of **Dr. Roy Johnson,** Scientist F and Team Leader, Centre for Ceramic Processing, International Advanced Research Centre for Powder Metallurgy and New Materials (ARC-I), An autonomous R&D Centre of Department of Science & Technology, Govt. of India, Hyderabad and **Dr. Dibakar Das,** Reader, School of Engineering Sciences and Technology, University of Hyderabad. To the best of my knowledge, this work is not submitted for any degree in any University or Institute.

KOTIKALAPUDI RAJESWARI

Place: Hyderabad
Date: 30.12.2011

INTERNATIONAL ADVANCED RESEARCH CENTRE FOR POWDER METALLURGY AND NEW MATERIALS
(An Autonomous Research & Development Centre of Department of Science & Technology, Govt. of India)

ARCI **Balapur P.O, HYDERABAD-500 005 (A.P), INDIA**

C E R T I F I C A T E

This is to certify that the work contained in this thesis entitled, "**Development of Nanostructured 8 mol% Yttria Stabilized Zirconia (8YSZ) Electrolytes with enhanced Ionic Conductivity for Solid Oxide Fuel Cell (SOFC) Applications**", has been carried out by **Mrs. KOTIKALAPUDI RAJESWARI** under my supervision and the same has not been submitted for the award of research degree of any university.

DR. ROY JOHNSON
Thesis Supervisor

Place: Hyderabad
Date: 30.12.2011

DIRECTOR
International Advanced Research Centre for Powder Metallurgy and New Materials
Hyderabad

C E R T I F I C A T E

This is to certify that the work contained in this thesis entitled, "**Development of Nanostructured 8 mol% Yttria Stabilized Zirconia (8YSZ) Electrolytes with enhanced Ionic Conductivity for Solid Oxide Fuel Cell (SOFC) Applications**", has been carried out by **Mrs. Kotikalapudi Rajeswari** under my supervision and the same has not been submitted for the award of research degree of any university.

Dr. Dibakar Das
Thesis Co-Supervisor

Place: Hyderabad
Date: 30.12.2011

DEAN
School of Engineering Sciences and Technology
University of Hyderabad

Acknowledgements

I wish to express my heartful thanks to **Dr. G. Sundararajan**, **DIRECTOR** ARC-I for providing me an excellent opportunity to carry out this research work at ARC-I and for their immense support and guidance without which I could not have been completed my work successfully. I am also grateful to **Prof. K. Bhanu Shankara Rao**, DEAN, School of Engineering Sciences and Technology (SEST), University of Hyderabad, Hyderabad, for providing necessary facilities and encouragement, and timely advice during this course of work.

I express my deep sense of gratitude to **Dr. Roy Johnson**, Scientist F and Team Leader, Ceramic for Ceramic Processing, ARC-I, Hyderabad, Research Supervisor of this piece of work. It was he who introduced me to the field of Material Science and Ceramics. He gave me great encouragement, confidence as well as the freedom to think while carrying out this work. Working under such a supervisor is an immensely pleasant and memorable experience. His valuable guidance and constant encouragement, excellent technical discussions and valuable advices are the motive force behind the timely completion of this research work. I take this opportunity to express my utmost gratitude to him.

It has been indeed a great privilege for me to have **Dr. Dibakar Das**, Reader, School of Engineering Sciences and Technology (SEST), University of Hyderabad, Hyderabad as my Co-Supervisor. I express my deep sense of gratitude for his valuable guidance throughout the course of this work. His valuable guidance and constant encouragement, adept technical discussions and relentless advice were much needed to complete this piece of research work. I take this opportunity to express my heartfelt thanks to him.

My special thanks are due to **Dr. G. Padmanabham** and **Dr. S. V. Joshi,** Associate Directors, ARC-I for their constant encouragements, timely suggestions during the course of my research at ARCI

My thanks are due to Dr. M. B. Suresh, Sc 'C', ARC-I, for introducing me to the Impedance Spectroscopy and guidance during the impedance analysis which is one of the significant parts of this thesis.

I am grateful to Dr. B. P. Saha, Sc 'E, Dr. Y. S. Rao, Sc 'E', Dr.U. S. Hareesh, Sc 'D', Mr. Pandu Ramavath, Sc 'C', Mr. R. Senthil Kumar, Sc 'C', Ms. Papiya Biswas, Sc 'C' of ARC-I, for extending their cooperation as and when required.

I would like to thank Dr. Ravi Chandra, Sc 'F' and Mr. L. Rama Krinshna, Sc 'C', for the discussions on characterization of the samples and Dr. R. Subasri, Sc 'E' for microwave sintering and Mr. Dibynedu Chakravarty, Sc 'C' of ARC-I, for spark plasma sintering of the specimens produced during the study.

My thanks are due to Mr. Mahender, TO 'B', Mr. A. Rajasekhar Reddy, TO 'A', Mr. G. V. R. Reddy, TO 'A' and Mr. L. Venkatesh, TO 'A' and in-particular technicians Mr. G. Venkata Rao, Mr. K. V. Ramana, Mr. S. Ahmed, Mr. M. Styanand, Mr. B. Subramanyam and Mr. M. Lingaiah of ARC-I and all the technical staff of School of Engineering Sciences and Technology, University of Hyderabad for their kind help during my project work.

I express my sincere thanks to all faculty members of School of Engineering Sciences and Technology (SEST), University of Hyderabad, for their help during the course of work.

I am also indebted to my classmates and friends for their constant encouragement, cooperation and support.

I indebted to my parents particularly my beloved mother Smt. K. Tripura Sundari for her concern and encouragement without which, I would not have reached this stage.

I express my indebtedness to my in-laws for their affection. I also thank my brothers and sister who have always been a source of strength to me.

Finally, I would like to acknowledge my husband Mr. N. Nagesh Kumar and my daughter baby N. Srimukhi for their perpetual support at home providing the right atmosphere for the successful completion of this thesis.

Place: Hyderabad **KOTIKALAPUDI RAJESWARI**

Date: 30.12.2011

Synopsis

8 mol% Yttria Stabilized Zirconia (8YSZ) is a pure ionic conductor with oxygen ions as the charge carriers at elevated temperatures and is the most commonly employed electrolyte material for Solid Oxide Fuel Cell (SOFC) applications. Though the basic requirements as an electrolyte material such as fast ionic transport, minimized electronic conduction, thermodynamic stability in the valence states and phases over a wide range of temperature and oxygen partial pressure, negligible volatilization of components, negligible interaction with electrode materials during fabrication and operation, thermal expansion matching with the electrodes and mechanical properties are met, enhancing the ionic conductivity of zirconia has been topic of continued interest of research world over. The various approaches experimented in this context include the type and concentration of dopants selected, novel processing and fabrication techniques and microstructural refinement based on nanotechnology. However, there are many pertinent questions still to be answered for establishing the dependence of ionic conductivity on grain sizes as studies in this area are limited. Hence, the present study is envisaged to engineer the grain sizes of sintered 8YSZ ceramics through a series of processing and sintering methodologies followed by its ionic conductivity measurements and its correlation with the observed microstructural features.

Accordingly, the thesis starts with the introductory chapter "Chapter: 1", which gives a brief overview based on the extensive literature survey on the evolution of Solid Oxide Fuel Cells (SOFCs) and its operating principles. The chapter also discusses the current status of the main components such as anode, cathode and electrolyte materials along with its properties and various configurations. The major technical challenges in development of SOFC electrolytes are listed and the scope of the work is then defined at the end of this chapter.

"Chapter: 2" describes three processes followed for the shaping of 8YSZ powder procured from a reputed source (TZ-8YS, Tosoh Corporation, Japan). Powders were characterized for their phase, particle size, BET surface area and chemical composition. The three processes of conventional compaction processing, colloidal shaping by slip casting and a newer novel process based on methyl cellulose based thermal gel casting

have been employed. Elucidation of flow behaviour patterns pertaining to the processing regime such as granule flow analysis for compaction, viscosity measurements of slurries for slip casting and methylcellulose based processing have been carried out. Thermal gelation behavior of methylcellulose was recorded through temperature controlled viscosity measurements as shown in Fig. 1(a). Suitable dies for compaction, plaster of paris mould for slip casting and Teflon moulds for thermal gel casting have been designed and fabricated. Compaction of pellets has been carried out using a hydraulic press under optimized compaction pressure of 160MPa based on the compaction trials. Slip casting has been carried out under ambient temperature and the samples were dried out under humidity controlled atmosphere.

Casting based on the thermal gelation of the methyl cellulose at around 45 -50°C has been employed for the first time in the colloidal shaping of 8YSZ electrolytes and the technique is demonstrated for complex shaping capability in the present study. The process has been extended to the development of a complex novel configured honeycomb based electrolyte structure as depicted in the Fig. 1(b). This developed process is an environmentally benign shaping technique utilizing nontoxic methyl cellulose in comparison to the conventional gel casting process which employs known neurotoxins of acrylamide and its derivatives. The technique has also been explored successfully for the development of new generation honeycomb configured 8YSZ electrolyte and also for components such as oxygen sensors, refractory tubes etc.

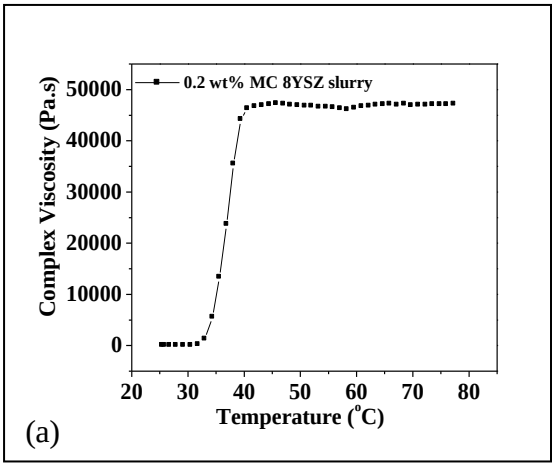

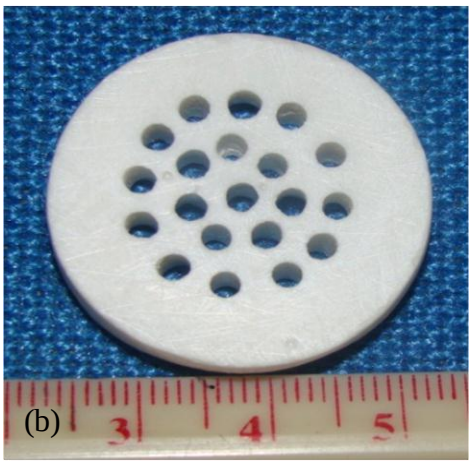

Fig.1 (a) Thermal gelation curves of methyl cellulose (b) 8YSZ Honeycombs electrolytes processed based on methyl cellulose based thermal gel casting process

“Chapter: 3” focuses on the systematic investigations carried out to elucidate the role of conventional and non-conventional sintering methodologies to engineer the microstructure under optimized sintering parameters. Green slip cast specimens were subjected to Conventional Ramp and Hold Sintering (CRH), Rate Controlled Sintering (RCS) and Two Stage Sintering (TSS) techniques under conventional sintering methodologies. Microwave Sintering (MWS) and Spark Plasma Sintering (SPS) are the two sintering techniques employed under non-conventional sintering methodologies. Densities close to 99% of the theoretical density are achieved for zirconia ceramics through optimized sintering parameters in case of CRH, TSS, MWS and SPS sintering techniques. However, densities > 97 % could not be achieved even after several trials, in case of RCS.

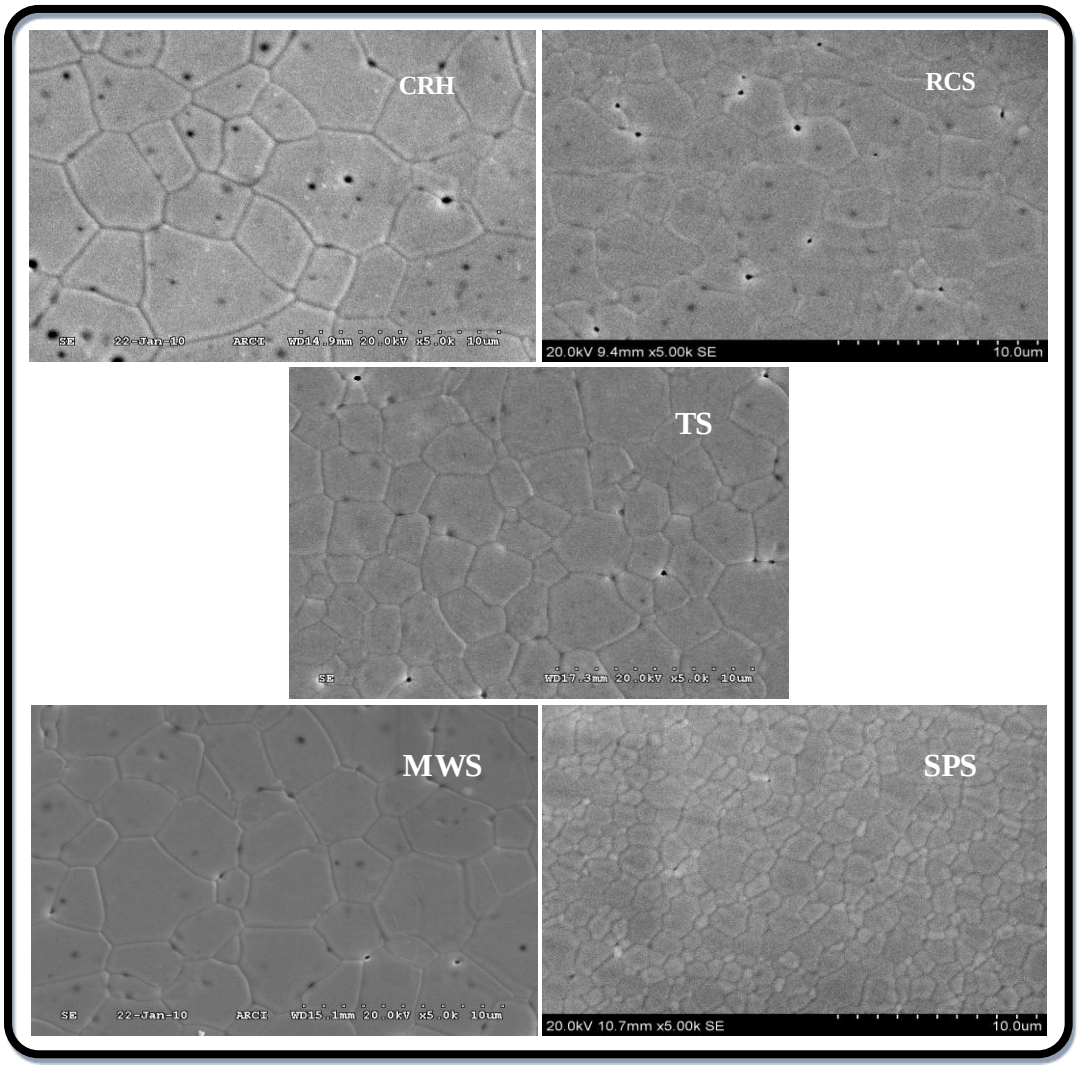

Fig. 2 Micrographs of 8YSZ samples sintered through various sintering methodologies

The samples were further subjected to ceramography and the microstructures were elucidated by Scanning Electron Microscopy (SEM). A maximum average grain size of 4.67 μm in CRH and a minimum of 1.16 μm in SPS sintering are achieved for 8YSZ with the identical density of 99%TD. Micrographs of the dense samples, polished as per ceramographic procedures followed by thermal etching are shown in Fig. 2 and the densities and grain sizes are shown in Table 1. Additionally, this chapter evaluates the sintering mechanisms and evolution of grain sizes through kinetic analysis and Master Sintering Curves (MSC) in conjunction with the experimental techniques employed. The dilatometric shrinkage curves and master sintering curve constructed are shown in Fig. 3(a) and (b) respectively. The activation energy estimated is 400 kJ/ mol, corresponding to grain boundary diffusion, and is in good agreement with the earlier reported values.

Table 1: Density and grain sizes of the 8YSZ samples processed through different sintering methodologies

Sintering methodology	**Sintering parameters (Selected as optimum)**	**Density (g/cc)**	**Theoretical Density (%)**	**Average grain size (μm)**
CRH	Peak temperature: 1525°C Dwell time: 2 hrs Heating rate: 5°C/minute	5.867	99.44	4.67
MWS	Peak temperature: 1525°C Dwell time: 15minutes Heating rate: 10°C/minute	5.850	99.15	3.70
RCS	Peak temperature: 1550°C Shrinkage rate: 22μm/min 15μm/min 5μm/min	5.720	96.95	3.45
TSS	Peak Temperature T1: 1525°C Dwell time: 5minutes T2: 1350°C Dwell time: 4 hrs Heating rate: 5°C/minute	5.865	99.40	2.64
SPS	Peak temperature:1325°C Dwell time: 5 minutes Heating rate: 170°C/minute	5.876	99.59	1.16

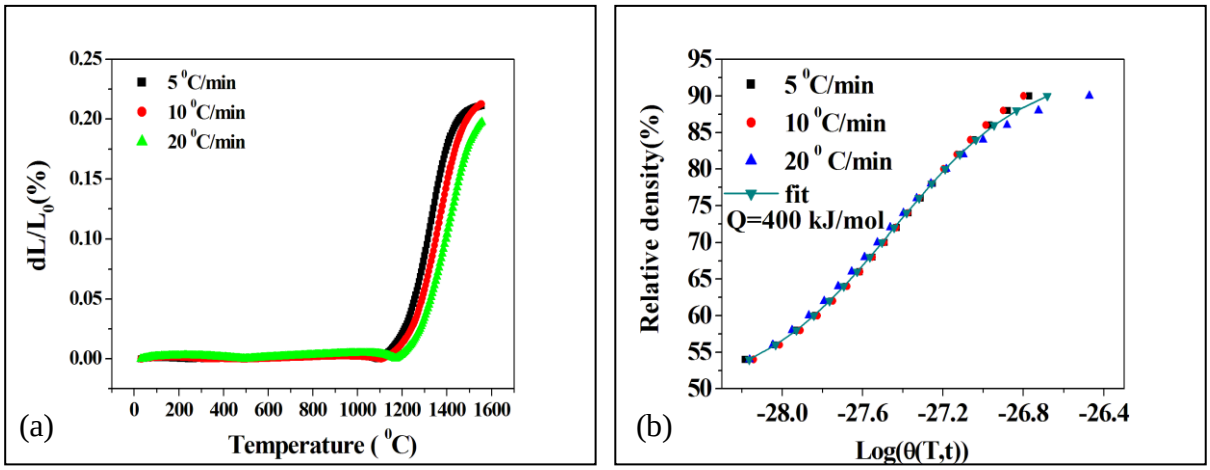

Fig.3 (a) Dilatometric shrinkage curves (b) Master Sintering Curves of 8YSZ samples sintered by CRH technique

Thus the direct comparison between specimens derived from the same starting powder densified using different sintering approaches clearly demonstrates that the selection of sintering methodology plays a major role in achieving the twin objective of densification with finer grain sizes.

"Chapter: 4" describes the evaluation of ionic conductivity of the sintered electrolyte through impedance analysis using a Solartron S-I1260 Impedance Analyzer attached with a hot stage facility. Sintered samples with > 99 % TD were machined into identical dimensions and were electroded with platinum paint and impedance measurements were carried out up to 800°C. Though the measurements were carried out at 50°C intervals, representative plots of complex impedance recorded at 300°C and 800°C are depicted in Fig. 4(a) and (b) respectively. It is evident that impedance plots are very distinctly showing the contributions of grain, grain boundary and electrode (Fig. 4(a)). However, single semicircle is observed at 800°C with high frequency intercept on real axis (Fig. 4(b)). Further, the Arrhenius plots for total conduction for the entire temperature range of measurements are also shown in Fig. 4(c) for the samples sintered by SPS and CRH techniques. The lower activation energy for the SPS sintered sample is evident in the plot.

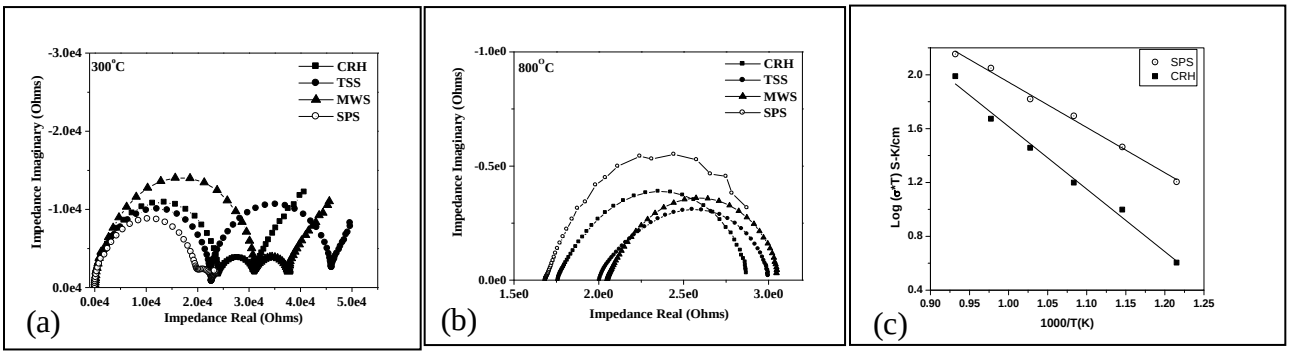

Fig.4 Complex impedance plane plot (300°C) (a), 800°C (b) and Arrhenius plot (c) of 8YSZ samples densified via different sintering methodologies

Table 2 shows the total ionic conductivity of 8YSZ at 800°C with respect to the sintering techniques and grain sizes. Total ionic conductivity of 8YSZ samples at 800°C sintered by CRH, TSS and MWS have exhibited only a marginal change between 0.094 S/cm – 0.088 S/cm irrespective of the variation in the average grain size from 4.67 to 2.64 µm. This clearly indicates that sintering methodology and grain sizes achieved in the range of 2- 5 µm have only minimum effect on ionic conductivity confirming the earlier observations of Verkerket. al., [Solid State Ionics, 6, (1982)] and Badwal [Appl. Phy.A, 50, (1990)]. Microstructures of the samples (Fig. 2) reveals that for samples sintered at temperature >1500°C, black spots are observed at the grain and grain boundary region, which are attributed to yttria segregation as confirmed by EDS analysis. This in-homogeneity also expected to cause hindrances to the oxygen ion transport. Interestingly, samples processed through SPS under optimized conditions of temperature and pressure have achieved the unique combination of ~100%TD with an average grain size of 1.16 µm and exhibited significantly higher conductivity of 0.13 S/cm. The observed increase in the ionic conductivity of SPS sintered samples could be primarily attributed not only to the unique combination of full density with low average grain size of 1.16 µm but also to the homogeneous fine-grained microstructure as evident in the SEM micrograph shown in Fig. 2. Further, in SPS sintered sample (peak temperature 1325°C and soaking time 5 minutes) however, no yttria segregation is observed either at the grain boundaries or in the matrix. In order to understand the high conductivity of SPS samples, the activation energy (E_a) was estimated in the operating temperature range of 500-800°C using Arrhenius plots and is compared with that of the CRH samples, which shows the maximum grain sizes of 4.67 µm. The comparison is shown in Table 2.

Table 2: Ionic conductivity and activation energies of 8YSZ samples densified by different sintering methodologies

Sr. No	Sintering technique	Grain Size (µm)	Ionic Conductivity (800°C), (S/cm)	Activation Energy (500-800°C), (eV)
1	CRH	4.67	0.090	0.79
2	TSS	2.64	0.094	-
3	MWS	3.70	0.088	-
4	SPS	1.16	0.130	0.68

It is well known that the grain conductivity remains almost unchanged with grain size but the grain boundary conductivity varies significantly with grain sizes. In order to further understand the role of grain boundaries in conductivity, estimations were also made for grain boundary conductivity and grain boundary blocking factor for the above samples as shown in Table 3.

Table 3: Grain Boundary conductivity and blocking factor of 8YSZ samples densified by CRH and SPS sintering methodologies

Sintering technique	Grain Size (µm)	Specific Grain Boundary Conductivity (800°C), (S/cm)	Grain Boundary Blocking factor
CRH	4.67	3.635×10^{-4}	0.38
SPS	1.16	3.303×10^{-3}	0.26

It is evident that there is an increase in grain boundary conductivity by an order of magnitude as the grain size reduces from 4.67 µm to 1.16 µm, which contributes to the increased total ionic conductivity observed with SPS samples. Estimation of grain boundary blocking factor also reveals the enhanced conductivity with decreasing grain sizes. Further, to correlate the grain size effect on conductivity an attempt has been made to grow the grains intentionally by increasing the peak sintering temperature from 1325°C to 1425°C in the SPS process. Complex impedance plane plot, recorded at 250°C for the SPS sintered samples with peak sintering temperature of 1425°C (8.8 µm grain size) and 1325°C (1.16 µm grain size) is shown in Fig. 5(a). It is evident from Table 4 that the specimens sintered at 1425°C, the grain boundary contribution and electrode effects are merged and the conductivity value is less by an order of magnitude. Table 4

shows that the total conductivity of the SPS 1325°C sample is marginally higher than that of SPS 1425°C sample, which suggests that, the ionic conductivity can not be directly correlated with the increase in grain sizes when processed by SPS route. SEM analysis indicated no signs of yttria seggregation which is further supported by the high activation energy of 0.79eV (Arrhenius plots shown in Fig. 5(b)). The blocking factor of 0.29 is low as compared to 0.38 observed with the CRH sample.

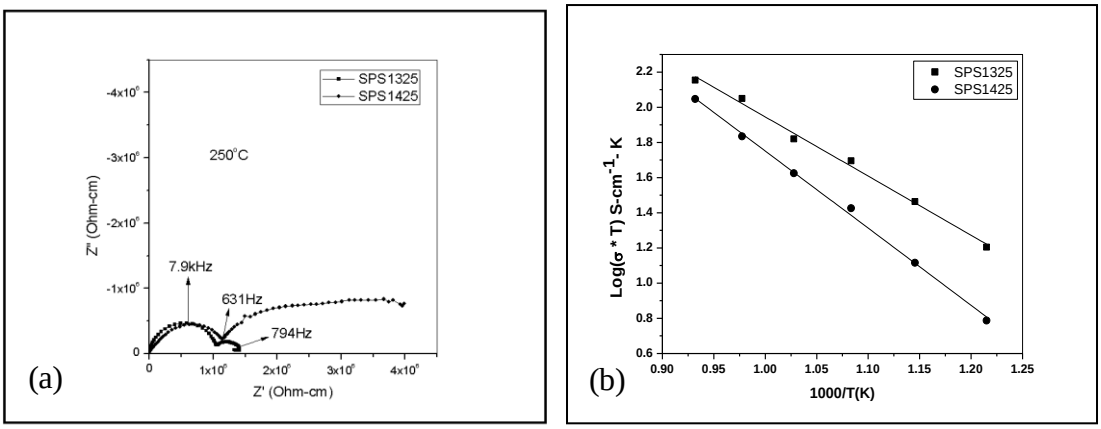

Fig.5 Cole-Cole Plots (a) and Arrhenius plot (b) of SPS samples sintered at 1325 and 1425°C

Table 4: Ionic conductivity, activation energy and blocking factor of 8YSZ samples densified by SPS methodology

Sintering technique	**Grain Size (µm)**	**Specific Grain Boundary Conductivity (800°C), (S/cm)**	**Total Ionic Conductivity (800°C), (S/cm)**	**Total Activation Energy (500-800°C), (eV)**	**Grain Boundary Blocking factor**
SPS1325°C	1.16	3.202×10^{-3}	0.13	0.68	0.26
SPS1425°C	8.80	2.727×10^{-4}	0.10	0.79	0.29

Attempts were made for the single cell fabrication of SPS specimens sintered at 1325°C with average grain size of 1.16 µm in view of the highest conductivity (0.13 S/ cm) obtained. Using screen printing method, the sample was coated with standard cathode (Lanthanum Strontium Manganite) and anode (NiO-8YSZ) materials procured from commercial sources. Electrochemical performance was evaluated at IIT, Chennai and a plot of Open Circuit Voltage (OCV) vs. Temperature is shown in Fig. 6. Pure H_2 is used

as a fuel and air as an oxidant for the measurement. An open circuit voltage close to one volt is observed at around 800°C.

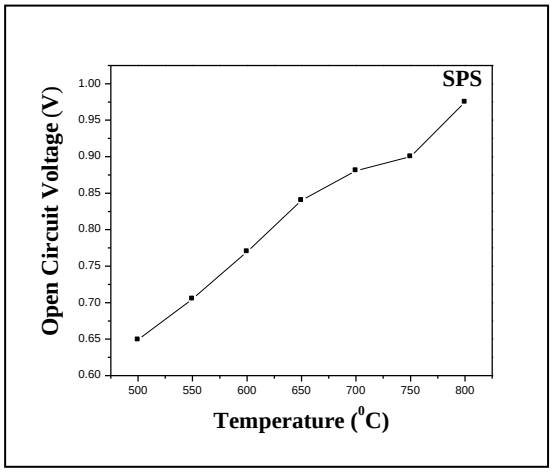

Fig. 6 Plot of Open Circuit Voltage Vs. Temperature of SPS sintered sample at 1325 °C

It may be noted that grain sizes of all the sintered samples evaluated for ionic conductivity are >1μm. This is mainly because of the submicron size particles of the starting zirconia powder (TZ-8YS Tosoh Corporation, Japan), which was measured to be around 205 nm. Attempts to reduce the particle size by milling several hours did not result in reduction in particle size. In view of the above, ultra-fine 8 mol % yttria stabilized zirconia (8YSZ) with an average particle size of 45 nm were recently procured from M/s. M.K. Nano, Canada. Based on the better properties obtained from the SPS processing of TZ-8YSzirconia powder the present experiments were only limited to SPS processing. SPS processing was carried out under various temperatures and at a constant pressure of 50 MPa. A hundred fold decrease in average grain size ranging from 10 μm to 80 nm is observed on decreasing the SPS sintering temperature from 1200°C to 1050°C with >99 % of theoretical densities. Choice of SPS temperature is found to be very critical to obtain simultaneously densification and grain size control to nano sizes. Impedance measurements at 800^{o}C revealed a seven fold enhancement of ionic conductivity with decrease in grain size from 10 μm to 80 nm. Activation energy, grain boundary conductivity and grain boundary blocking factor were estimated and are further correlated with the observed enhancement in ionic conductivity.

List of publications from thesis work

1. Effect of Nano Grain Size on the Ionic Conductivity of Spark Plasma Sintered 8YSZ Electrolyte, K. Rajeswari, M. Buchi Suresh, Dibyendu Chakravarty, Dibakar Das and Roy Johnson, International Journal of Hydrogen Energy (2011) 1-7.
2. Studies on Ionic conductivity of Stabilized Zirconia Ceramics (8YSZ) densified through Conventional and Non-Conventional Sintering Methodologies, K. Rajeswari, M. Buchi Suresh, U. S. Hareesh, Y. Srinivasa Rao, Dibakar Das and Roy Johnson, Ceramics International 37(2011) 3557-3564.
3. Microstructural control of stabilized zirconia ceramics (8YSZ) through modified conventional sintering methodologies, K. Rajeswari, A. Rajasekar Reddy, U. S. Hareesh and R. Johnson, Science of Sintering, 42 (2010) 91-97
4. Comparative Evaluation of Spark Plasma (SPS), Microwave (MWS) and Two stage sintering (TSS) on the densification and Micro structural Evolution of Stabilized Zirconia Ceramics, K. Rajeswari, U. S. Hareesh, R. Subasri, Dibyendu Chakravarty and R. Johnson, Science of Sintering, 42 (2010) 259-267
5. Colloidal Shaping of 8 mol% Yttria Stabilized Zirconia Electrolyte Honeycomb Structures by Microwave Assisted Thermal Gelation of Methyl Cellulose, K. Rajeswari, P. Biswas, M. Buchi Suresh, Dibakar Das, U. S. Hareesh and R. Johnson, Journal of American Ceramic Society, Recommended for publication (Final manuscript being submitted).

Conference Presentations:

1. Effect of sintering techniques on microstructure evolution of 8YSZ zirconia ceramics, K. Rajeswari, A. Rajasekar Reddy, U. S. Hareesh, and R. Johnson, Annual Technical Session of Indian Ceramic Society, December (2009) at Trivandrum.
2. Effect of sintering techniques on the densification and microstructure of fully stabilized zirconia electrolytes , K. Rajeswari and Roy Johnson and Dibakar Das,

A.P Science Congress and Annual Convention of A.P. Academi of Sciences, Science, Technology, Education for Prosperity (STEP), JNTUH, November (2010) at Hyderabad.

3. Ionic conductivity of 8 Y Stabilized Zirconia Ceramics Densified through Conventional and non-Conventional Sintering Methodologies, K. Rajeswari, M. B. Suresh, Y.S. Rao, U.S. Hareesh and R. Johnson, National Symposium on Energy Environment: Ceramics, Annual Technical Session of Indian Ceramic Society, January (2011) at Kolkata.

4. Master Sintering Curve: A unique tool for the predictions of sintering kinetics of 8Y Zirconia Ceramics, S. Padhi, K. Rajeswari, R. Johnson and Dibakar Das, Indian Institute of Metals, Annual Technical Meeting, November (2011) at Hyderabad.

5. Studies on Sintering Kinetics and Correlation with the Sinterability of 8Y Zirconia Nano Powders Based on the Dilatometric Shrinkage Curves, K. Rajeswari, A. R. S. Reddy, Dibakar Das and Roy Johnson, Annual convention of Indian Ceramic Society, December (2011) at Agra.

6. Microstructure and Ionic Conductivity Correlation of Nano-Structured 8 Y Zirconia Ceramics Sintered through Spark Plasma Sintering, K. Rajeswari, M. B. Suresh, D. Chakravarty and Roy Johnson, Annual convention of Indian Ceramic Society, December (2011) at Agra.

Other publications/Conference

1. Colloidal Shaping of Alumina Ceramics by Thermally Induced Gelation of Methylcellulose. Unnikrishnan Nair Saraswathy Hareesh, RakeshAnantharaju, Papiya Biswas, Kotikalapudi Rajeswari and Roy Johnson. J. Am. Ceram. Soc., 94 [3] (2011) 749–753.

2. Processing Of Aluminium Oxynitride Through Aqueous Colloidal Forming Techniques, Rajendran Senthil Kumar, Kotikalapudi Rajeswari, Balakrishnan Praveen, Unnikrishnan Nair Saraswathy Hareesh and Roy Johnson, J. Am Ceram. Soc. 93[2] (2010) 429–435.

3. A efficient Mg Al_2O_3 spinel additive for improved slag erosion and penetration resistance of high Al_2O_3 and MgO – C refractories, I. Ganesh, S. Bhattacharjee, B.P. Saha, R. Johnson, K. Rajewsari, R. Sengupta, M.V. Ramana Rao, Y.R. Mahajan, at the Ceramics International, 28 (2002) 245-253

4. Rate Controlled Sintering of Sol Gel Derived Alumina- Zirconia Composites", K. Rajeswari, Papiya Biswas, U. S. Hareesh and R. Johnson, 71st Annual Session of Indian Ceramic Society, (2008) 9 -11 at Bangalore.

5. Micronised Reactive Mag – Al spinel the ultra-modern refractory binding system", K. Rajeswari, M.V. Ramana Rao, R. Sengupta and D.P. Mukerjee. International Conference on Refractories, Iron & Steel Industries, (2004) at Jamshedpur.

6. Development & Commercialization of Mg Al_2O_3 spinel as an additive for high Al_2O_3 and MgO – C Refractories, I. Ganesh, Roy Johnson and K. Rajeswari,1st International Conference on Refractories Engineering, (2004) at Visakhapatnam.

7. Effect of compositional variation and additives on sintering of $MgAl_2O_4$ Spinel", K. Rajeswari, I. Ganesh, B.P. Saha, Roy Johnson, S. Bhattacharjee & Y.R. Mahajan, P 37, 63rd Annual Session of Indian Ceramic Society (2000)

8. Synthesis and Characterisation of ZTA Composites", K. Rajeswari, B.P. Saha, Roy Johnson & Y.R. Mahajan at the Annual Session of the Indian Ceramic Society, (1996) at Ranchi.

List of figures

Chapter IV:

List of tables

Table of Contents

Chapter III: Sintering of 8YSZ Green Compacts

Chapter - I

Introduction

1.0 Introduction

Industrialization and growth in world population have lead to enormous demand in world energy requirements. Today's energy and transport sectors are dominated by the fossil fuels. Though environmental friendly renewable energy sources are gaining importance in view of the depletion of natural resources and growing environmental concerns, an immediate replacement of fossil fuels seems to be impractical. Hence, the thrust should be towards conservation and efficiency, which necessitates advancements in processing and developments of ceramic materials with ultra-high temperature capabilities in combination with superior mechanical and chemical stability adaptable for better combustion technologies. This will significantly minimizes power generation losses, which in turn results in low emissions. With the emerging developments in non-fossil fuel energy sector, the challenge before the ceramist is to develop novel materials. In addition to attempts to achieve augmenting the inherent properties of the existing ceramics through advancement in synthesis, processing and microstructural control leading to innovative energy solutions. Advanced ceramics are already playing a key role as vital components for developing non fossil fuel based energy technologies such as Solid Oxide Fuel Cells (hydrogen/ hydrocarbon based SOFC), nuclear energy (fission and fusion), and solar energy (photovoltaic, transforming solar energy into chemical fuel and solar thermal storage).

A fuel cell is an electrochemical device that provides efficient and clean power generation. It is regarded as an energy conversion device that produces electricity (and heat) directly from a gaseous fuel by electrochemical combination of the fuel with an oxidant. Due to their unique operation and performance characteristics, Solid Oxide Fuel Cells (SOFCs) are important technology for future sustainable energy systems. SOFCs, in particular can be used with a wide variety of fuels and less affected by impurities than Polymer Electrolyte Membrane (PEM) fuel cells. This fuel tolerance is a result of the high operating temperature, which accelerates the fuel reactions, but it accelerates unwanted chemical reactions which lead to degradation of cell materials. Therefore progress in SOFCs relies heavily on materials development and although

significant progress has been made over the past several decades, many technical challenges remain to be solved before SOFCs can be widely commercialized.

1.1 Evolution of Solid Oxide Fuel Cells

Evolutions of SOFCs are shown in Figure 1.1. The technical history of SOFCs seems to be rooted until late 1930s. Swiss scientist Emil Baur and his colleague H. Preis experimented with solid oxide electrolytes in the late 1930s using oxides of zirconium, yttrium, cerium, lanthanum, and tungsten [1-2].Their designs were not as electrically conductive as projected and reported experienced unwanted chemical reactions between the electrolytes and various gases including carbon monoxide. In the 1940s, O. K. Davtyan of Russia added monazite sand to a mix of sodium carbonate, tungsten trioxide and soda glass in order to increase the conductivity and mechanical strength of the solid oxide electrolyte. Davtyan's designs, however also experienced unwanted chemical reactions and short life ratings of the solid oxide electrolyte [3].

By the late 1950s, research on solid oxide technology began to accelerate at the Central Technical Institute in The Hague, The Netherlands, Consolidation Coal Company in Pennsylvania, and General Electric in Schenectady, New York. Researchers at Westinghouse experimented with a cell using zirconium oxide and calcium oxide in 1962 [1]. One of the major hindrances in the use of SOFC is the long wake up time for the tubular and planar configurations. A new concept of the use of electrolyte or electrode material based on honeycomb configuration is being experimented with targets of faster start up (within one minute) and efficiency upto 50%. Recently, microtubular SOFCs with thin walled tubular ceramics have reported to be demonstrated with a wake up time within minutes. Further, the concept of DH-Q- SOFC (Direct Hydrocarbon, Quick start up/ shut down) is tested and a startup time of 10 to 20s is reported to be achieved. This opens up new avenues for application of SOFCs to transport sector in addition to the proven stationary power generation applications. The evolution of fuel cell configurations [4-9] is depicted in Fig.1.1.

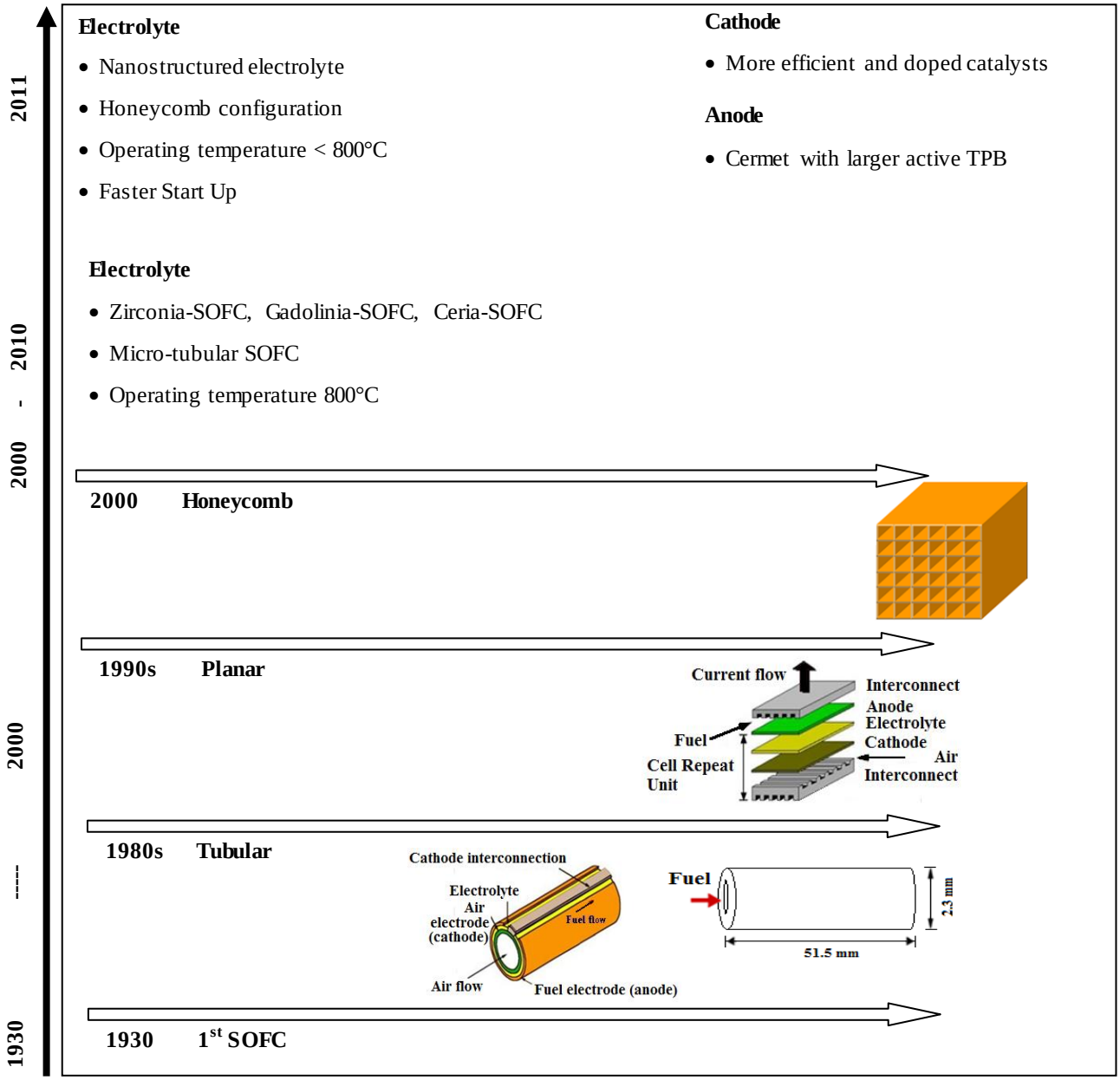

Fig.1.1 Evolution of SOFCs

More recently, advances in materials and processing technology have renewed interest in SOFCs and the increasing trend in R & D publications, especially during 2006 – 2011, depicted in Fig. 1.2 indicates the gaining importance of fuel cell world over. Among the various types of fuel cells, solid oxide fuel cells are a subject of great interest due to their higher efficiency.

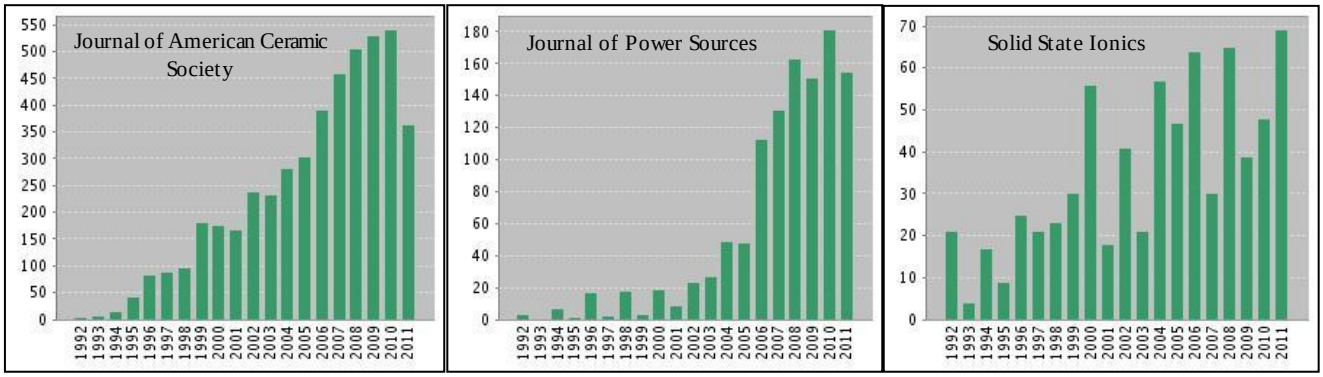

Fig.1.2. Status on publications (JACS, JPS, SSI on SOFC)

1.2 Operating principles of SOFC

A general schematic of SOFC in operation is shown in Fig.1.3. Oxygen from air supplied to the cathode is reduced to O^{2-} at the cathode, transported across the electrolyte, and reacted with fuel at the anode releasing electrons. The electrons released at the anode are transported through an external circuit where electrical power can be drawn.

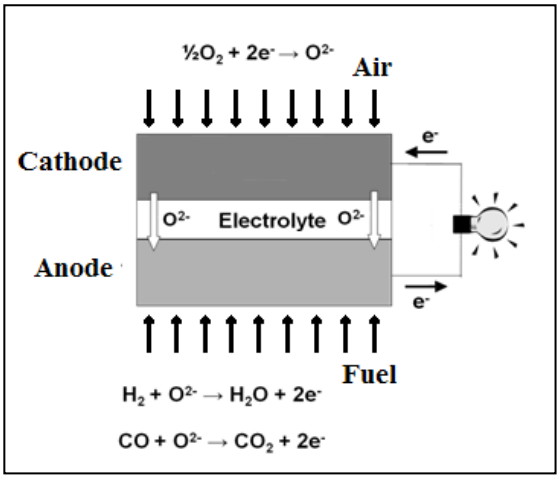

SOFC H_2 reactions:

Anode: $H_2 + O^{2-} \rightarrow H_2O + 2e^-$

Cathode: $\frac{1}{2} O_2 + 2e^- \rightarrow O^2$

Overall: $H_2 + \frac{1}{2} O_2 \rightarrow H_2O$

Fig.1.3 Schematic of SOFC in operation

One major advantage of fuel cell is that scaling fuel cell systems to meet specific power requirements is relatively easy, ranging from small portable applications to large stationary applications. Scaling fuel cell power is achieved by simply stacking fuel cells in series as schematically shown in Fig.1.4.

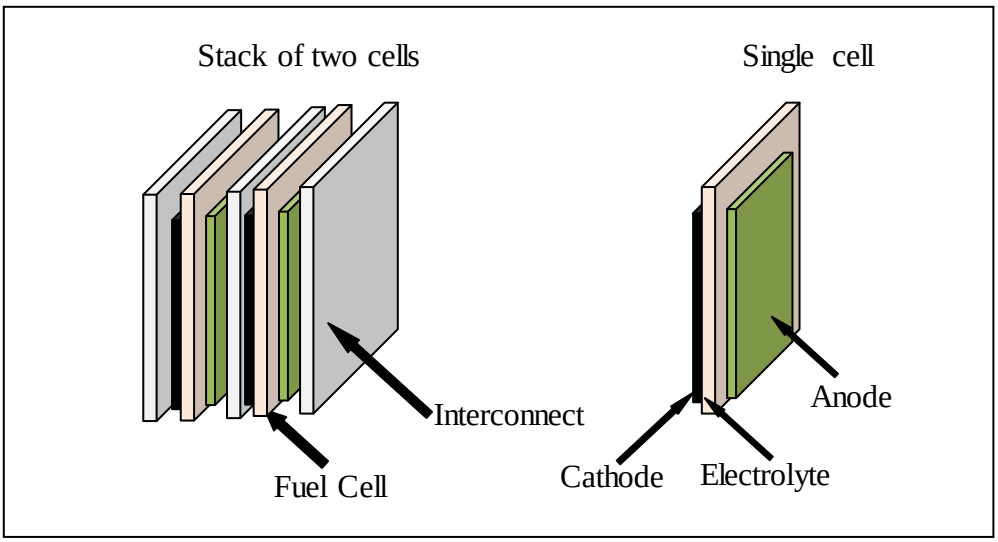

Fig.1.4 Schematic of two fuel cells stacked in series.

When fuel cells are stacked in series, the anode and cathode must be separated so that the fuel-rich atmosphere in the anode and oxygen-rich atmosphere in the cathode do not mix. The component that separates the anode and cathode is called an interconnect. For SOFCs designed to operate at relatively high SOFC operating temperatures (800°C-1000°C), interconnects are composed of expensive ceramic materials such as Strontium-doped Lanthanum Chromites coatings ($La_{1-x}Sr_xCrO_3$).

1.3 SOFC Components and materials

Advanced ceramic materials form key components for the fabrication of SOFC devices either in planar or tubular configurations. The current materials being employed are an oxygen ion conducting solid electrolyte of 8 mol% Yttria Stabilized Zirconia, doped Lanthanum Strontium Manganite as the air electrode (cathode) and Ni-8YSZ Cermet forming a fuel electrode (anode) [10]. Electronic or mixed conducting (ionic and electronic) electrodes have to be porous with a large number of active triple phase boundary (TPB) sites [11- 13]. With a higher TPB length per area, better electrochemical performance can be achieved [14]. The electrolyte has to be gas tight and a purely ionic conductor with good conductivity [10]. Much research has been done on the materials and the interface between the electrode/electrolyte and the reaction mechanisms of SOFC system. In addition to the above components La (Sr, Mn) CrO_3interconnects [15] are used for the integration of system. Though a theoretical efficiency of approximately 70% is predicted, the commercialization of SOFCs are limited by their high cost and operating temperatures

>800°C.Components and current materials along with the technologies, challenges and targets are shown in Figure 1.5.

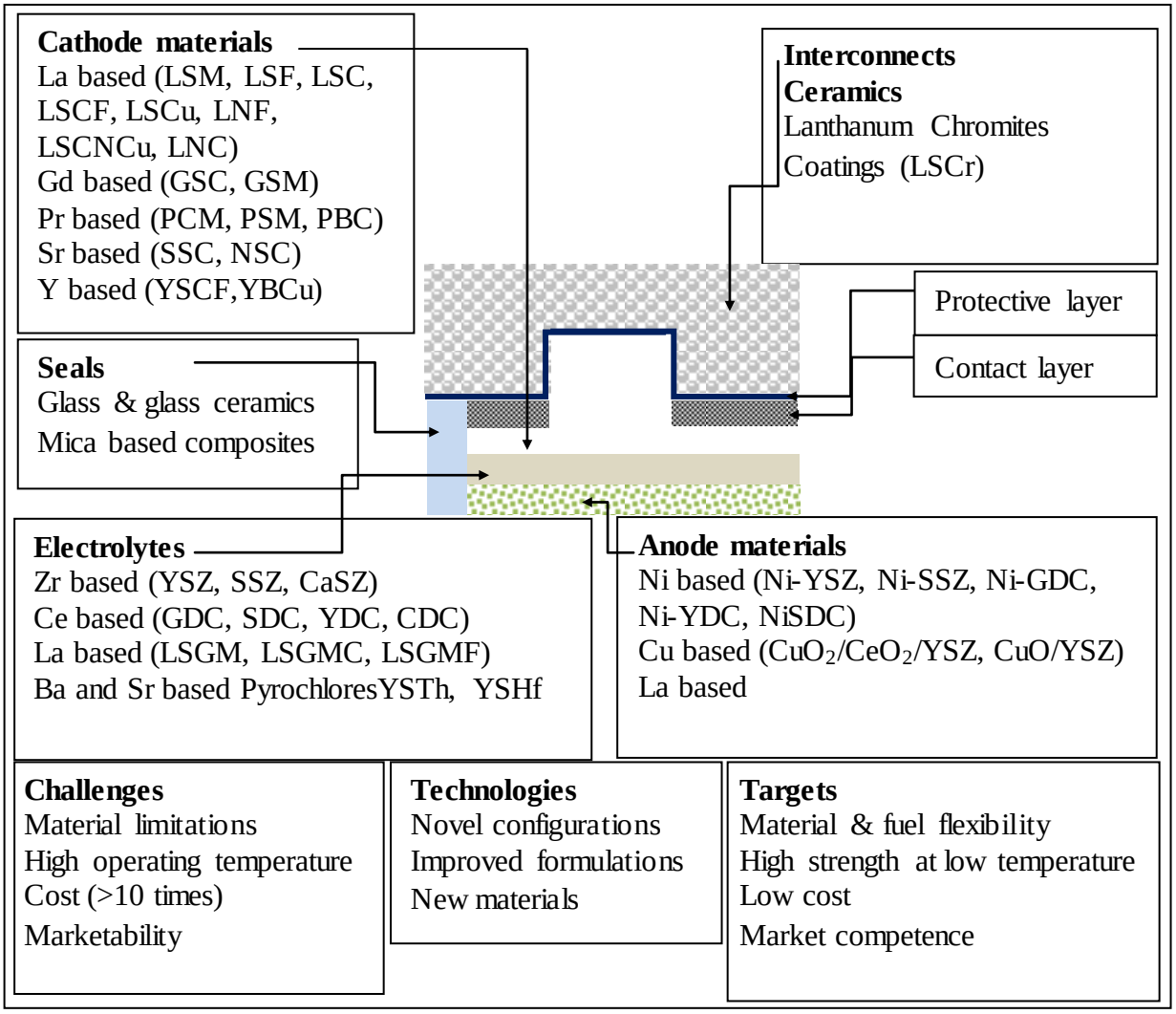

Fig.1.5 SOFC components and materials along with the technologies, challenges and targets

1.3.1 SOFC: Anode

The primary function of the anode for a solid oxide fuel cell is to promote the electrochemical oxidation of fuels. The general requirements for an SOFC anode material include [15- 17] good chemical and thermal stability during fuel cell fabrication and operation, high electronic conductivity under fuel cell operating conditions, excellent catalytic activity towards the oxidation of fuels, manageable mismatch in coefficient of thermal expansion (CTE) with adjacent cell components, sufficient mechanical strength and flexibility, ease of fabrication into desired microstructures (e.g., sufficient porosity and surface area), and low cost. Further, ionic

conductivity would be beneficial to the extension of active reaction sites for fuel oxidation from the TPBs to anode surfaces. Some other desirable but not yet readily achieved properties include tolerance to carbon deposition, sulfur poisoning and reoxidation, which are vital to achieving direct utilization of readily available fuels or renewable fuels in SOFCs.

The geometry of the electrodes and the design of the cells such as the thickness and the length of the current path from the anode to the current collector the specific values for each requirement may vary in a wide range to accept the general requirements. By Atikinson et al., the suggested anode electronic conductivity varies from 1 to 100 S/cm [18]. As explained elsewhere [18], the relaxed requirement of 1 S/cm for the effective electrical conductivity of a porous anode is valid only if a current collector layer is electrically well connected to the anode. Typically, the effective conductivity of a porous anode decreases rapidly as pores or an ionic conductor (such as 8YSZ) are introduced into the anode structure. For instance, the effective conductivity would be 10^2 to 10^3 S/cm for a conventional Ni-YSZ cermet anode with a composition of 50 vol% Ni and 50 vol% YSZ and a porosity of ~20 to 40% at 1000°C in a reducing atmosphere [19-24], whereas the electrical conductivity for pure Ni is ~ $2x10^4$ S/cm [25].

1.3.2. SOFC: Cathode

The main function of the cathode is to provide reaction sites for the electrochemical reduction of the oxidant. The key properties of the cathode are stability, electronic conductivity, compatibility, thermal expansion, porosity, and catalytic activity. The cathode material must be chemically, morphologically, and dimensionally stable in the oxidant environment and material must have no disruptive phase transformation between room temperature and fabrication temperature. It must maintain its desired microstructure in long-term operation since significant microstructural changes can cause degradation in cell performance.

The cathode must have sufficient electronic conductivity to support electron flow in the oxidizing environment and at the operating conditions. In general, maximum possible cathode conductivity is desirable to minimize ohmic losses. SOFC operates at high temperatures (800~1000^{o}C), the cathode must be chemically and thermally compatible with the other cell components, from room temperature to the operating temperatures and to the even higher temperatures at which the fuel cell is fabricated.

The cathode must be chemically compatible with other components, not only at the operating temperature but also at the much higher temperature at which the fuel cell ceramic structure is fabricated. Chemical interaction or elemental inter diffusion between the cathode and adjoining components must be limited in order to minimize the occurrence of unacceptable events such as second phase formation, stability reduction, change in thermal expansion, introduction of electronic conductivity in the electrolyte, etc.

Thermal expansion is concerned the thermal expansion of the cathode must match (from room temperature to operation and fabrication temperatures) with that of the other cell components to avoid cracking and delaminating during fabrication and operation, including thermal cycling.

The cathode must have sufficient porosity to allow gas transport to the reaction sites. The lower limit of porosity is set by mass transport considerations. The upper limit is based on consideration of the mechanical strength of the component.

Catalytic activity is concerned the cathode must have sufficient catalytic activity, and low polarization for the electrochemical reduction of the oxidant. In addition to these requirements, other desirable properties for the SOFC cathode are high strength and toughness, fabricability, and low cost.

Strontium doped lanthanum Manganite ($La_{1-x}Sr_xMnO_3$ or LSM) system is found to be the most effective cathode material in stabilized zirconia electrolyte based solid oxide fuel cell [26 - 30]. Most preferred candidate material in this system is $La_{0.8}Sr_{0.15}MnO_3$ owing to its high electronic conductivity, physical and chemical compatibility with other components at operating temperature and acceptable thermal expansion match with other cell components.

1.3.3 SOFC: Electrolyte

Electrical conduction in ceramics/crystalline solids depends on the material lattice defects. Lattice defects can be classified into two groups: (i) stoichiometric defects, in which the crystal composition is unchanged when defects are formed in the lattice and (ii) nonstoichiometric defects, which are formed as a consequence of a change in the crystal composition. Y_2O_3-stabilized ZrO_2 under the present investigation are doped crystalline oxides, thus having nonstoichiometric defects. Alternatively, defects can be classified into three groups by the size

and shape of the defect: (i) point defects, which involve interstitials or vacancies, (ii) line defects (dislocations), which are effectively point defects in two dimensions and (iii) plane defects, in which the whole layer in a crystal structure is defective. The three classical types of point defects are the Frenkel defect, Schottky defect (intrinsic point defects) and the Koch-Wagner defect (extrinsic point defect). The existence of the Frenkel or Schottky defect in a crystal can be estimated by comparing the ion radius, Vander Waals energy, and dielectric constant (i.e., comparing E_F- formation energy of the Frenkel defect and E_S - formation energy of the Schottky ionic pair). The Frenkel defect usually appears when the radii of the ions of the crystal differ considerably and the Vander Waals energy and the dielectric constant are somewhat large. The Schottky defect often occurs when the differences between the radii of the cation and anion and their abilities to be polarized are small and the Vander Waals energy and the dielectric constant are both relatively small [31-35].

Frenkel-type defect was introduced by Frenkel [34] and in this kind of defects some of the ions in an ionic crystal move from their normal lattice points to interstitial positions due to thermal fluctuation, forming interstitial ions (or interstitials). Interstitials vibrate at their sites and move to other interstitial sites by thermal fluctuation, chemical diffusion or an applied electric field. The vacant lattice sites or vacancies left by the interstitials can be occupied by other lattice point ions/atoms. As a result, vacancies also move in the crystal. These interstitials and vacancies are called the Frenkel defects. The number of interstitials in a unit volume (which is equal to that of vacancies), N_F, is given by eqn. (1.1) as,

$$N_F = N_i N \exp(-E_F/2kT) \tag{1.1}$$

Where, N and N_i are the total number of ions and interstitial positions per unit volume, respectively, k the Boltzmann constant, T the temperature, and E_F the formation energy of the Frenkel defect.

Schottky-type defect was introduced by Schottky [32]. According to this model, the same number of cationic and anionic vacancies exists in ionic crystals and the appearance and disappearance of vacancies are considered to occur mainly at the crystal surface or dislocation face. The number of the Schottky ionic pair per unit volume, N_S, is given by eqn. (1.2) as

$$N_s = N\exp(-E_S/2kT) \quad (1.2)$$

where N is the total number of ionic pairs per unit volume and E_s is the formation energy of the Schottky ionic pair. In these equations the thermal expansion of the crystal and the change in frequency of the lattice vibration are not considered. The number of defects increases with change in thermal expansion of the crystal and frequency of lattice vibration but the increase in the number of defects is usually small.

The Koch-Wagner type defect was introduced by Koch and Wagner [35] and this type of defects arise when impurities or dopants are introduced into the crystal lattice. For example, when Y_2O_3 is dissolved in ZrO_2 crystal to form a solid solution, the substitution of the trivalent Y^{3+} ion in the tetravalent Zr^{4+} sites create oxygen-ion vacancies in the ZrO_2 lattice in order to maintain the electro neutrality condition in the crystal.

1.3.3.1 Defect Generation in Zirconia Ceramics

At room temperature ZrO_2 has a monoclinic crystal structure. The monoclinic structure changes to a tetragonal form above 1170°C. The fluorite structure only exists at temperatures above 2370°C. The phase diagram is depicted in Fig. 1.6. However, the addition of certain aliovalent oxides stabilizes the fluorite structure of ZrO_2 from room temperature to its melting point of 2680°C. The fluorite structure of ZrO_2 is stabilized by direct substitution of divalent or trivalent cations of appropriate size for the host lattice cation Zr^{4+}. In this case, lattice defects are created to preserve the electro-neutrality condition in the solid solution. The probable models for structural defects in such cases are: (i) an oxygen-ion vacancy model with all metal ions being fixed at their lattice points, (ii) a cation interstitial model with all oxygen ions being fixed at their lattice sites (Frenkel type) and (iii) a mixed model of (i) and (ii) (Schottky type). It is well established that the oxygen-ion vacancy model applies to stabilize ZrO_2. The presence of a high oxygen-vacancy concentration in stabilized ZrO_2 gives rise to high oxygen-ion mobility, resulting in high oxygen-ion conductivity. Oxygen-ion conduction takes place in stabilized ZrO_2 by movement of oxygen ions via vacancies.

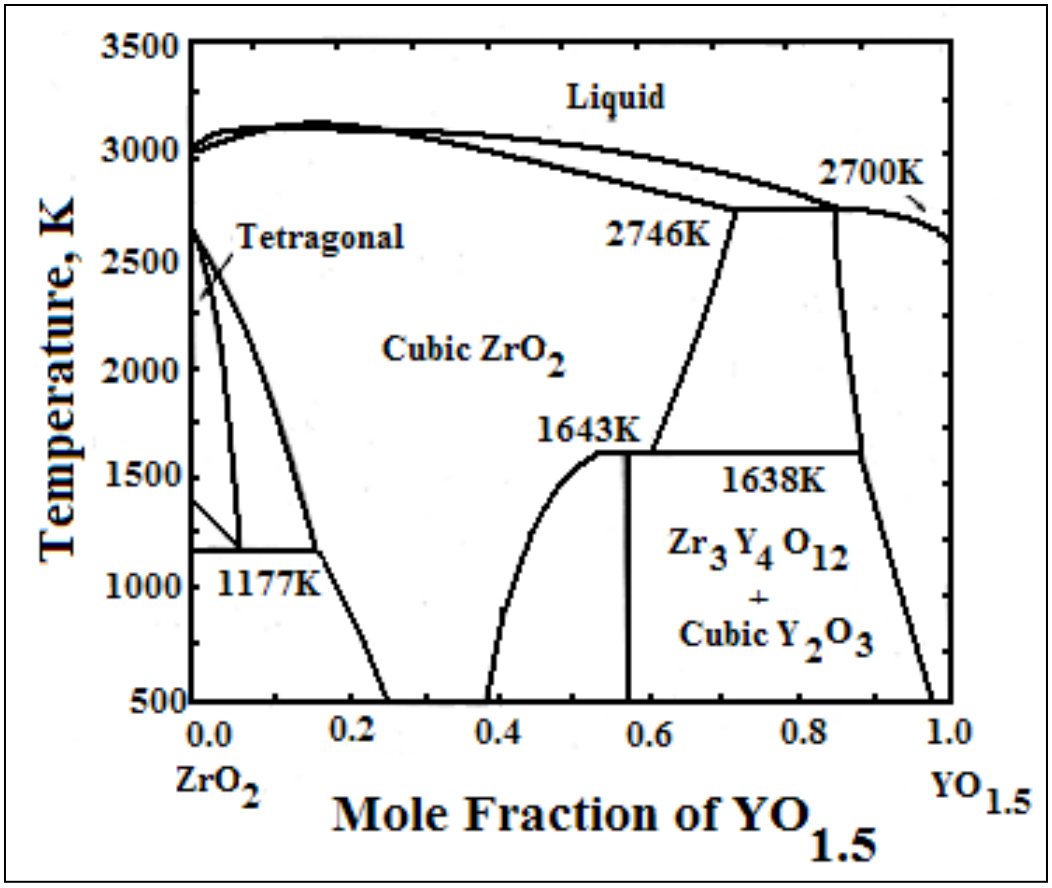

Fig. 1.6 Phase diagram of ZrO_2-Y_2O_3 system

When Y^{3+} substitutes Zr^{4+} at the corresponding lattice sites they creates vacancies in the oxygen sub lattice, since Y^{3+}cations have a lower valence than Zr^{4+}. The vacancy creation can be shown in Kroger-Vink notation [36],

$$Y_2O_3 \xrightarrow{ZrO_2} 2Y'_{Zr} + V_O^{\cdot\cdot} + 3O_O^X \qquad (1.3)$$

The vacancies are mobile and responsible for oxygen ion conduction in the stabilized zirconia. The composition with 8 mol% Y_2O_3 (8YSZ or yttria stabilized zirconia) has traditionally been dominated because the ionic conductivity exhibits a maximum at that yttria content [37-41] (Fig.1.7), which is supposed to be the minimum amount of yttria needed for the stabilization of the fluorite type cubic zirconia down to room temperature [42- 44]. The optimal concentration and the corresponding conductivity are largely dependent on the processing history and microstructural features such as dopant segregation, impurities, kinetically limited phase transitions and formation of ordered micro-domains [45].

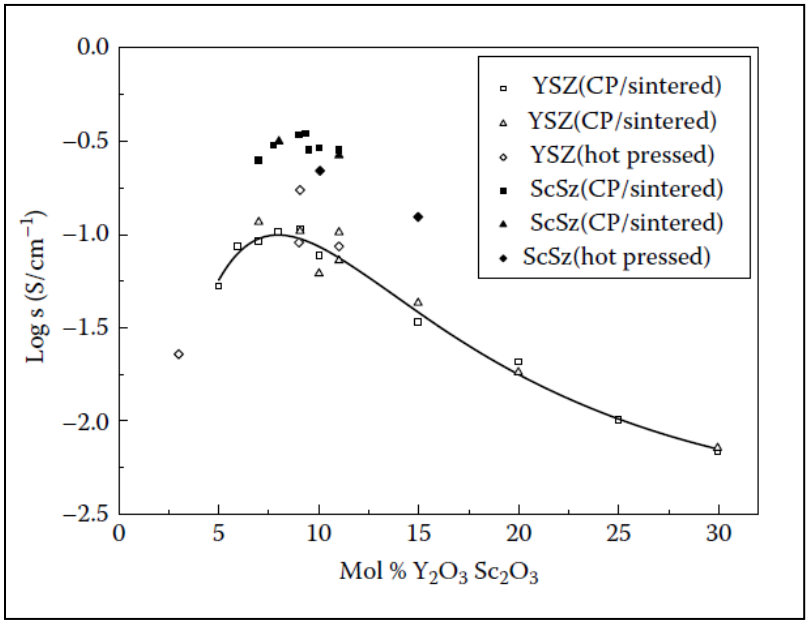

Fig.1.7 Conductivity of yttria- and scandia-stabilized zirconia in air at 1000°C [37]

1.3.3.2 Microstructure and ionic conductivity in fully stabilized zirconia ceramics

Yttria-stabilized zirconia (YSZ) is the state-of-the-art electrolyte for SOFCs due to its desirable chemical stability in both oxidizing and reducing atmospheres, low electronic conductivity, and high mechanical strength. The oxygen ion conductivity of YSZ is high enough for SOFCs operated at temperatures above 800°C. For SOFCs operated at intermediate temperatures YSZ electrolyte exhibit high resistance and hence low ionic conductivity.

There are conflicting reports concerning the grain size dependence of transport properties in nano- versus micro-scale YSZ [46]. Grain boundary conduction is very important because grain boundaries in YSZ exhibit blocking effect with regard to the ionic transport [47-49]. Grain-boundary consists of a grain-boundary core and two adjacent space-charge layers. The potential of the grain-boundary core of acceptor-doped ZrO_2 is positive; the enrichment of oxygen vacancies in the grain-boundary core is most probably responsible for the positive potential. The positively charged grain-boundary core expels oxygen vacancies while it attracts acceptor cations, thus causing the oxygen vacancy depletion and the acceptor accumulation in the space-charge layer [16, 50].

1.3.3.3 Schottky Barrier Model

A Schottky barrier model explains the grain-boundary electrical properties. In this model, a discontinuous grain-boundary impurity phase and direct grain-to-grain contacts are assumed. The ionic transport across the grain boundaries only takes place through the direct grain-to-grain contacts, rather than through the intermediate grain-boundary phase. The grain-boundary impurity phase blocks the ionic transport by decreasing the conduction path width and constricting current lines; this is the extrinsic cause of the grain-boundary blocking effect. The grain-to-grain contacts are electrically resistive in nature, which is due to the oxygen vacancy depletion in the space-charge layer and is considered to be the intrinsic as well as the decisive cause of the grain-boundary blocking effect [48, 50]. The intrinsic grain-boundary blocking effect becomes less pronounced at high temperatures and in the case of high-dopant concentrations. As a result, the grain-boundary contribution increases with decreasing temperatures, which is particularly important for intermediate-temperature SOFCs. For example, for YSZ materials produced by several methods, the fraction of the total resistance due to grain boundary resistance is negligible at 900°C, but increases to approximately 0 - 40% at 700°C, and then further to ~10 to 65% at 500°C [16, 51].

The Schottky barrier model shows that the space charge potential is typically 0.25 V for 8YSZ and decreases with decreasing grain size. Therefore, the concentration of oxygen vacancies in the space-charge layer increases, resulting in increasing conductivity with decreasing grain size. For e.g., YSZ with grain sizes less than 10 nm shows 50% higher conductivity than those (YSZ) consisting of larger grain sizes [52, 53].

1.4 Technical Challenges in SOFC: Electrolytes

Table 1.1 shows various desirable attributes and ranking of the currently used electrolyte material used for SOFC applications. Investigations have been made to address the issues of high operating temperatures through the development of low temperature electrolyte materials, such as nano ceria doped Gadolinia or Samaria. However, reduction of Ce^{+4} to Ce^{+3} at temperatures >600°C pose a major problem for its use [50, 54, 55]. Further, the reduction in operating temperature will reduce the electrochemical performance of the SOFC system due to the increased polarization resistance of the electrode reactions and decreased electrolyte

conductivity. This makes 8YSZ as the material of choice of SOFC electrolyte and maximizing the electrolyte ionic conductivity is of significant importance. Various approaches to improve the ionic conductivity of 8YSZ are shown in Fig.1.8.

Table 1.1: Ranking of electrolyte material based on major attributes:

Attributes	**Zirconia based**	**Ceria based**	**LSGM based**
Conductivity	▲ (JALCOM, 2010)	✓ (Nature, 2001)	✓ (JPS, 2011)
Thermal stability	✓ (JPS, 2007)	▲ (JPS, 2007)	▲ (JPS, 2007)
Chemical Stability	✓ (JPS, 2007)	▲ (SSI, 200I)	▲ (JPS, 2007)
Mechanical Stability	✓ (JPS, 2008)	▲ (JPS, 2007)	▲ (JES, 2001)
Thermal expansion	✓ (MRS, 2005)	X (JPS, 2011)	X (MRS, 2005)

Note:
✓ - acceptable , X - not acceptable, ▲-improvement required
Journal of Alloys and compounds (JALCOM) [56]; Nature [57]; Journal of Power Sources (JPS)[58, 59, 61, 62]; Solid State Ionics (SSI) [60]; Journal of European Ceram. Soc. (JES) [63], MRS Bulletin [64]

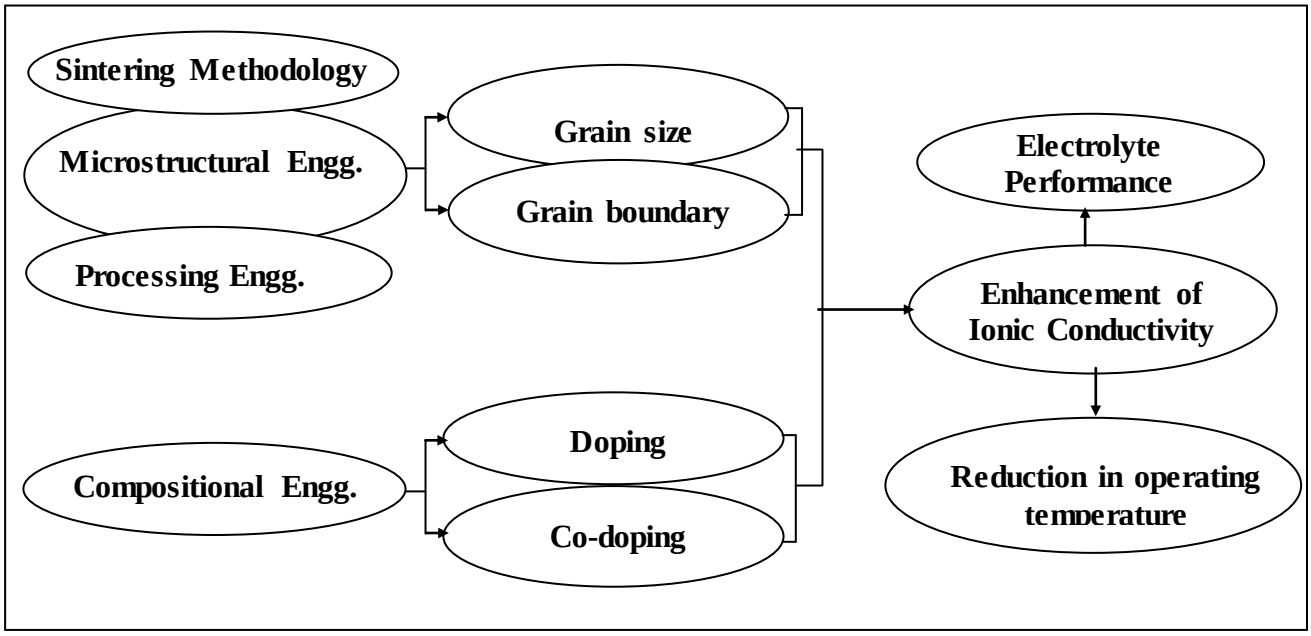

Fig.1.8 Approaches to improve the ionic conductivity of 8YSZ

1.5 Scope of the work

It is evident that the ionic conductivity of electrolyte can be influenced by many parameters such as, compositional engineering, microstructural engineering and process engineering. An enormous effort has been made for the improvement in ionic conductivity of 8YSZ by doping oxides of various elements Sc, Yb, Y, Dy, Gd or Eu [65 - 67]. From a practical point of view to enhancing the ionic conductivity of 8YSZ are extensively studied. From a detailed survey of literature, it has been found that the role of microstructure in the ionic conductivity of 8YSZ (for SOFC application) is not conclusive. Therefore, the current investigation will make an attempt to address this issue through:

- Processing of commercially available 8YSZ powders (TZ-8YS, Tosoh Corporation, Japan widely used for SOFC application) into compacts through compaction (uniaxial) and colloidal processing such as, slip casting and methyl cellulose based thermal gel casting followed by the comparative evaluation of the methods.
- Engineering the microstructure of sintered zirconia electrolytes with various grain sizes through various sintering methodologies such as, conventional (Conventional Ramp and Hold sintering), modified conventional (Rate Controlled Sintering, Two Stage Sintering) and non-conventional (Microwave Sintering, Spark Plasma Sintering) with commercially available 8YSZ powders.
- Ionic conductivity measurement through impedance analysis and estimation of grain and grain boundary contributions to the observed conductivity by estimating the activation energies.
- Elucidation of the effect of prominent sintering mechanisms for the evolution of microstructures and correlation of the role of grain and grain boundary with observed ionic conductivities of SOFC zirconia electrolytes.
- Fabrication of single cell using electrolytes of engineered microstructure and evaluation of its electrochemical performance.

1.6 References

1. http://www.fossil.energy.gov/programs/powersystems/fuelcells/fuelcells_solidoxide.html
2. Baur E. Preis H, Z. Uber BrennStoffketen mit Festleitern. Elektrochem., 1937; **43**: 727
3. Davtyan O.K. The problem of direct conversion of the chemical energy of a fuel to electrical energy [in Russia], Izd. ANSSSR, Moscow, 1947.
4. Kim J.W, Virkar A, Fung K.Z, Mehta K, Singhal S.C, Polarization effect in intermediate temperature, anode supported solid oxide fuel cells. J. Electrochem. Soc. 1999; **146**: 69
5. Versa Power Systems. Solid Oxide Fuel Cell Technology. [Online] 2007. http://www.versa-power.com/.
6. NexTech Materials. NextCell Advanced Electrolyte Planar Cell. fuelcellmaterials.com. [Online] May 2007. http://www.nextechmaterials.com/files/NextCell.pdf. 10-10101-100.
7. Acumentrics. About Fuel Cell Energy, Tubular, and Solid Oxide Generator Systems. Acumentrics.com. [Online] 2007. http://www.acumentrics.com/knowledge-center-about-fuel-cells.htm.
8. Adaptive Materials Inc. AMI-Adaptive Materials Inc. [Online]2007 http://www.adaptivematerials.com
9. Bance P, Brandon N.P, Girvan B, Holbeche P, O'Dea S, Steele B.C.H, Spinning out of fuel cell Company from UK University – 2 years program at Ceres Power. J. Power Sources. 2004; **131**:86.
10. Tiffee E.I, Weber A, Herbstritt D. Materials and technologies for SOFC-components. J. Euro. Ceram. Soc. 2001; **21**:1805.
11. Matsuzaki Y, Yasuda I. The poisoning effect of sulfur-containing impurity gas on a SOFC anode: Part I. Dependence on temperature, time, and impurity concentration. Solid State Ionics.2000; **132**: 261.
12. Berkel V. F. P. F, Heuveln V. F. H, Huijsmans J. P. P. Characterization of solid oxide fuel cell electrodes by impedance spectroscopy and I-V characteristics. Solid State Ionics.1994; **72**: 240.
13. Steele B. C. H.Behaviour of porous cathodes in high temperature fuel cells. Solid State Ionics.1997;**94**: 239.

14. Brant M. C, Matencio T, Dessemond L, Domingues R. Z. Electrical and microstructural ageing of porous lanthanum strontium manganite/yttria-doped cubic zirconia electrodes. J. Chemistry Material.2001; **13**: 3954.
15. Zhu W.Z, Deevi S.C. A review on the status of anode materials for solid oxide fuel cells. Mater. Sci. Eng.A 2003; **362**: 228.
16. Minh N.Q, Takahashi T. Science and Technology of Ceramic Fuel Cells. The Netherlands: Elsevier Science B.V. 1995.
17. McEvoy A. Anodes, In: Singhal S.C, Kendall K, editors. High Temperature Solid Oxide Fuel Cells: Fundamentals, Design, and Applications. Oxford, UK, Elsevier.2003; 140.
18. Atikinson A, Barnett S, Gorte R.J, Irvine J.T.S, McEvoy A.J, Mogensen M, Singhal S.C, Vohs J. Advanced anodes for high-temperature fuel cells. Nature Mater.2004; **3**:17.
19. Dees D.W, Claar T.D, Ealser T.E, Fee D.C, Marzek F.C. Conductivity of porous Ni/ ZrO_2-Y_2O_3cermets. J. Electrochem Soc.1987; **134**: 2141.
20. Tiffee E.I, Wersing W, SchieM, Greiner H. Ceramic and Metallic Components for a Planar SOFC. Berichte der Bunsen-GesellschaftfürPhysikalischeChemie1990; **94**: 978.
21. Itoh H, Yamamoto T, Mori M. Configurational and electrical behavior of Ni-YSZ cermet with novel microstructure for solid oxide fuel cell anodes. J. Electrochem. Soc. 1997; **144**: 641.
22. Pratihar S.K, Basu R.N, Mazumder S, Maiti H.S. Electrical conductivity and microstructure of Ni-YSZ anode prepared by liquid dispersion method. In: Singhal S.C, Dokiya M, editors. Proceedings of the Sixth International Symposium on Solid Oxide Fuel cells (SOFC-VI), Pennington, NJ: The Electrochemical Society. 1999; **99**(19): 513.
23. Lee J.H, Moon H, Lee H.W, Kim J, Kim J.D, Yoon K.H. Quantitative analysis of microstructure and its related electrical property of SOFC anode, Ni-YSZ cermet. Solid State Ionics 2002; **148**: 15.
24. Lide D.R. CRC Handbook of Chemistry and Physics, 82nd edition, Boca Raton, FL: CRC Press, 2001; 12.
25. Radovic M, Lara-Curizio M. Mechanical properties of tape cast nickel-based anode materials for solid oxide fuel cells before and after reduction in hydrogen. ActaMaterialia. 2004; **52**: 5747.

26. Kuo J.H, Anderson H.U, Sparlin D.M. Oxidation-reduction behaviour of undoped and Sr-doped $LaMnO_3$: defect structure, electrical conductivity and thermoelectric power. J. Solid State Chem. 1990; **87**: 55.
27. Kertesz M, Reiss I, Tannhauser D.S, Langpape R, Rohr F.J. Structural and electrical conductivity of $La_{0.84}Sr_{0.16}MnO_3$, J. Solid State Chem. 1982;**42**:125.
28. Hashimoto T, Ishizawa N, Mizutani N, Kato M. Electrical Resistivity and Seebeck coefficient of $La_{1-x}Mn_xMnO_3$ (M = Ca, Sr) single crystals. J. Mater. Sci. 1988; **23**: 1102.
29. Katayama K, Ishihara T, Ohta H, Takeuchi S, Esaki Y, Enukai E, Sintering and electrical conductivity of $La_{1-x}Mn_xMnO_3$. J. Ceram. Soc. Jpn. 1989; **97**: 1327.
30. Hammouche A, Schouler E.L, Henault M. Electrical and thermal properties of Sr doped $LaMnO_3$. Solid State Ionics. 1988; **28** (30): 1205.
31. Badwal S.P.S, Koger F. Solid oxide electrolyte fuel cell review, Ceram. Int. 1996; **22:**257.
32. SchottkyW. Z Phys. Chem.1935; **29**B: 335.
33. Jost W. Diffusion and electrolytic conduction in crystals (ionic semiconductors). J. Chem. Phys. 1933; **1**: 466.
34. Frenkel J, Über die Wärmebewegung in festen und flüssigen Körpern. Z. Phys. Chem. 1926; **35**: 652.
35. Koch E, Wagner C. Z. Phys. Chem. 1937; **38**B: 295.
36. Kroger F, Vink H. J, Solid State Physics, Seitz F, Turnbull D, Academic Press, New York. 1965; **3**:304.
37. Fergus J.W. Electrolytes for solid oxide fuel cell. J. Power Sour. 2006; **162**: 30.
38. Strickler D.W, Carlson W.G. Ionic conductivity of cubic solid solutions in the system CaO-Y_2O_3-ZrO_2. J. Am. Ceram. Soc. 1964; **47**: 122.
39. Dixon J.M, LaGrange L.D, Mergen U, Miller C.F, Porter J.T. Electrical resistivity of stabilized zirconia at elevated temperatures. J. Electrochem. Soc.1963; **110**: 276.
40. Haering C, Roosen A, Schichl H. Degradation of the electrical conductivity in stabilized zirconia system. Part I: Yttria – stabilized zirconia. Solid State Ionics. 2005; **176**: 253.
41. Etsell T. H, Flengas S.N. Electrical properties of solid oxide electrolytes. Chem. Rev. 1970; **70**: 339.
42. Badwal S.P.S. Zirconia based solid electrolyte, microstructure, stability and conductivity. Solid State Ionics. 1992; **52**: 23.

43. Kharton V.V, Naumovich E.N, Vecher A.A. Research on the electrochemistry of oxygen ion conductors in the former Soviet Union I. ZrO_2-based ceramic materials. J. Solid State Electrochem. 1999; **3**: 61.
44. Yamamoto O, Arachi Y, Sakai H, Takeda Y, Imanishi N, Mizutani Y, Kawai M, Nakamura Y. Zirconia based oxide ion conductors for solid oxide fuel cell. Ionics. 1998; **4:** 403.
45. Kharton V.V, Marques F.M.B, Atkinson A. Transport properties of solid oxide electrolyte ceramics: a brief review. Solid State Ionics. 2004; **174**: 135.
46. Perry N. H, Kim S, Mason T. O. Local electrical and dielectric properties of nanocrystalline yttria-stabilized zirconia. J. Mater. Sci. 2008; **43**: 4684.
47. Yamahara K, Jacobson C.P, Visco S.J, Jonghe L.C. De, Electrochem. Soc. Proc. 2003–07, SOFC VII, 2003; 187.
48. Guo X, Maier J. Grain boundary blocking effect in zirconia: A Schottky barrier analysis. J. Electrochem. Soc.2001; **148**: 121.
49. GuoX, WaserR. Electrical properties of the grain boundaries of oxygen in conductors: Acceptor – doped zirconia and ceria. Prog. Mater. Sci. 2006; **51**:151.
50. Zha S, Xia C, Meng G. Effect of Gd(sm) doping on properties of ceria electrolyte for solid oxide fuel cells. J. Power Sour. 2003; **115**: 44.
51. Minh N.Q. Ceramic Fuel Cells, J. Am. Ceram. Soc. 1993; **76**: 563.
52. Patil D. S, Prabhakaran K, Dayal R, Prasad C.D, Gokhale N.M, Samui A. B, Sharma S. C. Eight mole percent yttria stabilized zirconia powders by organic precursor route. Ceram. Inter. 2008; **34**:1195.
53. Dahl P, Kaus I, Zhao Z, Johnson M, Nygren M, Wiik K, Grande T, Einarsrud M.A. Densification and properties of zirconia prepared by three different sintering techniques. Ceram. Inter. 2007; **33**: 1603.
54. Iguchi E, Ueda K, Jung W. H. Conduction in $LaCoO_3$ by small-polaron hopping below room temperature. Phys. Rev. 1996; B **54**:17431.
55. Prabhakaran K, Beigh M. O, Lakra J, Gokhale N. M, Sharma S. C. Characteristics of 8 mol% yttria stabilized zirconia powder prepared by spray drying process, J. Mater. Proc. Tech. 2007; **189**: 178.

56. Hesabi Z. R, Mazaheri M, Ebadzadeh T. Enhanced electrical conductivity of ultrafine-grained $8Y_2O_3$ stabilized ZrO_2 produced by two step sintering technique. J. Alloys Compound. 2010; **494**: 362.
57. Steel B.C.H, Heinzel A. Materials for fuel cell technologies. Nature 2001; **Y**: 345.
58. Huang J, Xie F, Wang C, Mao Z. Development of solid oxide fuel cell materials for intermediate to low temperature operation. J. Power Sour.2011;1
59. Molenda J, Swierczek K, Zajac W. Functional materials for IT solid oxide fuel cell. J. Power Sour. 2007; **173**: 657.
60. Badwal S.P.S, Stability of SOFC cell components. Solid State Ionics.2001; **143**: 39.
61. Yokokawa H, Hu T, Iwanschitz B, Mai A. Fundamental mechanisms limiting solid oxide fuel cell durability. J. Power Sour. 2008;**182**:400
62. Hui S, Roller J, Yick S, Zhang X, Petit C.D, Xie Y, Maric R, Ghosh D. A brief review of the ionic conductivity enhancement for selected oxide electrolytes. J. Power Sour. 2007; **172**: 493.
63. Ivers-Tiffee E, Weber A, Herbstritt D. Materials and technologies for SOFC components. J. Euro. Ceram. Soc. 2001; **21**: 1805.
64. Yokokawa H, Sakai N, Horita T, Yamaji K, Brito M.E. Electrolytes for Solid-Oxide Fuel Cells. MRS Bull. 2005; 30: 591
65. Bard J, Faulkner L.R. Electrochemical Methods - Fundamentals and Applications, John Wiley & Sons, New York, 2001.
66. Siemens A.G. The Principle behind the technology. Siemens Power Generation. [Online] 2007.http://www.powergeneration.siemens.com/products-solutions-services/products-packages/fuel-cells/principle-behind-technology/.
67. Arachi Y, Sakai H, Yamamoto O, Takeda Y, Imanishi N. Electrical conductivity of the ZrO_2-Ln_2O_3 (Ln=lanthanides) system. Solid State Ionics. 1999; **121**: 133.

*****

Chapter II

Processing of 8 mol % Yttria Stabilized Zirconia (8YSZ) Specimens

2.0 Introduction

Processing of polycrystalline ceramic components requires number of stages: synthesis of powders, milling, sieving and mixing with proper additives, shape forming, drying and densification followed by machining. Parameters of each processing step are critical as it affects the final ceramic properties of the products. Therefore it is very critical to have an in-depth understanding of each stage, when processing ceramic materials. For example, flow behaviour of ceramic precursors is the combination of physical and chemical properties of the material such as particle size and their distribution, morphology, surface area and surface chemistry. It is also observed that flow property of a mix that is suitable for a particular processing regime may not be suitable for the other regimes. Granules used for compaction processing are not suitable for extrusion processing as the mix will restrict the flow and gets compacted under extrusion shear limits. Further, slurry suitable for casting will creep under its own load and does not have sufficient mechanical strength to maintain its shape integrity while in extrusion or compaction. In order to define the flow property of the processing regimes the concept of Binder Volume Concentration (BVC) provides an estimate of the maximum amount of medium accommodated to facilitate the flow in the compaction, extrusion and casting regime.

This chapter highlights the three processes followed for the shaping of fully stabilized zirconia, which includes characterization of 8YSZ powder followed by conventional compaction processing, colloidal shaping by slip casting and a novel process developed for the first time based on methyl cellulose thermal gel casting (Complex shaping). The chapter also covers powder characterization, elucidation of flow behaviour with respect to the processing regime, shaping followed by drying and characterization of green pellets.

2.1 Characterization of 8YSZ ceramic powders

Fully stabilized zirconia powder (TZ-8YS) was procured from Tosoh Corporation, Japan and is characterized for phase analysis using X-ray Diffraction Technique (XRD) and particle size by

Dynamic Light Scattering (DLS). Chemical composition and surface area of the powder has been analyzed using X- Ray fluorescence (XRF) and BET nitrogen adsorption method (BETSA) respectively. The details of the measurements are discussed below.

2.1.1 Phase Identification by X-Ray Diffraction

Phase analyses of the as received powders were performed by x-ray diffraction (XRD) using CuKα radiation in Bruker D8 Advanced system (Bruker AXS GmbH, Karlsruhe, Germany). The XRD system was equipped with LynxEye^{TM} (Bruker AXS) 1-dimensional compound silicon strip detector for high quality diffraction data. The powder samples were loaded on a non-diffracting sample holder placed in the Bragg-Brentano diffractometer setup.

The as recorded XRD profiles were normalized to 100% in each case. The background correction as well as $K\alpha_2$ stripping using Rachinger's method was performed prior to the phase analysis using search-match program with ICDD-PDF4+ database. Identification of a crystalline phase was based on comparison of the observed d-spacing and relative intensities with those of a reference material pattern compiled in the ICDD database.

The X-ray diffraction pattern for zirconia sample is shown in Fig.2.1. It is evident from the XRD patterns that the powder sample contains pure cubic phase indicating full stabilization of the cubic structure.

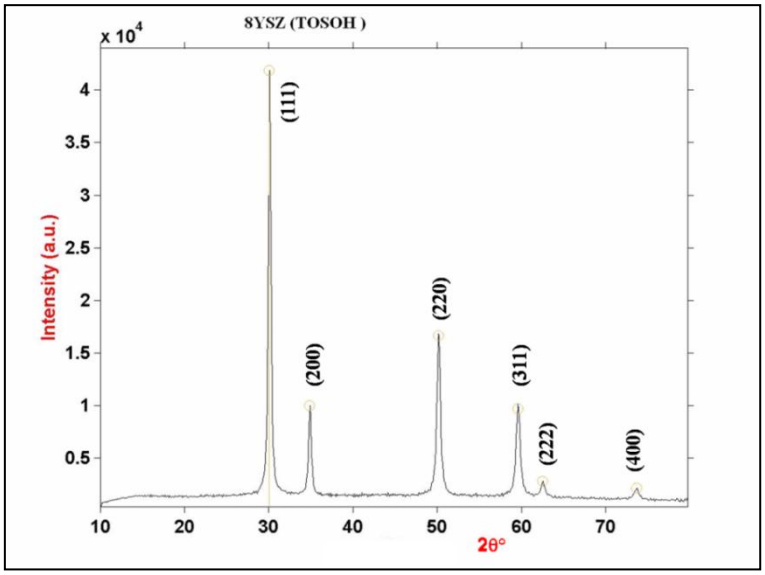

Fig.2.1 XRD Pattern of the sample

2.1.2 Particle Size Analysis by Dynamic Light Scattering

Particle Size Analysis of the as received powder was carried out using Photon Correlation Spectroscopic measurements. Photon Correlation Spectroscopy is based on the measurement of the velocity of particles diffusing due to Brownian motion. The random movement of particles in a liquid media due to the inter-particle collision is known as Brownian motion. This motion causes fluctuations of the local concentration of the particles resulting in local in-homogeneities in the refractive index of the material. This in turn leads to Rayleigh scattering spectrum with line width Γ (defined as the half-width at half-maximum), which is proportional to the diffusion coefficient D of the particles (2.1):

$$\Gamma = Dk^2 \tag{2.1}$$

Where k = (4πn/λ) sin (θ/2), n is the refractive index, λ the laser wavelength, and θ the scattering angle. Assuming the particles to be spherical and non-interacting, one can obtain the mean radius 'r' from the Stokes-Einstein equation (2.2).

$$D = \frac{K_B T}{6\pi\eta r} \tag{2.2}$$

D – Diffusion coefficient, k_B-Boltzmann constant, T - absolute temperature, r – particle radius, and η – Coefficient of viscosity of the medium.

Particle size analysis was carried out by dispersing 0.05 gram of as received powder in 100 ml de-ionized water using dispersant darvan 821A i.e., ammonium polyacrylate (R. T. Vanderbilt Co., Inc., Norwalk, CT, USA). Suspensions were ultrasonicated for 15 minutes using Sonics (VCX 750, Sonics & Materials Inc., Newtown CT, USA) to ensure the homogeneity and filled into the glass cuvette. The well dispersed suspensions based on zeta measurements were subjected to DLS measurements using a Nanosizer (Fig.2.2) and particle size distribution curve is shown in Figure 2.3. An average particle size of 205 nm with a particle size distribution ranging from 78.8 – 615 nm is exhibited by the measurements.

Fig.2.2 Nanosizer used for analysis

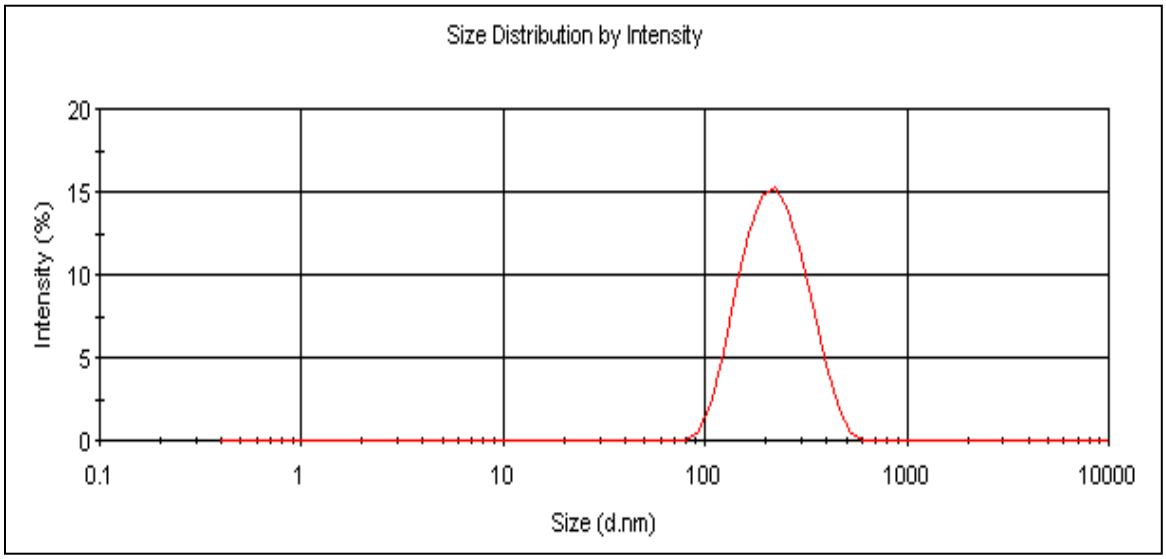

Fig.2.3 Particle size distribution curve

2.1.3 BET Surface Area analysis

Surface area measurements were carried out by BET surface area analyzer (Micromeritics Instruments Corp, ASAP 2020, Norcross GA, USA), which works on the principle of static volumetric technique, introducing consecutive known doses of adsorbate (nitrogen) inside the sample holder kept at liquid nitrogen temperature (77K). This facilitates adsorption on sample

surface once a dose of gas is injected, the pressure slowly decreases until an equilibrium pressure is established in the manifold.

BET theory is an extension of the Langmuir theory for monolayer molecular adsorption to multilayer adsorption with the following assumptions: (a) gas molecules physically adsorb on a solid surface in infinite layers; (b) there is no interaction between each adsorption layer. The resulting adsorption isotherm, known as **BET equation** as per the name of the Scientists, Brunauer, Emmett, and Teller, is expressed as (2.3):

$$\frac{1}{[Q(P_0/P-1)]} = \frac{C-1}{Q_m C}\left(\frac{P}{P_0}\right) + \frac{1}{Q_m C} \tag{2.3}$$

Where, P and P_0 are the equilibrium and the saturation pressure of adsorbates at the temperature of adsorption, Q is the adsorbed gas quantity, and Q_m is the monolayer adsorbed gas quantity. C is the BET constant, which is expressed by the equation (2.4):

$$C = \exp\left(\frac{E_1 - E_L}{RT}\right) \tag{2.4}$$

E_1 is the heat of adsorption for the first layer, and E_L is that for the second and consecutive layers and is equal to the heat of liquefaction.

Equation (2.3) is an adsorption isotherm and can be plotted as a straight line with $1 / Q [(P_0 / P) - 1]$ on the y-axis and $\varphi = P / P_0$ on the x-axis. This plot is called a **BET plot**. The linear relationship of this equation is maintained only in the range of $0.05 < P / P_0 < 0.35$.

In the present study, 0.3925gm of the 8 Y zirconia powder was degassed at a temperature of 300°C to remove adsorbed gases and BET analysis was carried out at liquid nitrogen temperature. Relative pressure, quantity of nitrogen adsorbed and $1 / Q [(P_0 / P) - 1]$ obtained through BET analysis is shown in Table 2.1 and the plot of $1/ [Q (P_0/P-1)]$ against (P/P_0) is shown in Fig.2.4.

Table 2.1 Relative pressure, Quantity adsorbed and $1 / Q [(P_0 / P) - 1]$ obtained from BET experiment

Relative Pressure (P/P_0)	**Quantity Adsorbed, Q (cm^3/g STP)**	**$1/[Q(P_0/P-1)]$**
0.05464	1.2691	0.045543
0.11467	1.4420	0.089820
0.17519	1.5811	0.134340
0.23723	1.7085	0.182032
0.30309	1.8443	0.235815

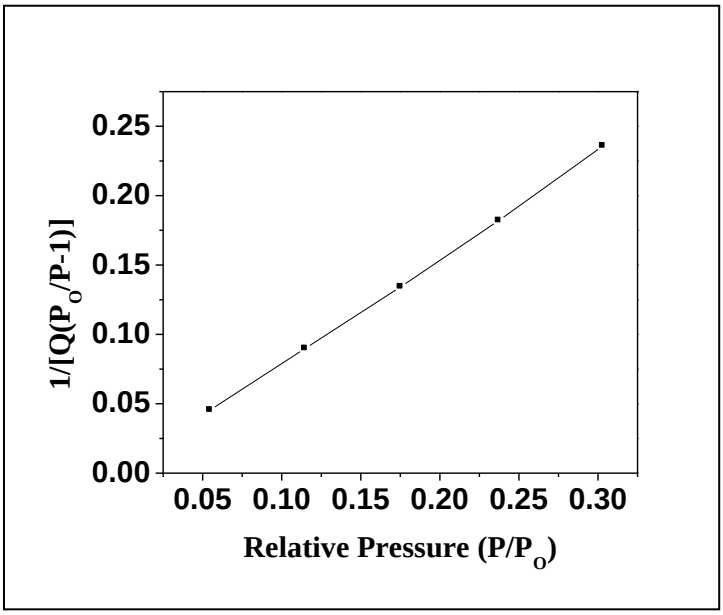

Fig.2.4 BET plot of 8YSZ –Tosoh powder

From the BET plot, the value of the slope *A* and the y-intercept *I* were estimated and the monolayer adsorbed gas quantity Q_m and the BET constant *C* were determined using the following equation (2.5 & 2.6):

$$Q_m = \frac{1}{A + I} \tag{2.5}$$

$$C = 1 + \frac{A}{I} \tag{2.6}$$

Further the total surface area S_{total} and a specific surface area S were evaluated by the following equations (2.7):

$$S_{BET,total} = \frac{(Q_m N s)}{V} \tag{2.7}$$

Where Q_m is in units of volume which are also the units of the molar volume of the adsorbate gas nitrogen

$$S_{BET} = \frac{S_{total}}{a} \tag{2.8}$$

N: Avogadro's number, (6.02×10^{23} mol^{-1})

s: adsorption cross section of the adsorbing species [$16(A°)^2$]

V: molar volume of nitrogen

a: mass of 8mol% yttria stabilized zirconia powder (0.3925gm)

BET Surface Area of the 8 Y Zirconia samples were estimated to be 5.7 m^2/gm

2.1.4 Chemical Composition by X- Ray Fluorescence (XRF) Analysis

XRF is a non-destructive elemental analysis technique which enables rapid compositional analysis of sample. When polychromatic X- rays strike a sample containing several elements, electrons from inner (core) shells (K, L, M, N) of the atoms of the elements are expelled, and electrons from the outer shells fill these vacancies. Each electron transition constitutes an energy change in the atom from a higher to a lower energy state, and the energy difference between the two states of the atom is emitted as an X-ray photon. Since these energy differences are characteristic of each element, the elements in the sample are identified by the characteristic X-ray and the intensity is proportional to their concentration in the sample. As received powder of 8YSZ was subjected to XRF analysis using an X- ray Fluorescence Spectroscope (ARL quanta, EDXRF, Thermo make) installed at Centre for Materials for Electronics Technology (CMET), Hyderabad and the chemical compositions are shown in Table 2.2. A weight percentage of 13.10% Y_2O_3 further confirms full stabilization.

Table 2.2 Chemical Compositions 8YSZ –Tosoh powder

Chemical Analysis	**Wt. (%)**
Y_2O_3	13.10
Al_2O_3	< 0.1
SiO_2	< 0.02
Fe_2O_3	< 0.01
Na_2O	< 0.12
ZrO_2	Balance

2.2 Estimation of Critical Binder (Water) Volume Concentration (CBVC)

Critical Binder Volume Concentration (CBVC) was estimated using 60 gm of zirconia mix titrating against the linseed oil using a Brabender Rheometer PL2000 mixer and the plot of torque against the binder volume concentration was recorded (Fig.2.5). In this mixing experiment (in Banbury mixer), wetting liquid such as linseed oil (binder) is added stepwise to the powder and the mixing torque is monitored as the mix is continuously sheared by means of a specially contoured rotating blades. Considering the volume of the oil added and the equilibrium torque value achieved after each addition a plot is drawn with the ordinate representing the equilibrium torque values and the abscissa in terms of the volume% of binder in the mix. Initially, when the amount of the liquid media is very small, compared to CBVC, all the liquid goes to replace the powder-air interface with powder-liquid interface forming an adsorbed monolayer on the particles (pendular state observed in oil rub out test, Fig.2.6 (a).) Therefore, the torque value is very low. As the liquid amount is increased, pendular bonds begin to form as a result of the liquid bridging amongst the individual particles, leading to the formation of particle clusters. As the powder mass undergoes shearing and mixing continuously, there exists a dynamic equilibrium, where the particle clusters are repeatedly broken down and formed again in a new particle packing arrangement in a cyclic fashion. The interparticle bonding occurs in the clusters due to the negative capillary pressure existing in the liquid bridge and the interfacial

forces at the liquid-gas interface. Any disruption of the clusters during shearing has to overcome these forces along with the frictional forces due to mechanical interlocking of particles. Therefore, the mixing torque, which is a measure of the extent of resistance offered by the clusters to deform in a shear field, starts rising once particle clusters begin to form.

As the amount of the liquid is further increased, the powder mass moves from the pendular state to the funicular state (Fig.2.6 (b)), where the liquid is distributed partly as bridge bonding and partly as entirely filled voids. In any partially filled void, if the liquid lenses at the point of contact between the particles overlap a small gas bubble forms in the interparticle space. Such bubbles are inherently unstable because of high capillary pressure, 4τ /d, (τ is the surface tension and d is the bubble diameter) and hence will collapse to form either a liquid bridge or a completely filled void. The interparticle bonding in this state is a result of liquid bridging as well as interfacial force at the surfaces of the clusters. Subsequent additions of the liquid will maintain the powder mass in the funicular state. But bigger clusters form by the growth of smaller ones as more and more liquid is added, until ultimately the mass becomes a coherent paste at the point of CBVC, which is the capillary state (Fig.2.6(c)). Once the point of CBVC is crossed, the particle structure gets dilated, and reduces interparticle friction and thereby freeing the entrapped liquid. The mean interparticle distance increases, and the mix are akin to a dispersion of solid particles in a liquid medium. The mixing torque then becomes primarily the viscosity of the liquid medium as altered by the presence of the powered particles and it falls off as the binder content is increased [1]

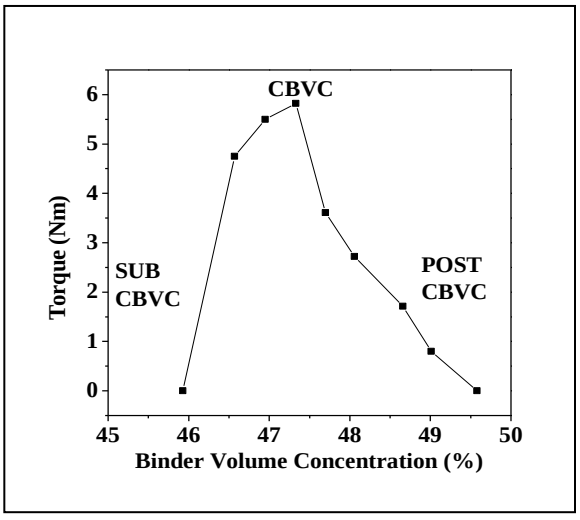

Fig.2.5 Torque vs. binder volume concentration, showing the region of Sub-CBVC, CBVC, Post-CBVC

2.2.1 Oil Rub Out Test

In order to track the various stages of formation of the dough, an oil rub out test was also employed as the use of the actual binders is not generally recommended in a Banbury mixer. In the oil rub out test, 10 gm of zirconia powder was accurately weighed and mixed with 0.2 wt% of methyl cellulose as a binder. The powder binder mix was titrated with water and simultaneously mixed using a nickel spatula. Careful observations were made during each stage of mixing. A plot of water added against the processing regime is shown in Fig.2.7.

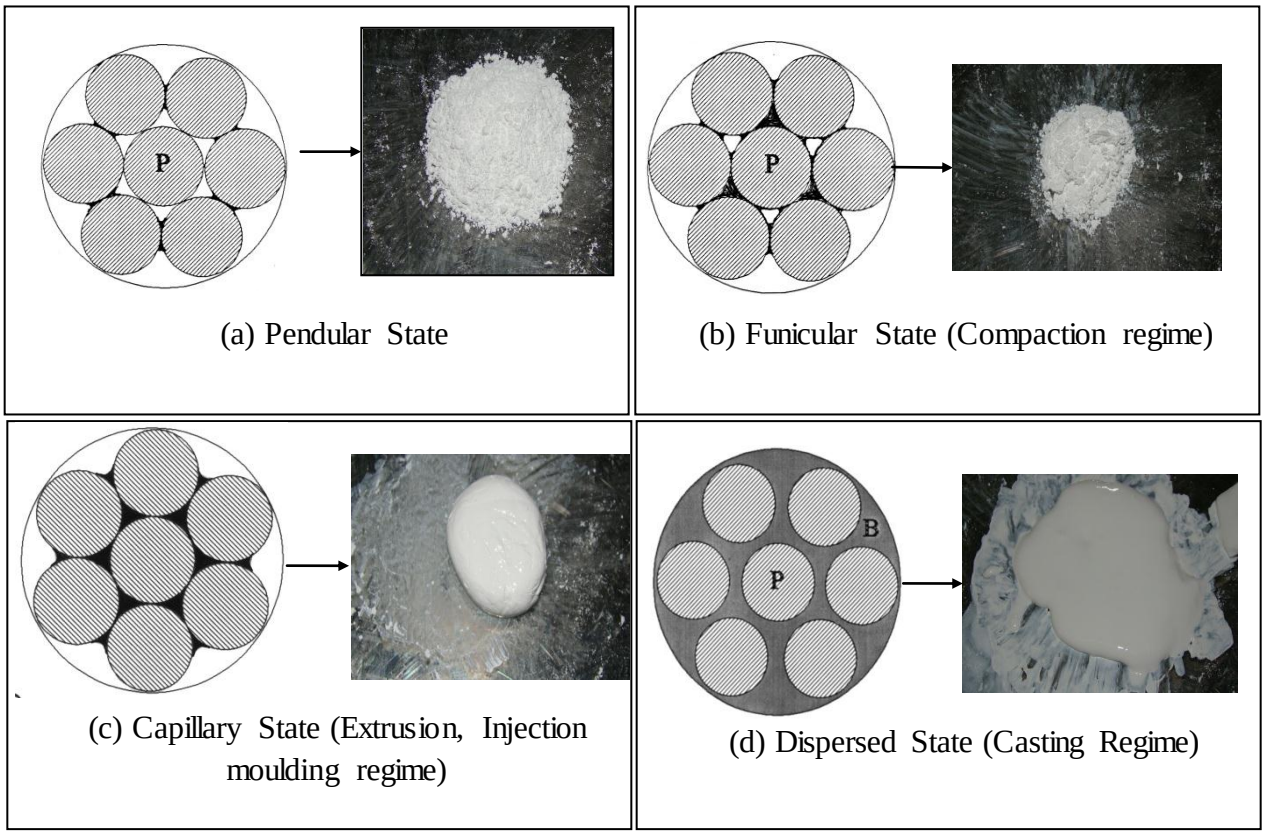

Fig.2.6 (a) Particles with monolayer coating, (b) Liquid bridging and formation of clusters exhibiting the volume of binder liquid just sufficient to form a strong, adsorbed layer on the particles, and completely fill the inter-particulate void space, (c) Particles forming a single lump, (d) Particles forming slurry

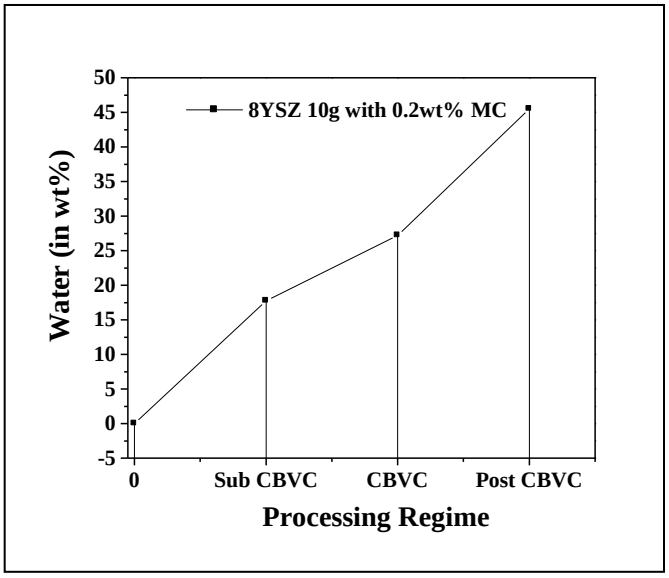

Fig.2.7 Plot of water addition Vs. Processing regime for zirconia raw mix

When the amount of the liquid is very small, > 15 wt% all the liquid goes to replace the powder-air interface with powder-liquid interface forming an absorbed monolayer on the particles (pendular state) as already discussed. This corresponds to low torque values shown in Fig.2.5. As the liquid amount is increased to ~17 wt% the torque value indicates a steep increase corresponds to pendular bonds formation as a result of the liquid bridging between the individual particles leading to the formation of particle clusters as shown in Fig.2.6 (b).

As the liquid is further increased to > 23 wt% the smaller clusters form bigger clusters forming a single lump where the liquid fills the entire voids. This corresponds to the peak torque value observed for CBVC region in the Fig.2.5. At this stage the particle structure gets kneaded easily the inter particle bonding can be attributed to strong and complete liquid bridging, a stage referred as capillary state (Fig.2.6(c)). Powder-Binder mix with 30 wt% water content forms a stiff coherent paste with very high viscosity.

On addition of further liquid to the mix (> 35 wt%) the particles separate themselves and interparticle friction reduces to a minimum and forms a completely dispersed state at around 45 wt% addition of water as shown corresponding to sudden fall of the torque observed in Fig.2.5.

Methylcellulose solution (0.2 wt %) in water was prepared and viscosity measurements were carried out and the same is used for further processing studies.

2.3 Compaction processing

The common method used for forming ceramic powders into a green body is compaction process. A key factor in compaction processing is the packing density and packing homogeneity of the green body. For advanced ceramics, both the packing density and the packing homogeneity are important. The powder characteristics and the forming method control the particle packing of the green body, which in turn has a significant influence on the microstructural development during sintering. Large variations in the packing density lead to the development of microstructural heterogeneities such as large voids during the sintering step thereby limiting the ability to achieve high density and fine grain size [2-4]. It is necessary to incorporate an organic binder to give the dry shape sufficient strength to survive the handling necessary between shaping and sintering. One of the most important prerequisite for a binder is its easy removal from the compact without any disruptive effect.

The key problems with die pressing are the non-uniform filling of the die, agglomeration of the dry powders, the friction between the dry particles and the friction between the powder and the walls of the die. They lead to non-uniform pressure transmission during compaction, which in turn produces density variations in the green body. Improving the flowability of the powder through the use of granulation can ease the problems of die pressing.

Dry pressing is carried out in a die with movable top and bottom punches. A cavity is formed with the bottom punch in a low position is filled with granulated powder and is level with the top of the die. The top punch then descends and compresses the granulated powder to a predetermined volume or in more elaborate presses to set pressure. Both punches then move upwards until the bottom punch is level with the top of the die and the top punch is clear of the powder –feeding mechanism. The compact is then removed, the bottom punch is lowered and the cycle is repeated.

2.3.1 Preparation and characterization of 8 YSZ granules

Zirconia with binder volume concentration (BVC) value of 17wt% binder solution (containing 0.2wt% binder on the powder content basis) was added and mixed homogeneously to form a semisolid mix. This semisolid mix in a partially dry condition are forced through a SS- 316 wire mesh of ASTM size (-) 30 and granules of the required size for compaction are extracted from the dried product by sieving using ASTM mesh size (-) 60 and (+) 100. The shapes of the granules are irregular.

2.3.2 Powder flow Analysis

Granule flow properties were estimated in terms of cohesion index (CI), which is defined as the ratio of Cohesion Coefficient and sample weight (Eqn. 2.9), and measured using Powder Flow Analyser (Stable Micro Systems). The powder flow analyser used in the present study utilizes a specified rotating blade (25mm in diameter and 100mm in height), which is able to move up and down while rotating clockwise and anti-clockwise as shown in Fig.2.8. The cohesion coefficient (g, mm) is regarded as the work required to lift the blade up at the speed of 50 mm sec^{-1} through the powder column during the decompression phase; this is determined by integrating the negative areas under the force-displacement curve in Fig.2.9.

$$\text{Cohesion Index (mm)} = \frac{\text{Cohesion Coeficient (g, mm)}}{\text{Sample wt (g)}} \tag{2.9}$$

Fig.2.8 Powder flow analyzer along with specified rotating blade

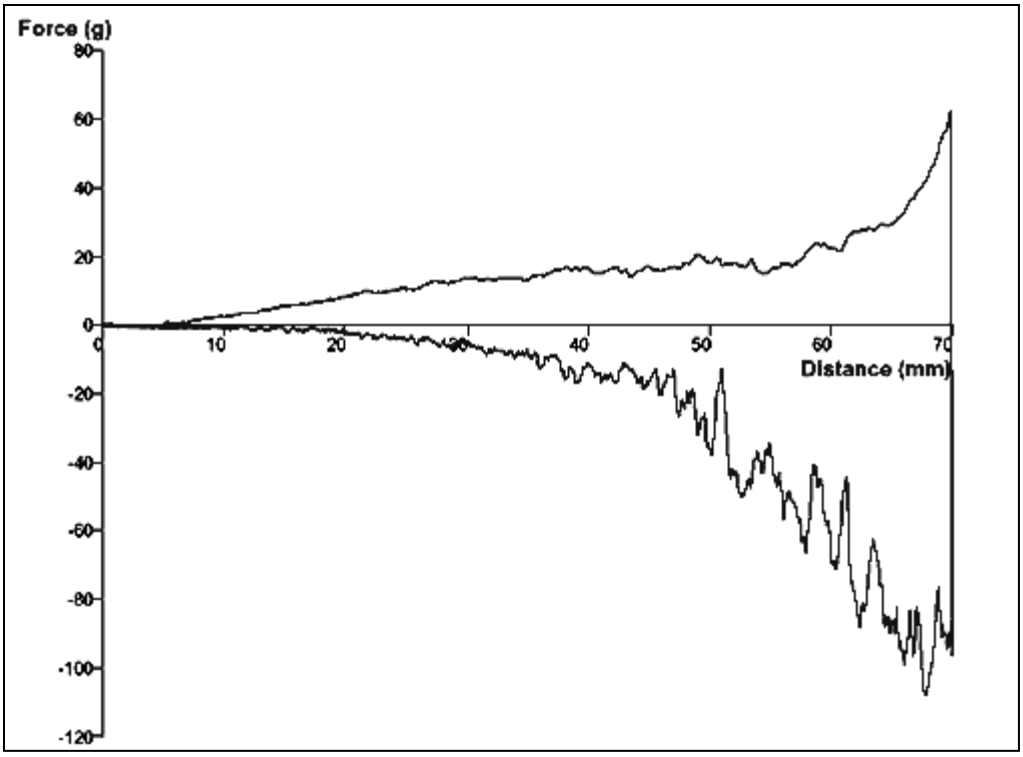

Fig.2.9 Force –displacement curve

50gm of the powder was used for estimating the flowability of the granules and was evaluated from the displacement during a programmed rotation of the blade inside the standard vessel. Firstly, two conditioning cycles were performed to remove any stress history from the powder and to normalize the powder column after filling. The rotating blade was then allowed to move down through the powder column using a "cutting" action to minimize compaction. The upward part of the cycle lifted the powder and the force of the powder on the vessel base was recorded.

Table 2.3 shows classification of cohesion index; it is evident that a low cohesion index is associated with non-cohesive free-flowing powders, while a high cohesion index is associated with cohesive, poorly flowing powders. Cohesive Index values obtained with zirconia granules in the present study are shown in Table 2.4 indicating a cohesion index value 9 for free flowing behavior [5]

Table 2.3 Classification of Cohesion Index (CI)

Sr. No	Cohesive Index (CI)	Flow behavior
1	>19	Hardened/extremely cohesive
2	19-16	Very cohesive
3	16-14	Cohesive
4	14-11	Easy-flowing
5	<11	Free-flowing

Table 2.4 Cohesion Index (CI) values

Sr. No	Cohesive Index (CI)	Flow behavior
1	9	Free flowing

2.3.3 Design and fabrication of the Die

Designs of the die with dimensional details are shown in Fig.2.10 (a) and the actual die used for compaction is shown in Fig.2.10 (b). The die consists of a die body fitted with top and bottom punches and an ejection rod. The die was fabricated out of die steel with a maximum tonnage of 8 Tons (~ 2550kg.cm^{-2}).

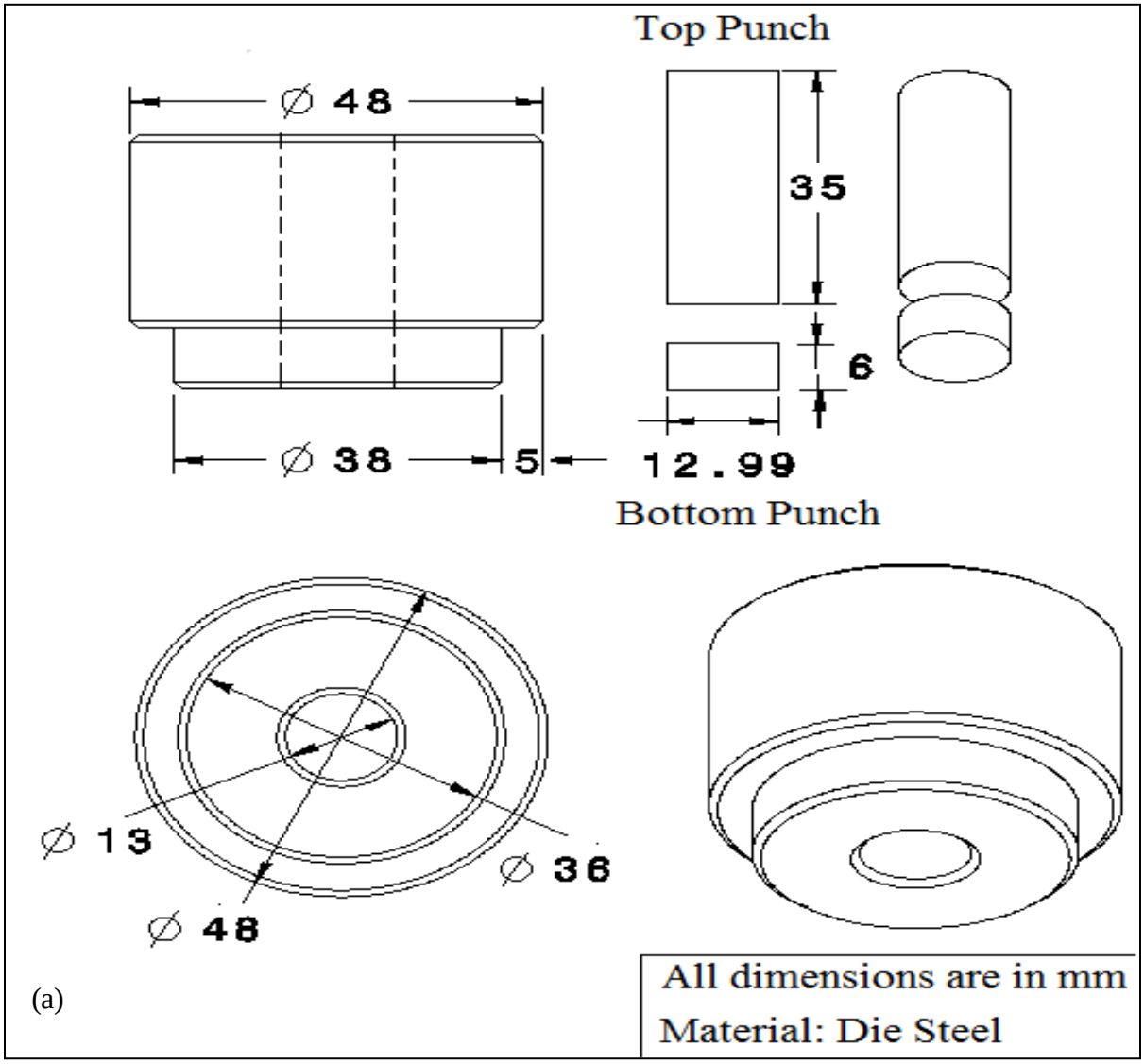

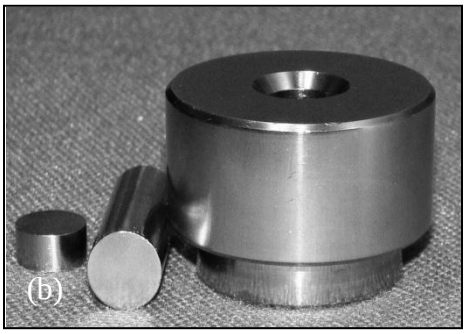

Fig.2.10 (a) Engineering drawing of the Compaction Die and (b) compaction die along with bottom and top punches

2.3.4 Compaction of the granules into pellets

Approximately 1.50 gm of the granules was filled in a compaction die and was compacted. The corresponding loads versus displacement curves were recorded using a Universal Testing Machine (INSTRON) as shown in Fig.2.11 (a). Granules were compacted at a constant ram rate of 1mm/min under loads varying from 5 - 8KN. The compressive load versus displacement curve for various compaction loads are shown in Fig.2.11 (b). All the curves represents at peak pressure have shown a steep increase in compressive loads indicating compaction.

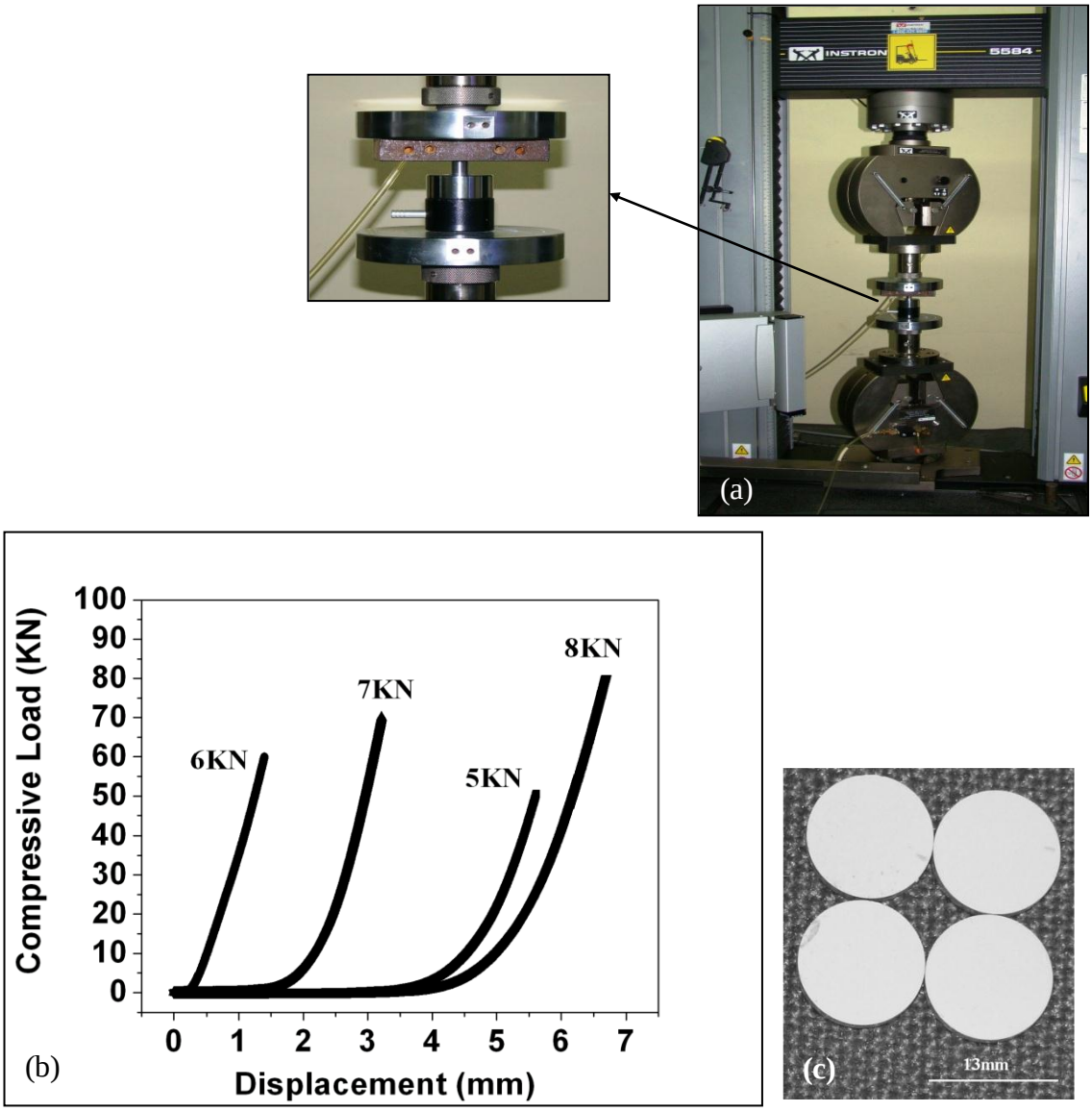

Fig.2.11 (a) Compaction Die Mounted on Universal Testing Machine (Instron Model 8812), (b) Compaction curves of granules and (c) 8YSZ green compacts

2.3.5 Characterization of the green pellets

Green densities of the pellets were calculated by dimensional method. Dimensions of the samples were measured using a digital Vernier caliper and corresponding weight were determined using an analytical balance. The compaction pressure, green densities along with sample dimensions are shown in Table 2.5

Table 2.5 Compaction pressure, specimen dimensions and green density of the samples

Compressive Load (KN)	Dimensions (mm)		Weight (g)	Green density (g/cc)	Average green density (%TD)
	Diameter	Thickness			
5	13.00	4.02	1.5010	2.814	
		4.03	1.5015	2.808	
		4.04	1.5012	2.801	
		4.06	1.5013	2.787	47.5
6	13.00	3.92	1.5006	2.886	
		3.91	1.5004	2.893	
		3.90	1.5005	2.900	
		3.92	1.5008	2.886	49.00
7	13.00	3.83	1.5005	2.953	
		3.84	1.5011	2.947	
		3.84	1.5012	2.947	
		3.83	1.5009	2.954	50.00
8	13.00	3.82	1.5000	2.960	
		3.83	1.5011	2.954	
		3.83	1.5011	2.954	
		3.82	1.5000	2.960	50.12

2.4 Slip Cast processing of ceramics

Slip casting is a ceramic shaping process in which the partial separation of liquid from a particulate-liquid suspension contained in a permeable mould forms a condensed deposit with the general conformity of the working surface of the mould. In conventional casting, the capillary

suction of the mould creates a pressure gradient across the deposit, and the kinetics of casting are a function of the capillarity of the mould.

In the slip casting process the ceramic powder is suspended in a fluid vehicle, usually water. These suspensions have to fulfill several requirements such as the particles should not settle fast under the effect of gravity to minimize the segregation leading to density in-homogeneities in the cast objects. These slurries should have high solids content to achieve reasonable casting rates and to reduce energy consumption in the subsequent drying stage due to the lower moisture content of the cast [6, 7]. Furthermore, the prevailing trend in ceramic processing is the development of very fine particles in order to enhance sintering rates as well as to reduce the size scale for mixing uniformity in powder blends. However, the combination of high solid loading and small particles leads to a viscosity increase because of increased particle-particle interactions and consequently to difficulties in slurry handling [8].

Ceramic powders have the tendency to agglomerate due to the attractive interparticle Van der Waals forces. This tendency can be eliminated with the addition of appropriate dispersants which alter the powder surface properties so that repulsive forces - either due to electrostatic repulsion resulting from the overlapping of electrical double layers or due to steric hindrance resulting from absorption of large molecules - become higher than the attractive ones and the particles can remain suspended in the slurry [9]. Dispersants that functions both via the electrostatic and the steric mechanism are called polyelectrolytes, which usually consist of a hydrocarbon chain and a polar head group (COO^-, SO_3^-) [10-12]. Dispersant addition can dramatically reduce the viscosity of slurries with very high solid content [13].

Fabrication of the mould is also critical in the slip casting process. A suitable mould is prepared using plaster of paris and is made by casting around the pattern of the required shape designed based on shrinkage allowance for drying and firing. The inner surface of the plaster of paris mould had a very smooth finish; free from any holes originates from air bubbles in the plaster so that the cast article is removed without damage. The mould is dried and the slip is poured into it. Water passes into the porous plaster leaving a layer of the solid on the wall of the mould. This is continued until the part is solid, or is interrupted to make a thin walled part and cast are allowed to dry.

2.4.1 Slip casting of Zirconia Pellets

Schematic of the slip casting process employed in the present study is shown in Fig.2.12

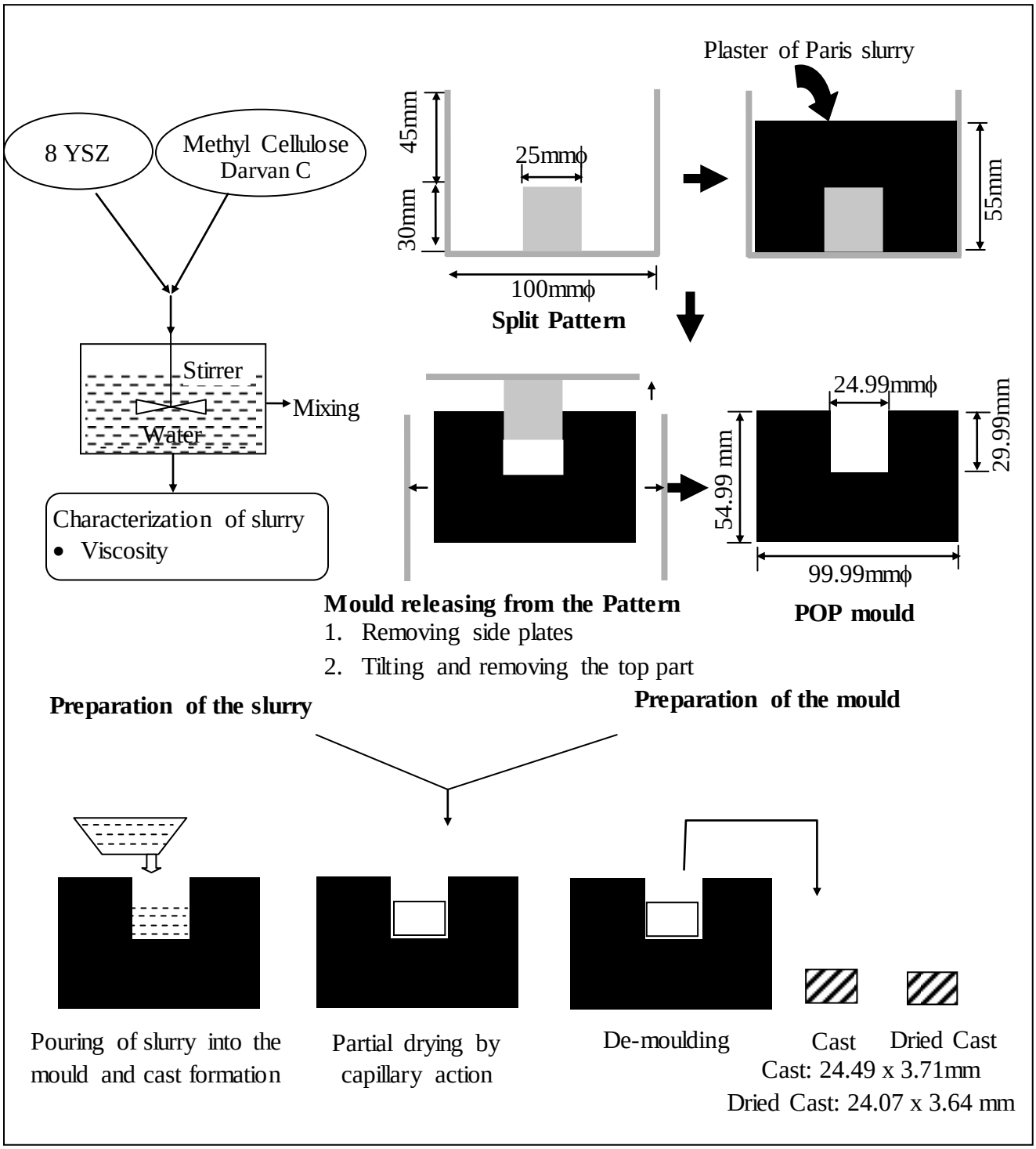

Fig.2.12 Slip Casting Process (Schematic)

2.4.2 Design and Fabrication of Pattern

Slip casting of zirconia starts with the pattern fabrication. In the present study patterns are fabricated with stainless steel with circular core rod and a casing with the dimensional tolerance of 0.05% and 0.1% for the drying and sintering shrinkage allowance respectively based on the initial trials. The casing was made into a split design in order to have an easy release of the mould. The pattern was also buffed to achieve proper surface finish of the mould surface.

2.4.3 Fabrication of Plaster of Paris Mould

Plaster of Paris ($CaSO_4.H_2O$) procured from the commercial sources (Khushi Premium Quality, New Vinyl Chemicals. Hyderabad, India) is mixed with 35% of water by weight and the slurry was poured into the casing placing the core rod located at the centre and was left for 30 minutes under laboratory conditions. During this process the plaster of Paris crystallizes and hardens, releases heat, and increases in volume slightly. The plaster mould was removed after drying and the inconsistencies or imperfections of the mould are slowly scraped off using a small craft knife. After scrapping of the excess material the mould was laid out on a plate or rack overnight to harden. Fig.2.13 shows the photograph of the mould fabricated for the slip casting in the present study.

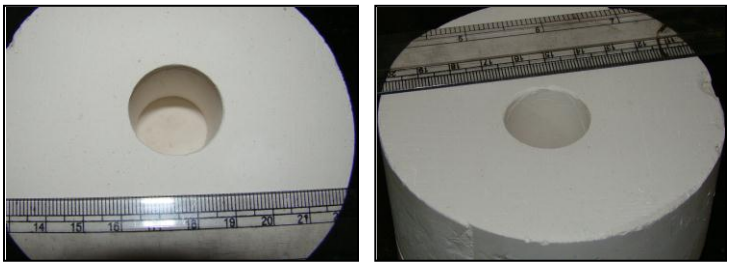

Fig.2.13 Photo of Plaster of Paris mould

2.4.4 Preparation of slurry

8 mol% yttria stabilized zirconia powder was dispersed in aqueous medium to form slurries having solid loading in the range of 55 - 70 wt% using 1wt% Darvan 821A as dispersant and n-Octanol ($C_8H_{18}O$) as the antifoaming agent. Suspensions were then milled for 6 hrs in polypropylene bottles in a pot jar mill using zirconia balls of 1mm diameter and 1:1 charge to

balls ratio to achieve homogeneous slurry. The rheological properties of the slips were measured using Rheometer (MCR 51, Anton Paar, Austria). The slip is optimized with respect to the solid loading based on the rheological property.

Table 2.6 shows the composition and viscosities for the slip used for casting process. Fig.2.14 (a) presents the viscosity measurements with shear rates of 8YSZ slurries with different solid loadings. It is also evident that the slurries are pseudo-plastic at lower shear rates and as the shear rate is increased beyond 1000 s^{-1} the slurries exhibit close to Newtonian behavior. It is evident that the slurries with 55, 60, 65 and 70 % of solid loading exhibited a high viscosity of 0.033, 0.0884, 0.231, 0.494 Pa.s respectively in the shear rate range 200 s^{-1}. The average viscosities of the slurries with 55, 60, 65 and 70 % of solid loading are found to be 0.019, 0.032, 0.064, and 0.127 Pa.s respectively in the entire shear rate range upto 2000 s^{-1} and the details are presented in Table 2.6

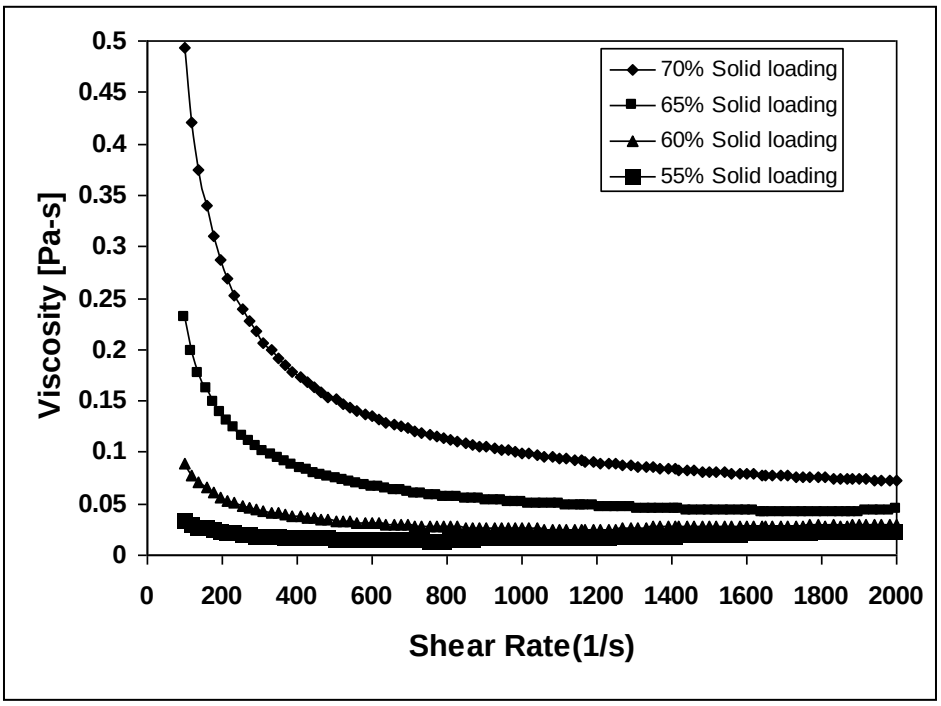

Fig.2.14 (a) Plots of Viscosity with shear rates for 8YSZ slurries of varying solid loadings

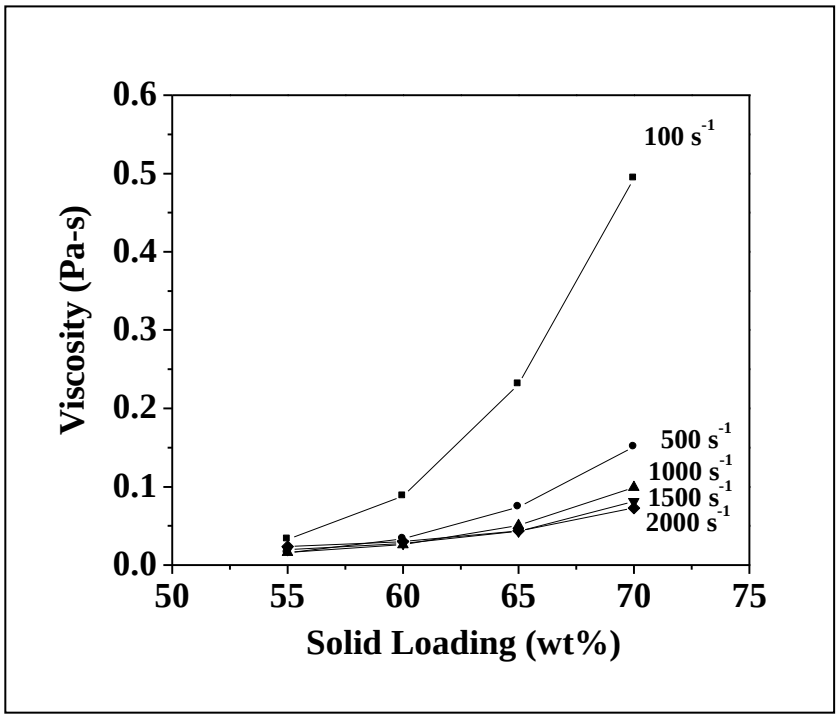

Fig.2.14 (b) Plots of Viscosity vs. % solid loading of 8YSZ slurries at various shear rates

Table 2.6 Details of solid loading, additives and results of viscosity

Solid Loading (wt %)	Wt. of 8YSZ powder(g)	Wt. of water (g)	Additives on solid content		Average Viscosity in the entire shear rate range upto 2000 s^{-1} (Pa.s)
			Binder (g)	Dispersant(g)	
55	55	45	0.11	0.55	0.019
60	60	40	0.12	0.60	0.032
65	65	35	0.13	0.65	0.064
70	70	30	0.14	0.70	0.127

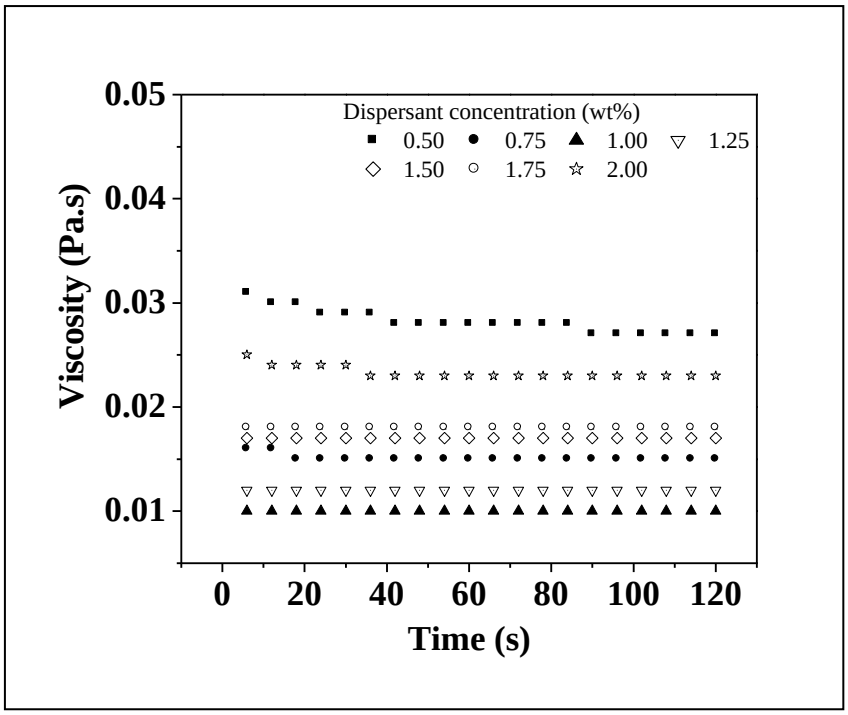

Fig.2.15 Effect of dispersant concentration on the viscosity of 65wt% solid content slurry at constant shear rate

It is observed that average viscosity steeply increased for slurry with 70wt% solid loading which in turn affects the pourability during casting. Hence, slurry with 65wt% solid loading was selected in studying the effect of dispersant on the slurry rheology and viscosities measured with dispersant concentration varying from 0.5 to 2.00wt% at constant shear rate of $500s^{-1}$. It is evident from the plot (Fig.2.15) that slurry with 65wt% solid loading is having a constant viscosity of 0.010Pa.s with dispersant content in the range of 0.90-1.10wt% and is suitable for the slip casting process.

2.4.5 Casting of circular discs and mould release

8YSZ slurry with 55, 60, 65 and 70wt% of solid loading were thoroughly stirred with a glass rod without introducing any air bubbles (observing with naked eye) and casted into circular discs of 25mm diameter in porous plaster of paris moulds fabricated under laboratory conditions. The slurry with 70wt% solid loading is found to have poor flowability and posed difficulties while casting and hence the experiments were continued with slurries 55, 60, 65wt% solid loading.

After the slip is poured in to the mould the wall thickens, the plaster mould absorbs water and the level of the slip kept inside the mould, continuously dropping which was compensated by adding small amounts of slip into the mould. After draining off the excess slip the mould was left for drying. The mould absorbs water from the cast gets dried causing shrinkage to the cast piece.

2.4.6 Drying of cast piece

The cast samples were subjected to final drying in a humidity oven at 50°C and at relative humidity of RH70%. Drying curve obtained for the cast samples made from slurries with 55, 60 and 65wt% of solid loading is shown in Fig.2.16 and the dried samples are shown in Fig.2.17

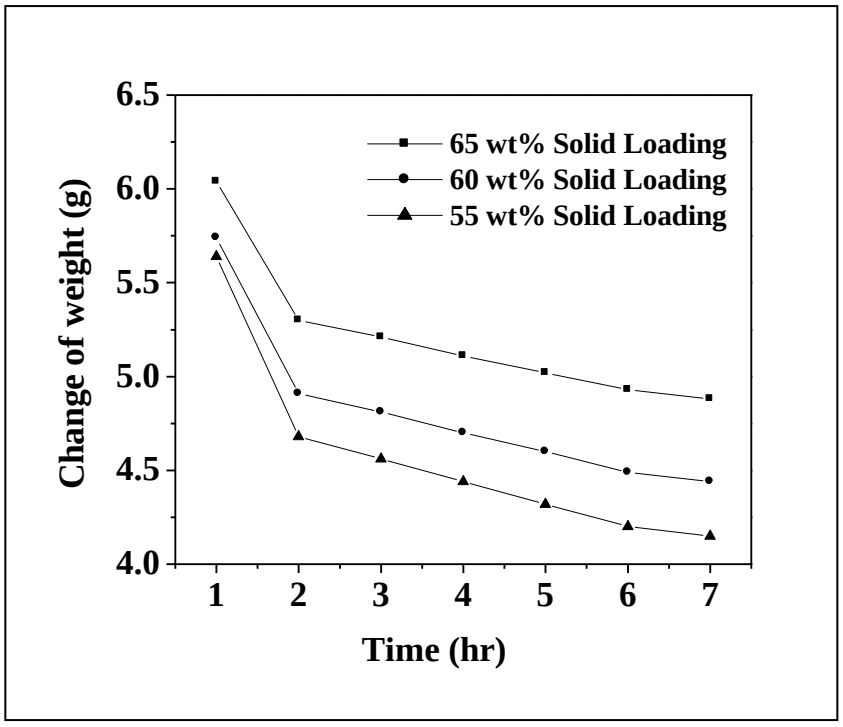

Fig.2.16 Drying curve obtained for the cast samples with 55, 60, and 65 of solid loading

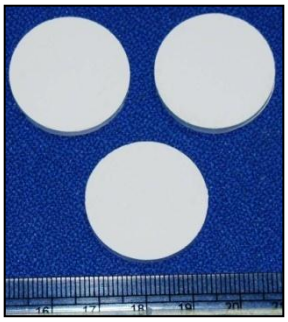

Fig.2.17 Dried samples of different solid loading

2.4.7 Characterization of the green pellets

Green densities of the pellets were calculated by dimensional method. Dimensions of the samples were measured using a digital Vernier caliper and corresponding weight were measured using an analytical balance. The green densities along with dimensional details of the samples are shown in Table 2.7

Table 2.7 Solid loading, specimen dimensions and green density of the samples

% Solid Loading	Dimensions (mm)		Weight (g)	Green Density (g/cc)	Green Density (%TD)	Green Density Average (%TD)
	Diameter	Thickness				
55	24.00	4.24	4.8888	2.550	43.23	
	23.99	4.24	4.8759	2.546	43.16	
	24.00	4.22	4.8657	2.551	43.23	
	23.99	4.25	4.8960	2.550	43.23	43.21
60	24.05	3.70	4.4561	2.652	44.96	
	24.04	3.69	4.4456	2.656	45.01	
	24.05	3.68	4.4358	2.655	45.00	
	24.06	3.66	4.4258	2.661	45.10	45.02
65	24.08	3.67	4.8755	2.920	49.49	
	24.07	3.64	4.8759	2.947	49.94	
	24.08	3.63	4.8757	2.950	50.00	
	24.08	3.63	4.8762	2.952	50.04	49.87

2.5 Methylcellulose based thermal gel casting

In addition to the conventional slip casting process a new colloidal processing based on thermal gelation property of methylcellulose, which is not so far reported for near net casting of 8YSZ ceramics has been developed in the present study. Methyl cellulose is a natural polymer which gels on heating. The molecular structure of methyl cellulose is shown in Fig.2.18. The cellulose is a linear chain polymer based on β 1, 4 - Glucosile linkage of D-Glucose. It is usually not soluble in solvent because of high crystallinity. This is because of the firm hydrogen bonds

formed by the hydroxyl groups in glucose residues [14]. However on methyl group ($-CH_3$) substitutes to a degree of 1.6 – 2.0 can enhance dissolution of the same in cold water [15, 16, 17]. This aqueous solution of methyl cellulose gels on increasing the temperature primarily because of hydrophobic interaction of the molecules containing methoxyl substitution.

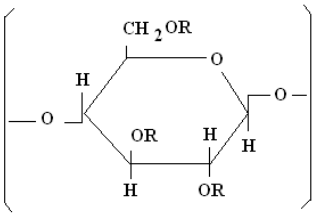

Fig.2.18 Structure of methylcellulose, $R=CH_3$

In an aqueous solution with low temperature the molecules are hydrated and two little polymer – polymer interaction with increase of temperature as can be seen from the Fig.2.19. There is a drop in the viscosity with sudden increase in the viscosity at incipient gelation temperature and it is evident that on cooling the gel completely transform in to its original state of consistency as observed by several workers [18 – 23].

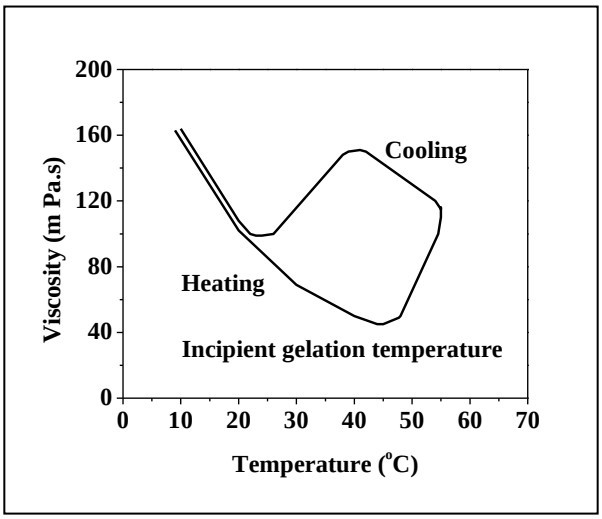

Fig. 2.19 Gelation of 2% aqueous solution of MC, having normal viscosity of 100mPa.s, when heated at 0.25°C/min; rate of shear $86s^{-1}$ [24].

In the present study the single thermal gelation phenomena observed by several workers has been successfully employed for the first time for colloidal shaping of ceramics. It is well known that MC is an effective binder for processing of ceramics especially for the extrusion, compaction etc., however never explored for colloidal shaping through a gelation process. It is observed that the present process developed of the following advantages in comparison to conventional gel casting process.

- Process is based on naturally occurring methalated polymer
- Shaping by simple thermal gelation phenomena
- Very low binder concentration as low as 0.2wt%
- Organic burnout to 100% with low ash content.
- Can be adoptable for common ceramic powders
- Simple and complex shaping capability

2.5.1 Conventional thermal gelation studies of methyl cellulose solution

In order to study adaptability of the MC gelation phenomena for the ceramic shaping varying concentrations 0.08 – 0.5 wt% aqueous MC solutions were prepared. The solutions were subjected to rheological measurements with a controlled stress rheometer (Model: MCR 51, Anton Par, Austria) with a progressive heating with different heating rates of 1, 2.5 and 5°C/min. The effect of heating rate on gelation is shown in Fig. 2.20. The complex viscosity measurements have been made using parallel plate and the curves were recorded under oscillated shear mode in the viscoelastic regime.

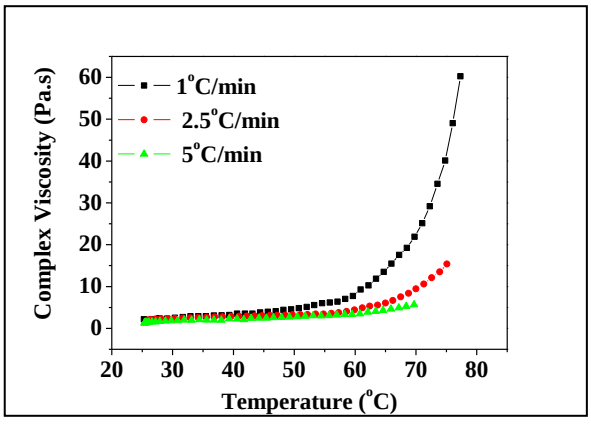

Fig.2.20 Effect of heating rate on gelation behavior of 0.2 wt% MC concentration

The heating rate is found to have a significant effect on gelation at constant shear rate of $10s^{-1}$ and it is evident that a heating rate of $1^{o}C$/min results in completion of gelation at low temperature as is seen from steep rise in the viscosity values.

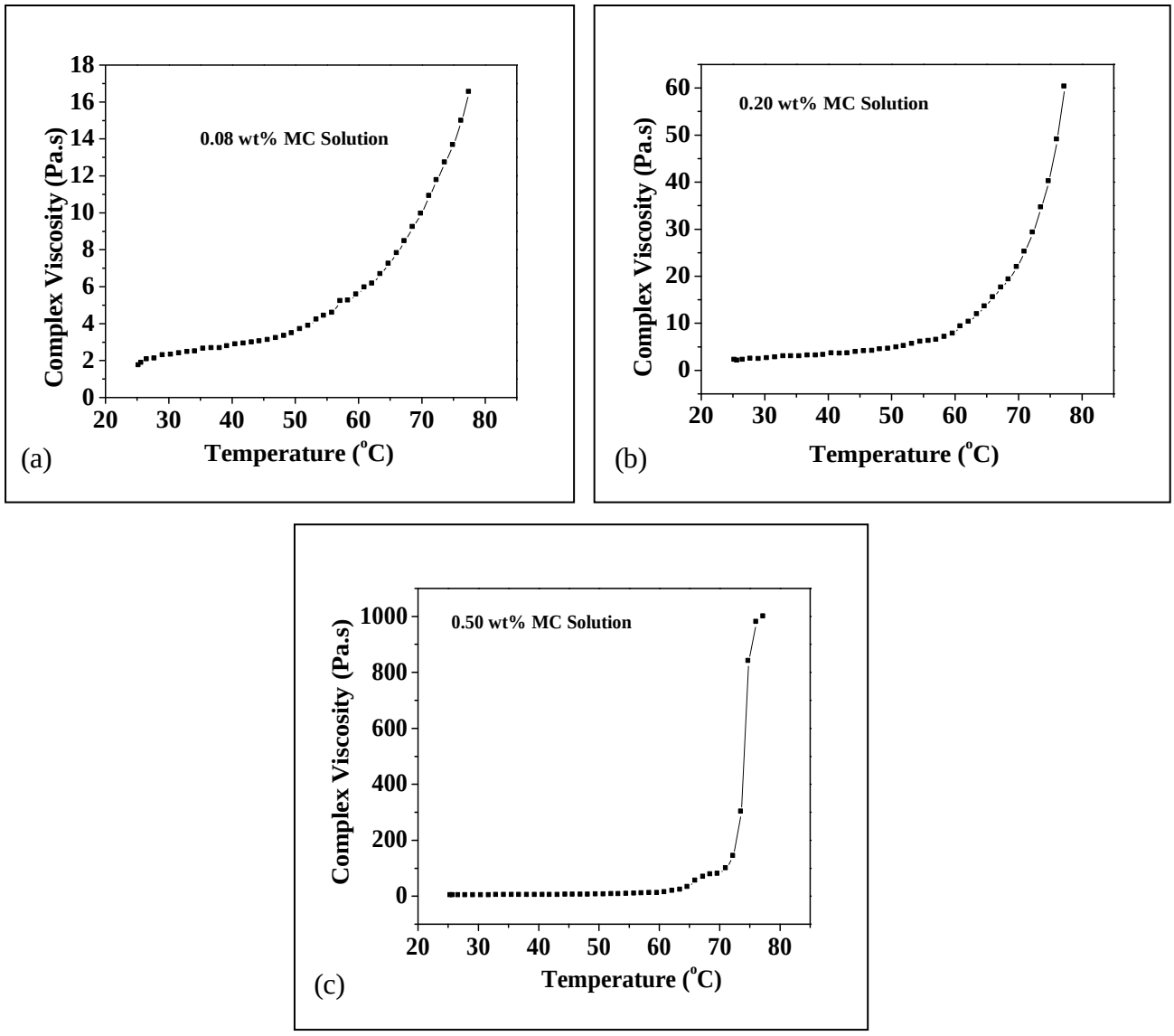

Fig. 2.21 Effect of methyl cellulose concentrations on gelation behavior (a) 0.08wt% MC, (b) 0.2 wt% MC, and (c) 0.50 wt% MC

Fig.2.21(a), (b) and (c) shows the effect of MC concentration on the gelation behaviour when subjected to $1^{o}C$/min. It is evident that all aqueous methyl cellulose solutions behave identical with incipient gelation with 55 ± 5°C while subjecting to heating. However the rise in viscosity values was minimal i.e., 16Pa.s to 60Pa.s at 70°C which is followed by a steep increase in the viscosity to ~1000Pa.s at 70°C with a concentration of 0.5wt% MC. It can also be noted that the

curve of viscosity vs. temperature of 0.5wt% MC indicated saturation as evident from the plateau observed at the temperature regime at 70°C. In order to confirm these observations, methyl cellulose solutions of concentrations 0.08, 0.2 and 0.5wt% MC were subjected to progressive heating on a hot plate while monitoring the temperature within the solution using a laboratory thermometer. The photographs of gelation process at different temperature are shown in Fig.2.22. It is evident that all the solutions are clear and transparent at 40°C with slight turbidity incase of 0.08, 0.2wt% MC and opaque emulsion like system for 0.5wt% MC solution. This can be attributed to simultaneous occurrence of gelation in combination with precipitation. A uniform gelation has been observed with 0.08 and 0.2wt% MC. However the precipitates cross over gelation leading to non-uniform aggregation.

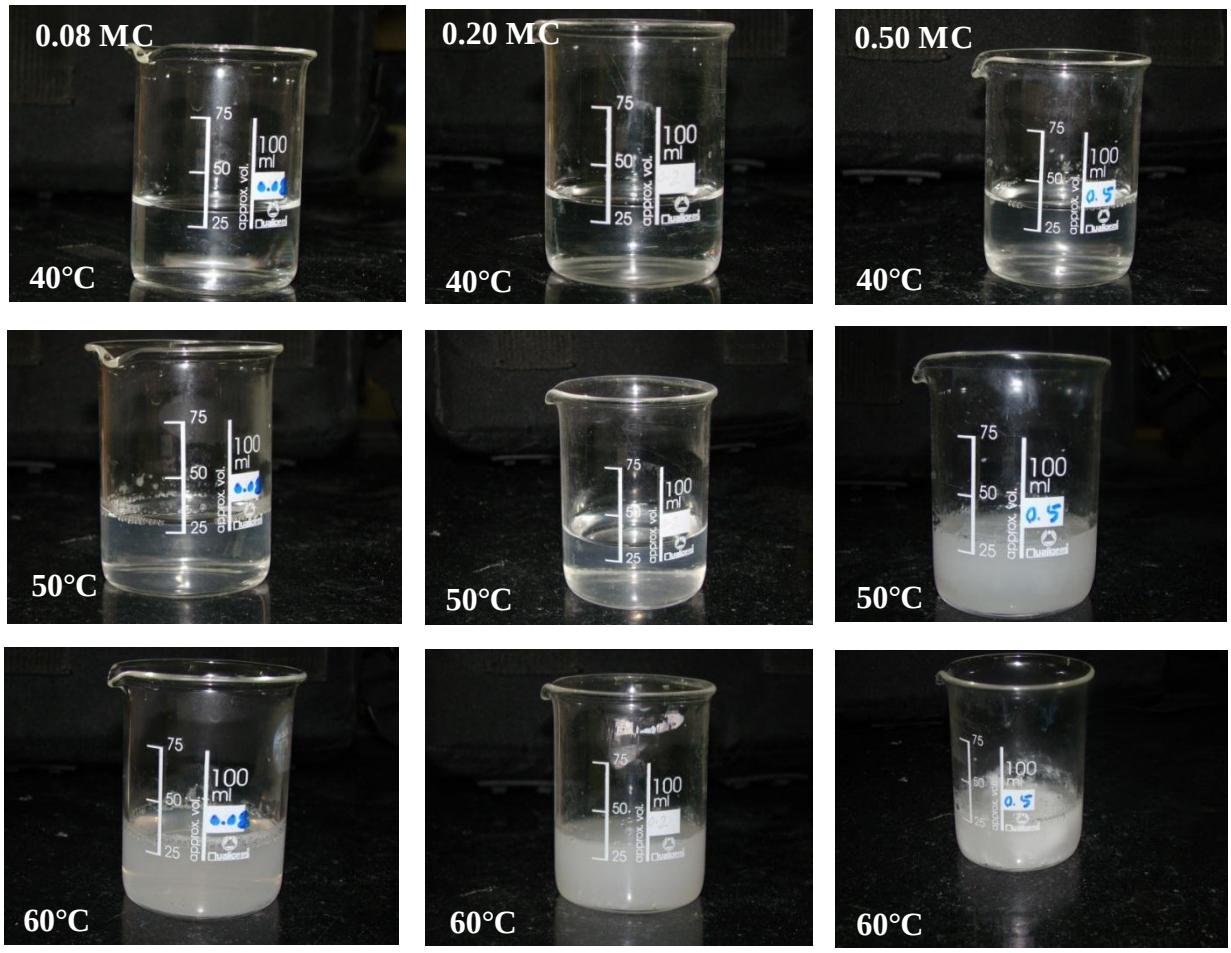

Fig.2.22 Effect of methyl cellulose concentration on gelation

2.5.2 Microwave based thermal gelation of methyl cellulose solution

It is well known that MC couple with microwave which can be successfully employed for in-situ thermal gelation. As described above as the concentration of 0.5wt% MC leads to segregation and 0.08wt% of MC shows low viscosities. The concentration of 0.2wt% MC was selected and employed in the present study.

Microwave assisted thermal gelation is carried out by irradiating 0.2wt% MC solution with microwaves of frequencies 2.45 GHz using a "kitchen" microwave oven (Model: BMO-700T, Power: 1.2 KW, India)a preset 10 % microwave power. Progressive gelation process of 0.2wt% aqueous methylcellulose (without 8YSZ) on exposure to microwave is shown in Fig.2.23. The transparent methylcellulose solution becomes translucent as the temperature reaches 50°C and an opaque thick gel is obtained on increasing the temperature to 60°C. However, on exposure to a pre-set microwave power greater than 10 % of 1.2 KW, instantaneous boiling and splashing of the solution out of the beaker was observed. Hence, the experiments were carried out using 10 % of the total microwave power with intermittent interruption. The temperature rise of the solution was recorded occasionally using thermometer during the interruption. The recorded value of temperature is 3-5°C lower than the actual value due to manual error.

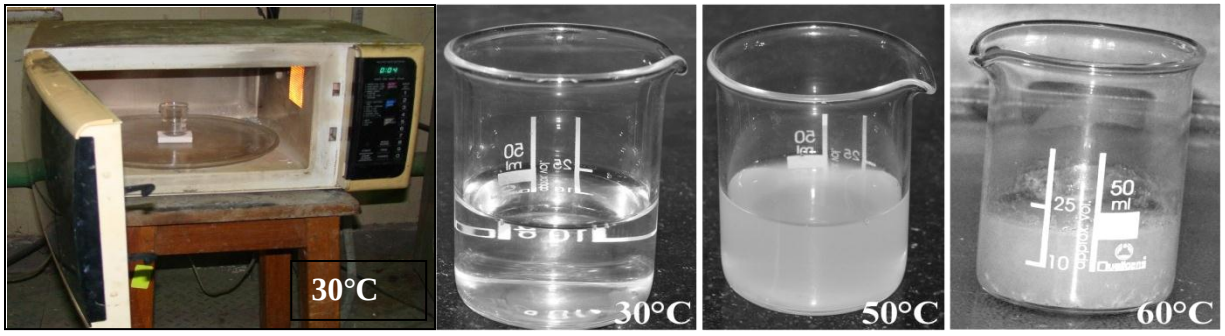

Fig.2.23 Progressive gelation process on exposure to microwave irradiation

2.5.3 Preparation of 8 Y zirconia slip and gelation studies

8mol% yttria stabilized zirconia powder (TZ-8YS, Tosoh, Japan) was dispersed in aqueous medium to form slurries having solid loading in the range of 76 -77wt% and Darvan 821A as a dispersant. The suspension was then milled for 6 hrs in polypropylene bottles in a pot jar mill using zirconia balls of 1mm diameter and 1:1 charge to balls ratio. The slurry after de-airing

(using vacuum desiccator) was mixed with methylcellulose (Methocel F7M, Dow Deutschland GmbH& Co. OHG, Stade, Germany) in concentrations ranging from 0.08wt% to 0.5wt%. In order to study the interactions of methyl cellulose with 8YSZ powder, 8YSZ slurry with varying in concentrations of 0.08, 0.2 and 0.5wt% MC has been prepared. The plot of temperature vs. complex viscosity is shown in Fig.2.24 (a), (b) and (c). It is evident that the trend in the viscosity is almost similar to that of the MC solution. However the incipient gel point has reduced to 30°C in comparison to 55 ± 5°C aqueous MC solutions. The premature gelation observed with the slurry can be attributed to the enhanced hydrophobic interactions in presence of zirconia powders. A schematic of gelation process proposed is reported shown in Fig.2.25 and the process flow chart is shown in Fig. 2.26

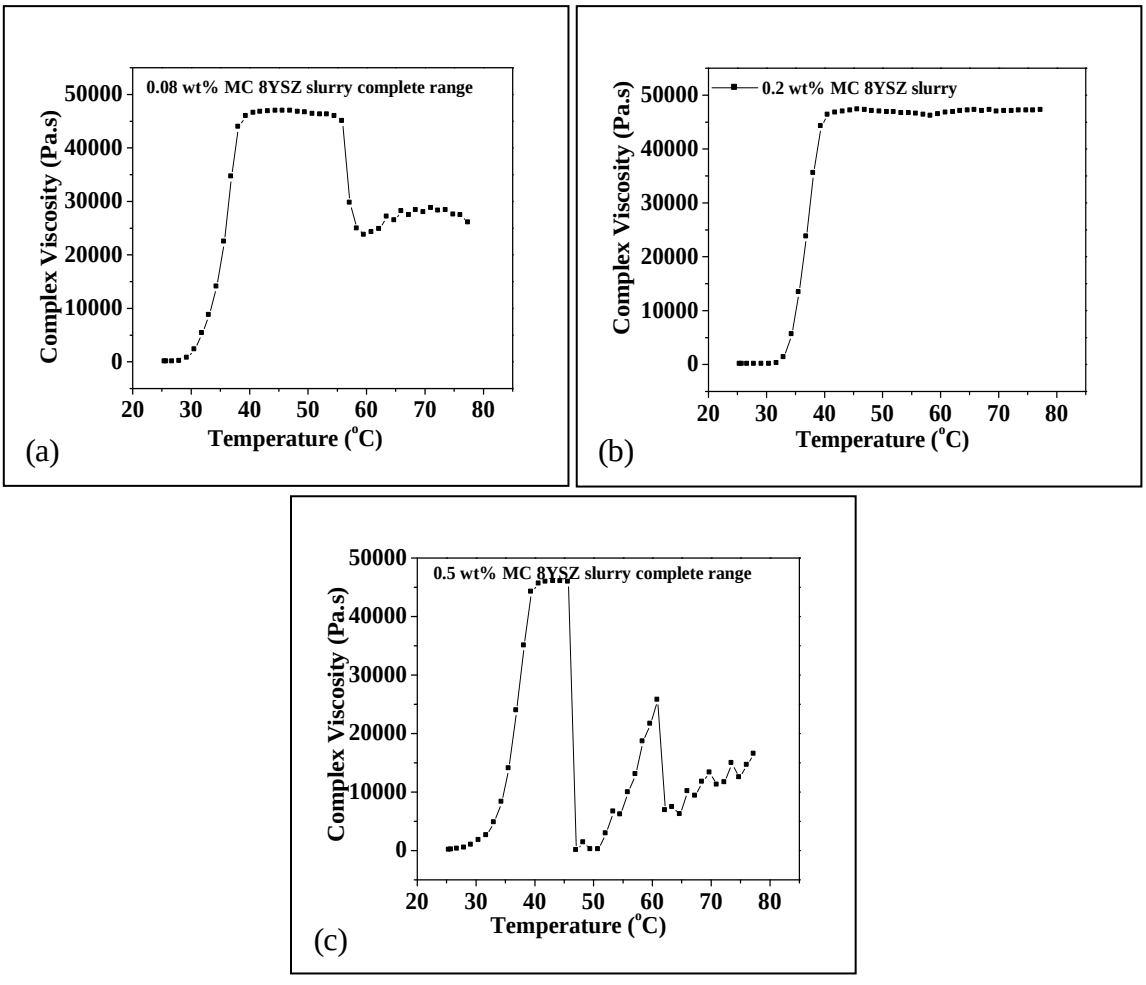

Fig.24 Temperature vs. complex viscosity of 8YSZ slurry with varying concentrations of MC

A close observation of the viscosity vs. temperature curve indicated a non-steady behavior with respect to 0.2wt% MC and also a totally unstable behavior with 0.5wt% MC confirming the precipitation as observed with MC solution.

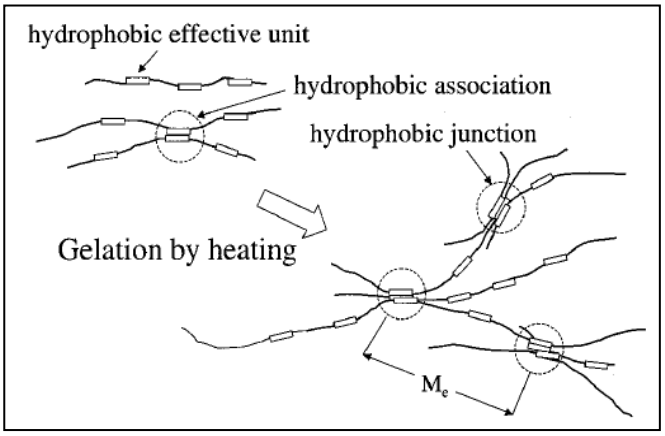

Fig.2.25Schematic drawing showing gelation though the hydrophobic effective units of methylcellulose chains [25]

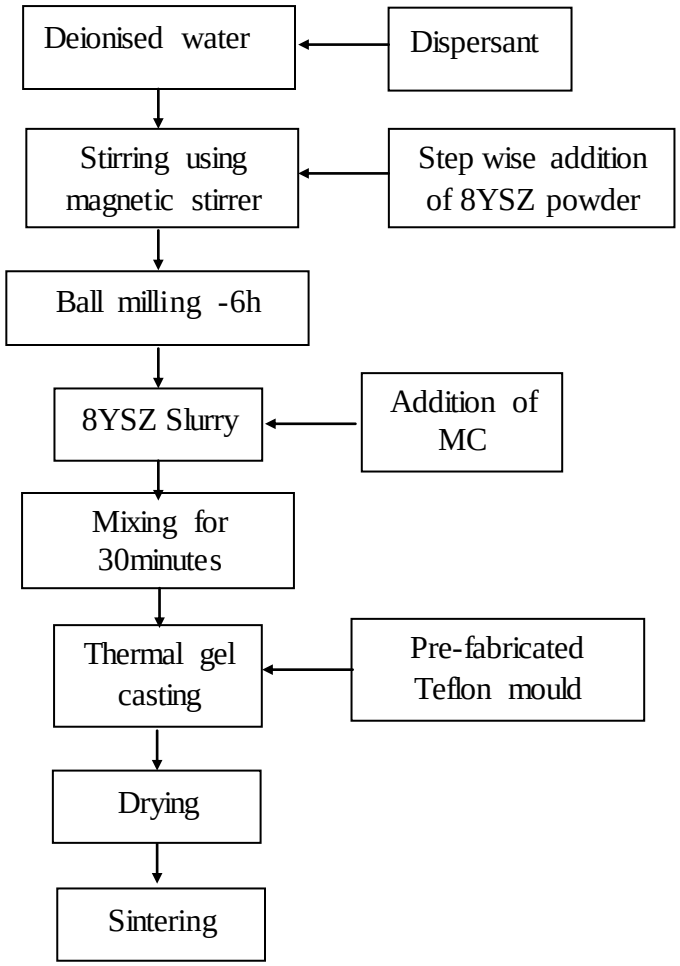

Fig.2.26 Schematic of the process flow chart of MC thermal gel casting

2.5.4 Shaping of 8YSZ pellets

Shaping of 8YSZ slurry by thermal gel casting is carried out as per the flow chart shown in Fig.2.26.

2.5.4.1 Design and Fabrication of Moulds

The mould was fabricated by machining the simple and complex shapes out of the Teflon blocks. While designing the moulds care was taken to achieve necessary tapering to facilitate easy release and associated shrinkage factors. The mould fabricated are shown in Fig.2.27

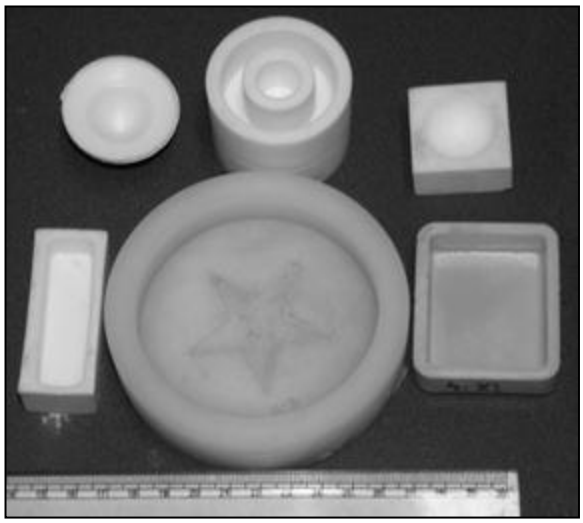

Fig.2.27 Teflon Mould Designs

2.5.4.2 Casting and gelation

8YSZ powder having solid loading in the range of 76- 77wt% with concentration of 0.2wt% MC is subjected to casting. Slurry was cast into prefabricated Teflon moulds of simple and complex shaped geometries and exposed to conventional heating (1^{o}C/min) and microwave heating(2.45GHz)in order to ensure the complete gelation. The microwave gelation is carried out using the microwave oven (Model: BMO-700T, Power: 1.2 KW, India) using microwave power of 10% in the present study. Plot of temperature (upto 60°C) vs. cumulative time of Microwave Thermal Gelled (MWTG) and Conventional Thermal Gelled (CTG) are shown in Fig.2.28. It is evident from the figure that there is a significant reduction in time of exposure in case of microwave-assisted gelation.

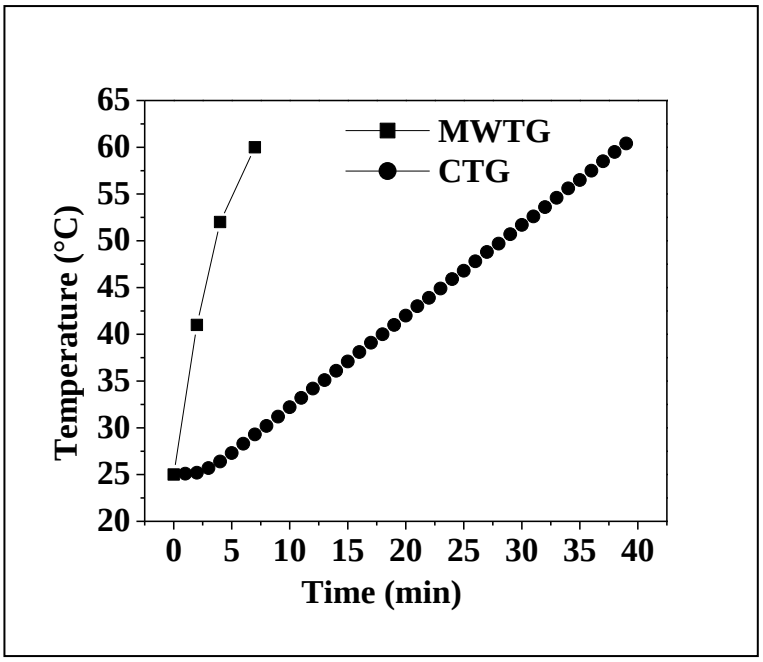

Fig.2.28 Plot of temperature (upto 60°C) vs. cumulative exposure time of MWTG and CTG

Microwave energy in this frequency region is too low to break chemical bonds and hence cannot induce chemical reactions. Microwave-induced polymerization in the present case is based on the absorption of microwave energy by methylcellulose and its ability to align with the frequency of the applied field. These enhancements of the methylcellulose polymerization reactions essentially are thermal effects although it is difficult to experimentally determine the exact reaction temperature. This efficiency of microwave energy can be attributed to minimize wall effects and also to the direct coupling of methyl cellulose to microwave energy dissipated as thermal energy. This microwave irradiation produces efficient in-core volumetric heating by direct coupling of microwave energy with the methyl cellulose molecules leading to a homogeneous polymerization transforming the slurry to a solid.

In contrast, conventional heating with an external heat source is comparatively slow and inefficient method for transferring energy into the system. It depends on the thermal conductivity of the various materials that must be penetrated and results in the temperature of the vessel being higher than that of the polymerization mixture. Aqueous solution of methylcellulose exhibits a reversible gelation irrespective of the gelation process whether it is conventional or microwave assisted. It was observed that the gels are transformed completely to its original consistency upon cooling. However, it was observed that in case of 8YSZ slurry gelation properties are

substantially altered and gelation process becomes irreversible, which can be attributed to the adsorption of water on the powder particles.

2.5.5 Drying of cast piece

The samples thus obtained from microwave and conventional thermal gel cast processes were further dried in a hot air oven for 2 hours. The dried samples with consistent weight were characterized for their green densities. 8YSZ samples of simple and complex shapes with 0.2wt% methylcellulose cast by microwave induced thermal gelation under above conditions are shown in Fig.2.29 (a). The green density of the samples cast by microwave gelation process is found to be close to 46 % of the TD and the samples are amenable to green machining as is evident from the machined samples presented in Fig.2.29 (b).

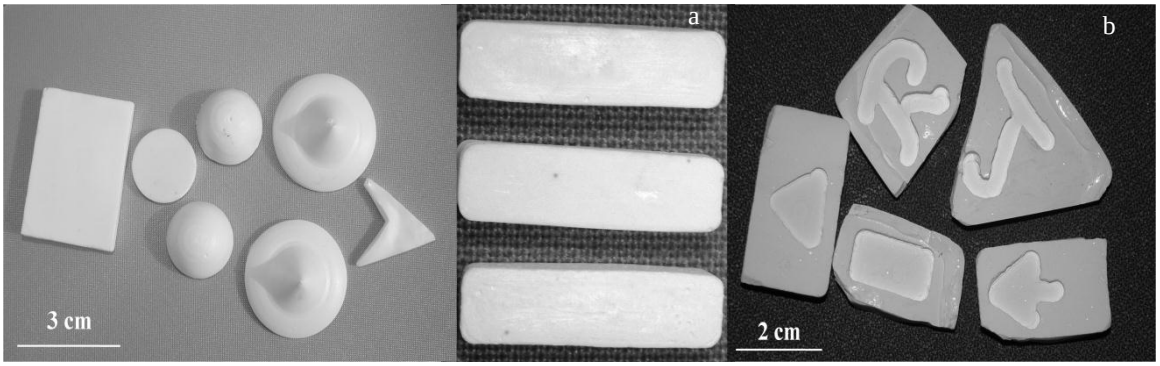

Fig.2.29 Dried 8YSZ samples cast through MWTG and CTG process (a) Simple and complex geometries (b) machined.

2.5.6 Characterization of the green pellets

Green densities of the various shapes were estimated by extracting pellets of standard dimensions. Dimensions of the samples were measured using a digital Vernier caliper and corresponding weight were determined using an analytical balance. The physical properties of the samples including dimensions and densities are shown in Table 2.9.

Table 2.8 Solid Loading, specimen dimensions and green density of the samples

Solid Loading (%)	Dimensions (mm)			Weight (g)	Green density (g/cc)	Average green density (%TD)
MWTG	**Length**	**Breadth**	**Thickness**			
65	5.02	5.01	5	0.310	2.465	
	5.02	5.03	5	0.309	2.447	
	5.01	5.02	5	0.304	2.417	
	5.02	4.99	5	0.306	2.443	41.41
68	5.01	5.02	5	0.319	2.537	
	5.03	5.02	5	0.320	2.535	
	5.02	5.01	5	0.319	2.537	
	4.99	5.02	5	0.318	2.539	43.00
76.5	5.02	4.98	5	0.335	2.680	
	5.02	4.96	5	0.334	2.683	
	5.01	4.95	5	0.332	2.677	
	5.02	4.98	5	0.335	2.680	45.42
CTG						
65	4.99	4.98	5	0.300	2.414	
	5.02	4.92	5	0.304	2.462	
	4.99	4.96	5	0.292	2.448	
	4.98	4.98	5	0.301	2.427	41.32
68	5.01	4.98	5	0.310	2.485	
	5.01	5.02	5	0.322	2.561	
	4.99	5.04	5	0.319	2.537	
	4.99	5.02	5	0.318	2.539	42.89
76.5	4.98	4.96	5	0.334	2.704	
	5.03	4.96	5	0.336	2.694	
	5.02	4.95	5	0.331	2.669	
	5.02	4.97	5	0.335	2.685	45.56

2.5.7 Fabrication of zirconia electrolyte honeycomb structure based on thermal gel casting

Honeycomb shaped Solid Oxide Fuel Cell Design (HC SOFC) is considered to be one of the innovative concepts for the miniaturization of cell size [26 – 29]. These cellular structures are produced generally by extrusion processing, which involves the shaping of a visco-plastic formable paste through a specially designed die [30]. Though, these honeycombs provide high geometrical surface area it generally exhibit high porosities even after sintering at high temperatures.

In the present study, the above developed eco-friendly process has been used for the fabrication of honeycomb structures. Aqueous zirconia slurry with 76.5wt% solid loading and containing 0.2wt% methyl cellulose was subjected to microwave induced thermal gelation in a prefabricated Teflon mould. The mould was fabricated using a Teflon block by machining pins protruding out of a base plate with an outer casing as depicted in the Fig. 2.30. Design of the mould along with mould fabricated out of Teflon is shown in Fig.2.30

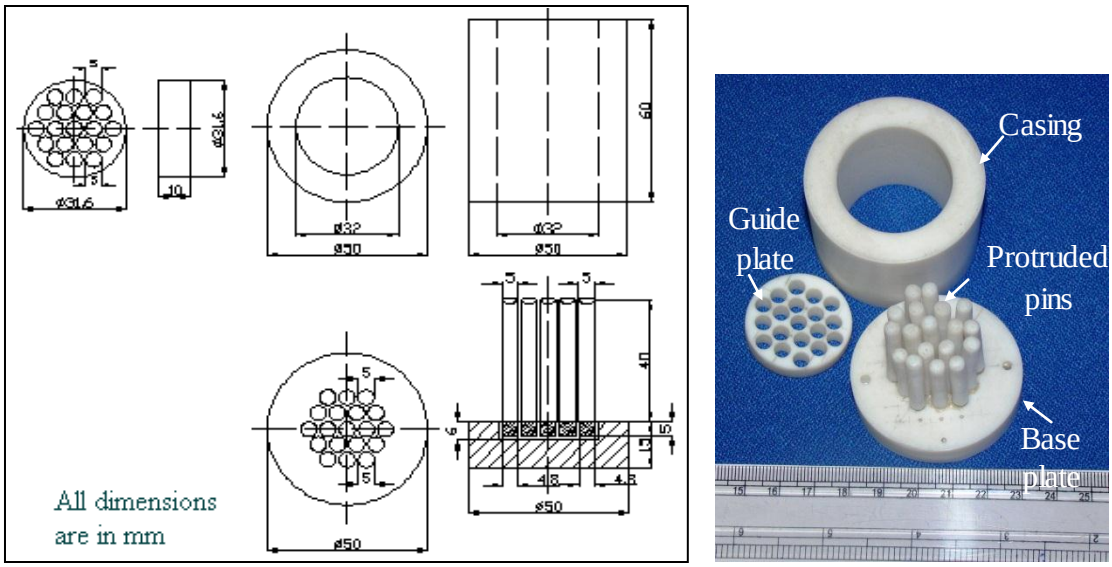

Fig.2.30 Design of the mould along with mould fabricated out of Teflon

2.5.7.1 Casting and gelation of honeycomb

Slurry was cast into prefabricated Teflon moulds into honeycomb geometries along with a solid sample for the sake of comparison and exposed to the microwave radiation under identical conditions and as per the procedures mentioned above. A dried electrolyte based honeycomb fabricated in the present study is shown in Fig.2.31. Honeycombs were further sintered at temperatures of 1500, 1525 and 1550^{o}C.

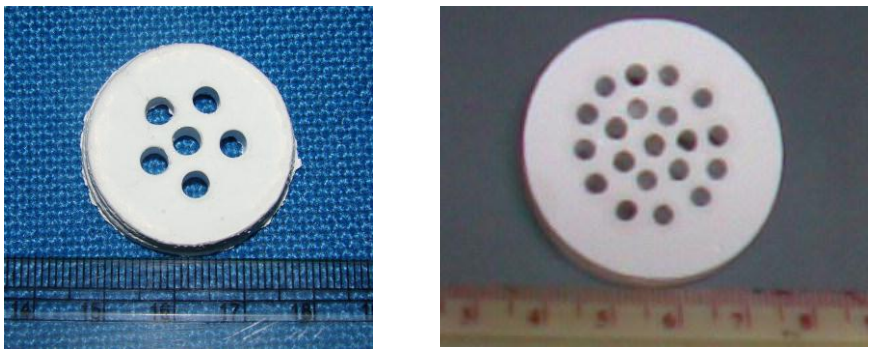

Fig.2.31 Green 8YSZ Honeycomb electrolytes produced by methyl cellulose casting

Cellular properties were calculated using the unit cell diameter and wall thickness of the green and sintered honeycombs [31]. Surface area/ unit volume of honeycomb configuration is estimated in the present study using the equation $S = \mathbf{k} \times r/(a + r)^2$, where, S is the surface area, r is a radius of the channels, a, is the wall thickness and **k** is a coefficient depends on channel shape and is $\pi/\sqrt{3}$ for the circular channel. Hagen-Poisuille equation is well known to determine the relative pressure drop across the honeycombs I and II for laminar gas flow passing through circular shaped channels, and is calculated by

$$\Delta P = 8\mu LQ/ (N\pi r^4)$$

Where μ is gas viscosity, L length of the honeycomb, Q gas flow rate, N number of channels and r is the radius of the channel. Cellular properties of honeycombs thus calculated for the samples cast by microwave/ thermal gelation process are presented in Table 2.9 and 2.10.

Table 2.9 Cell parameters of green honeycomb samples of 8YSZ

Sample ID	Bulk Density (g/cc)	% TD	Channel Diameter (mm)	Wall thickness (mm)	Pitch (mm)
HC I	2.678	45.38	3.65	1.46	5.11
HC II	2.679	45.40	2.55	1.28	3.83

Table 2.10 Properties of sintered honeycombs and solid sample of 8YSZ

Sample ID	Bulk Density (g/cc)	% TD	Channel Diameter (mm)	Wall thickness (mm)	Pitch (mm)	Relative Density	Surface to volume ratio (cm^2/cm^3)	Gas Pressure Drop (Pa)
HC I	5.855	99.23	3.00	1.20	4.20	0.6348	2.77	$6.813x10^{-04}$
HC II	5.854	99.23	2.00	1.00	3.00	0.6847	1.67	$1.720x10^{-03}$
Solid	5.856	99.24	-	-	-	1.0000	0.27	-

Honeycomb Solid Oxide Fuel Cell (HCSOFC) design being a monolith with plurality of tubes provides various structural advantages. The major difficulty in exploiting the commercial viability of SOFC is the long start up time for which various cell configurations are proposed to arrive at practical solutions. HCSOFC is one of the most promising designs among the proposed configurations due to their low relative densities and inherent high geometrical and physical surface areas. Unlike solids, the properties of honeycombs are based on three major variables such as, relative density (r^*/ r_s where r^* is the density of the cellular material and r_s is that of the solid of which it is made), cell wall material and geometry of the cells. Honeycomb extrusion process generally practice or rather complex involving lateral flow of the dough followed by the knitting with adjacent cross section within the die and is controlled to a larger extent by the rheological properties of the dough. Rheological properties depend on a variety of factors such as, choice of the binder, extent of solid loading in the dough, morphological characteristics of the

ceramic powder used, etc. The honeycomb structures thus produced provide high geometrical surface area and also generally exhibit high porosities even after sintering at high temperatures. However, the present process is rather simple and provides the possibility of engineering the configurations of the channels to the desirable shapes such as circular, triangular, square etc. depending on the geometry of the projections. Circular channels are especially useful as it encounters with fewer sealing problems and also less stress concentration points in actual SOFC applications. The flexibility of the present casting process is useful in engineering the channel diameter and wall thickness of honeycombs. It is evident from the Table 2.10 that the honeycomb configuration produced in the present study have clear advantages of increased surface to volume ratio in combination with a reduction in relative density of ~30% or more in comparison to the their solid counter parts of similar geometrical dimensions. This low relative density reduces the thermal inertia to a greater extent and in addition the channelized heat flow, due to the unique configuration of honeycombs results in enhanced heat transfer leading to faster warm up. Further, honeycomb designs and open frontal areas can be optimized through engineering the process to achieve minimum gas pressure drop.

Colloidal shaping of 8 mol% Yttria Stabilized Zirconia Electrolyte Honeycomb Structures by Microwave Assisted Thermal Gelation of Methyl Cellulose, 2011, J. Am. Ceram. Soc., Recommended for publication (Final manuscript being submitted).

2.6 Summary and conclusions

In order to have a total complete view on the shaping process the samples with the maximum densities (refer Table 2.11) were subjected to sintering at sintering temperature of 1525°C (recommended by the supplier of the 8YSZ powder).

Table 2.11 Comparative evaluation of the shaping process

Shaping process	Green density (g/cc)	Maximum green density (%TD)	Advantages	Sintered density (g/cc)	Maximum sintered density (%TD)	Remarks
Compaction	2.957	50.12	High green density	5.854	99.22	Low sintered density
Slip Casting	2.942	49 .87	High green density	5.867	99.44	High sintered density
MC Gel casting (Conventional)	2.680	45.42	Low green density Complex shaping	5.853	99.21	Low sintered density
MC Gel casting (Microwave)	2.688	45.56	Low green density	5.856	99.24	Low sintered density
Honey comb (Microwave)	2.678	45.38	Low green density	5.855	99.23	Low sintered density

It is evident that though compaction processing provided high green density, sintered density is relatively low, which can be attributed to the poor homogeneity. Thermal gel casting exhibited comparatively low green and correspondingly low sintered densities, however, it is advantageous for complex shapes, especially novel configurations like honeycombs. Slip casting not only provides a high green density it provides with high sintered density as well, which is advantageous in processing simple shapes.

Thermal gel casting is an environmentally friendly process utilizing non toxic methyl cellulose and employing microwave irradiation resulting in significant reduction in processing time

producing specimens with > 99 % density and microstructure as confirmed by the present study. Further considerable reduction in the duration of drying and binder removal and even with the possibility to sinter the samples directly without any binder removal process as the methyl cellulose in the cast samples are only about 0.2wt%.

2.7 References

1. Vijayakumar M, Loading of solids in a liquid medium: The concept of CBVC. Metals Materials and Processes.1995; **7**: 139.
2. Moulson A.J, Herbaert J.M. Electroceramics 2nd Edition, John Wiley & Sons Ltd, England. 2003; 95.
3. Reed J.S. Principles of Ceramic Processing, 2nd Edn, J. Wiley and Sons Inc., New York.
4. Rahaman M.N. Ceramic Processing and Sintering, Marcel Dekker Inc., New York. 1995
5. Ramavath P, Senthilkumar R, Saha B. P. Johnson R. Determination of Cohesion Index, Flow behavior and Caking properties of spray dried granules, [1] Report from Stable Micro Systems, ARCI Customer Report 2006 [2] Operation manual, Stable Micro Systems.
6. Schilling C, H, Aksay I.A. Slip casting. In Engineered Materials Handbook, Vol. 5, Ceramics and Glasses. American Technical Publishers, Herts. 1991; 153.
7. Lange F.F. Powder processing science and technology for increased reliability. J. Am. Ceram. Soc. 1989; **72**: 3.
8. McCauley R.A, Rheology. In Ceramic Monographs – Hand book of Ceramics. Verlag Schmid GmbH, Freiburg. 1983; 1.
9. Horn R.G, Surface forces and their action in ceramic materials. J. Am. Ceram. Soc. 1990; **73:** 1117.
10. McHale A.E. Processing additives. In Engineered Materials Handbook, Ceramics and Glasses. American Technical Publishers, Herts. 1991; **4**:115.
11. Brinker C, Scherer G, Sol-Gel Science. The Physics and Chemistry of Sol-Gel Processing. Academic Press. 1990.
12. Pugh R.J, Bergstrom L. Surface and Colloid Chemistry in Advanced Ceramic Processing. Surfactant Science Series. Marcell Dekker, New York.1994; **51**.

13. Tsetsekou A, Agrafiotis C, Milias A. Optimisation of the rheological properties of alumina slurries for ceramic processing applications Part I: Slip-casting. J.Euro.Ceram.Soc. 2001; **21**: 363.
14. Kato T, Yokoyama M, Takahashi A. Melting temperatures of thermally reversible gels IV. Methyl cellulose-water gels.Colloid Polym.Sci. 1978; **256**: 15.
15. Kobayashi K, Huang C, Lodge T.P. Thermoreversible gelation of aqueous methyl cellulose solutions. Macromolecules.1999; **32**: 7070.
16. Haque A, Morris E.R. Thermogelation of methylcellulose. Part I: molecular structures and processes.Carbohydr. Polym. 1993; **22**:161.
17. Sarkar N.Kinetics of thermal gelation of methylcellulose and hydropypropyl methylcellulose in aqueous solutions.Carbohydr.Polym. 1995; **26**: 195.
18. Sarakar N. Methylcellulose Polymers as multifunctional processing aids in ceramics. Ceram. Bull.1983; **62**: 1280.
19. Hirrien M, Desbrie`res J, Rinaudo M. Physical properties of methylcelluloses in relation with the conditions per cellulose modification. Carbohydr. Polym. 1996; **31:** 243.
20. Hirrien M, Chevillard C,Desbrie`res J, Axelos M. A.V,Rinaudo M, Thermogelation of methylcelluloses: new evidence for understanding the gelation mechanism.Polymer.1998;**39**: 6251.
21. Nishinari K, Hofmann K. E, Moritaka H, Kohyama K, Nishinari N. Sol-gel transition of methylcellulose. Macromol. Chem. Phys. 1997; **198**: 1217.
22. Vigouret M, Rinaudo M, Desbrie`res J. Thermogelation of methylcellulose in aqueous solution. J. Chim, Phys. 1996; **93**: 858.
23. Yuguchi Y, Urakawa H, Kitamura S, Ohno S, Kajiwara K. Gelation mechanism of methyl hydroxypropyl cellulose in aqueous solution. Food Hydrocolloids. 1995; **9**: 173.
24. Sarkar N. Thermal Gelation properties of methyl and hydroxypropyl methyl cellulose. J. Appl. Polym. Sci. 1979; **24**:1073
25. Li L, Thangamathesvaran P.M, Yue C.Y, Tam K.C, Hu X, Lam Y.C. Gel network structure of methylcellulose in water. Langmuir.2001; **17**: 8062.
26. Wetzko M, Belzner A, Rohr F. J, Harbach R. Solid oxide fuel cell stacks using extruded honeycomb type elements. J. Power Sour. 1999; **83:** 148.

27. Zhong H, Matsumoto H, Ishihara T, Toriyama A. Self-supported $LaGaO_3$-based honeycomb type solid oxide fuel cell with high volumetric power density. Solid State Ionics. 2008; **179:**1474.
28. Ruiz-Morales J.C, Marrero-Lopez D, na-Martínez J.P, Canales-Vazquez J, Roa J. J , Segarra M, Savvin S. N, Nunez P. Performance of a novel type of electrolyte-supported solid oxide fuel cell with honeycomb structure. J. Power sour. 2010; **195:** 516.
29. Suzuki T, Funahashi Y, Yamaguchi T, Jufishiro Y, Awano M. Cube-type micro SOFC stacks using sub-millimeter tubular SOFCs. J Power Sour. 2008; **183:** 544.
30. Bagley R. D. February 1974; US patent No.3,790,654.5.
31. Shimizu S, Yamguchi T, Suzuki T, Fujishiro Y, Awano M. Development of honeycomb type SOFC integrated with multi micro cells: concept and simulations. Advances in Solid Oxide Fuel Cells III. 2008; **28:** 49.

Chapter -3

Sintering of 8YSZ Green Compacts

3.0 Introduction

Sintering of ceramics is the method involving consolidation of ceramic powder particles by heating the green compact to a high temperature below the melting point. The driving force for sintering is the reduction of the total interfacial energy. The change in interfacial energy is due to the change in interfacial area as a result of elimination of pores (densification) and coarsening of grains (grain growth). For solid-state sintering, interfacial energy is related to the replacement of solid/vapor interfaces (surfaces) by solid/solid interfaces (grain boundaries). In sintering, the reduction in total interfacial energy occurs through densification and grain growth, which are indeed two competing processes.

Present chapter presents the densification and microstructure development strategies followed and direct comparison is made between sintered samples derived from the same starting powder densified using different conventional and non-conventional sintering techniques. The various sintering methodologies followed are Conventional Ramp and Hold Sintering (CRH), Rate Controlled Sintering (RCS), Two Stage Sintering (TSS) and non-conventional sintering techniques such as Microwave Sintering (MWS) and Spark Plasma Sintering (SPS).

3. 1 Conventional Sintering Methodologies

3.1.1 Conventional Ramp and Hold Sintering (CRH)

The conventional ramp and hold sintering employs longer duration of dwell time at final temperature for the elimination of residual porosity and often results in abnormal grain growth. Fig.3.1 represents the schematic of CRH sintering profile. As was discussed by many investigators, the two processes of densification by pore closure and grain growth are competitive and depend on temperature and grain size. Assuming that surface and grain boundary diffusions dominate in nanocrystalline compacts, the corresponding rates of densification and grain growth during the intermediate and final stages of pressure-less sintering may be expressed respectively as [1].

$$\frac{1}{\rho}\frac{d\rho}{dt} \approx \frac{733 D_{gb}\delta_{gb}\gamma_{SV} V_m}{RTG^4\rho} \tag{3.1}$$

$$\frac{1}{G}\frac{dG}{dt} \approx \frac{110 D_S\delta_S\gamma_{gb} V_m}{RTG^4}(1-\rho)^{-\frac{4}{3}} \tag{3.2}$$

where D_{gb} and D_S are the diffusivities at the grain boundary and surface, δ_{gb} and δ_S are the grain boundary and surface thicknesses, where effective diffusion takes place, γ_{SV} and γ_{gb} are the specific surface and grain boundary energies, G is the grain size, ρ is the density, V_m is the molar volume, T is the absolute temperature, and R is the gas constant. Following equations (3.1) and (3.2) as was discussed by Rahaman [2] and Kang [3] et al., it is evident that under present assumptions the low sintering temperatures are preferred to keep the grain sizes low preserving the nanostructure during the densification. Further, at high temperatures the lattice diffusion dominates and grain growth occurs predominantly simultaneously with densification.

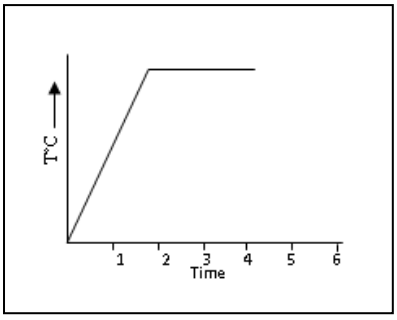

Fig.3.1 Schematic of CRH sintering

As stated earlier, during sintering, grain growth is also active and this reduces the total interfacial energy. When grain boundaries and pores are displaced simultaneously grain growth is controlled either by the grain boundaries or by the pores. If grain growth is controlled by grain boundaries, the pore dragging effect on the grain boundary migration is negligible. If grain growth is controlled by pores, the displacement rate of a pore/grain boundary together is fixed by the displacement rate of the pore. When grain growth is controlled by grain boundaries, the matter displacement involved is the atomic migration from one grain towards another through the separating grain boundary. In the case of grain growth controlled by pores, matter displacement proceeds either by surface-diffusion at the pore surface, gas phase transport in the pore or bulk diffusion in the grains. The determination of the mechanisms controlling grain

growth and densification during sintering of ceramics is not an easy task and most of the time results require critical analysis.

3.1.2 Rate Controlled Sintering (RCS)

The Rate Controlled Sintering (RCS) of nano powders is an advanced and progressive sintering concept, which has many advantages over conventional methods of sintering. The concept of RCS originally introduced by H. Palmour III and D. R. Johnson in 1965 from North Carolina State University (NCSU)in order to achieve controlled grain sizes has received attention in recent past [4-9].

A progressive reduction (fast to slow) in densification rates, accomplished by a feedback controlled dilatometer, enable development of fine grained microstructures in dense ceramics by RCS technique. In RCS shrinkage is dependent parameter whereas the temperature is independent parameter, contrary to Conventional Ramp Hold (CRH) sintering. RCS is the method of non-isothermal, non-linear sintering protocol. A feedback has to be established between the sintering temperature and the instantaneous density to develop the best temperature - time path for sintering. There is a maximum safe rate of shrinkage for each level of fractional density is necessary to control both pore and grain structure evolution. Sintering proceeds through the competition between densification and grain growth. This competition allows flexible grain size control. The balance between surface and grain boundary mass transfer is responsible for grain size diminishing in the course of RCS. This balance leads to perfect, well-conjugated grain boundaries in sintered ceramics. The improved microstructures from RCS can be attributed due to the maximized efficiency of densification and optimized time-temperature profile for grain growth.

The schematic comparisons between CRH and RCS profiles of the time - temperature and the relative density - time profiles are presented in Fig.3.2 (a) and (b). The density time profile is characterized by three regimes with linear, slower linear and log decreasing dependence of relative density with time after onset of shrinkage. The principle of RCS is as follows: The green compact is heated in a dilatometer at constant heating rate until dl/dt, i.e. the slope of length change versus time curve, becomes larger than a threshold value at which the temperature rise is

stopped. The shrinkage now takes place under isothermal condition. RCS generally proceed in 3 stages. The details of each step are listed below:

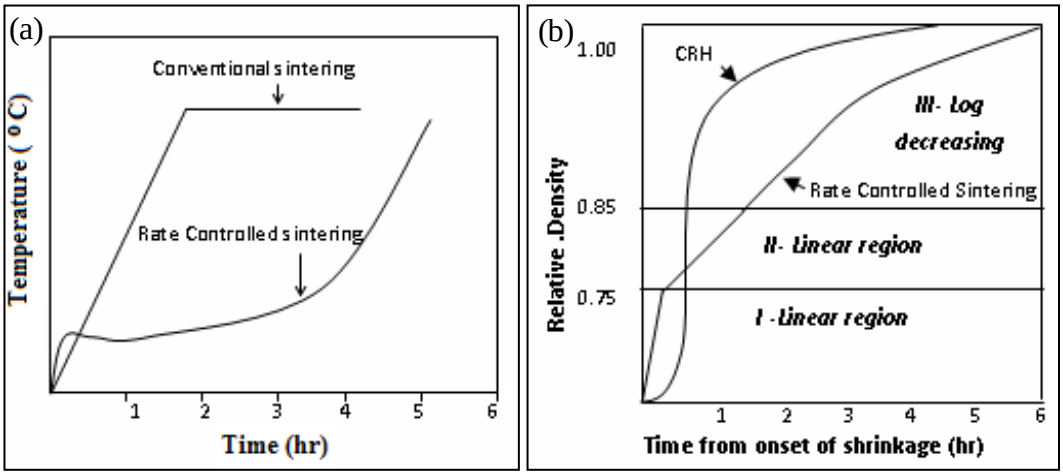

Fig.3.2 Schematic comparisons between CRH and RCS profiles of, (a) Temperature - Time and (b) Relative density - Time

First Stage: A fast and nearly linear densification rate is applied until the sample reaches a theoretical density (TD) of approximately 75%. Fast heating rates are used to bypass the surface diffusion regime, in which grain coarsening tends to take place with little densification.

Second Stage: The densification rate is held constant at maximum safe level until a 75 % to 85% of TD is attained. A considerably slower densification rate is applied. This step helps pores within the microstructure to remain open as long as possible, because in this stage they are very effective at pinning grain boundaries.

Third Stage: From 85% to 100% of TD a slower densification rate is applied, which is decreased logarithmically with density. The purpose of this step is to allow sufficient time for the closed pores to disappear by diffusion without being detached from the grain boundaries, otherwise excessive grain growth will occur.

RCS is a method of non-isothermal, non-linear sintering process attracts the attention of ceramists due to its wide possibilities of microstructural control. Specimens under the RCS conditions are characterized by finer grains and avoid gas entrapment in the pores and minimize pore-grain boundary separation.

3.1.3 Two Stage Sintering (TSS)

Two Stage Sintering (TSS) method was originally proposed by Chen and Wang [10]. In this method the sample is heated to an elevated temperature (T_1) and then immediately cooled to a lower temperature (T_2) and then held there for longer times. The schematic of TSS sintering profile is presented as Fig.3.3. To fabricate nanocrystalline ceramics by pressure-less conventional sintering route, grain boundary migration has to be abated. The TSS procedure consists of the following steps: (1) sintering at a constant heating rate until the relative sample density >75% TD is achieved (2) temperature decrease by ~100°C and sample sintering for a period of tens of hours at a lowered temperature. In this technique the first step guarantees the disappearance of supercritical pores while the other pores become unstable so that the body can subsequently sinter at a lower temperature. The grain growth becomes limited at the lower temperature of second sintering step. TSS then yields samples of identical density as that of conventionally sintered samples but with smaller grain sizes. The temperature of the first sintering step was chosen on the basis of the evaluation of dilatometric measurements [11]. The temperature of the second sintering step (T_2) was lower than T_1. To succeed in two-stage sintering, a sufficiently high starting density should be obtained during the first step. When the density is greater than a critical value the pores become subcritical and unstable against shrinkage which is induced by capillary action. These pores can be eliminated as long as grain boundary diffusion allows, even if the particle network is frozen. This process takes advantage of grain boundary diffusion with no or negligible grain boundary migration. Chen and Wang have successfully retained the final microstructure of yttria at 60 nm or four to six times grain growth using TSS [12].

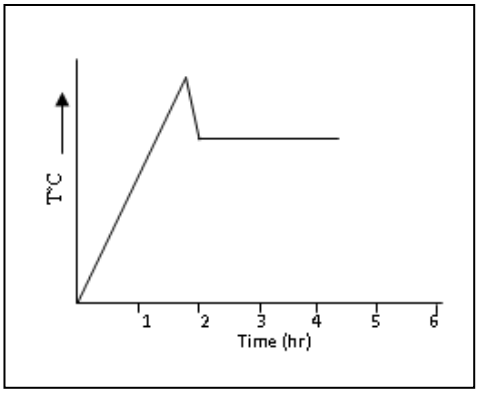

Fig.3.3 Schematic of TSS sintering profiles

Chen and co-workers [12] explained that to achieve densification without grain growth grain boundary diffusion needed to remain active, while the grain boundary migration had to be suppressed. A mechanism to inhibit grain boundary movement was a triple-point (junction) drag. Consequently, to prevent the accelerated grain growth, it was essential to decrease grain boundary mobility. The grain growth proceeds through a competition between grain boundary mobility and the junction mobility. Once the latter became less at low temperatures in which junctions were rather immobile, the mentioned drag would occur. The grain growth was, therefore, prohibited under that condition. This grain boundary diffusion accompanied by triple point drag at low temperatures (T_2), contributed to a fully dense microstructure with a constant grain size.

Mazaheri et al. [13] have suggested proper temperatures for first (T_1) and second stages (T_2) in two stage sintering to prohibit grain growth without degradation of densification. On the contrary, the inappropriate regime can serve no evolution in densification as well as no remarkable grain growth difference in comparison with normal sintering [13]. Han et al. [14] used TSS technique to control the grain growth of YSZ nanopowder synthesized by a liquid phase method. Laberty-Robert et al. [15] as well as Ghosh et al. [16] have also investigated the effect of TSS on microstructure of yttria stabilized zirconia. Yu et al. [17] took the benefit of this technique for sintering of powder injection-moulded zirconia parts. In addition to 8YSZ, TSS technique has been successfully conducted on ZnO [11], Ni–Cu–Zn ferrite [17], Al_2O_3 [18, 19] and liquid phase sintering of SiC [20].

Mazaheri et al. [13] reported that for nanocrystalline ZnO, there was a critical temperature of second step to gain fully dense structure without accelerated grain growth. At temperatures lower than that, even after long dwell time, no improvement in densification could be gained. They reported that surface diffusion contributed to grain growth without densification at temperatures lower than critical one.

Two stage sintering was employed to consolidate nanocrystalline 8 mol% yttria stabilized zirconia processed by glycine-nitrate method [22]. The grain size of the high density compacts (>97%) produced by TSS method was seven times less than the specimens made by the conventional sintering technique. Up to ~96% increase in the fracture toughness was observed

(i.e. from 1.61 - 3.16 MPa $m^{1/2}$) with decrease in grain size from ~2.15μm to ~295 nm. A better densification behavior was also observed at higher compacting pressures.

So far the TSS method has been successfully applied to a number of ceramic materials like Y_2O_3 [12], $BaTiO_3$ [23–25], $SrTiO_3$ [26, 27], c-ZrO_2 [22, 28, 29] and $CoFe_2O_4$ [30] but, with less successful examples in tetragonal zirconia and hexagonal alumina ceramics [19, 20, 31-33] is also known. Achieving a high density and at the same time a small grain size is very important for the latter two kinds of structural ceramic materials because it can bring about an improvement in mechanical properties such as hardness [33], wear resistance [34], strength [35], fracture toughness [36] or optical transparency in alumina ceramics [37].

The influence of TSS process on the final microstructure of oxide ceramic materials with three different crystal structures was studied [38]. Two kinds of alumina (particle size 100 nm and 240 nm) as well as tetragonal zirconia (stabilized with 3 mol% Y_2O_3, particle size 60 nm) and cubic zirconia (8 mol% Y_2O_3, 140 nm) powders were cold isostatically pressed and pressure-less sintered with different heating schedules. The microstructures achieved with TSS method were compared over microstructures achieved with conventional ramp and hold Sintering (CRH). The results showed that the efficiency of the TSS of these oxide ceramics was more dependent on their crystal structure than on their particle size and green body microstructure. The method of TSS brought only negligible improvement in the microstructure of tetragonal zirconia and hexagonal alumina ceramics. On the other hand, TSS was successful in the sintering of cubic zirconia ceramics; it lead to a decrease in grain size by a factor of 2.

3.2 Non-Conventional Sintering Methodologies

It is reported that high heating rates, applied pressure, and strain rates, each enhances the densification process of nanocrystalline powder compacts lead to the development of various nonconventional sintering methodologies. Two non-conventional methodologies employed for sintering comprises of microwave sintering (MWS) and spark plasma sintering (SPS).

3.2.1Microwave sintering (MWS)

Microwave energy is a form of electromagnetic energy with the frequency range of 300 MHz to 300 GHz and the corresponding wavelengths are between 1 m and 1 mm. Microwave heating is a

process in which the materials couple with microwaves absorb the electromagnetic energy, which gets transformed into heat. Microwave heating generates heat within the material and is a volumetric heating [39]. This heating mechanism is advantageous due to enhanced diffusion processes, reduced energy consumption, very rapid heating rates and considerably reduced processing times, decreased sintering temperatures, improved physical and mechanical properties. These features are not observed in conventional heating processes [39-43]. Microwave energy has been in use for variety of applications for over 50 years. These applications include communication, food processing, wood drying, rubber vulcanization, medical therapy, polymers, etc. Use of microwave technology in materials science and processing is not rather new. The areas where this technology has been applied include process control, drying of ceramic sanitary wares, calcination, and decomposition of gaseous species by microwave plasma, powder synthesis, and sintering [44, 45]. Microwave processing of materials was mostly limited until the year 2000 to ceramics, semiconductors, inorganic and polymeric materials. Now it has been extended as efficiently and effectively to powdered metals as to many ceramics. Electromagnetic spectrum, frequency and the wavelength range of microwaves are shown in Fig.3.4.

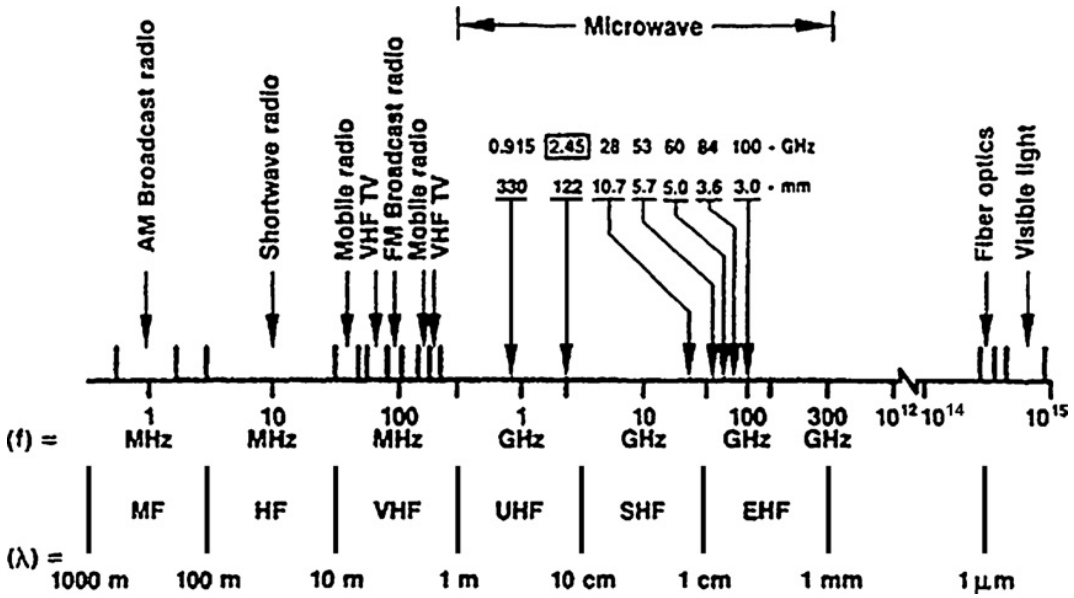

Fig. 3.4 Electromagnetic spectrum and frequencies used in microwave processing.

Microwaves have longer wavelengths and lower available energy quanta than other forms of electromagnetic energy such as visible, ultraviolet or infrared light. The application of microwave heating is widely is used in different materials. The most commonly used frequencies for heating purposes are 915MHz and 2.45 GHz, which are derived from the electrical energy with the transformation efficiency of about 85% and 50%, respectively [45]. The dielectric interaction of materials with microwaves is described by two important parameters, absorbed power and depth of microwave penetration. These two factors determine the uniformity of heating throughout the material. The average absorbed power is the volumetric absorption of microwave energy in the material.

Microwave heating has been used successfully to sinter a wide variety of oxide and non-oxide ceramic, metal and composite powders. It differs from the conventional heating processes because the use of microwaves facilitates the transfer of energy directly into the materials, providing volumetric heating [46]. This mode of direct heating eliminates wastage of energy and also offers the potential of applying high heating rates. Hence, microwave methods drastically reduce the energy consumption, particularly when compared with high temperature processes where heat losses increase drastically with rising process temperatures and it is possible to reduce the time required to complete a process [43]. A remarkable saving in energy and time can be obtained and the resulting products often shows enhanced mechanical properties compared to conventional treated ones [47], because the heating is more uniform and volumetric [42].

Microwave sintering technique can effectively promote the forward diffusion of ions and thus accelerate the sintering process, resulting in the grain growth and the densification of matrix. It is well known that sintering process consists of densification stage and grain growth stage [48]. The densification rate strongly depends on the diffusion of ions between particles and the grain growth rate is mostly determined by the grain boundary diffusion. Dube et al. have found that the intense microwave field concentrates around samples during microwave sintering [49]. Especially, the power of microwave field between sample particles is almost 30 times larger than the external field giving rise to ionization at the surface of sample particles. As a result, the diffusion of ions between sample particles is accelerated and the densification stage is promoted. Moreover, surrounding electromagnetic field can intensely be coupled with ions at grain boundaries. Under the microwave field the kinetic energy of ions at grain boundaries increases,

which results in decreasing the activation energy for a forward jump of ions and increasing the barrier height for a reverse jump [38]. So the forward diffusion of inter grain ions is promoted and thus accelerates the grain growth during sintering [50]. In many cases, the microwave sintering has shown to produce samples with more uniform grain size distribution and higher density [42].

3.2.2Spark plasma sintering (SPS)

Spark plasma sintering simultaneously applies pulsed electrical current and pressure directly on the sample leading to densification at relatively lower temperatures and short retention times [51-56]. As both the die and sample are directly heated by the Joule effect extremely high heating rates are possible due to which non-densifying mechanisms like surface diffusion can be surpassed.

The versatility of SPS allows very quick densification to near theoretical density for a number of metallic, ceramic and multi-layer materials under a low vacuum /inert environment [56, 57]. It is a novel hot pressing technique where very high heating rates upto (~ 500°C/min) were achieved by the application of pulsed electrical current and pressure (150MPa) simultaneously. In hot pressing, the precursor powder is loaded in a die and a uniaxial pressure is applied during the sintering. In the SPS technique, where a pulsed direct current is passed through an electrically conducting pressing die working as the heating element gives more rapid densification rate due to the use of pressure and rapid heating rate. The presence of a pulsed electrical field might create sparks during the initial part of the sintering, which clean the particles surface and thus facilitate grain boundary diffusion. Electrical field induced diffusion processes might also contribute to increased densification rate [55].

The die acts as a heating source and the sample is heated from both outside and inside, as outlined in the schematic drawing in Fig.3.5. Rapid sintering by SPS made it possible for the sample to skip over low temperature regime where the non-densifying mechanism (surface diffusion) is active and to proceed directly to the elevated temperature regime where densifying mechanisms (grain boundary and volume diffusion) are predominant [56].

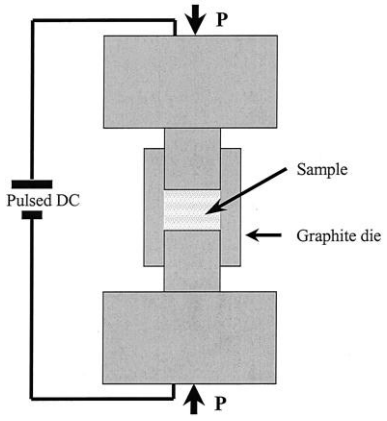

Fig.3.5Schematic drawing illustrating the features of an SPS apparatus

Plasma activated sintering (PAS) and spark plasma sintering (SPS) apparatus were developed in 1988 and 1990 respectively. Using SPS & PAS a variety of materials such as metallic materials, structural ceramics, oxide superconductors, ceramic composites, polymers, thermoelectric materials, and functionally graded materials have been prepared.

The unique features of the process are the possibilities of using very fast heating rates (~500°C/min) and very short holding times (within few minutes) to obtain fully dense samples. Three factors that contribute to the rapid densification process are (i) the application of a mechanical pressure; (ii) the use of rapid heating rates; and (iii) the use of pulsed direct current, implying that the samples are also exposed to an electrical field. It is generally accepted that application of mechanical pressure is helpful in removing pores from compacts and enhancing diffusion. The heat transfer from the die to the compact is very efficient in this process because, the die itself acts as a heating element. However, it is frequently argued that the improved densification rates stem mostly from the use of direct current pulses of high energy. Thus, the process inventors originally claimed that the pulses generate spark discharges and even plasma between the powder particles, which explains why the process is named spark plasma sintering. During the initial part of the sintering process the generated spark discharge and/or plasma is said to clean the surfaces from adsorbed species such as, CO_2, H_2O, and OH^-. In the later part of the process this cleaning is expected to enhance the grain-boundary diffusion processes that, together with the proposed spark discharges and/or plasma processes, are assumed to promote transfer of material and, thus, also enhance the densification [57]. SPS has been demonstrated to enable the consolidation of ceramic materials within minutes. However, the use of a rapid

densification process does not always guarantee that extensive grain growth can be avoided. The rapid densification of nano sized precursor powders under inappropriate sintering conditions can easily yield densified compacts composed of micrometer-sized grains. Various sintering conditions such as, the sintering temperature, holding time, heating rate, applied pressure, and pulse sequence, influence the densification and grain-growth rate. Spark plasma sintering (SPS), or field assisted sintering (FAS) combines these processing parameters needed for efficient densification of nanocrystalline compacts. These sintering conditions lead to superfast densification of nanocrystalline powder compacts and to retention of the nanostructure. This technique was found to be especially compatible for the densification of nanocrystalline powders. Many atomic transport mechanisms may be active during the sintering and densification of nanocrystalline oxide powders. Neglecting the evaporation–condensation and viscous sintering mechanisms that are limited to specific material systems, the main transport mechanisms are surface, grain boundary, and lattice diffusion. While surface diffusion during pressure-less sintering can change the pore shape, the corresponding pore volume is barely affected. Consequently, mass transport by surface diffusion is not considered as a densification mechanism. This is not valid for densification via SPS. The main advantage of SPS is the preservation of the particle specific surfaces during heating. Under applied load the compact densification may benefit from the low temperature mass transport mechanisms provided by the nanoparticle surfaces and interfaces. The short sintering durations at low temperatures are expected to limit the diffusion controlled grain growth.

In the SPS process, a graphite die set is filled with the raw material powder and placed between the lower and upper electrodes. A pressure is applied on the compact during sintering. A pulsed direct current (dc) is then applied to the sintering powder and the activation of powder particles is achieved by the application of electrical discharges. For electrically conductive powders heating up is mainly due to the Joule effect. For non-conductive powders heating is likely achieved through the heat transfer from the die and punches. For conductive powders electrical discharges can occur along the particles surface during the SPS process. For oxides ion conduction takes place at high temperatures. With the application of a altering pulse DC current thermal and electrical breakdown phenomena are most likely to occur at high temperatures for non-conductive ceramic powders and skin current can be formed [58, 59, 60]. With the alternative current powder contacts and gaps work like small capacitors and plasma may be

generated by the electrical discharges across these capacitor gaps. The application of an external electric field leads to improved densification during sintering and requires a considerably shorter time cycle compared to conventional methods of sintering. The high-temperature sputtering phenomenon generated by spark plasma and spark impact pressure eliminates absorbed gas and impurities present on the surface of the powder particles. There are several anticipated merits of SPS: 1. Generation of spark plasma; 2. Effect of electric field; 3. Effect of electric current on diffusion in conductor or skin current on the semiconductor and insulator; 4. Impact of spark plasma; 5. Rapid Joule heating and cooling.

The potential of the SPS method is most promising, at least at high temperatures, for conducting materials. For interpretation of the densification behavior and the properties of the materials a critical analysis of temperature measurements and temperature distribution is necessary [61]. The current distribution varies as a function of the conductivity of tool and sintering materials during heating. In non-conducting materials the current runs only through pistons and the die, whereas in conducting materials most of the current perfuse through the sample resulting in direct heating of the sample itself. In the case of non-conducting ceramics the tool material (graphite) is the only source for joule heat production. Also, most electrically non-conductive materials show a lower thermal conductivity compared with electrically conductive materials. For larger samples both facts can result in large temperature gradients accompanied by gradients in the material properties [62]. An estimation of the current distribution between the material and the dies can be made using the resistivity of the materials and the resistivity of applied graphite (8.5 - 13μΩcm). For most of the conventional ceramics even at high temperature only a low amount of current runs through the sample volume. Therefore no direct effect of the electric current can be expected and temperature gradients have to be taken into account for larger samples.

Recently, appreciable attention has been paid to the investigation and fabrication of high melting point, optically transparent polycrystalline ceramic oxides. Optically transparent ceramics are often fabricated by either hot-isostatic pressing (HIP), or vacuum sintering at very high temperatures using ultrapure ultrafine powders [63-68]. Combining the high sinterability of nanocrystalline powders with the rapid densification rates characteristic of spark plasma sintering (SPS) the latter technique has been widely promoted as a method for fabricating transparent polycrystalline oxides [69-82]. Transparent polycrystalline ceramics of various

technical oxides such as, Al_2O_3 [69-73], MgO [74], $MgAl_2O_4$ spinel [75-79], mullite ($3Al_2O_3.2SiO_2$) [80], YAG ($Y_3Al_5O_{12}$) [81], Y_2O_3 [82] and yttria-stabilized ZrO_2 [83] have been fabricated by SPS.

Effects of particle size on the various parameters during spark plasma sintering (SPS) were examined [84]. Nanometric ceramic particle compacts enable accumulation of high electric charge and discharge under conventional voltages (6–20 V) applied during the SPS. The critical particle size for the electric discharge depends on both material properties and the particle morphology. Nanocrystalline cubic oxides were used as model systems to examine the densification behaviour during the SPS. Two atomistic mechanisms were identified at the early stages of the densification. Densification by plastic deformation dominates in nanocrystalline ceramics with low yield stress, whereas densification by grain rotation and sliding dominates in those with high yield stress. The active densification mechanism depends on the changes in both the mechanical and electrical properties with temperature. Densification of nanocrystalline MgO with low yield stress proceeds by plastic deformation at 700°C. However, densification of nanocrystalline YAG with high yield stress proceeds by nano-grain rotation aided by particle surface softening. Densification at the final stages of sintering is associated with diffusional processes, where curvature driven grain growth predominates.

For the first time, the mechanisms controlling the densification of granulated stabilized zirconia raw powder during SPS experiments were also determined [85]. When the effective compaction stress and the temperature were low, a pure diffusion mechanism (bulk) was probably responsible for the densification. At intermediate effective compaction stresses and medium temperatures, stress exponents of two associated with apparent activation energy 450 kJ mol^{-1}, were determined using a densification law derived from an analogy with high-temperature creep models. In that case, it was proposed that densification proceeded by grain boundary (GB) sliding accommodated by an in-series (interface-reaction/lattice diffusion of Zr^{4+} and/or Y^{3+} cations) mechanism controlled by the interface-reaction step. For high-temperatures and/or high effective compaction stresses, a similar analysis showed a stress exponent between 3 and 4.8. Then, it was proposed that densification should proceed by a dislocation-climb controlled mechanism.

3.3Sintering studies of 8YSZ pellets

Slip cast 8YSZ specimens as described in processing, are subjected to conventional sintering Conventional Ramp and Hold (CRH), Rate Controlled Sintering (RCS), Two Stage Sintering (TSS) and nonconventional microwave sintering (MWS). Further 8YSZ powders were also subjected to nonconventional Spark Plasma Sintering (SPS). The sintering methodologies are described as follows.

3.3.1 Conventional Ramp and Hold Sintering (CRH)

8YSZ slip cast pellets made into dimensions of 10 mm diameter and 5 mm thickness were subjected to dilatometric measurements. Sintering curves were recorded from room temperature to 1550°C at a heating rate of 5, 10 and 20°C/min using a single pushrod dilatometer (Model No. 402C, Netzsch, Germany). Photograph and schematic diagram of the parts are presented in Fig.3.6 (a) and (b). A calibrated alumina sample holder and pushrod were employed for the measurements.

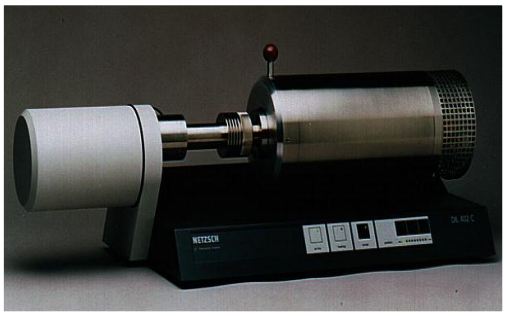

Fig.3.6 (a) Dilatometer

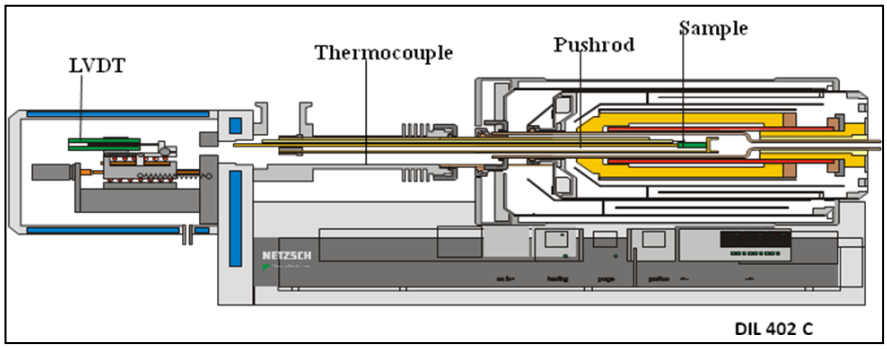

Fig.3.6 (b) Schematic diagram of the dilatometer used for the measurements

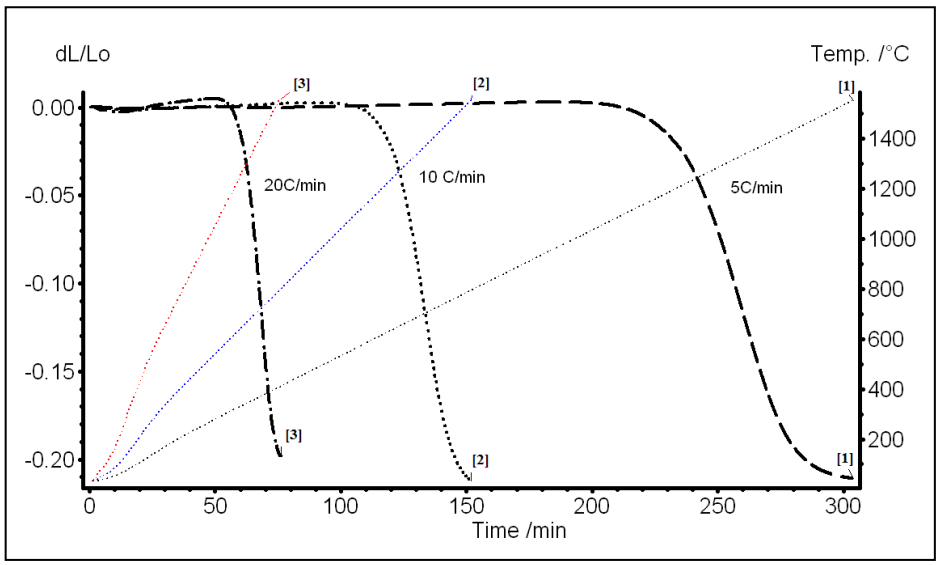

Fig.3.7 Linear shrinkage of the 8YSZ slip cast specimens during sintering at three different heating rates 5 (dashed line), 10 (dotted line) and (dot-dash line) 20 °C /min.

The plot of dilatometric shrinkage for the constant heating rates of 5, 10, and 20°C/min for slip cast samples are shown in Fig.3.7. Samples exhibited almost a similar shrinkage pattern with an onset of shrinkage at temperatures around 1000°C and extending to 1550°C with the highest shrinkage observed for the heating rate of 5°C/min as is evident from the closed to plateau behavior.

3.3.1.1 Estimation of activation energy through the construction of Master Sintering Curve (MSC)

Sintering involves several diffusion mass transport mechanisms and is accompanied by the geometric evolution of the sample throughout the whole process. Generally it is not possible to quantitatively predict the sintering behaviour of a particular ceramic specimen even though its thermal history is known [86]. A number of theoretical models have been developed to describe the sintering kinetics of ceramic systems [87-92]. Among all, the master sintering curve model [90] has been most successful in simplifying the process and making the final-density prediction possible.

We use the method to construct the master sintering curve by relating sintered density to the work of sintering for the sample. In order to accurately determine the apparent activation

energy(Q) for sintering the mean residual square for different activation energy value has been calculated. The various steps involved in the process are as follows.

Step1. Analysis of dilatometric shrinkage data

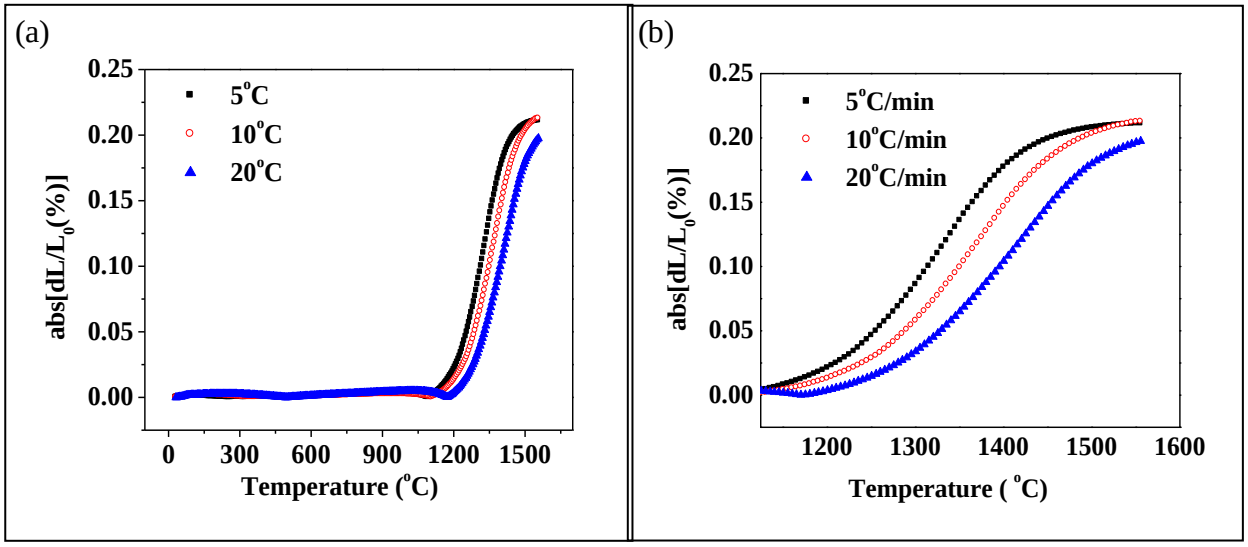

Fig.3.8Shrinkage vs. temperature plots of (a) entire dilatometer data (b) shrinkage region

As shown in the Fig. 3.8(a), the entire dilatometer data for the three different heating rates has been plotted. The absolute value of shrinkage in percentage is taken as ordinate. As an indication of the above plot there is no shrinkage upto a temperature of nearly 1150°C and above this temperature the shrinkage of the sintered material gains significance. The second plot Fig. 3.8(b) shows the shrinkage region. The data of the shrinkage region (1170.5-1555.5 °C) has been considered for MSC construction.

Step 2: Calculation of relative densities

The expression for instantaneous relative density (ρ) is given by the following equation as

$$\rho = \frac{\rho_0}{\left(1 - \frac{dl}{l_0}\right)^3} \times 100 \qquad (3.3)$$

where$\rho_0$is the green density of the sample. The absolute value of shrinkage in percentage is inserted into the equation (3.3) for the three different heating rates. The plot shows that the sample undergoing sintering at lower heating rate is having higher relative density.

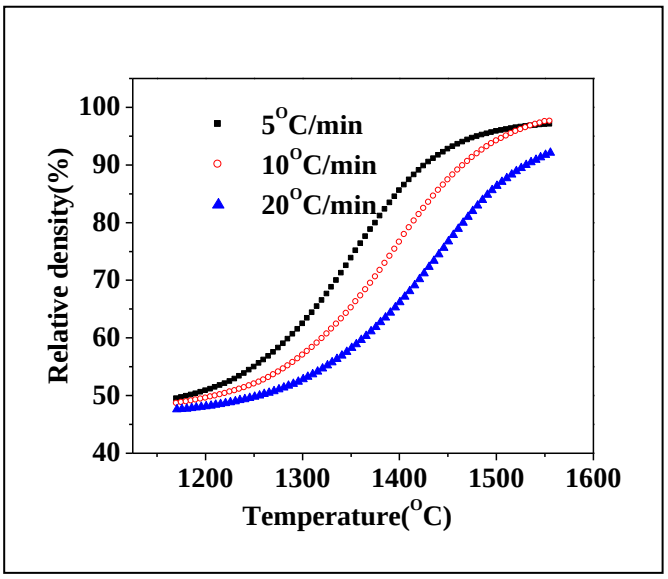

Fig.3.9 Plot of Relative density (%) vs. Temperature (°C) for different heating rates.

Step 3: Calculation of work of sintering and MSC

The other important parameter for the construction of MSC is work of sintering as defined by the equation given below

$$\theta\left(t, T(t)\right) \equiv \int_0^t \frac{1}{T} \exp\left(\frac{-Q}{RT}\right) dt \tag{3.4}$$

In this equation (3.4), t is the total time taken by the sintering process in seconds. At a particular temperature (T) since the integrand is independent of time. Then the simplified form of the above equation used for calculation of work of sintering is

$$\theta(t_r, T) \equiv \{I(T)\}(t_r - t_i) \tag{3.5}$$

Where I(T)is the integrand of equation (3.5), t_r is the time in second at which work of sintering required and t_i is the initial sintering time taken as zero for all the three heating rates. The three different heating rates (5, 10, 20 °C/min) corresponding to a time span (t) of 0 to18300, 9150 and 4575seconds respectively. For different chosen Q values corresponding to a particular temperature and time, θ (t, T) is calculated. Then the MSC Log θ (t, T) vs. ρ is plotted.

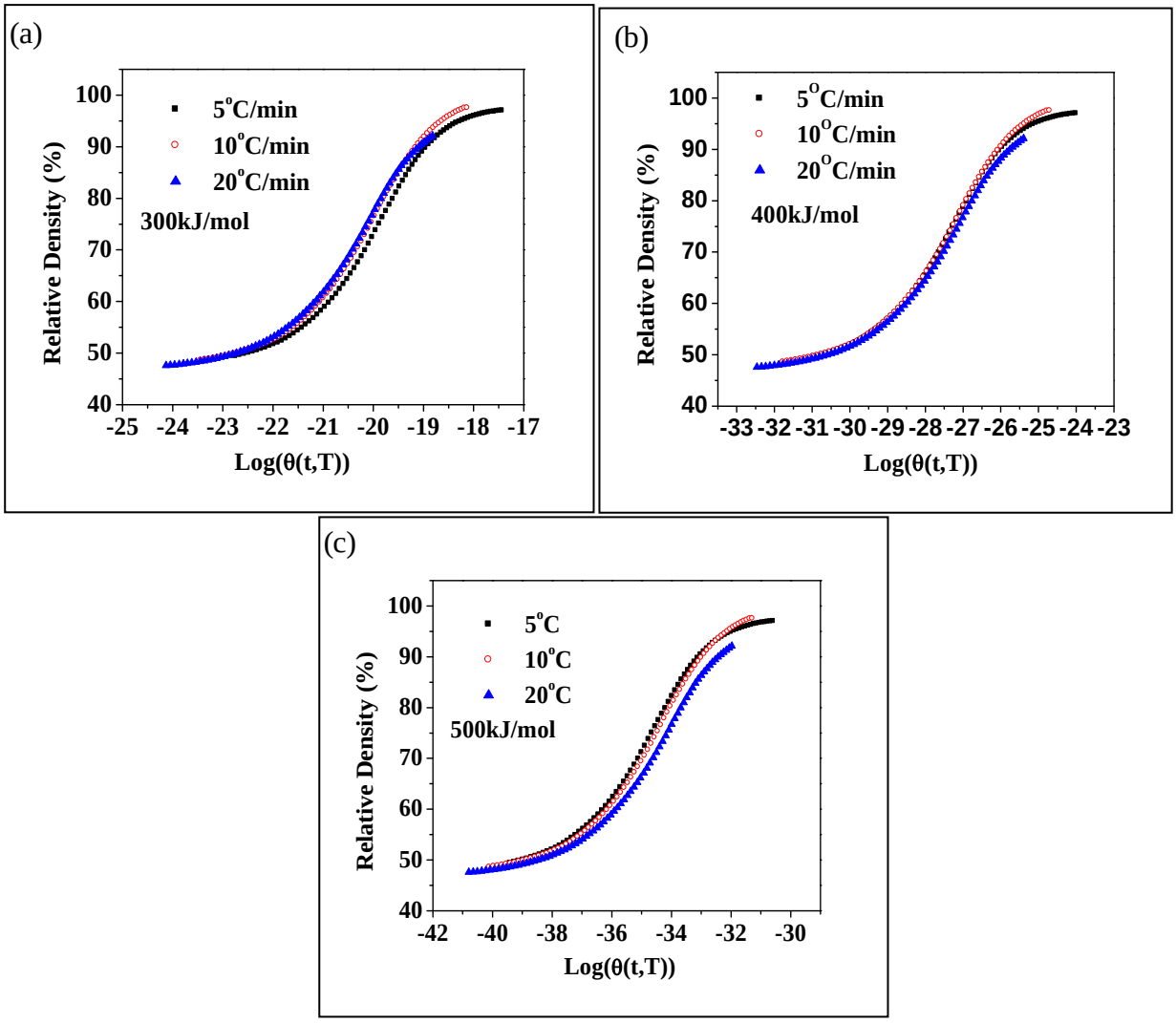

Fig.3.10Plot of MSC for different chosen activation energy values (a) 300kJ/mol, (b) 400kJ/mol and (c) 500kJ/mol

As stated above different values of activation energy (100-900 KJ/mol) is considered and MSC Log (θ(t,T))vs. ρ is plotted.

Step 4: Calculation of apparent activation energy of sintering

Another important parameter in sintering is the apparent activation energy. Since the magnitude of the apparent activation energy will give an insight into the kinematics of sintering. The determination of this parameter can be done in two ways. The first one is to use the concept of MSC itself. In this method the MSC will be plotted for different 'Q' values and when all the heating rate curves will become convergent, gives the apparent activation energy.

The second method is the mean square residue method. The span of the shrinkage region in terms of relative density is 49.38-92.13 for the three different heating rates. In this method nearly 15 to 20 equally spaced relative density values considered in the above mentioned region (54, 56,……90%). For these 20 equally spaced relative density values the corresponding Log [θ (t,T)] is computed using reverse sigmoid fitting. The equation used as follows

$$\mathrm{Log}\theta = \mathrm{Log}\theta_0 + \Delta\mathrm{Log}\theta_0 \times \mathrm{Log}\left[\frac{\rho i - \rho_{54-90\%}}{\rho_{54-90\%} - \rho f}\right] \quad (3.6)$$

Where the different parameters used in equation (3.6) such as Log θ_0, ΔLogθ_0, $\rho_i$and $\rho_f$are determined as follows. Firstly the MSC constructed in step 3 of result and discussion can be fitted by appropriate sigmoid function of the form given below

$$\rho = \rho_f + \frac{\rho_i - \rho_f}{1+\exp\left[\frac{\log\theta - \log\theta o}{\Delta\log\theta o}\right]} \quad (3.7)$$

For an particular value of activation energy (q= 200,300, ..) the Log[θ(t,T)] vs. ρ data is fitted by the sigmoid function given in equation (3.7). The parameters of the equation (3.7) are noted down. These parameters are used in equation (3.7) for getting Log [θ(t,T)] values, when fixed spacing densities (54-90%) are taken.

The residual square is calculated using the formula (3.8)

$$(\mathrm{Residual})^2 = [\log\theta(\mathrm{Rate},\rho) - (\mathrm{Average}\ \log\theta(\mathrm{allRate},\rho))]^2 \quad (3.8)$$

A total of 19 equally spaced relative density values (from 54% to 90%) are considered. The respective values of log θ(Rate, ρ) are calculated for the different heating rates. For each relative density value an average value of log θ (all Rate, ρ) for all heating rate is calculated. Then the deviation of the 57 data points (for all heating rates) from the calculated average log θ (all Rate, ρ) is taken and squared in order to get the residual square. Finally all the residual squares are added and divided by the total number of data points to get the mean residual square for one Q value. The same procedure is repeated for all estimated activation energies.

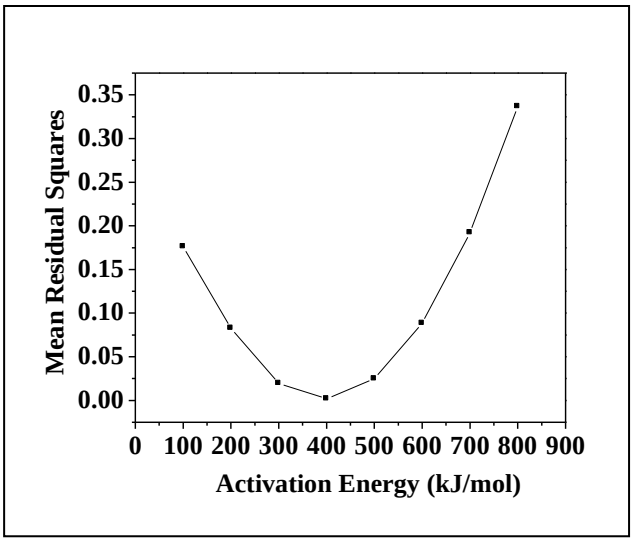

Fig.3.11 Mean residual square minimization curve for calculation of apparent activation energy

Step 4: Construction of Master Sintering Curve

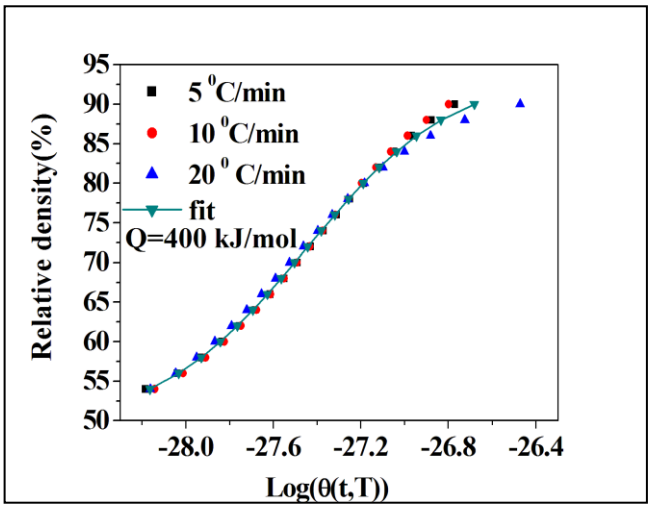

Fig.3.12 Constructed MSC for the sintered 8YSZ sample using an activation energy of Q=400 kJ/mol.

From the plot of mean Residual Square vs. activation energy of sintering, it is found out that the minimum value 0.0018 of mean Residual Square is at 400 KJ/mol. This value is the apparent activation energy of sintering. For this value of activation energy all the heating rate curves and the fitted curve converge.

---

1. **Master Sintering Curve: A unique tool for the predictions of sintering kinetics of 8Y Zirconia Ceramics. Oral presentation at Annual Technical Meeting, Indian Institute of Metals, 2011, Hyderabad.**

2. **Studies on Sintering Kinetics and Correlation with the Sinterability of 8Y Zirconia Nano Powders Based on the Dilatometric Shrinkage Curves. Poster presentation at Annual convention of Indian Ceramic Society, 2011, Agra.**

Step 5: Density evolution and densification rate as a function of temperature

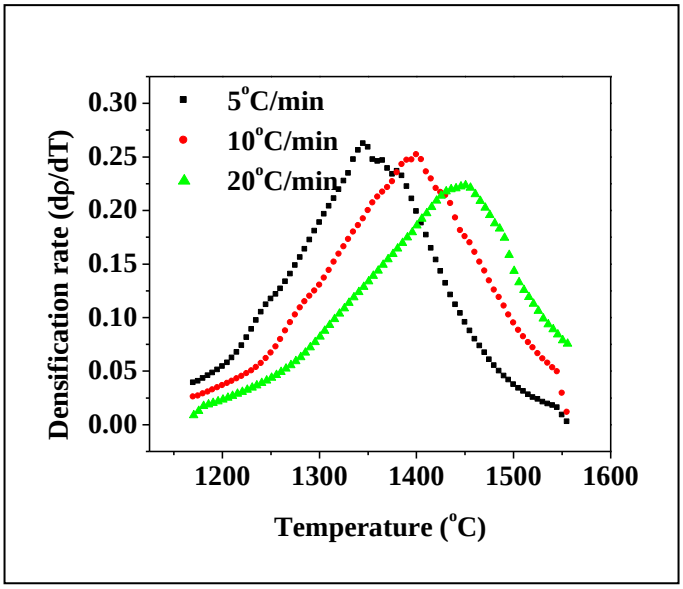

Fig.3.13 Densification rate as a function of temperature

This plot shows the maximum densification temperatures increases with heating rate and a decrease in rate of densification.

The activation energy of sintering and the kinematics of sintering were determined by the help of MSC. The analysis of dilatometer data for construction of MSC is also explained. The dilatometer temperature vs. shrinkage data for three different heating rates 5, 10 and 20 °C/ min have been analyzed for the construction of a Master sintering curve. The mean residual square method was employed for the calculation of apparent activation energy of sintering. It has a value nearly 400kJ/mol for a range 54% to 90% of relative density. This value of apparent activation energy was used to construct the MSC of the sintered sample.

3.3.1.2 Conventional Sintering in Laboratory Furnace

Based on the dilatometric plots under CRH methodology the samples were subjected to a final sintering temperatures of 1500°C, 1525°C and 1550°C with a constant heating rate of 5°C/min

and a soaking period of 2 hrs in a PID controlled laboratory furnace (Nabertherm R, Model: HT 64/17, Germany). The heating schedules followed for CRH sintering is shown in Fig.3.14.

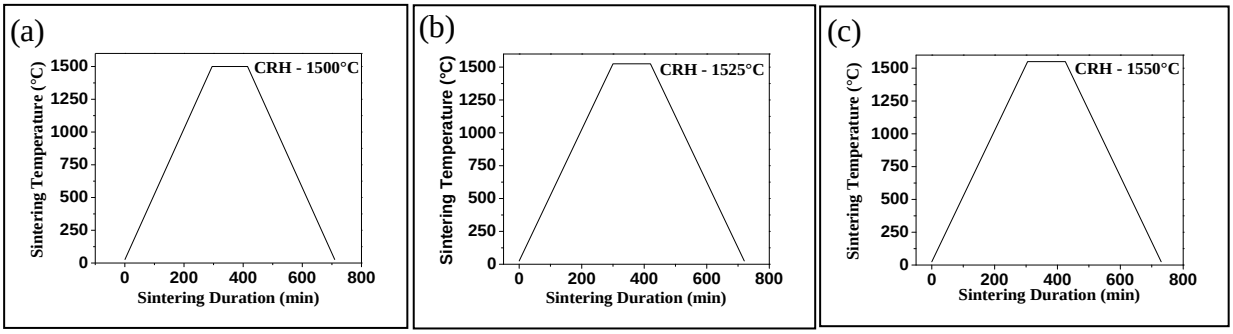

Fig.3.14 Temperature profiles employed to sinter 8YSZ pellet by CRH sintering method (a) 1500°C, (b) 1525°C, and (c)1550°C

The sintering schedules were optimized to obtain the sintered density of the samples > 99% of theoretical density.

3.3.1.3 Characterization of sintered samples

The sintered samples were characterized for density using Archimedes principle. Microstructural analyses of polished and thermally etched samples were carried out using Field Emission Scanning Electron Microscope (FESEM, HITACHI S-3400N,Tokyo, Japan). Grain size analyses of the samples were carried out by Linear Intercept method using Image Analyzer (Optical Microscope: Olympus GX 51).

3.3.1.4 Physical characterization (Density, porosity and water absorption)

Bulk density and porosity of the sintered samples were measured by adopting the ASTM C373 procedure using analytical balance with density measuring kit (LA 120S, Sartorius AG Germany). The weight of the samples were first taken in air (D) followed by boiling the same samples in distilled water for 4 hours and allowed to cool to room temperature for 24 hours. The saturated weight (W) and the suspended weight in water (S) were measured accurately. The bulk density, percentage porosity and water absorption were calculated using the equations (3.9), (3.10) & (3.11) respectively, discussed below and are shown in the Table 3.1. The effect of temperature on density and porosity is shown in Fig.3.15.

$$\text{Bulk Density} = \frac{D}{(W - S)} \quad (3.9)$$

$$\text{Apparent Porosity}(\%) = \frac{(W - D)}{(W - S)} \times 100 \quad (3.10)$$

$$\text{Water Absorption}(\%) = \frac{(W - D)}{D} \times 100 \quad (3.11)$$

Table 3.1 Sintering parameters and results of the CRH sintered 8YSZ samples

Specimen Identity	**Sintering temperature (°C)**	**Dwell Time (hr)**	**Density (g/cc)**	**%TD**	**Porosity (%)**	**Water absorption (%)**
1	1500	2	5.810			
2			5.820			
3			5.800			
4			5.810			
5			5.820			
			5.810	**98.50**	**0.20**	**0.034**
1	1525	2	5.868			
2			5.867			
3			5.868			
4			5.868			
5			5.864			
			5.867	**99.44**	**0.06**	**0.010**
1	1550	2	5.869			
2			5.870			
3			5.868			
4			5.869			
5			5.873			
			5.870	**99.49**	**0.05**	**0.008**

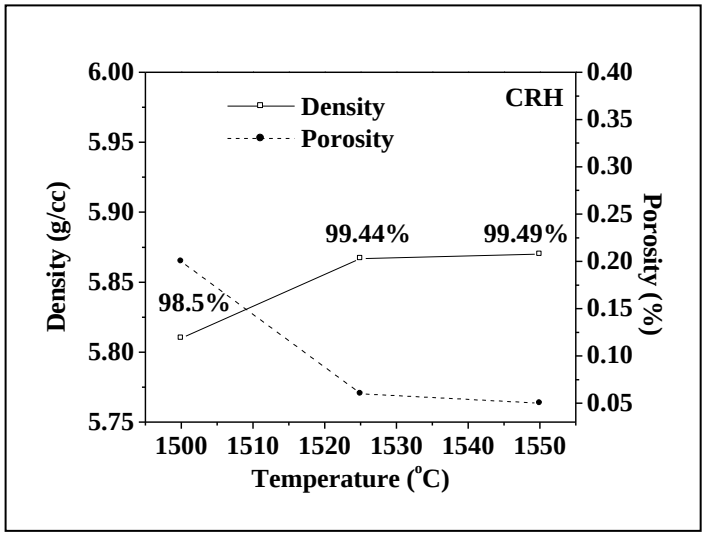

Fig.3.15 Dependence of density, porosity on sintering temperature of 8YSZ specimens sintered by CRH sintering method

3.3.1.5 Ceramographic specimen preparation for microstructural characterization

Ceramographic specimen preparation normally requires a specific sequence of operation such as sectioning, mounting, grinding, polishing and etching. Further to obtain an accurate interpretation of a microstructure the prepared specimen should be representative of the material being examined. Representative samples were cut from the parent piece of a sintered zirconia samples using a diamond cutter (Isomet Model No. 11-1280-250, Buehler, Lake IL, USA.). The cut samples were coarse ground to remove deformation produced during sectioning and to make flat surface.

Mounting and polishing

The cut samples were mounted in acrylate based resin moulds. An automatic grinding and polishing machine (Struers, Tegraforce -5, Germany) used for grinding and polishing the sample is shown in Fig.3.16. Mounted samples were placed in the sample holder and was ground using polishing disc of SiC grit size 120µm and number of revolutions were fixed at 250 per minute The ground samples were further polished using diamond suspensions of 15, 9, 6, 3, 1 µm particle size to achieve the required surface finish. The samples were cleaned and are examined under optical microscope for scratches, stains, and other imperfection.

Fig.3.16 Automatic Polishing Machine

Thermal etching

Polished samples were removed from the mount, cleaned with acetone and thermally etched at 1450°C with soaking time of 30 minutes in a laboratory furnace.

3.3.1.6 Microstructural Analysis

The polished and thermally etched 8YSZ samples were gold coated using ion sputtering device (Fig. 3.17(a)) to make the sample electrically conductive. The samples were fixed onto the carbon tape, which is pasted on the sample holder. Silver paste was applied to minimize charging effects.

Fig.3.17 (a).Ion Sputtering Device and (b) Scanning Electron Microscope

Microstructural analysis was carried out using FSEM at an accelerating voltage of 20KV at magnifications ranging from 2K - 20K. Photograph of the scanning electron microscope is presented in Fig. 3.17 (b). The micrographs at different temperatures of magnification 5K are shown in Fig. 3.18.

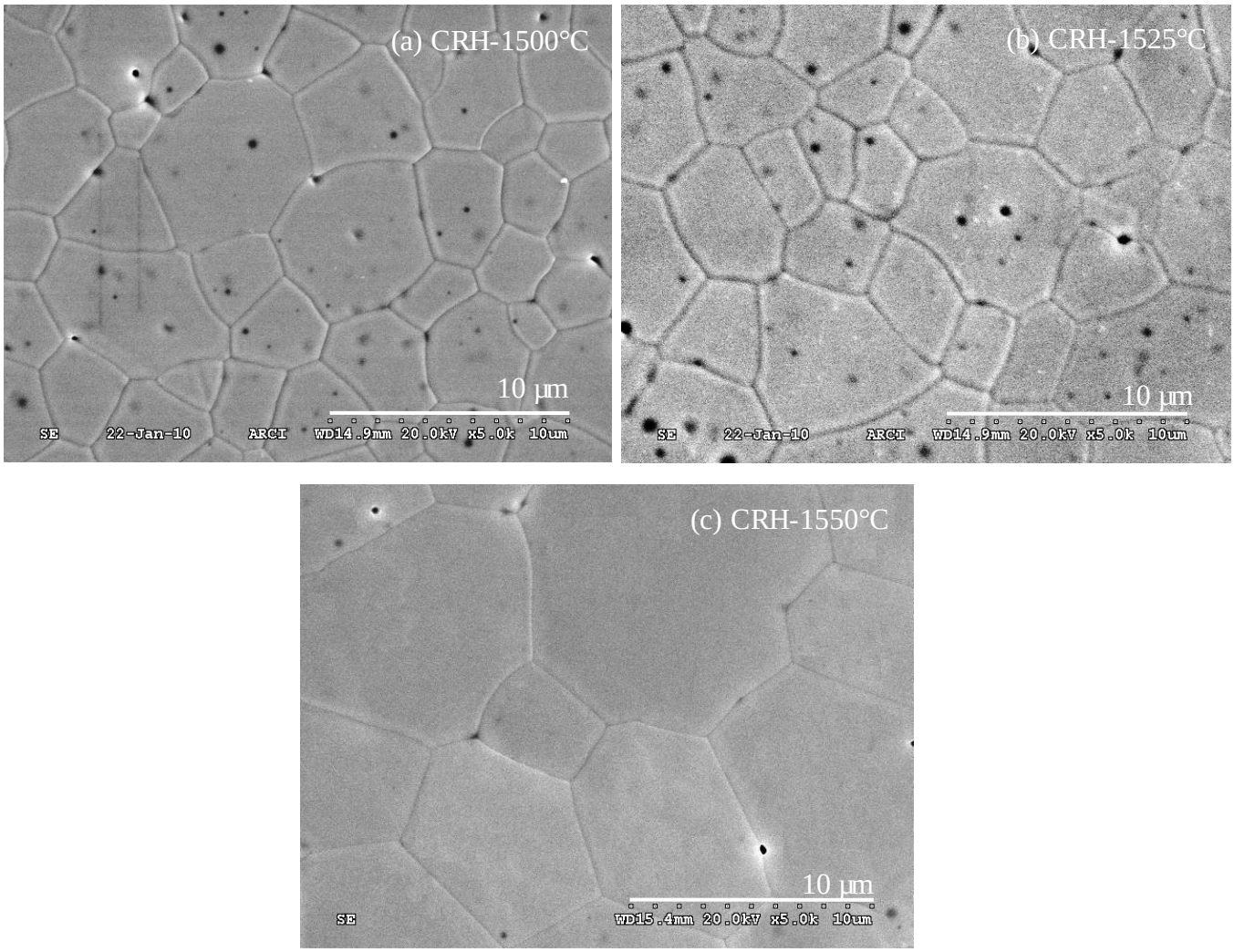

Fig.3.18 Microstructures of 8YSZ samples of CRH sintered at (a) 1500°C, (b) 1525°C, and (c) 1550°C

3.3.1.7 Grain size and distribution analysis through Image Analyzer

Grain size analysis was carried out using an Inverted Optical Microscope (Optical Microscope: Olympus GX 51) and Image analysis software (Olympus Soft Imaging Solutions, AnalySIS**,** Version 5.0) as shown in Fig.3.19 (a).

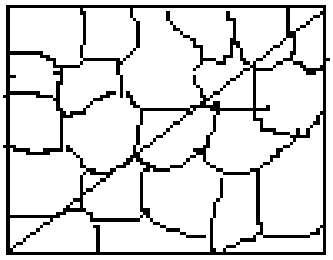

(b)

Fig.3.19 (a) Image analyzer (b) Grain size measurement by Linear Intercept method

For grain size measurement, the grains along a line are counted as shown in Fig.3.19 (b). From the SEM images the grain sizes of the sintered materials were measured by Linear Intercept method using the relation (3.14) [93]

$$\bar{G} = \frac{1.570}{N_L} \tag{3.12}$$

Here $\bar{G}$ is the mean grain size and N_L is the number of counted grains divided by the length of the test line

The constant 1.570 is a dimensionless correction factor [94] accounting for the arbitrary intercepts of the plane and of the test line with intercept to the grains. The SEM images of the actual measurement on the micrographs of 8YSZ samples sintered at 1525°C using Linear Intercept method is shown in Fig. 3.20(a).

Grain size distribution is calculated statistically by measuring the diameter of each grain Figure 3.20(b) shows the grain size analysis of the SEM micrographs of the samples sintered by CRH sintering method. For the sake of clarity we have presented only representative SEM image to demonstrate the grain size. SEM image of lower magnifications has been selected to count minimum 100 grains from each image for grain size distribution.

Dependence of density, grain size on sintering temperature is shown in Fig.3.21. Table 3.2 presents the sintering parameters, densities and sintered grain sizes of 8YSZ samples. The grain size distribution is shown in 3.22.

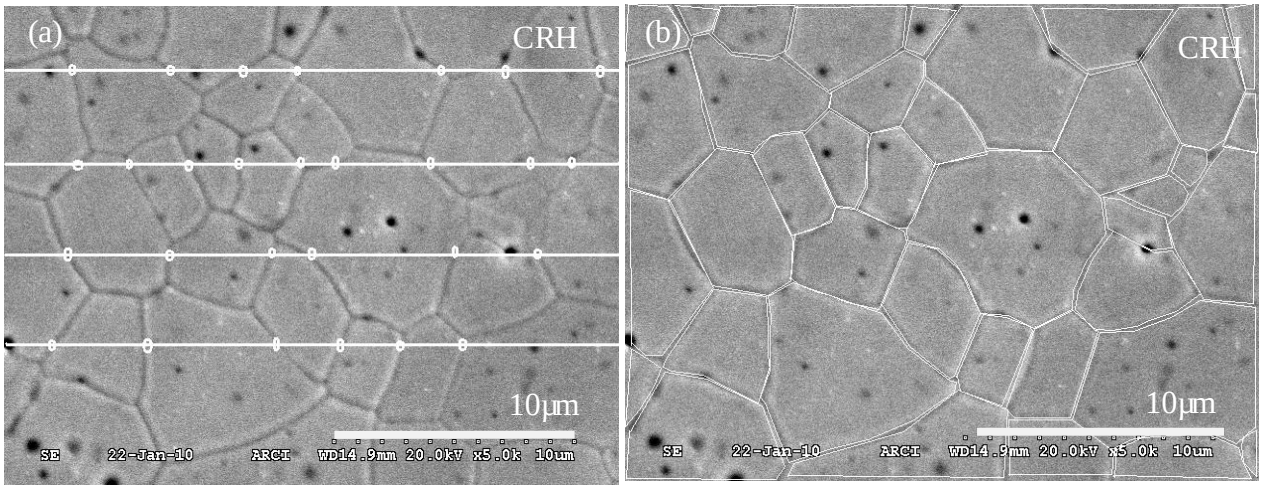

Fig.3.20 SEM images of the CRH sample (representative) sintered at 1525°C (a) Grain Size analysis by Linear Intercept Method, (b) Grain size distribution

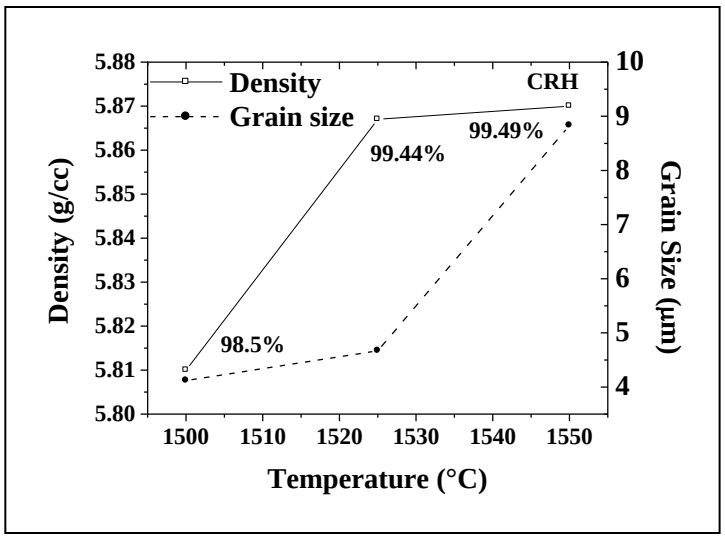

Fig.3.21Dependence of density, grain size on sintering temperature of 8YSZ specimens sintered by CRH sintering method

Though analysis were carried out with all samples as presented in Table 3.2 and grain size distribution of sintered 8YSZ specimens of CRH -1525°C, above 99%TD is selected for further studies are depicted in the form of bar graph in Fig.3.22.

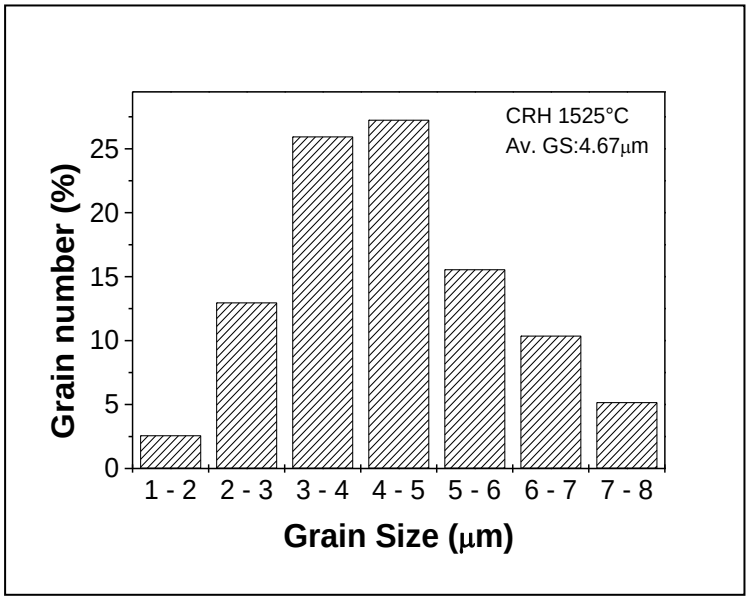

Fig.3.22 Grain size distribution of sintered 8YSZ specimens of CRH -1525°C

Table 3.2 Sintering parameters, densities and sintered grain sizes of 8YSZ samples densified using CRH methodology

Specimen Identity	Sintering temperature (°C)	Dwell Time(hr)	Average Density (g/cc)	% TD	Average grain size (μm)
1	1500	2	5.810	98.50	4.12
2	1525	2	5.867	99.44	4.67
3	1550	2	5.870	99.49	8.83

3.3.1.8Energy Dispersive Spectroscopy (EDS) Analysis of Microstructure

Analysis of the microstructureFig.3.23 (a) further indicated the black spots with varying intensities (intense and diffuse). These spots could be the residual porosity and localized interior segregations of constituents within the grains.

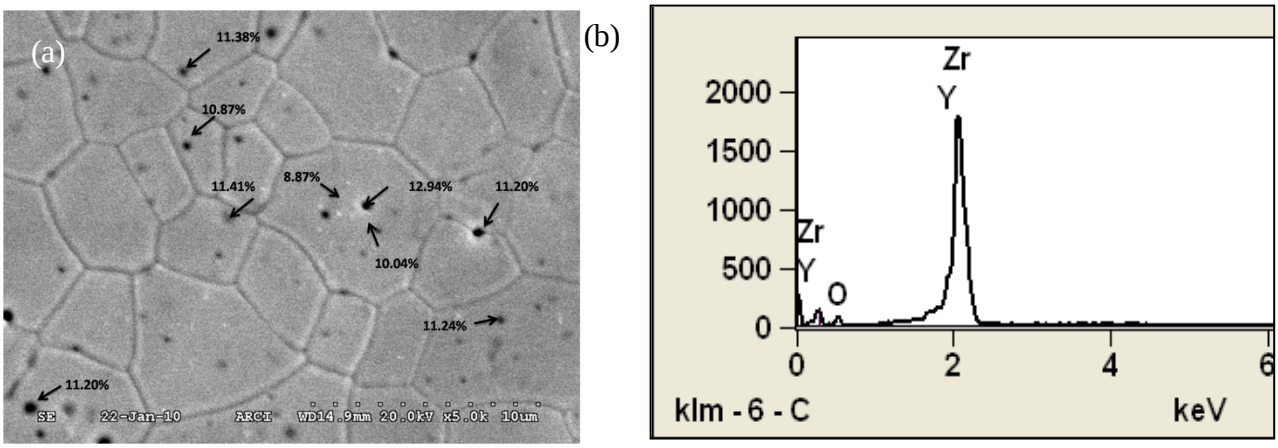

Fig.3.23 (a) Microstructure showing the distribution of yttrium (at different locations), (b) EDS Spectrum of 8YSZ samples sintered by CRH sintering method

Table: 3.23(b)EDS analysis of 8YSZ sample sintered by CRH sintering method

CRH Sample Location	**Weight (%)**			
	O-K	**Y-L**	**Zr-L**	**Y_2O_3**
1	17.46	8.87	73.67	11.26
2	13.04	10.04	76.92	12.75
3	14.14	12.94	72.92	16.43
4	17.23	11.38	71.39	14.45
5	14.19	11.24	74.58	14.27
6	15.83	10.87	73.30	13.80
7	14.48	11.41	74.11	14.49
8	14.19	11.20	74.61	14.22

In order to distinguish between the intense and diffused spots, the samples are subjected to EDS. Fig.3.23 (b) shows the elemental spectrum and Table 3.3 shows the elemental concentration revealed by EDS analysis. It is evident that there is a significant variation in concentrations of yttria ranging from 14.30 to 10.17wt%. This variation in yttria concentration can be attributed to

high temperatures of sintering that is >1500°C which is essential for achieving a density of >99%TD. This observed segregation in the present study may not be desirable in the context of ionic conductivity. This is because of the fact that this segregation not only impedes the ion transport but also reduces the defect concentration/ pile up. This will be investigated and reported based on the ionic conductivity measurement planned in the present study.

3.3.2 Rate Controlled Sintering (RCS)

A ramp and hold sintering curve recorded for 8Y zirconia pellet (diameter:10mm;length: 4.72mm)at a heating rate of 10°C/ min to the peak temperature of 1550°C (RCS will be effective till 1525°C only) for a soaking period of 2h are shown in Fig. 3.24(a). Sintering curve indicated a total shrinkage of ~21% corresponding to a shrinkage rate of 22.72µm/min. For RCS protocol the temperature regimes corresponding to 75 % of TD, 85 % of TD and 100 % of TD were calculated from shrinkage curve using equation (3.3) and depicted in the Fig. 3.24(b) and Table 3.4.

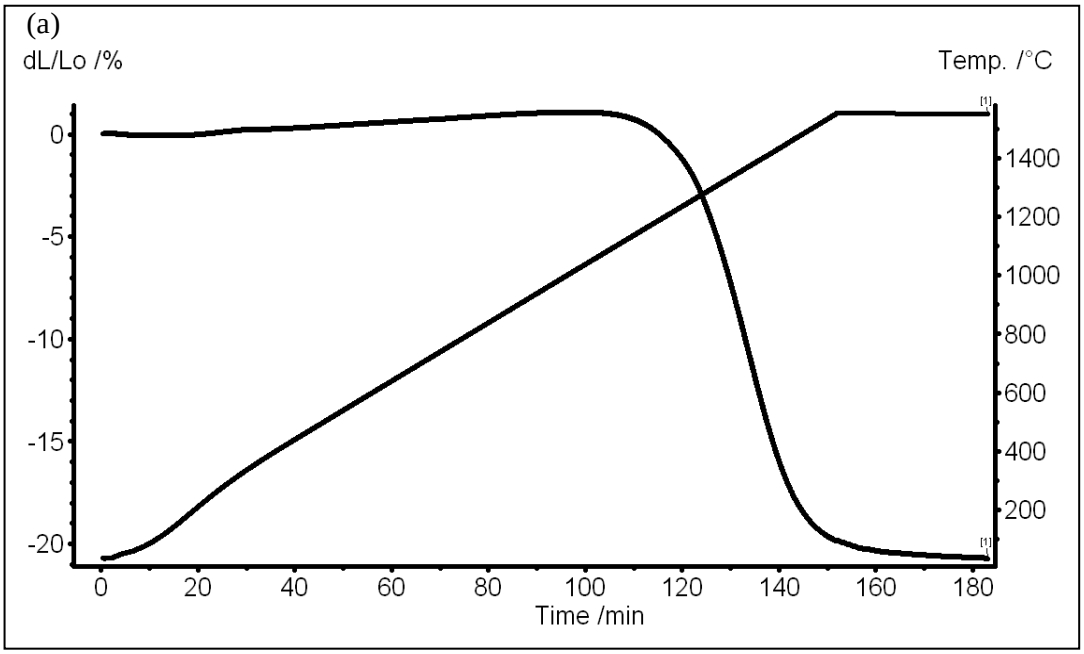

Fig.3.24 (a) Linear shrinkage of the 8YSZ slip cast specimens during sintering at heating rate of 10 °C /min

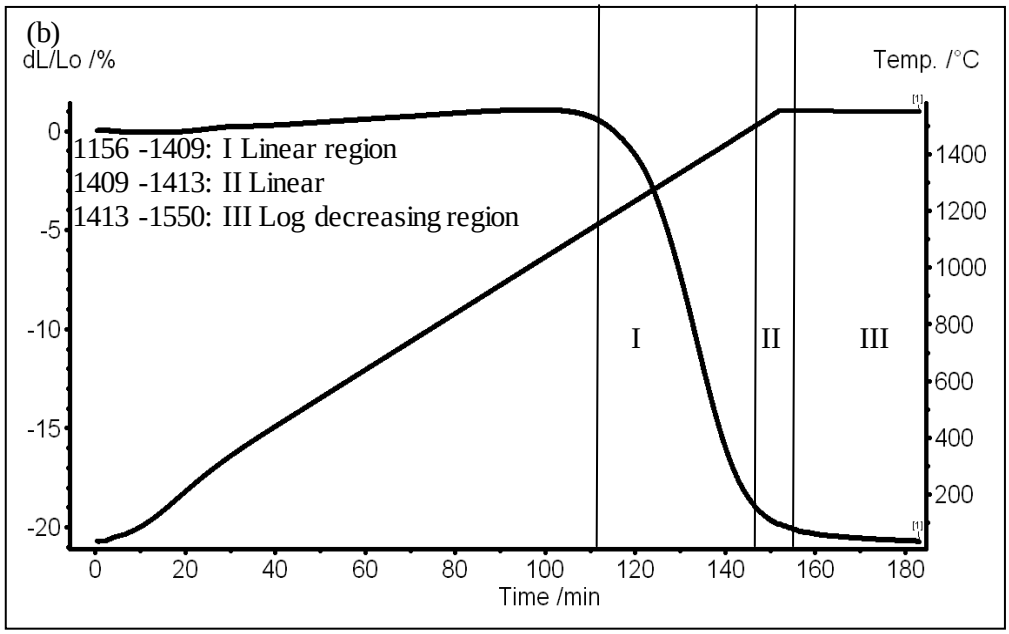

Fig.3.24 (b) Temperature regimes of RCS protocol

$$\rho = \frac{\rho_0}{\left(1 - \frac{dl}{l_0}\right)^3} \times 100 \qquad (3.3)$$

Table 3.4 Temperature Regimes for RCS Schedule

Specimen Identity	**%TD**	**Temperature for % TD(°C)**	**Temperature regimes for RCS (°C)**
8Y zirconia compact	75	1409	1156-1409
	85	1413	1409-1413
	100	1550	1413-1550

The temperature regimes and shrinkage rate of RCS schedules are calculated from the linear shrinkage curve (Fig. 3.24(a)). Though a few shrinkage rates were employed based on arbitrary selection, could not achieved the densities greater than 99%TD in any of these runs. The shrinkage rates which have yielded the maximum density ~97%TD is shown in the Table 3.5. It is evident that first linear region wherein, the fastest shrinkage rate of 20 µm/ min is applied to the temperature regime of 1156 – 1409°C (1156°C being the onset of shrinkage). At this stage the sample attains a density of ~75% TD. The second regime, a slower linear rate dependence of temperature on densification, a shrinkage rate of 15 µm/ min is applied to the temperature regime

of 1409-1413°C. At this stage the sample attains a density of ~85% TD. The last regime, a log decreasing dependence on densification rate, a shrinkage rate 5 µm/ min is applied to the temperature regime of 1413-1550°C.

Table 3.5 Temperature Regimes and shrinkage rate for RCS Schedule

Specimen Identity	**Sintering temperature Range**	**Shrinkage rate proposed**	**Actual Shrinkage rate**
RCS	RT to 1156°C	10 °C /min	
	1156 - 1409°C	20 µm/min	22.0 µm/min
	1409 - 1413°C	15 µm/min	15.2 µm/min
	1413 - 1550°C	5 µm/min	4.46 µm/min

RCS profile recorded with shrinkage rates applied in the three temperature regimes is shown in Fig.3.28 and a comparison with dilatometer CRH sintering curve is shown in Fig.3.25.

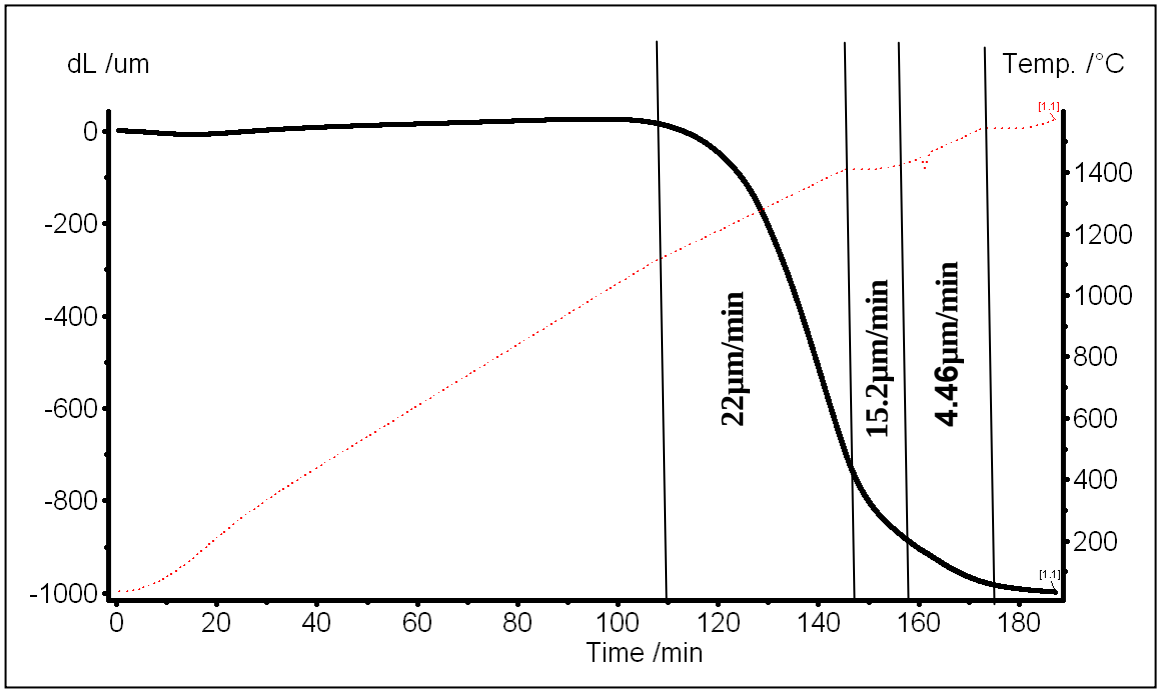

Fig.3.25 RCS sintering curve of8YSZ sample

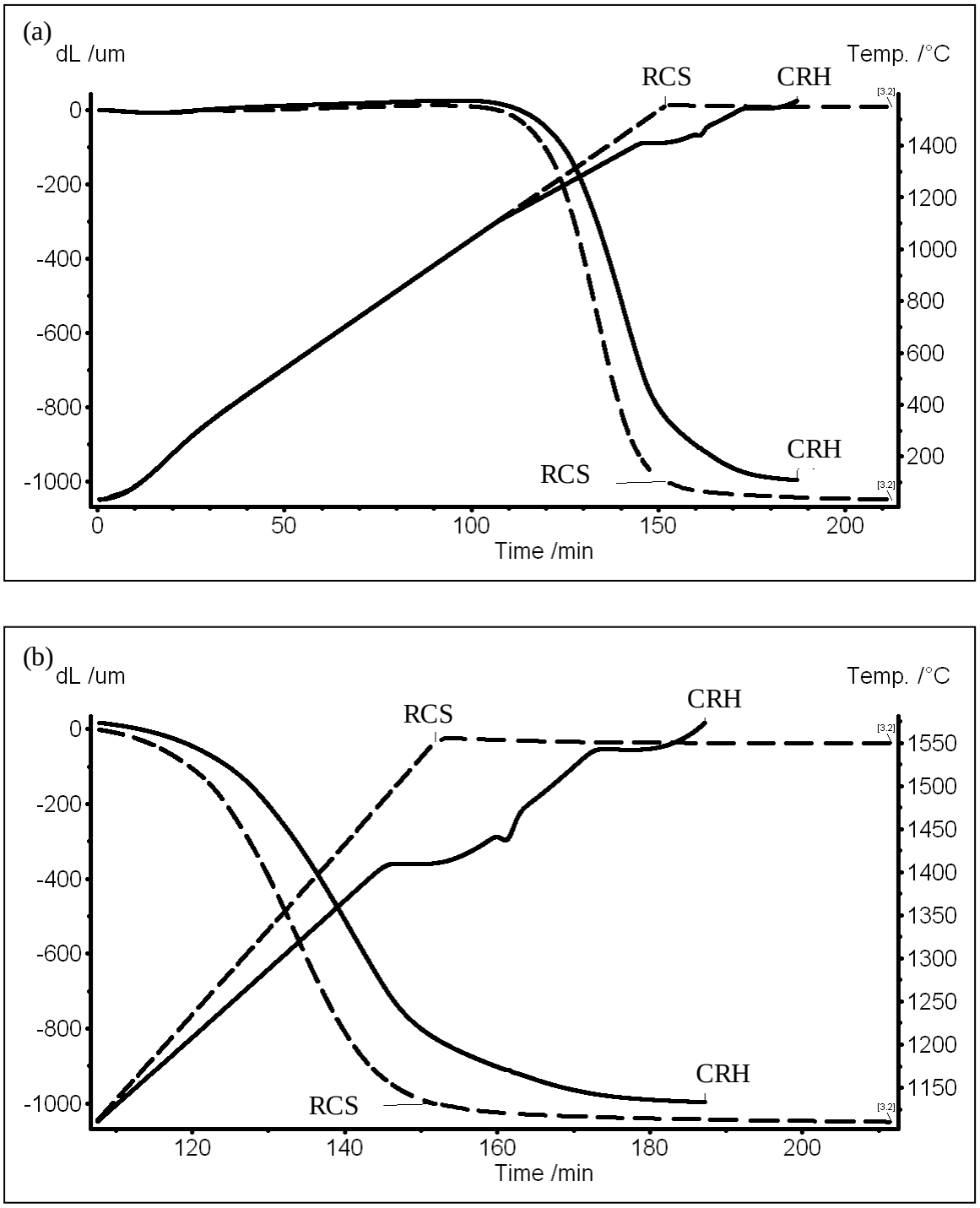

Fig.3.26 RCS sintering curve of 8YSZ sample: a comparison with CRH (Solid line CRH, Dashed line RCS) (a) complete range (b) from shrinkage region

3.3.2.1 Physical Characterization (Density, porosity and water absorption)

Bulk density, porosity and water absorption of the RCS sintered samples were measured using ASTM C373 as mentioned in Section 3.3.1.4 and the results were presented in Table 3.6.

Table 3.6 Sintering parameters and results of the Rate Controlled sintered 8YSZ samples

Specimen Identity	Density (g/cc)	%TD	Porosity (%)	Water absorption (%)
RCS	5.720	96.95	**1.50**	**0.26**

3.3.2.2 Micro structural Analysis

The specimens were polished, etched and gold sputtered as per the method already mentioned in Section 3.3.1.5& 3.3.1.6. Microstructural analysis of ceramographically prepared samples were carried out using SEM (Hitachi 3200S, FESEM, Japan) and the micrograph is shown in Fig.3.27.

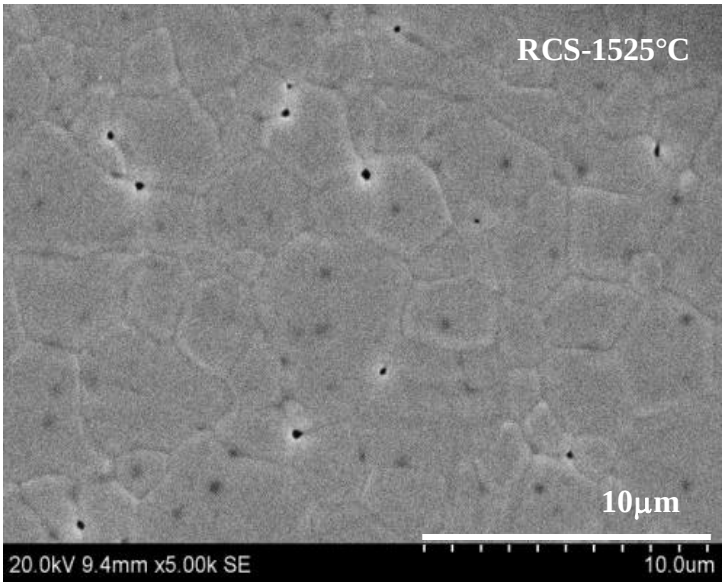

Fig.3.27 Microstructure of 8YSZ sample sintered by RCS method

3. 3.2.3 Grain size and distribution analysis through Image Analyzer

The Grain size analysis of the samples was carried out by the linear intercept method as mentioned earlier in the Section 3.3.1.7. Fig.3.28(a) & (b) shows the grain size and distribution of Rate Controlled sintered 8YSZ specimen at 1525°C which is depicted in the form of bar graph Fig.3.29.

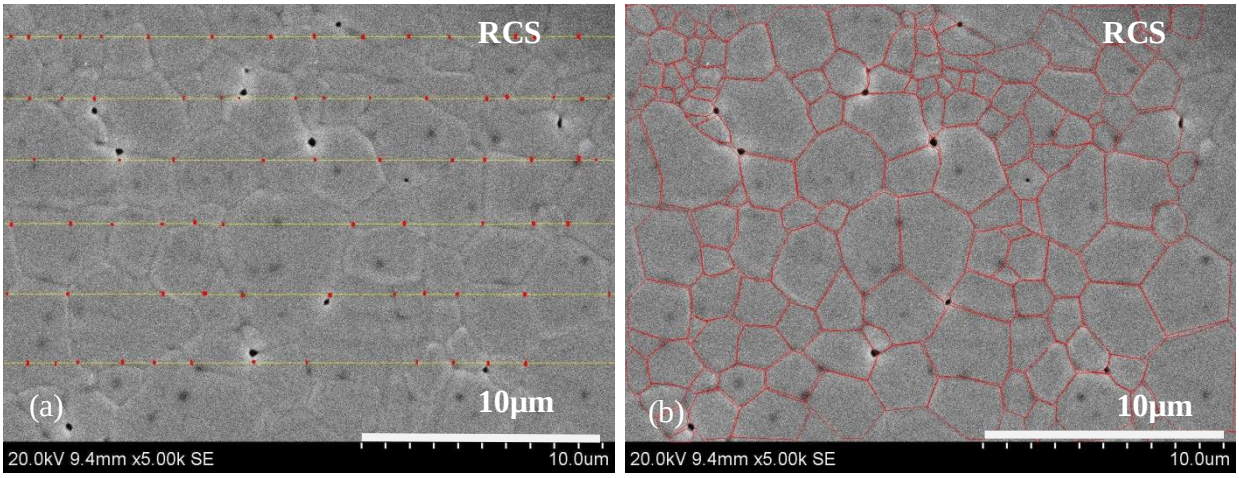

Fig.3.28 SEM image of the RCS sample (a) Grain size analysis by Linear Intercept Method (b) Grain size distribution

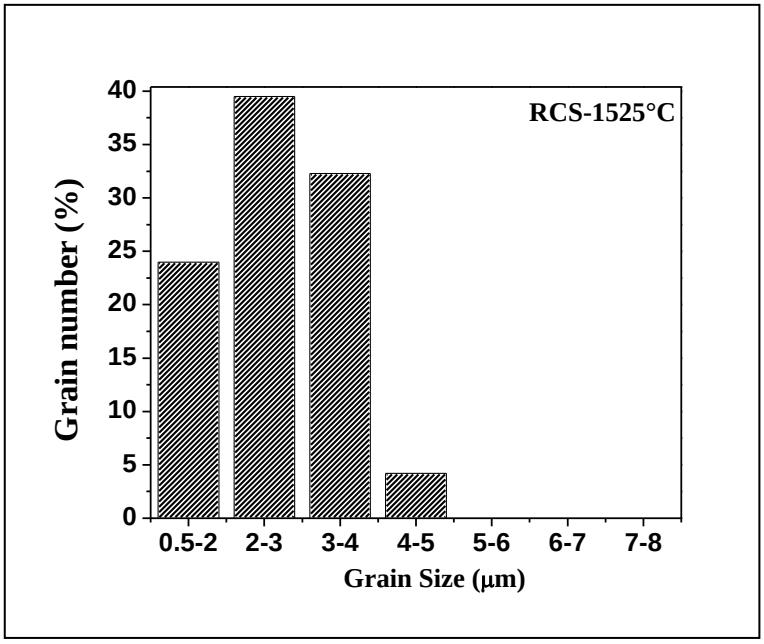

Fig.3.29 Grain size distribution of sintered 8YSZ specimens of RCS -1525°C

3. 3.2.4 Proposed mechanism for microstructure evolution in RCS process

In order to elucidate the mechanism for this grain growth control the evolution of microstructure during the RCS protocol was followed by microscopy. The samples were characterized for its density and microstructural features. The calculated and observed values of density are presented in Table 3.7. Density values measured were almost in agreement with the values calculated from the dilatometric data. For the sake of comparison the microstructures of conventional and RCS

samples were shown in Fig. 3.30(a) and (b) respectively. As is already discussed in last section 3.3.1.5.5, the CRH samples have shown non-uniform grains with grains as large as 4.67microns whereas RCS derived samples shown very uniform grains with average grain size of 3.45µm as calculated by the linear intercept method. However it may be also noted that the maximum density that could achieved through RCS is 97%.

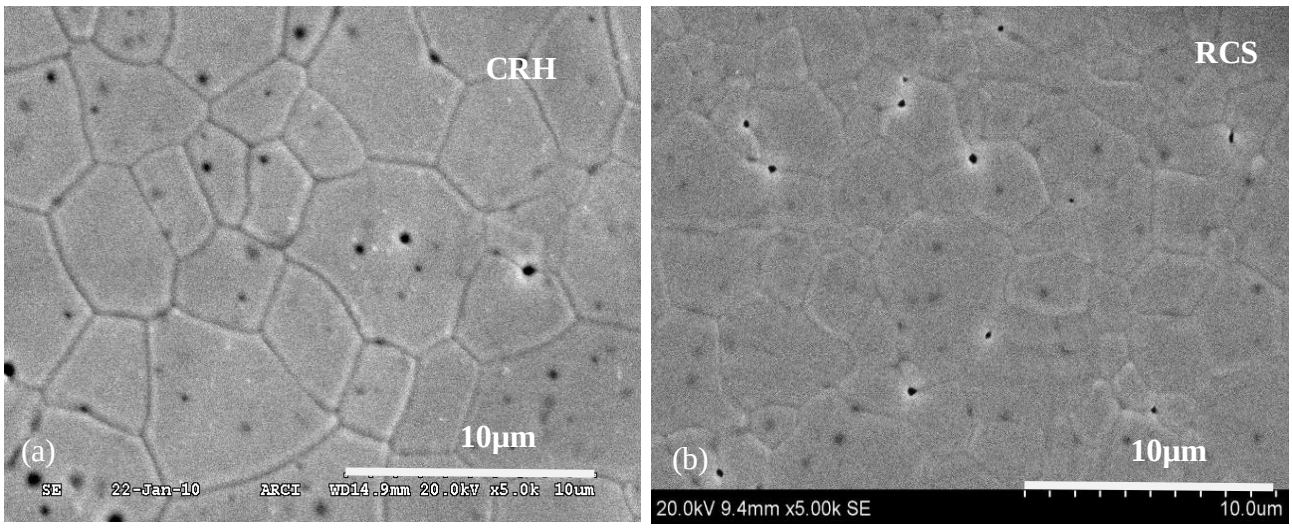

Fig.3.30 Comparison of microstructure of 8YSZ samples sintered (a) under CRH (1525°C/2h) (b) Under RCS protocol

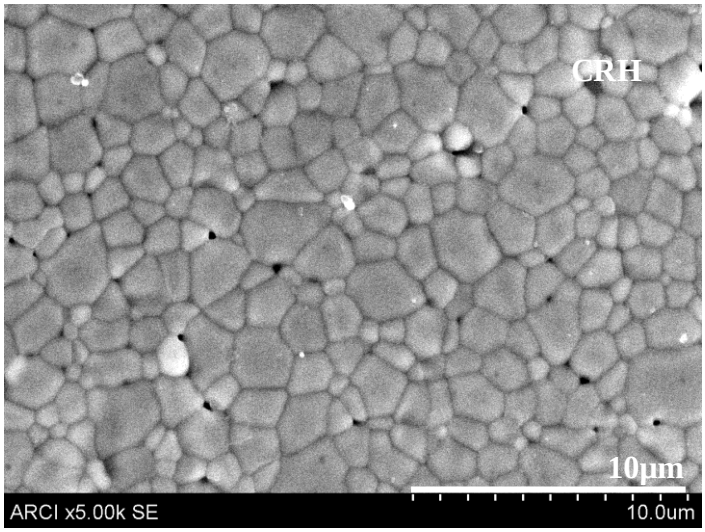

Fig.3.31 Microstructure of 8YSZ sample sintered under CRH at 1415°C

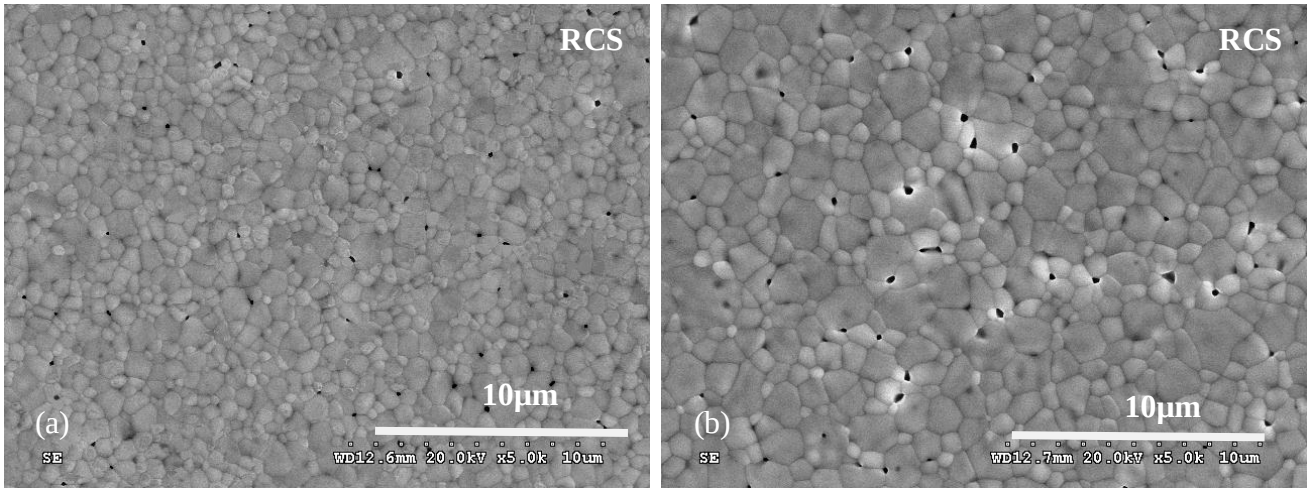

Fig.3.32 Microstructure evolution in 8YSZ samples sintered under RCS protocol and heat treated at a) 1409°C b) 1413°C

In order to evolve a mechanism for the finer grain sizes observed with RCS the samples were withdrawn at various temperature and density regimes of sintering as per RCS protocol. Further a sample corresponding to 88-90% TD were also subjected to microstructural analysis as shown in Fig.3.31 along with RCS microstructures Fig.3.32(a) & (b). At 1409°C, where the sample reaches a density of only 75% TD, the microstructure shows a highly porous structure with very little growth of the particles (Fig.3.32 (a)). The sample at 1413°C indicates growth in grain sizes, suggesting adequate interparticle contact for diffusion (Fig.3.32 (b)). At 1525°C the sample shows a density of ~ 97%TD and grain size of the order of 3.45 µm.

Table 3.7 Density evolution of 8YSZ samples during RCS process.

Specimen Identity	Density (g/cc)	Temperature Regime RCS	Shrinkage Rate	Calculated %TD	Measured %TD
		Up to 1156°C	10°C/min		
1	4.720	1156-1409°C	20 µm/min	75	80
2	5.192	1409-1413°C	15 µm/min	85	88
3	5.720	1413-1525°C	5 µm/min	100	96.95

The observed reduction in grain size in RCS can be attributed to the following proposed mechanisms. It has been postulated that in RCS all the mass transfer mechanisms competing in the sintering process are in balance and their particular rates follow the minimum free energy

dissipation principle. The driving forces for these mechanisms change non-linearly and RCS establishes a variable and non-linear dependence of densification with temperature. In the case of conventional sintering when the density is around 88-90% of theoretical density the topology of the pores changes from open cylinder to close spherical shapes. As a result the concentration of pores is reduced leading to enhanced grain growth. The pore growth is controlled to a minimum in RCS compared to conventional ramp and hold method. At the same porosity level the number of cylindrical shaped pores before their splitting and the number of isolated spherical shaped pores are much higher in the case of RCS than those for the case of CRH sintering.

3.3.3 Two Stage Sintering (TSS)

Under TSS the samples were first heat treated at the peak temperature with a fast heating rate and was followed by a second step of dwell at lower temperature. In the present study the peak temperature was selected at 1525°C based on the dilatometric studies (Fig.3.7) and further held at the lower temperature of 1300°C, 1350°C and 1375°C for 4hrs. The three heating schedules followed are shown in Fig.3.33. The experiments were carried out in a laboratory furnace.

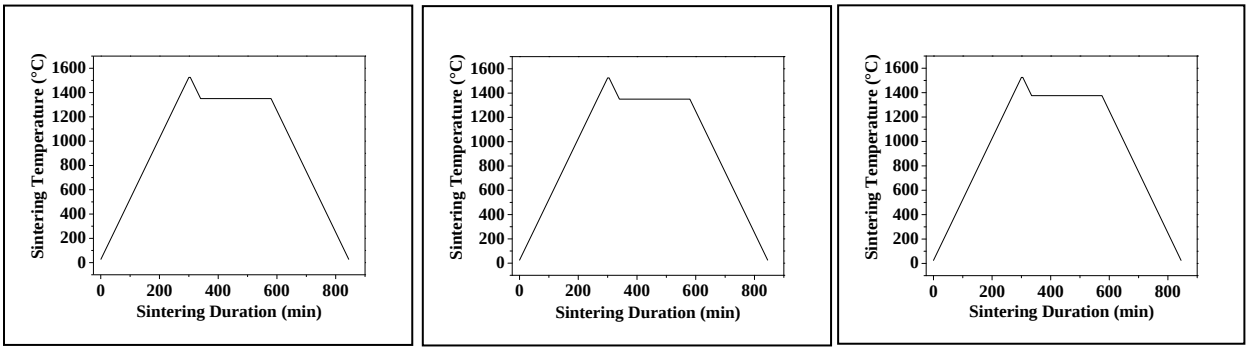

Fig.3.33 Temperature profile employed to sinter 8YSZ pellet by TSS

3.3.3.1 Physical Characterization (Density, porosity and water absorption)

Bulk density, porosity and water absorption of the TSS sintered samples were measured using ASTM C373 as mentioned in Section 3.3.1.4 and the results are presented in Table 3.8.The effect of TSS schedule on density is shown in Fig.3.34.

Table 3.8 Sintering parameters and results of the Two Stage sintered 8YSZ samples.

Specimen Identity	Sintering temperature(°C)	Dwell Time	Density (g/cc)	%TD	Porosity (%)	Water Absorption(%)
1(a)	T_1:1525	5minutes	5.830			
1(b)	T_2:1300	4 hr	5.850			
1(c)			5.810			
1(d)			5.800			
1(e)			5.860			
			5.830	**98.81**	**0.15**	**0.025**
2(a)	T_1:1525	5minutes	5.865			
2(b)	T_2:1350	4 hr	5.864			
2(c)			5.867			
2(d)			5.865			
2(e)			5.866			
			5.865	**99.40**	**0.08**	**0.015**
3(a)	T_1:1525	5minutes	5.870			
3(b)	T_2:1375	4 hr	5.871			
3(c)			5.872			
3(d)			5.869			
3(e)			5.870			
			5.870	**99.50**	**0.06**	**0.010**

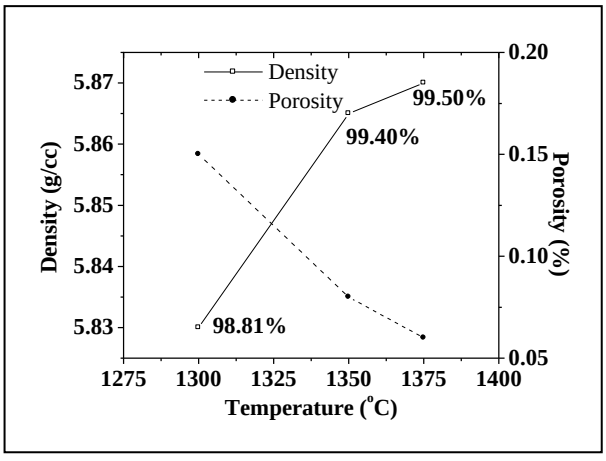

Fig.3.34 Dependence of density on sintering temperatureT_2 of 8YSZ specimens sintered by TSS method

3.3.3.2 Micro structural analysis (SEM)

The specimens were polished, etched and gold sputtered as discussed in Section 3.3.1.5& 3.3.1.6. Microstructural analysis of ceramographically prepared samples were carried out using SEM (Hitachi 3200S, FESEM, Japan). The micrographs are shown in Fig.3.35

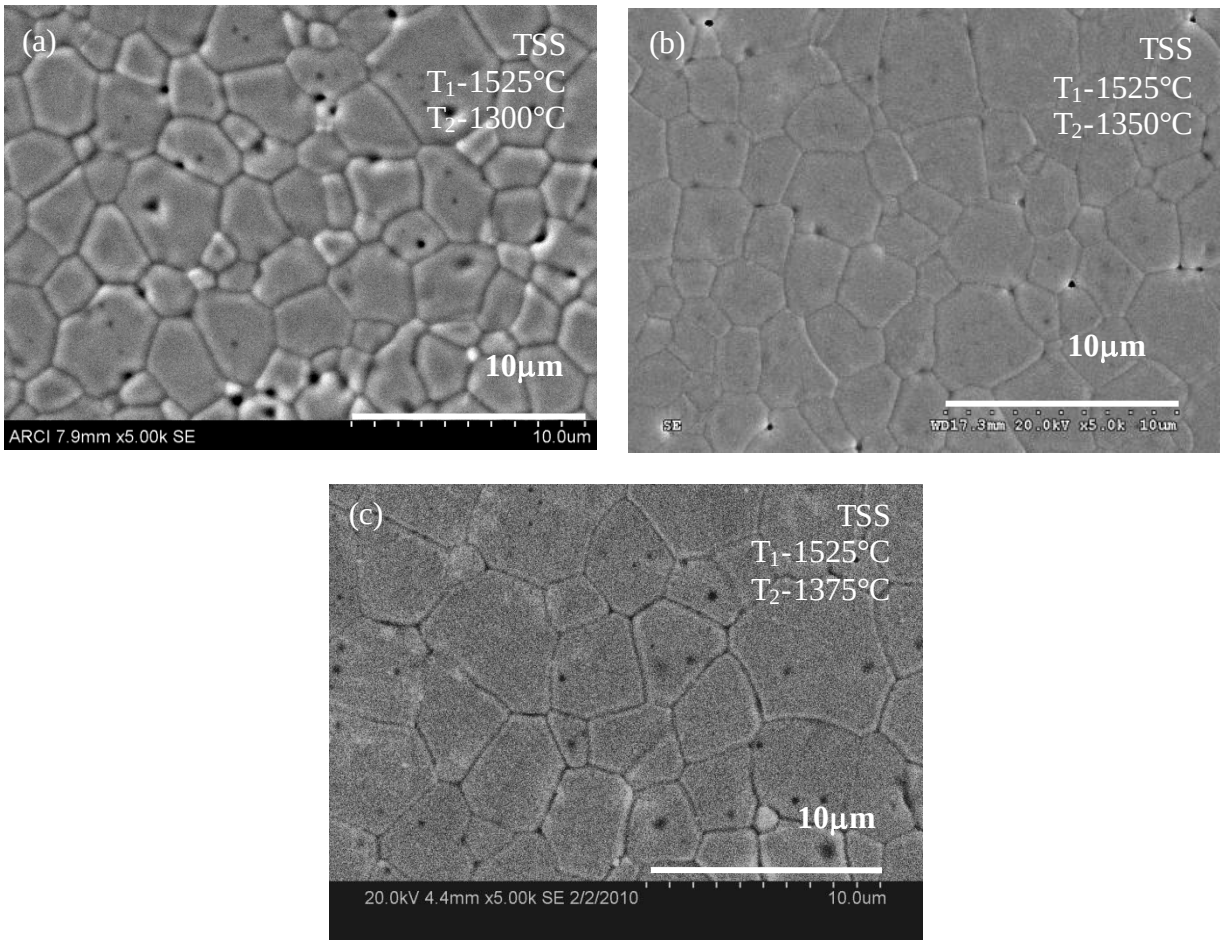

Fig. 3.35 Microstructures of 8YSZ samples of TSS sintered at 1525°C and (a) 1300, (b) 1350 and (c) 1375°C

3.3.3.3 Grain size and distribution analysis through Image Analyzer

The Grain size analyses of the samples were carried out by linear intercept method as mentioned earlier in the Section 3.3.1.7. Fig. 3.36(a) & (b) shows the grain size and distribution of 8YSZ specimen at 1525°C sintered by TSS method. Dependence of density, grain size on sintering temperature T_2 is shown in Fig.3.37. Table 3.9 presents the results of the average grain size of samples sintered at different T2 temperatures. The grain size distribution is depicted in the form of bar graph Fig.3.38.

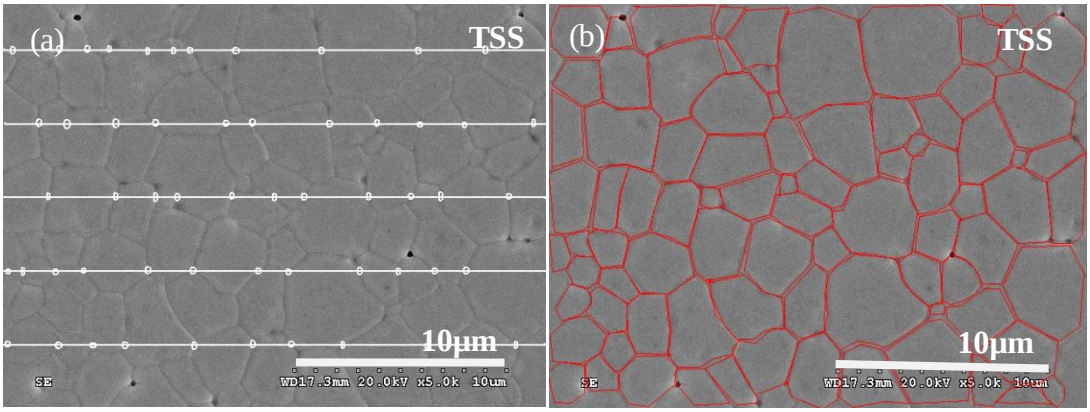

Fig.3.36 SEM image of the TSS sample (a) Grain Size analysis by Linear Intercept Method, (b) Grain size distribution

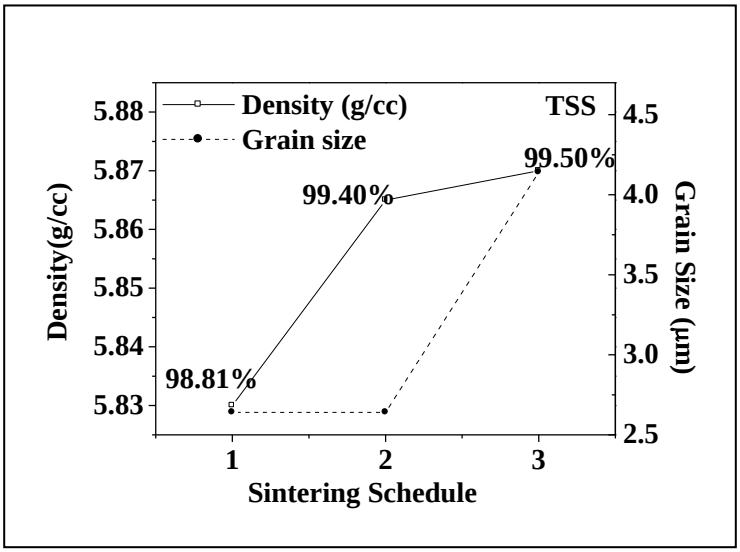

Fig.3.37Dependence of density, grain size on sintering temperature T_2 of 8YSZ specimens sintered by TSS method

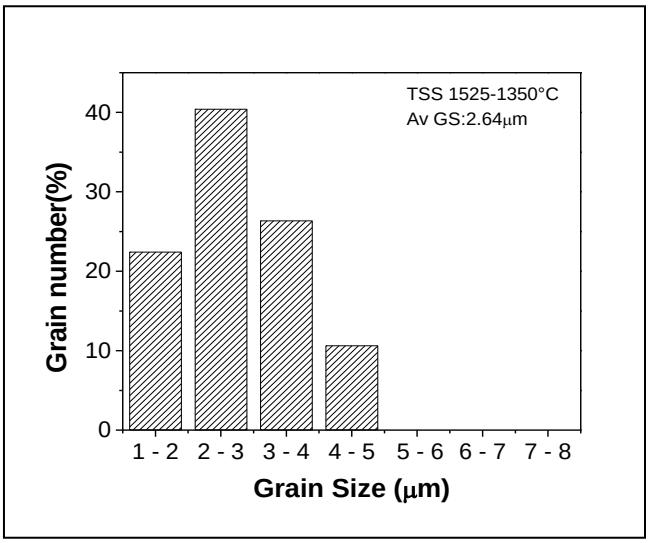

Fig.3.38 Grain size distribution of TSS 8YSZ specimens sintered at 1525-1350°C

Table 3.9 Sintering parameters, densities and sintered grain sizes of 8YSZ samples densified using TSS methodology.

Specimen Identity	Sintering temperature (°C)	Dwell Time	Density (g/cc)	%TD	Average grain size (μm)
1	T_1:1525 T_2:1300	5minutes 4 hr	5.830	98.81	2.64
2	T_2:1350	4 hr	5.865	99.40	2.64
3	T_2:1375	4 hr	5.870	99.50	4.14

3.3.3.4 Proposed mechanism for microstructure evolution in TSS process

TSS method modifies the sintering regimes by firing to final temperature followed by rapid cooling to low temperature and soaking of the samples at that temperature for longer duration. In order to elucidate the mechanism for this grain growth control, the evolution of microstructure during the TSS, the samples were sintered using dilatometer upto 1525°C. The temperatures of the first sintering step were chosen on the basis of the evaluation of dilatometric measurements. During first stage 1525°C (T_1), the fine pores disappear, leading to coarsening and becomes unstable. The temperature of the second regime of TSS sintering step (T_2) at 1350°C/4h, the coarsened and unstable pores can be eliminated as long as grain boundary diffusion allows, even if the particle network is frozen. It is evident that the low dilatometric shrinkage in the step II indicates the fact that in second stage of sintering only elimination of residual porosities is

effected and further the growth of grains is limited at the lower temperature of the second sintering step. Thus TSS yields a body of high density but with smaller grains than conventional sintering.

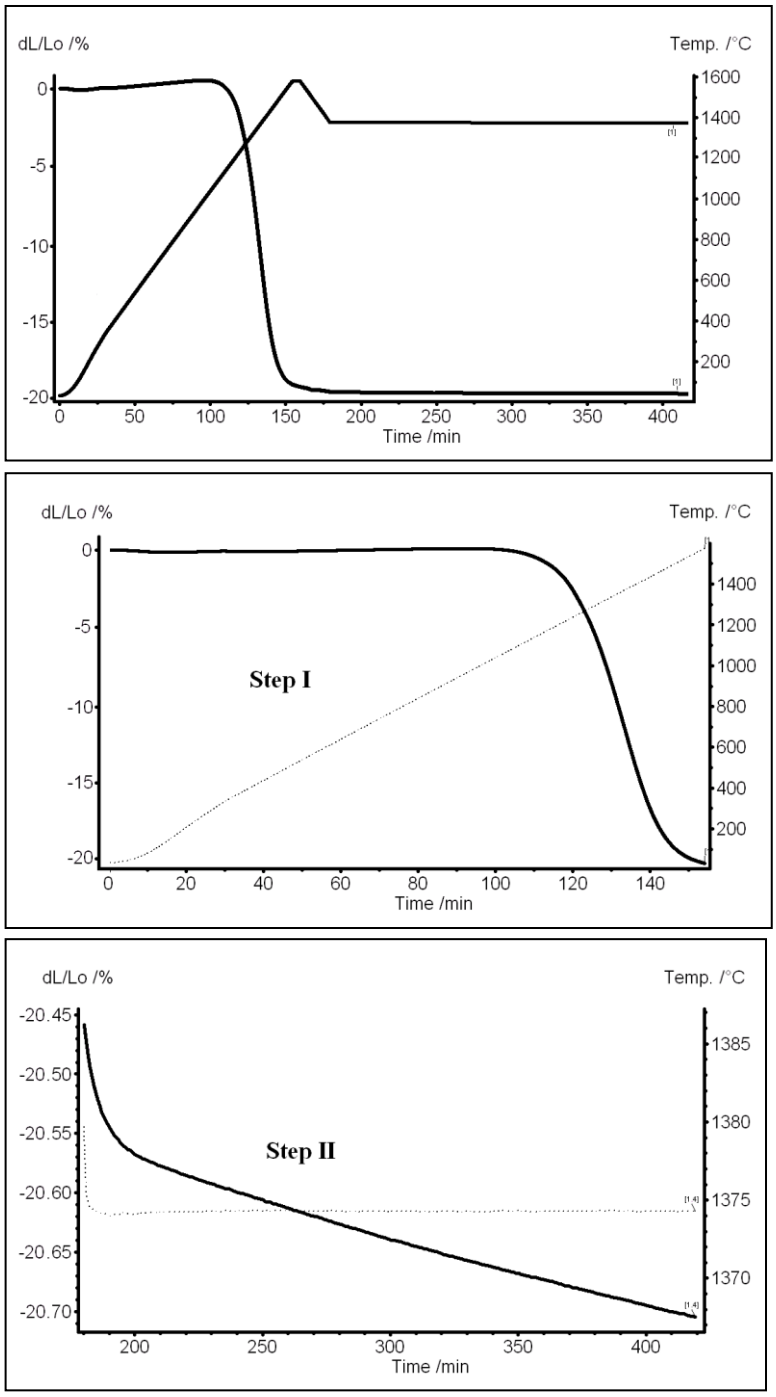

Fig.3.39 Linear shrinkage of the 8YSZ slip cast specimens as per TSS heating schedule

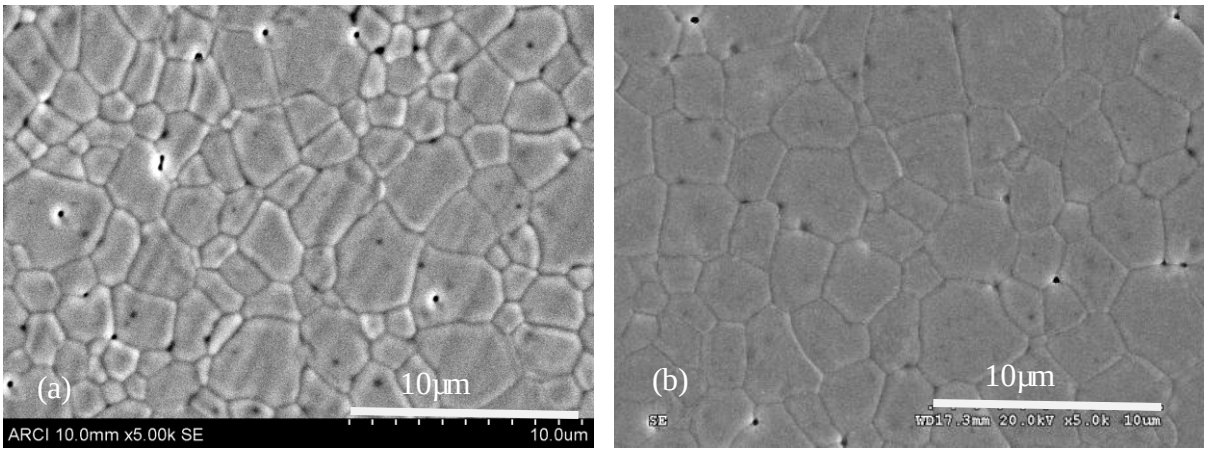

Fig.3.40 Microstructure evolution in 8YSZ samples sintered under TSS protocol at a) 1525°C b) 1350°C

The linear shrinkage of the 8YSZ slip cast specimens as per TSS heating schedule is shown in Fig.3.39.The maximum shrinkage is effected in first step with minimal shrinkage in step II. To confirm the proposed mechanism, samples subjected to TSS sintering at step I and step II were withdrawn and characterized for its density and microstructure evaluation are presented in Fig.3.40. The results are shown in Table 3. 10.

Table 3.10 Density, average grain size details of 8YSZ at each stage of TSS.

Specimen Identity	Sintering temperature (°C)	Dwell Time	Density (g/cc)	% TD	Average grain size (µm)
1	T1:1525	5minutes	5.664	96.00	2.50
2	T2:1350	4 hr	5.865	99.40	2.64

3.3.4 Microwave Sintering (MWS)

Microwave sintering was carried out using an industrial micro oven with 2.45 GHz frequency, (Model: MHTD 1800-6, Linn High Therm GmbH, Germany) at a heating rate of 10°C/min to peak temperatures of 1475°C, 1525°C and 1550°C with dwell time of 15 minutes were employed in the present study. SiC tubes were used as susceptors, since it is known that zirconia does not effectively couple (absorb) with microwaves at room temperature because of its poor dielectric properties. The sintering furnace and the heating schedules followed for MW sintering are shown in Figure 3.41 and 3.42 respectively.

Fig.3. 41 Microwave sintering furnace ((Linn High Therm GmbH, Germany)

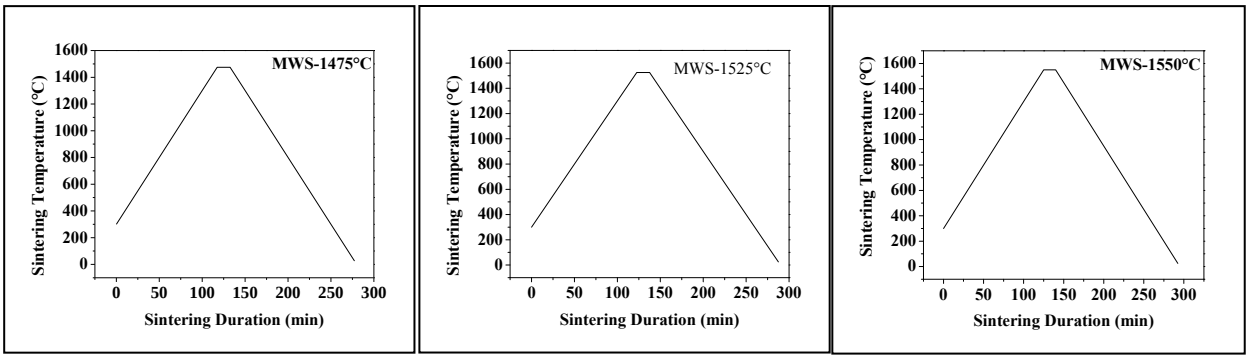

Fig.3.42. Temperature profile employed to sinter 8YSZ pellet by MWS

The sintering schedules were optimized based on the sintered density of the samples to be achieved, which are targeted to be of > 99% of theoretical density.

3.3.4.1 Physical characterization (Density, porosity and water absorption)

Bulk density, porosity and water absorption of the MWS sintered samples were measured using ASTM C373 as mentioned in Section 3.3.1.4 and the results are presented in Table 3.11 and dependence of density on sintering temperature is shown in Fig.3.43.

Table 3.11 Sintering parameters and results of the MW Sintered 8YSZ samples

Specimen Identity	Sintering temperature (°C)	Dwell Time(min)	Density (g/cc)	% TD	Porosity (%)	Water absorption (%)
1	1475	15	5.820			
2			5.819			
3			5.820			
4			5.820			
5			5.819			
			5.820	**98.64**	**0.19**	**0.03**
1	1525	15	5.850			
2			5.852			
3			5.851			
4			5.849			
5			5.850			
			5.850	**99.15**	**0.09**	**0.015**
1	1550	15	5.852			
2			5.850			
3			5.850			
4			5.851			
5			5.849			
			5.850	**99.15**	**0.09**	**0.015**

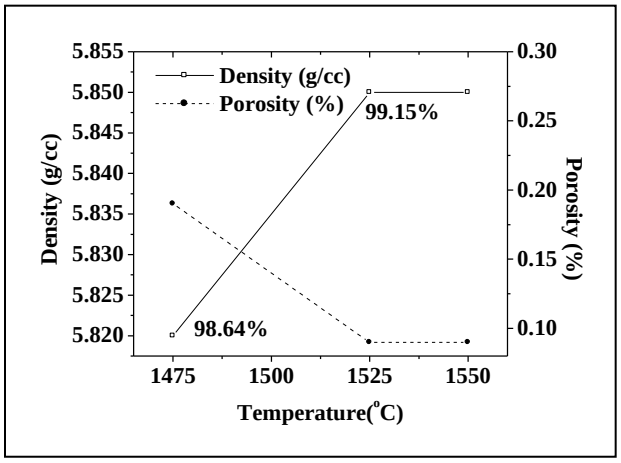

Fig.3.43 Dependence of density and porosity on sintering temperature

3.3.4.2 Microstructural analysis

The specimens were polished, etched and gold sputtered as per the method already mentioned in the Section 3.3.1.5& 3.3.1.6. Microstructural analysis of ceramographically prepared samples were carried out using SEM (Hitachi 3200S, FESEM, Japan). The micrographs are shown in Fig.3.44

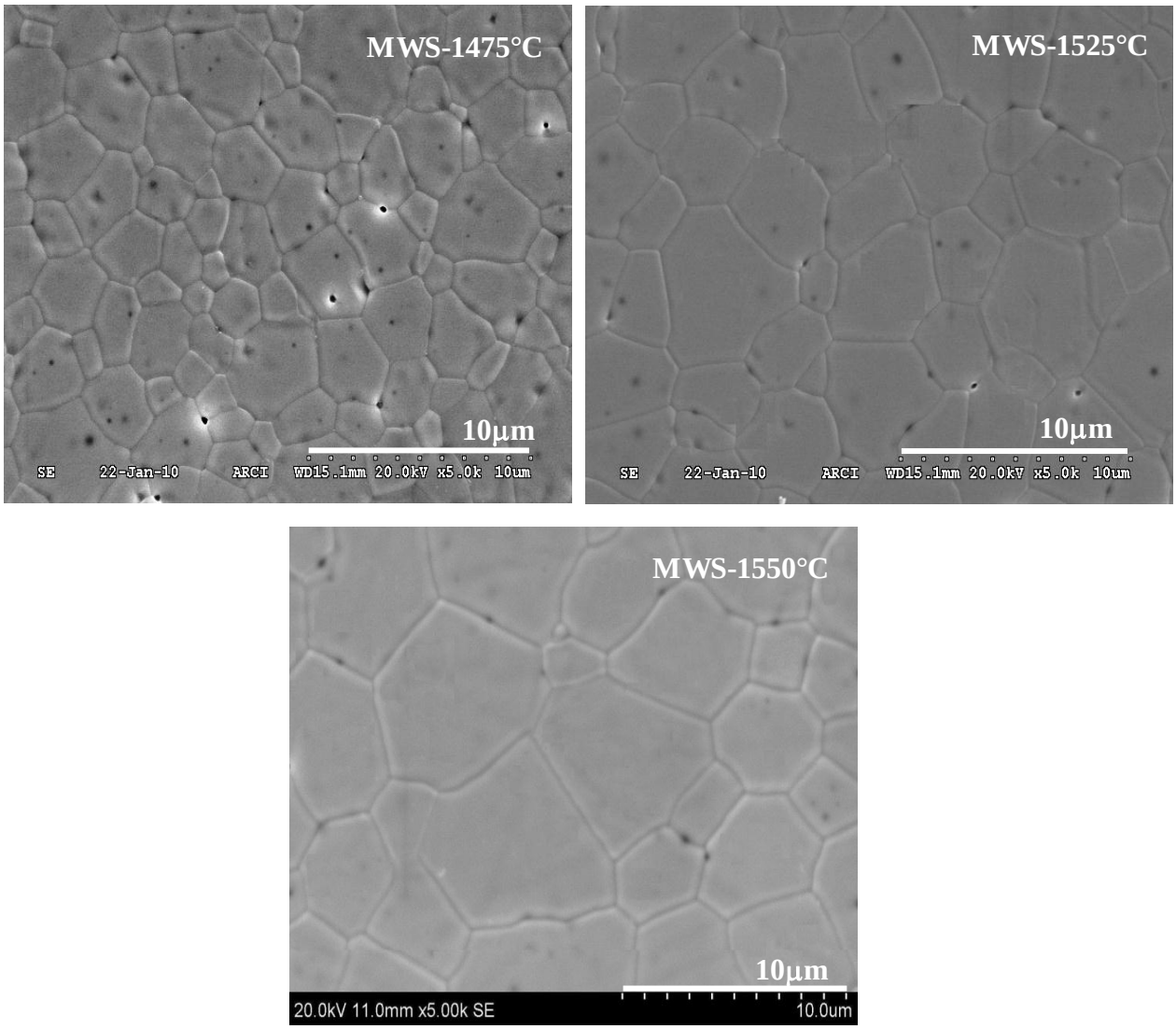

Fig.3.44 Microstructures of 8YSZ samples of MWS (a) 1475°C (b) 1525°C and (c) 1550°C

3.3.4.3 Grain size and distribution analysis through Image Analyzer

The Grain size analyses of the samples were carried out by linear intercept method as mentioned earlier in the Section 3.3.1.7.

The images of the actual measurement on the micrographs of 8YSZ samples sintered at 1525°C using Linear Intercept method, plot of temperature vs. density and grain size and the grain size distribution are shown in Fig.3.45, 3.46 and 3.47 respectively. Table 3.12 presents the sintering parameters, densities and sintered grain sizes of 8YSZ samples sintered by MWS method.

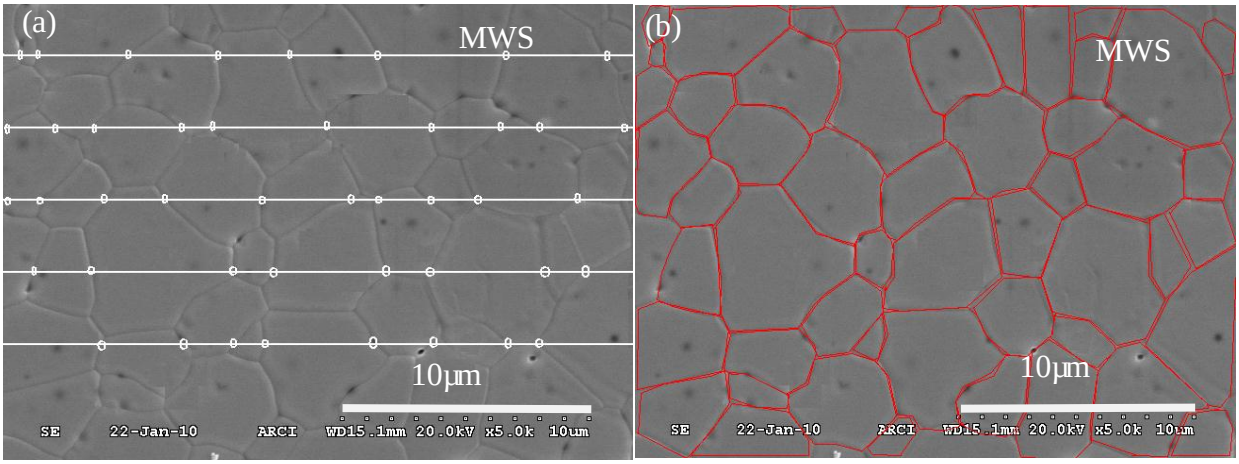

Fig.3.45 SEM image of the MWS sample sintered at 1525° (a) Grain Size analysis by Linear Intercept Method, (b) Grain size distribution

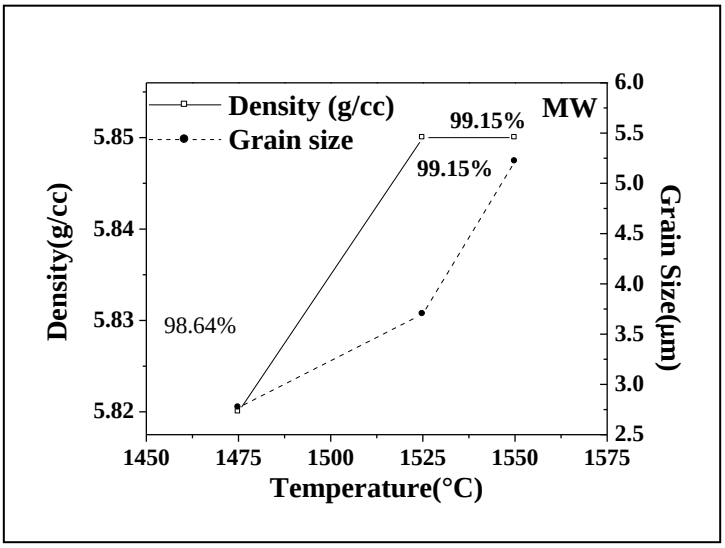

Fig.3.46. Dependence of density, grain size on sintering temperature of 8YSZ specimens sintered by MWS method

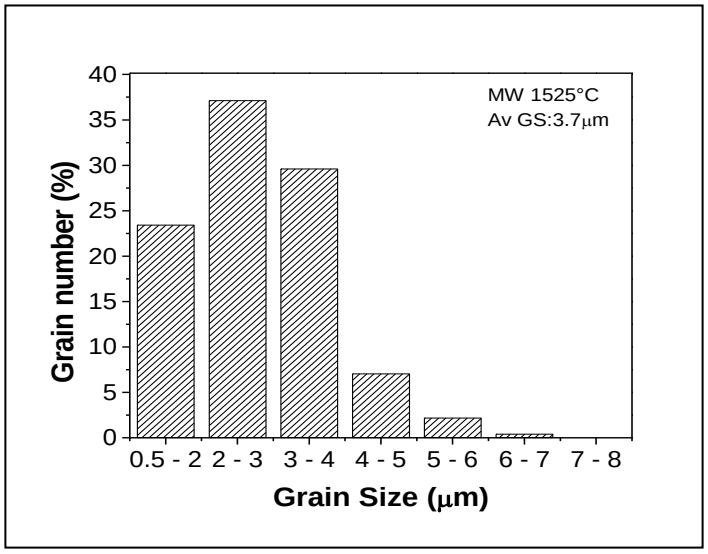

Fig.3.47 Grain size distribution of sintered 8YSZ specimens > 99 %

Table 3.12 Sintering parameters, densities and sintered grain sizes of 8YSZ samples densified using MWS methodology.

Specimen Identity	Sintering temperature(°C)	Dwell Time(min)	Average Density (g/cc)	% TD	Average grain size (μm)
1	1475	15	5.820	98.64	2.77
2	1525	15	5.850	99.15	3.70
3	1550	15	5.850	99.15	5.22

Specimens sintered by microwave technique at the temperature of 1525 °C have shown a density of 99.15 % with average grain size of 3.7μm and grain size distribution similar to conventional sintered specimens.

3.3.4.4 Proposed mechanism for microwave sintering

In the case of microwave sintered samples sintering parameters in comparison to CRH varies in terms of heating rate and dwell time to achieve similar densities greater than 99%TD. The reduction in grain size at 1525°C by 26% in comparison to CRH can be attributed to the faster heating rate of 10°C/min and minimum dwell time of 15minutes which minimizes the grain growth leading to finer grains. MW sintering because of its inherent uniform volumetric heating induces minimum stresses and allows faster heating in comparison to CRH. It is also evident that the grains growth is much faster when the temperature increased to 1550°C.

3.3.5 Spark Plasma Sintering (SPS)

In spark plasma sintering of 8YSZ Tosho powder, 5g of 8YSZ powder was accurately weighed and the powder was poured into a conductive die made of high strength graphite and held between two graphite punches. Graphite foil is used as spacers between the powder and the punches to avoid the damage of the die. The die had an inner diameter of 20mm, an outer diameter of 50mm, and a depth of 50mm. A hole of 1.8mm diameter was drilled into the outside of the die for temperature measurements. A schematic of the die, punches, and spacers is shown in Fig.3.48. For the sake of comparison, though not in the scope of this study 8YSZ powder from another source of M/s. MKnano, M.K. Impex Corp., Canada (particle size of 45 nm) procured is processed under SPS conditions at different peak temperatures.

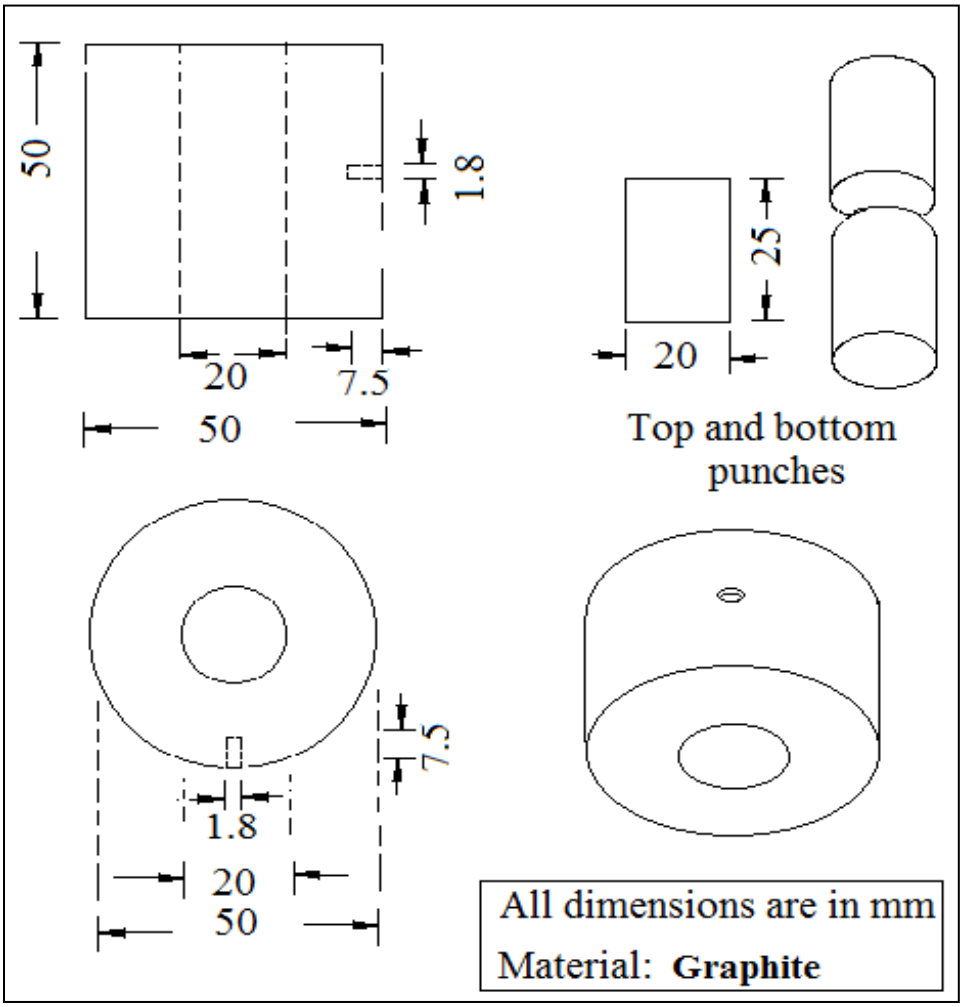

Fig.3.48 Schematic drawing to the scale and the dimensions of the die, punches, and spacers that were used to process 8Y zirconia powder with SPS

The 8YSZ powders were sintered to disks by SPS with Dr. Sinter 1050, Sumitomo Coal Mining Co Ltd, Kanagawa, Japan Fig.3.49. 8YSZ powder was placed in a graphite die and the die was placed in SPS set up. The SPS system was evacuated to 5 Pa and uniaxial pressure of 50 MPa was applied with a heating rate of 170°C/min to peak temperatures of 1250°C, 1325°C and 1425°C with dwell time of 5 minutes in case of 8YSZ (205 nm Tosho) powder. The temperature profile used to sinter 8YSZ by SPS is shown in Fig.3.50. However, in the case of 8 YSZ (45 nm M/s. M K Nano) processing was carried out at uniaxial pressure of 50 MPa was applied with a heating rate of 170°C/min to peak temperatures of 1050°C, 1100°C,1150°C and 1250°C with dwell time of 5 minutes . The samples were furnace cooled to room temperature and the SPS pellets were annealed in air at 1000°C for 2hrs to remove carbon contamination.

Fig.3.49 Spark Plasma Sintering Furnace

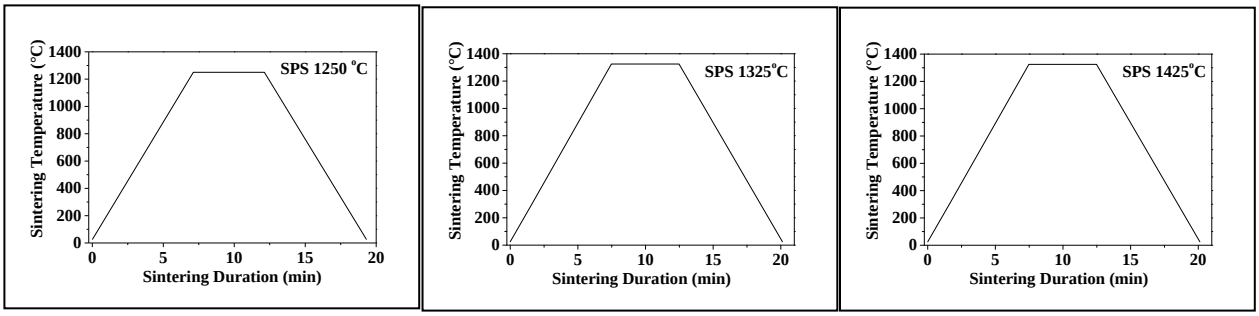

Fig.3.50 Temperature profile employed to sinter 8YSZ powder by SPS

3.3.5.1 Physical characterization (Density, Porosity and Water absorption)

Bulk density, porosity and water absorption of the SPS sintered samples were measured using ASTM C373 as mentioned in Section3.3.1.4and the results are presented in Table 3.13 and Fig 3.51 (a) and (b) respectively.

Table 3.13 Sintering parameters and results of the Spark Plasma sintered 8YSZ samples

Specimen Identity	Sintering temperature (°C)	Dwell Time (min)	Density (g/cc)	% TD	Porosity (%)	Water absorption (%)
8YSZ Tosoh(205nm)						
1	1250	5	5.847	99.10	0.12	0.02
2	1325	5	5.876	99.59	0.06	0.01
3	1425	5	5.876	99.59	0.06	0.01
8YSZ MKnano (45nm)						
1	1050	5	5.874	99.56	0.06	0.01
2	1100	5	5.895	99.90	0.05	0.01
3	1150	5	5.895	99.90	0.05	0.01
4	1200	5	5.895	99.90	0.05	0.01

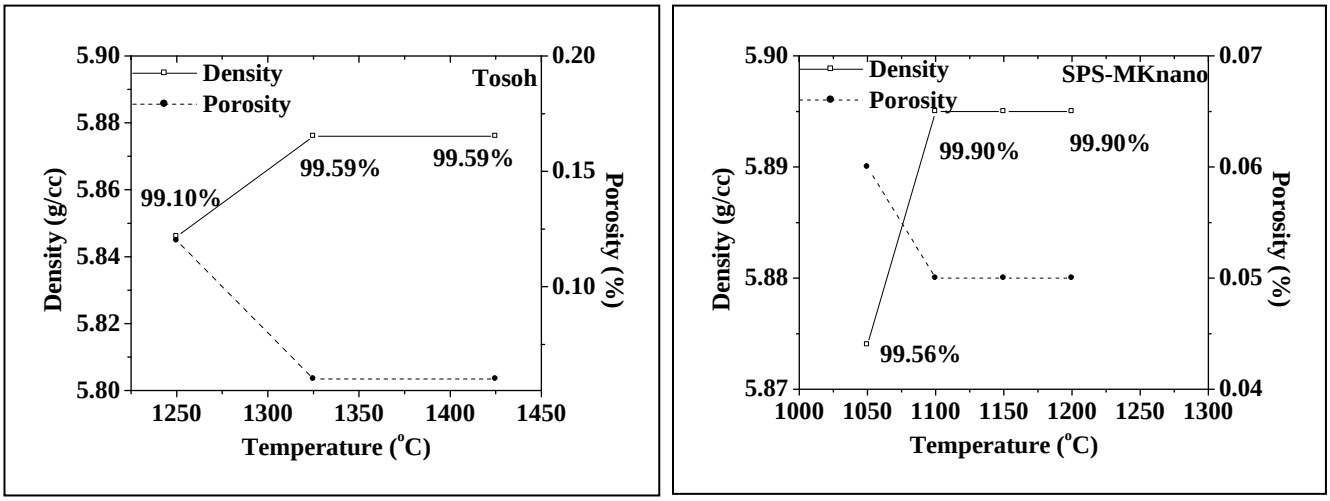

Fig.3.51 Dependence of density and porosity on sintering temperature of (a) 8YSZ - Tosoh and (b) 8YSZ - MKnano

3.3.5.2 Micro structural Analysis (SEM)

The specimens were polished, etched and gold sputtered as per the method already mentioned in the Section 3.3.1.5& 3.3.1.6. Microstructural analysis of ceramographically prepared samples were carried out using SEM (Hitachi 3200S, FESEM, Japan). The micrographs of 8YSZ –Tosoh samples are shown in Fig.3.52 (a), (b) and (c).The micrographs of 8YSZ –Mknano samples are also shown in Fig.3.53 (a), (b) (c)and (d).

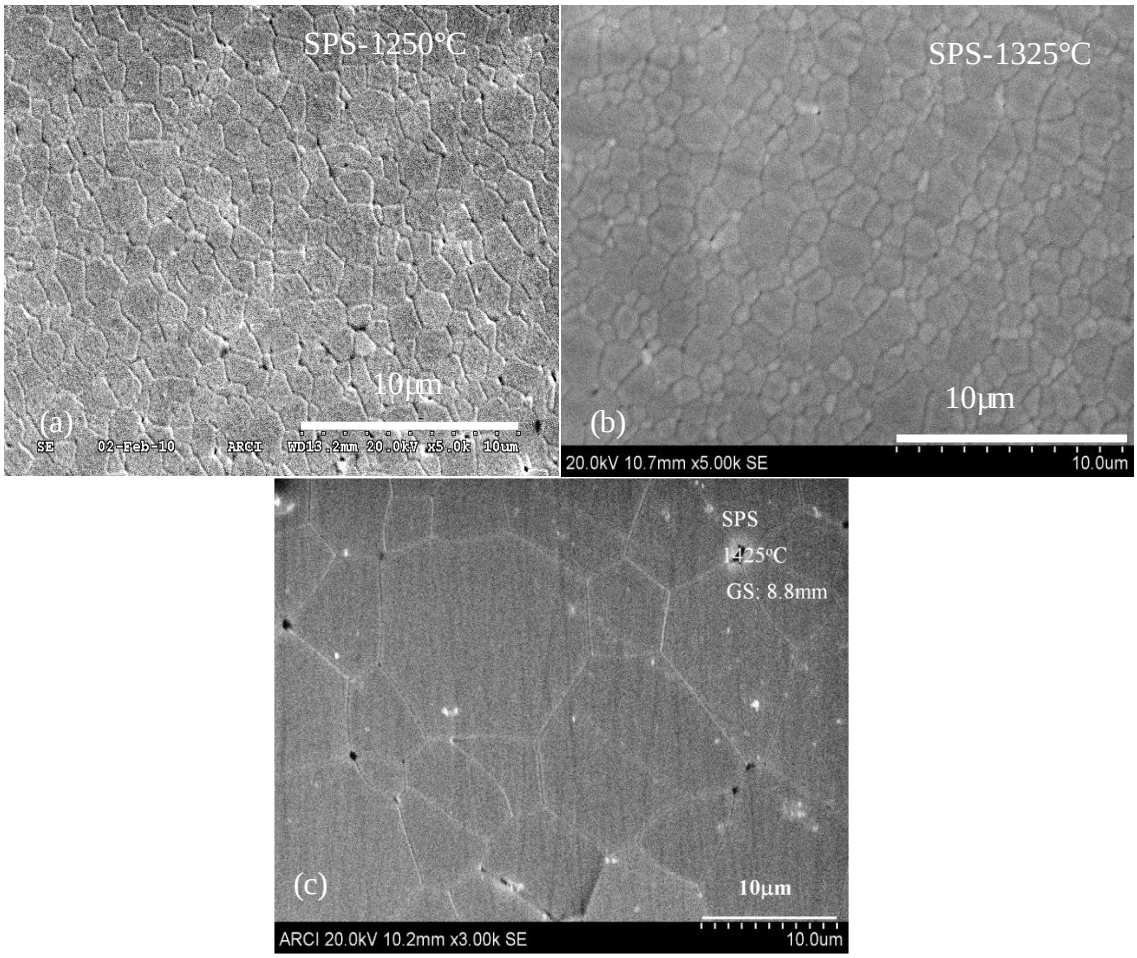

Fig.3.52 Microstructures of 8YSZ (Tosoh) samples of SPS sintered at (a) 1250°C (b) 1325°C and (c) 1425°C

Comparative Evaluation of Spark Plasma (SPS), Microwave (MWS) and Two Stage Sintering (TSS) on the Densification and Microstructural Evolution of Stabilized Zirconia Ceramics.

Published in Science of Sintering, 2010; 42: 259.

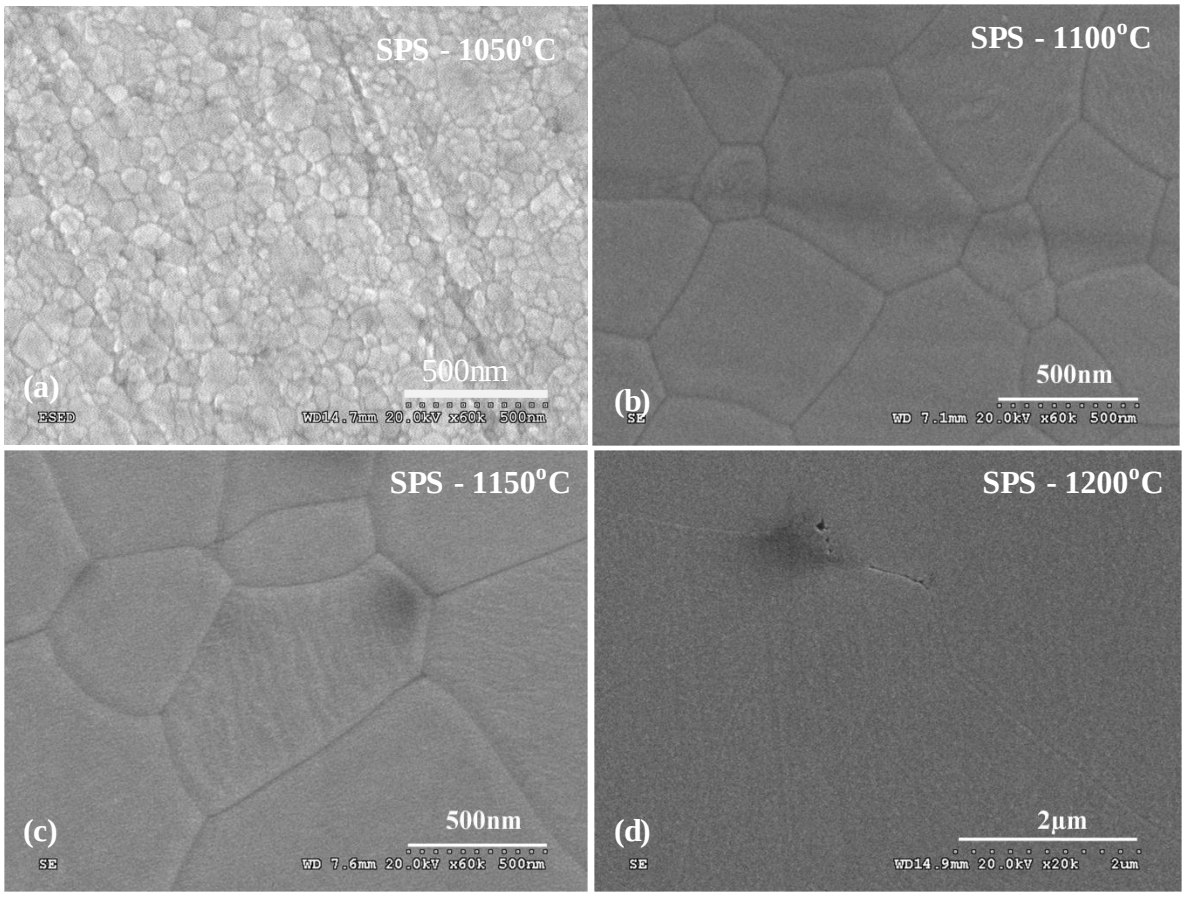

Fig.3.53 Microstructures of 8YSZ (MKnano) samples of SPS sintered at (a) 1050°C (b) 1100°C (c) 1150°C and(d) 1200°C

3.3.5.3 Grain size and distribution analysis through Image Analyzer

The grain size analyses of the samples were carried out by linear intercept method as mentioned earlier in the Section 3.3.1.7.The images of the actual measurement on the micrographs of 8YSZ (Tosoh) samples sintered at 1325°C and 8YSZ (MKnano) using Linear Intercept method, plot of temperature vs. density, grain size and the grain size distribution are shown in Fig.3.54(a),(b), 3.55(a) and 3.56(a) respectively. Further, plot of temperature vs. density, grain size and the grain size distribution of (MKnano) are shown in Fig.3.54(c), (d), 3.55(b) and 3.56(b) respectively. Table 3.14 presents the sintering parameters, densities and sintered grain sizes of 8YSZ samples.

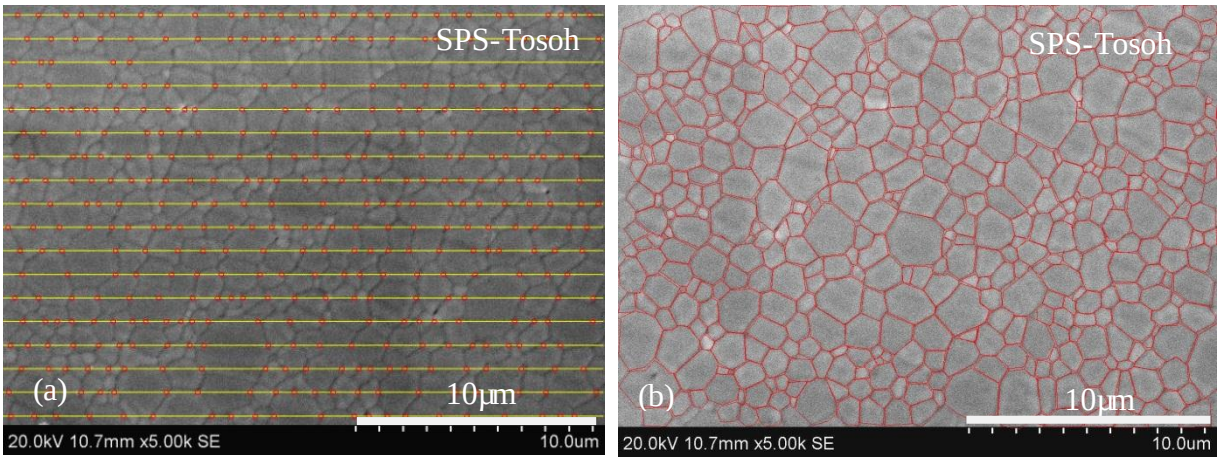

Fig.3.54 SEM image of the 8YSZ (Tosoh) samples of SPS sintered at 1325°C (a) Grain Size analysis by Linear Intercept Method (b) Grain size distribution

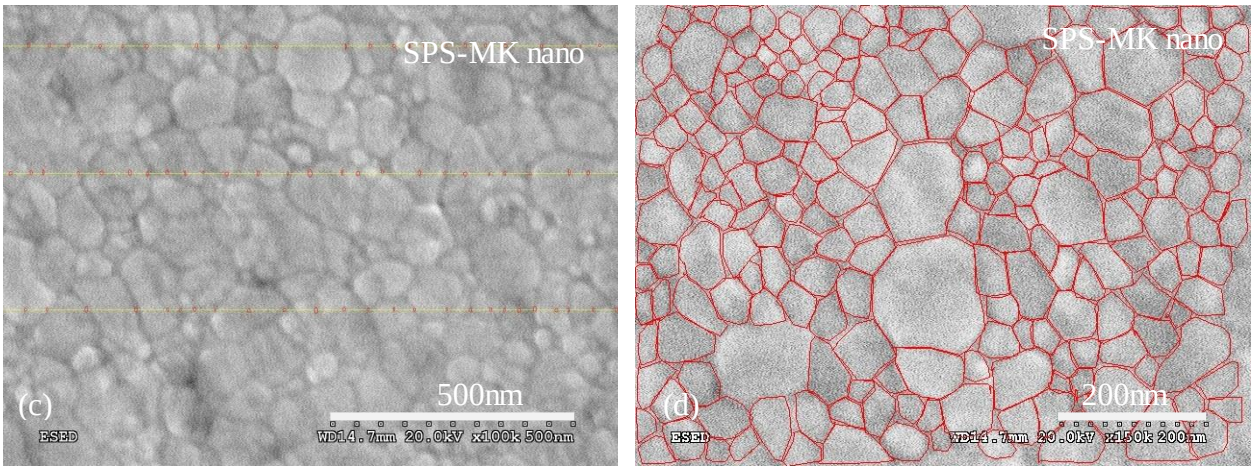

Fig.3.54 SEM image of the 8YSZ (MKnano) samples of SPS sintered at 1050°C (c) Grain Size analysis by Linear Intercept Method (d) Grain size distribution

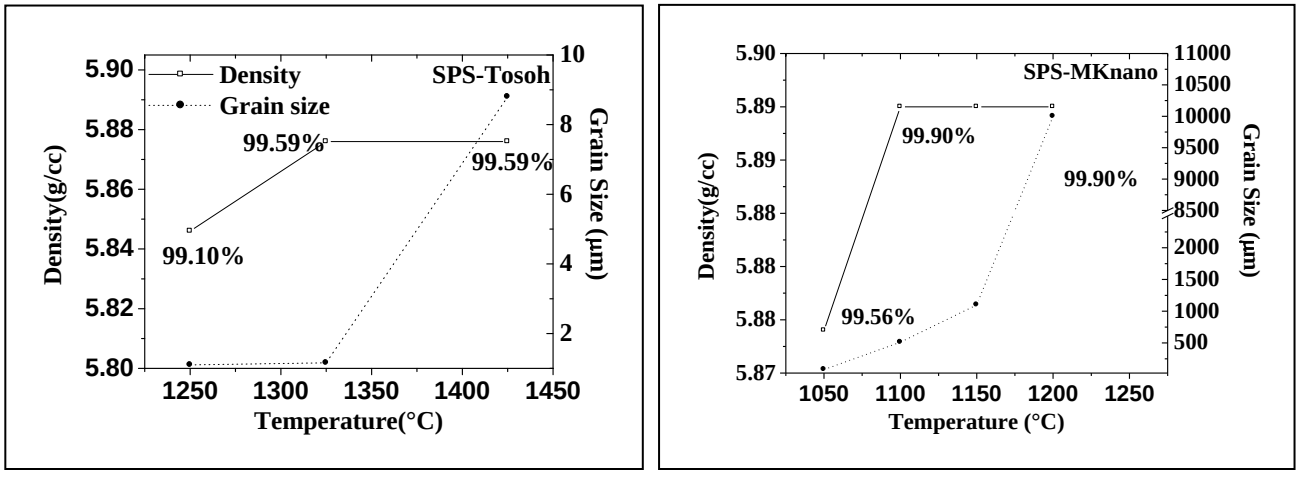

Fig.3.55 Dependence of density, grain size on sintering temperature of 8YSZ specimens sintered by SPS method (a) Tosoh (b) MKnano

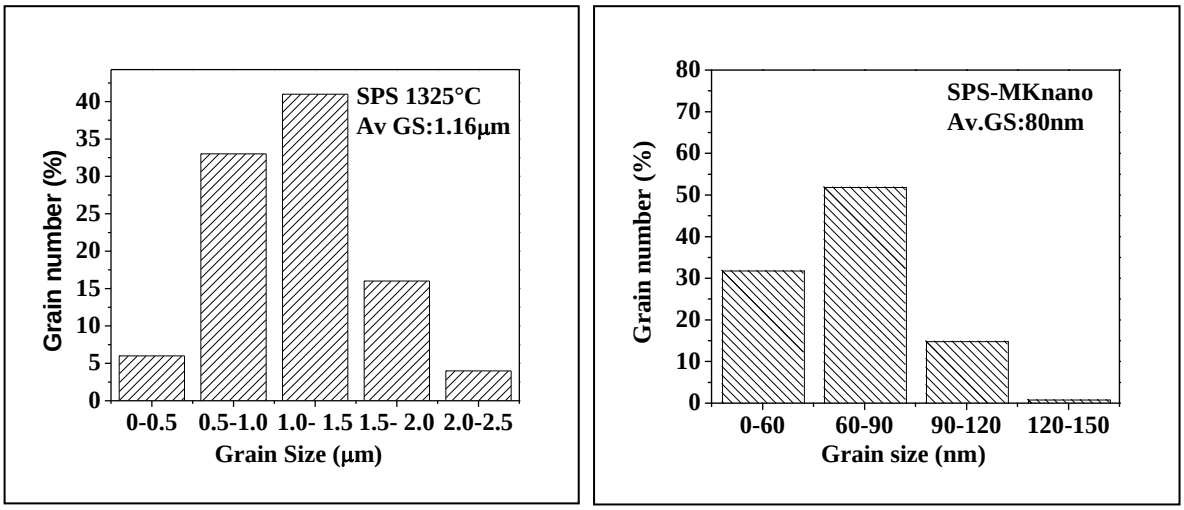

Fig.3.56 Grain size distribution of sintered 8YSZ specimens of SPS (a) Tosoh (b) MKnano

Table 3.14 Sintering parameters, densities and sintered grain sizes of 8YSZ samples densified using SPS methodology.

Specimen Identity	Sintering temperature (°C)	Average Density (g/cc)	% TD	Average grain size
Tosoh (205nm)				
1	1250	5.846	99.10	1.13 μm
2	1325	5.876	99.59	1.16 μm
3	1425	5.876	99.59	8.80 μm
MKnano (45nm)				
1	1050	5.874	99.56	80 nm
2	1100	5.895	99.90	510 nm
3	1150	5.895	99.90	1.10μm
4	1200	5.895	99.90	10.0μm

3.3.5.4 Transmission Electron Microscopy (TEM) image analysis of the sample

In order to further investigate the microstructural features the 8YSZ (Tosoh) samples were subjected to TEM analysis. The specimen for TEM has been prepared as per the following sequence. The samples were subjected to dimpling using dimple grinder to a thickness of 20µm. Dimpled samples were further thinned to electron transparency using focused argon ion beam milling facility at about 4KV. The TEM observations were made using a Transmission Electron Microscope (Model: G 20, FEI, 200KV Microscope with Gaton image filter and EDS facility) and observations are as follows.

Fig. 3.57(a) & (b) shows the typically microstructure confirming the SEM observations of ~ 1µm though smaller grains are also seen. The close observation of the microstructure also reveals Moire´ patterns along the grain boundaries indicating the grain boundary controlled densification. It is well known that Moiré patterns are related to two elemental grains with similar crystallographic orientation. The observed intergranular Moiré patterns reveals high dislocation density in the zirconia grains under SPS conditions.

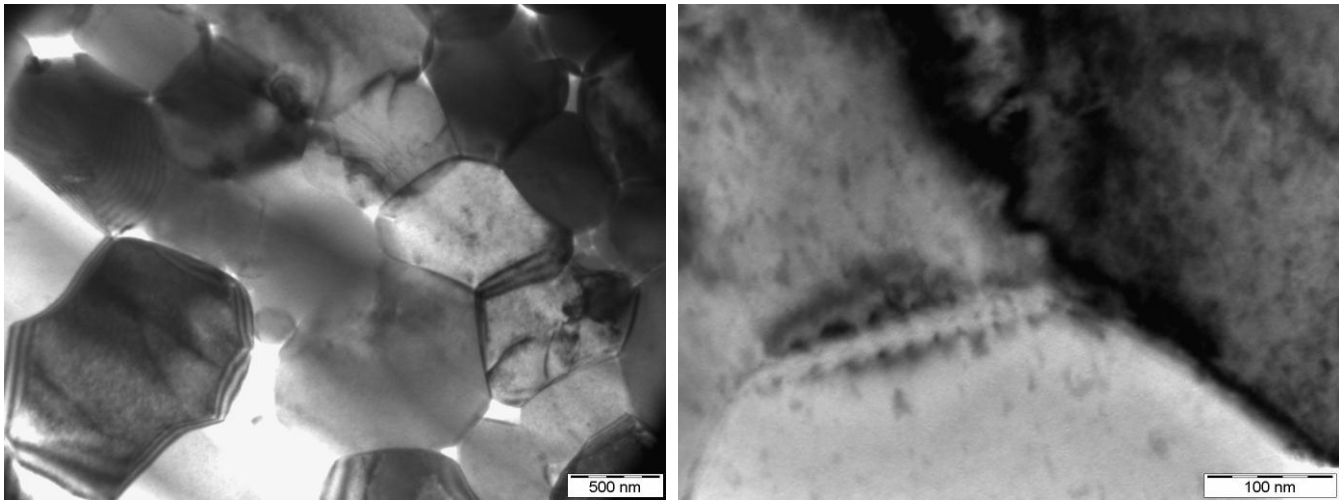

Fig.3.57 (a) Typical aspect observed by TEM in 8YSZ sample sintered by SPS at 1325^{o}C for 5 min (b) Moire´ patterns are observed everywhere

3.3.5.5 Proposed mechanism for spark plasma sintering

It is evident that the SPS sintering of the specimens results in densities close to theoretical with finer grain sizes. This can be attributed to the various novel mechanisms that are associated during SPS process. It is well known that in spark plasma sintering results in the generation of

momentarily plasma [57, 60, 95 - 98] between the particles. Though 8Y zirconia powders are non-conducting in nature at room temperature, during the initial stage of sintering, as the powders are loosely packed and the effect of plasma exists in the gap between the particles [60]. This plasma generated in the initial stages expected to clean the particle surfaces and results in nascent reactive surfaces for the enhanced neck formation at low temperatures in comparison to the other sintering techniques. It is also obvious that the plasma sites are minimized as the sintering proceeds because of the gap disappear between the particles, and zirconia becomes conducting at the temperature range >800^{o}C. At this high temperature ranges, it is also expected that in addition to the indirect heating through the die which is operative at low temperatures, direct electrical heating also play a major role contributing to the enhanced sintering through SPS process [99-101]. Further in the SPS the applied mechanical pressure though it is 50 MPa in the present study because of dies limitation it plays a major role in comparison to other sintering techniques employed. On simultaneous application of temperature and pressure the particles get not only rearranged but also the crushing of the soft agglomerates which takes place and in turn improve the packing factor leading to uniform microstructure to the compact after sintering is complete (Fig.3.52(b)). The powders used in the present study being finer with around 205nm and occasional agglomerations are essentially present. Under the applied pressure of 50MPa results in crushing, this is not only expected to enhance the densification process but also results in uniform microstructures. The BET surface area of the powder has measured to be around 5.7m^{2}/g. Hence, the intrinsic driving force of surface energy being small it necessitates high temperatures of 1525^{o}C for the effective sintering to > 99 % of TD in the conventional process. However, with SPS the applied pressure have a significant role to play to bring down the final sintering temperatures to 1325^{o}C. During SPS as the applied pressure is expected to enhance the mass transport significantly as the driving force of normal sintering process is limited in the present case due to low active surface areas involved.

The applied stresses, though the compaction stresses are low (50 Map) it is well known that the substitution of Y^{3+} in Zr^{4+}lattice in the cubic systems each additional yttria molecule creates one oxygen vacancy [102]. This will form highly defective structure which not only enhances the diffusion process but also expected to facilitate grain boundary sliding at high temperatures and under applied pressure leading to enhanced densification [103].It is well reported [104,105,106] that SPS processed sample is enriched with dislocations as is evident from the Moiré patterns

observed in the TEM microstructures. This enhanced dislocation density can be attributed to the unique sintering parameters such as relatively high ramping rates (170^{o}C/min) and very low dwell time (5min) employed during the SPS.

The smaller grain size ~1µm in comparison to 4.67µm with CRH in case of (Tosoh) can be attributed to low peak densification temperature as a consequence of unique sintering parameters associated with SPS as discussed above resulting in effective densification which retains the grain size under control. However, it is very important that the peak temperature and dwell time should be optimum which otherwise leads to highly exaggerated grain growth as is evident from the samples sintered at 1425^{o}C (Fig.3.52(c)) [107, 108]. In the present study the densification 99.5%TD in comparison with uniform grain size and its distribution can be a result of optimum sintering parameters employed in the present study.

A similar result is also observed with MKnano samples. The grain sizes as low as 80 nm could be retained even with close to theoretical densities. The lower grain sizes can be attributed to significantly low starting particle size. However, there is a 100 fold enhancement in grain size on increasing temperature from 1050^{o}C to 1200^{o}C (Fig.3.53).

Based on the above observations the main advantage of the spark plasma sintering in the context of ionic conductivity are relatively clean grain boundaries due to the limited migration of the impurities leading to segregation along grain boundary which act as the barrier for ions to transport. Additionally, the higher dislocation densities along the grain boundaries as is evidenced by the Moiré patterns also promote the ionic conductivity to a greater extent [105,106]. Further, the effect of grain sizes and its uniform distribution effects of the SPS sintered samples will also be evaluated by comparing their conductivities. It may be concluded that SPS operates at unique mechanisms and processes which can effectively engineer the density and microstructure desirable for a functional superior intrinsic properties.

3.4 Summary and conclusions

Sintering methodologies, optimum sintering parameters corresponding density values and average grain sizes are shown in Table 3.15 and in Fig.3.58.

Table 3.15 Sintering methodologies, optimum parameters and results

Sample Id	Sintering methodology	Sintering parameters (Selected as optimum)	Density (g/cc)	% Theoretical density	Average grain size(µm)
I	CRH	Peak temperature:1525°C Dwell time:2 hrs Heating rate:5°C/minute	5.867	99.44	4.67
II	MWS	Peak temperature:1525°C Dwell time:15minutes Heating rate:10°C/minute	5.850	99.15	3.70
III	RCS	Peak temperature:1550°C Shrinkage rate: 22µm/min 15µm/min 5µm/min	5.720	96.95	3.45
IV	TSS	Peak temperature(T1):1525°C Dwell time: 5min T2:1350°C Dwell time: 4h Heating rate:5°C/minute	5.865	99.40	2.64
V	SPS Tosoh	Peak temperature:1325°C Dwell time:5 minutes Heating rate:170°C/minute	5.876	99.59	1.16
VI	SPS MKnano	Peak temperature:1050°C Dwell time:5 minutes Heating rate:170°C/minute	5.874	99.56	80nm

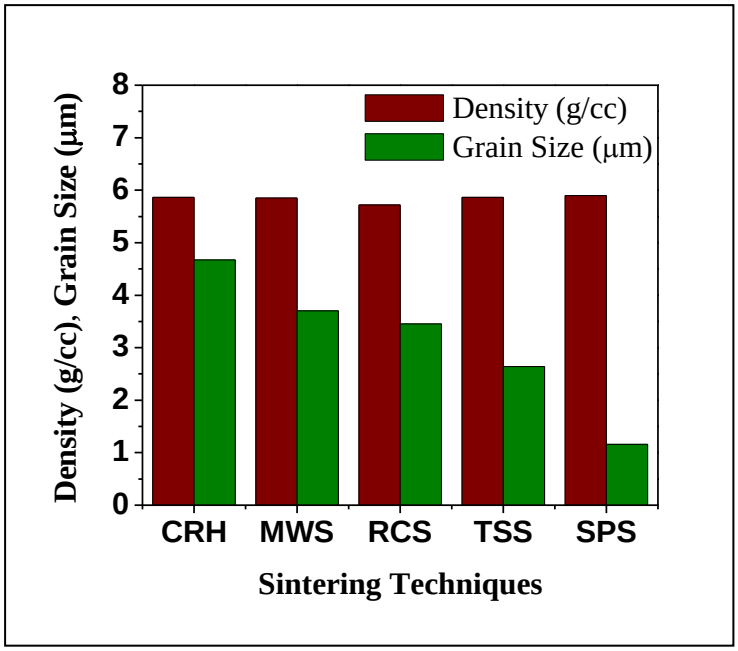

Fig.3.58 Effect of sintering methodology on density and grain size

Based on the study the following conclusions can be made:

- Densities close to 99% of the TD could be achieved in slip cast Zirconia ceramics with Conventional Ramp and Hold (CRH), Two Stage Sintering (TSS), Microwave Sintering (MWS) and Spark Plasma Sintering (SPS) sintering methodologies except for RCS for which a maximum density of 97% is obtained. It is evident that the densification strategies and their driving mechanisms play a vital role in sintering 8Y zirconia ceramics in order to achieve the twin objectives of full densification and finer sintered grain sizes.

---

1. **Effect of sintering techniques on microstructure evolution of 8YSZ zirconia ceramics.**
   Oral presentation, the annual session of Indian Ceramic Society, 2009, Trivandrum
2. **Effect of sintering techniques on the densification and microstructure of fully stabilized zirconia electrolytes.**
   Oral presentation, the A.P Science Congress and Annual Convention of A.P. Academy of Sciences, 2010, Hyderabad.

- Significant difference is observed with respect to the grain growth accompanied by densification. The average grain size of sintered zirconia grains after conventional sintering was 4.37μm. A twofold decrease in grain size (2.64 μm) was observed with the two stage sintering. This decrease in grain size during the two-step sintering process significantly controls the grain growth, which can be attributed to the fact that the first heating step to high temperature at 1525°C for a shorter duration closes the porosity without significant grain growth. The second step at 1350°C for a longer period of time imparts densification with limited grain growth.

- Rate controlled sintering resulted in smaller grain size (3.45 μm) and lower density (97%) compared to those CRH sintered grain size (4.67 μm) and density (99.44%) obtained in conventional sintering methodology. Unlike in CRH, topology of the pore and pore growth is controlled to a minimum in RCS leading to much higher pore density with small diameter of pores at same porosity level resulting in reduced grain growth. One of the major issues observed in RCS is that it does not result in complete elimination of pores.

- Specimens sintered by microwave technique at 1525 °C have shown a density of 99.15 % with an average grain size of 3.7μm and grain size distribution similar to conventional sintered specimens. During microwave heating energy is transferred to the material electro-magnetically and not as a thermal heat flux enabling the material to be heated at rapid rates. The higher oxygen vacancies associated with 8 mol% yttria stabilized zirconia provides higher ionic conductance at elevated temperatures leading to high dielectric losses and enhanced absorption of microwaves. This mechanism could be one possible reason for the shorter sintering times in MWS. A significant decrease in grain size (to 2.6 μm) was observed in two stage sintering in comparison to conventional sintering and is attributed to the lower soaking temperatures compared to conventional CRH. The microstructure was found to be more homogeneous with a narrow grain size distribution in two stage sintering.

- Specimens (Tosoh-205nm) sintered through Spark Plasma Sintering at 1325°C for a period of 5 minutes have resulted in highest sintered density of 99.89 % with lowest grain

size of ~1 μm. Maximum densification at the lowest sintering temperature was provided by SPS wherein samples could be sintered to >99%TD at a temperature of 1250°C for 5 minutes. The rapid densification of samples by SPS is attributed to the enhanced densification rate due to mechanisms like particle rearrangement and breaking up of agglomerates aided by the applied pressure and faster heating rates. By rearrangement of particles the SPS process also impedes the pore size increase generally observed in the first and intermediate stages of sintering. Further, applied electric field also promotes the diffusion of ions and vacancies which enhances the sintering rate. TEM studies also revealed the existence of Moiré patterns which in turn corresponds to high dislocation densities. These high dislocation densities observed in the TEM studies is expected to enhance the ionic conductivity. The microstructure of SPS sintered specimen at 1325°C looks unique with dense microstructure composed of fine grain sizes and the average grain size was found to be ~1 μm. The particle size to sintered grain size ratio is quite low (a factor of 5) compared to the other sintering techniques employed. The specimens (MKnano - 45nm) also exhibited a similar behavior with SPS conditions. The grain sizes as low as 70-80nm could be achieved with almost 100% theoretical densities. SPS sintering temperatures was around 1050^{o} C due to the ultra-fine grain sizes of the starting powder in the range of 45nm. However the effect SPS sintering temperature was found to be very critical exhibiting a hundred fold increase in average grain size ranging from 80 nm at 1050^{o}C to10 μm at 1200 ^{o} C.

3.5 References

1. Kang S-J.L, Jung Y-II. Sintering kinetics at final stage sintering: model calculation and map construction, Acta Mater. 2004; **52:** 4573.
2. Rahaman M.N. Ceramic processing and sintering, New York, Marcel Dekker. 2003; 602.
3. Kang S.J.L. Sintering, densification, grain growth and microstructure, Amsterdam, Elsevier. 2005; 153.
4. Palmour H.III, Huckabee M.L, Hare T.M. Rate controlled sintering: Principles and practice. In Sintering New Developments, ed. M. M. Ristic. Elsevier, Amsterdam. 1979; 46.

5. Palmour H.III, Hare T. M.Rate controlled sintering revisited. In Sintering ’85. ed. G. C. Kucynski, D. P. Uskovic, H. Palmour, Plenum Publishing Corporation, New York. 1987.
6. Palmour H.III, 6th Round Table 3. Conference on Sintering. Plenum Press, 1987; **3**:16.
7. Skorokhod V.V, Ragulya A.V. Rate-controlled sintering as method for controlling microstructure of cermets and similar sintered materials (review), Powder Metallurgy (Russian), 1994, N**3-4**, 1.
8. Ragulya A.V. Recent Achievements in the Rate-Controlled Sintering of Nanostructured Ceramics.
9. Agarwal G, Speyer R.F, Hackenberger W.S. Microstructural development of ZnO using a rate-controlled sintering dilatometer.J. Mater. Res. 1996;**11**: 671.
10. Chen I, Wang X.H. Sintering dense nanocrystalline ceramics without final stage grain growth. Nature. 2002; **404**: 168.
11. Wang C.J, Huang C. Y, Wu Y.C. Two-step sintering of fine alumina–zirconia ceramics. Ceram. Inter. 2009; **35**: 1467.
12. Wang X.H, Chen P.L, Chen I-W. Two-step sintering of ceramics with constant grain size, I. Y_2O_3.J. Am. Ceram. Soc. 2006; **8**: 431.
13. Mazaheri M, Zahedi A.M, Sadrnezhaad S.K. Two-step sintering of nanocrystalline ZnO compacts: effect of temperature on densification and grain growth. J. Am. Ceram. Soc. 2008; **91**: 56.
14. Han M, Tang X, Yin H, Peng S. Fabrication, microstructure and properties of a YSZ electrolyte for SOFCs. J. Power Sour. 2007; **165**: 757.
15. Robert C.L, Ansart F, Deloget C, Gaudon M, Rousset A. Dense yttria stabilized zirconia: sintering and microstructure. Ceram. Inter. 2003; **29**: 151.
16. Ghosh A, Suri A.K, Rao B.T, Ramamohan T.R. Low-temperature sintering and mechanical property evaluation of nanocrystalline 8 mol% yttria fully stabilized zirconia. J. Am. Ceram. Soc. 2007; **90**: 2015.
17. Yu P.C, Li Q.F, Fuh J.Y.H, Li T, Lu L. Two-stage sintering of nanosized yttria stabilized zirconia process by powder injection moulding, J. Mater. Process. Techn. 2007; **192–193**: 312.

18. Wang X.H, Deng X.Y, Bai H.L, Zhou H, Qu W.G, Li L.T, Chen I.W. Two-step sintering of ceramics with constant grain-size, II: $BaTiO_3$ and Ni–Cu–Zn ferrite. J. Am. Ceram. Soc. 2006; **89**: 438.
19. Li J, Ye Y. Densification and grain growth of Al_2O_3 nanoceramics during pressureless sintering. J. Am. Ceram. Soc. 2006; **89:** 139.
20. Bodisova K, Sagalik P, Galusek D, Svancarek P. Two-stage sintering of alumina with submicrometer grain size. J. Am. Ceram. Soc. 2007; **90:** 330.
21. Lee Y.I, Kim Y.W, Mitomo M, Kim D.Y. Fabrication of dense nanostructured silicon carbide ceramics through two-step sintering. J. Am. Ceram. Soc. 2003; **86:** 1803.
22. Mazaheri M, Valefi M, Hesabi Z. R, Sadrnezhaad S.K. Two-step sintering of nanocrystalline $8Y_2O_3$ stabilized ZrO_2 synthesized by glycine nitrate process. Ceram. Inter. 2009; **35**: 13.
23. Polotai A, Breece K, Dickey E, Randall C. A novel approach to sintering nanocrystalline barium titanate ceramics. J. Am. Ceram. Soc. 2005; **88**: 3008.
24. Karaki T, Yan K, Adachi M. Barium titanate piezoelectric ceramics manufactured by two-step sintering. Jpn. J. Appl. Phys. 2007; **46**: 7035.
25. Wang D.H, Deng X.Y, Bai H.L, Zhou H, Qu W.G, Li L.T. Two-step sintering of ceramics with constant grain size, II: $BaTiO_3$ and Ni–Cu–Zn ferrite. J. Am. Ceram. Soc. 2006; **89**: 438.
26. Balaya P, Ahrens M, Kienle L, Maier J, Rahmati B, Lee B. S, Sigle W, Pashkin A, Kuntsher C, Dressel M. Synthesis and characterization of nanocrystalline $SrTiO_3$.J. Am. Ceram. Soc. 2006; **89**: 2804.
27. Maca K, Pouchly V, Shen Z.J. Two-step sintering and spark plasma sintering of Al_2O_3, ZrO_2 and $SrTiO_3$ ceramics. Integrated Ferroelectrics. 2008: **99**: 114.
28. Ghosh A, Suri A.K, Rao B.T, Ramamohan R.T. Low-temperature sintering and mechanical property evaluation of nanocrystalline 8 mol% yttria fully stabilized zirconia. J. Am. Ceram. Soc. 2007; **7:** 2015.
29. Binner J, Annapoorani K, Paul A, Santacruz I, Validhyanathan B. Dense nanostructured zirconia by two stage conventional/hybrid microwave sintering. J. Eur. Ceram. Soc. 2008; **28**: 973.
30. Rafferty A, Prescott T, Brabazon D. Sintering behaviour of cobalt ferrite ceramic. Ceram. Inter. 2008; **34**: 15.

31. Granger G.B, Guizard C, Addad A. Sintering of an ultra-pure alumina powder I. Densification, grain growth and sintering path. J. Mater. Sci. 2007; **42**: 6234.
32. Mikoczyova M, Galusek D. Influence of forming method and sintering process on densification and final microstructure of submicrostructure of submicrometre alumina ceramics. Proc. Appl. Ceram. 2008; **2**: 13.
33. Krell A, Blank P. Grain size dependence of hardness in dense submicrometre alumina. J. Am. Ceram. Soc. 1995; **78**: 1118.
34. Krell A, Klaffke D. Effect of grain size and humidity on fretting wear in fine grained alumina, Al_2O_3/TiC and zirconia. J. Am. Ceram. Soc. 1996; **76**: 1139.
35. Krell A, Blank P. The influence of shaping method on the grain size dependence of strength in dense submicrometre alumina. J. Eur. Ceram. Soc. 1996; **16**: 1189.
36. Trunec M, Chlup Z. Higher fracture toughness of tetragonal zirconia ceramics through nanocrystalline structure. Scripta Materialia 2009; **61**: 56.
37. Apetz R, Van Bruggen M. P. B. Transparent alumina: a light-scattering model. J. Am. Ceram. Soc. 2003; **86**: 480.
38. Maca K, Pouchly V, Zalud P. Two-Step Sintering of oxide ceramics with various crystal structures. J. Euro. Ceram. Soc. 2010; **30**: 583.
39. Yadoji P, Peelamedu R, Agrawal D, Roy R. Microwave sintering of Ni_ Zn ferrites: comparison with conventional sintering. Mater. Sci. Engg. B. 2003; **98**: 269.
40. Agrawal D. Microwave Sintering of Ceramics, Composites, Metals, and Transparent Materials. J. Mater. Edu. 1999; **19**: 49.
41. Clark D.E, Folz D.C, West J.K. Processing materials with microwave energy. Mater. Sci. Engg. A. 2000; **287**: 153.
42. Leonelli C, Veronesi P, Denti L, Gatto A, Iuliano L.Microwave assisted sintering of green metal parts. J. Mater. Proces. Tech. 2008; **205**: 489.
43. Menezes R.R, Souto P.M, Kiminami R.H.G.A. Microwave hybrid fast sintering of porcelain bodies. J. Mater. Proces. Tech. 2007; **190**: 223.
44. Agrawal D, Sohn International Symposium, Advanced Processing of Metals and Materials. 2006; **4**: 183.
45. Clark D.E, Sutton W.H. Microwave Processing of Materials. Annual Review Mater. Sci.1996; **26**: 299.

46. Haque K.E. Microwave energy for mineral treatment process – a brief review. Inter. J. Mineral Process. 1999; **57**: 1.
47. Gupta M, Wong W.L.E. Enhancing overall mechanical performance of metallic materials using two-directional microwave assisted rapid sintering. Scripta. Materilia. 2005; **2**: 479.
48. Barba A, Clausell C, Feliu C, Monzo M. Sintering of $(Cu_{0.25}Ni_{0.25}Zn_{0.50})Fe_2O_4$ Ferrite J. Am. Ceram. Soc. 2004; **87**: 571.
49. Dube D.C, Ramesh P.D, Cheng J, Lanagan M.T, Agrawal D, Roy R. Experimental evidence of redistribution of fields during processing in a high-power microwave cavity. Appl. Phys. Lett. 2004; **85**: 3632.
50. Yan M, Hu J. Microwave sintering of high-permeability $(Ni_{0.20}Zn_{0.60}Cu_{0.20})Fe_{1.98}O_4$ ferrite at low sintering temperatures. J. Magnetism Magnetic Mater. 2006; **305**: 171.
51. Yang J.H, Song K.W, Lee Y. W, Kim J. H, Kang K. W, Kim K. S, Jung Y. H. Microwave process for sintering of uranium dioxide. J. Nuclear Mater. 2004; **325**: 210.
52. Khor K.A, Yu L.G, Chan S.H, Chen X.J. Densification of plasma sprayed YSZ electrolytes by spark plasma sintering (SPS).J. Eur. Ceram. Soc. 2003, **20**: 1855.
53. Chen X.J, Khor K.A, Yu L.G. Preparation yttria-stabilized zirconia electrolyte by spark-plasma sintering. Material Sci. Eng. A. 2003; **341**: 43.
54. Takeuchi T, Tabuchi M, Kayeyam H. Preparation of dense $BaTiO_3$ Ceramics with submicrometer grain by spark plasma sintering. J. Am. Ceram. Soc. 1999; **82**: 939.
55. Shen Z, Johnsson M, Zhao Z, Nygren M. Spark Plasma Sintering of Alumina. J. Am. Ceram. Soc. 2002; **85**: 1921.
56. Harmer M.P, Brook R.J. Fast Firing - Microstructural Benefits. Tran. Br. Ceram. Soc. 1981; **80**:147.
57. Tokita M. Trends in Advanced SPS Spark Plasma Sintering Systems and Technology. J. Soc. Powder Tech. Jpn. 1993; **30**: 790.
58. Gao L, Shen Z, Miyamoto H, Nygren M. Superfast Densification of Oxide/Oxide Ceramic Composites.J. Am. Ceram. Soc. 1999; **82**: 1061.
59. Groza J.R, Zavaliangos A. Sintering activation by external electrical field. Mater. Sci. Engg. A. 2000; **287**: 171.
60. Omori M. Sintering and consolidation, reaction and crystal growth by the spark plasma system (SPS). Mater. Sci. Eng. A. 2000; **287**:183.

61. Herrman M, Rathel J, Schulz I. Spark Plasma Sintering/Field Assisted Sintering of ceramic materials. Inter. Ceram. 2009; **58**: 109.
62. Raethel J, Herrman M, Beckert W. Temperature distribution for electrically conductive and non-conductive materials during Field Assisted Sintering Technology (FAST). J. Eur. Ceram. Soc. 2009; **29:** 1419.
63. Ikegami T, Mori T, Yajima Y, Takenouchi S, Misawa T, Moriyoshi Y. Fabrication of transparent yttria ceramics through the synthesis of yttrium hydroxide at low temperature and doping by sulfate ions. J. Ceram. Soc. Jpn. 1999; **107**: 297.
64. Wen L, Sun X, Lu Q, Xu G, Hu X. Synthesis of yttria nanopowders for transparent yttria ceramics. Opt. Mater. 2006; **29**: 239.
65. Tsukuma K. Transparent $MgAl_2O_4$ ceramics produced by HIP post sintering.J. Ceram. Soc. Jpn. 2006; **114**:802.
66. Granger G. B, Guizard C, Miguel L. S. Sintering Behavior and Optical Properties of Yttria. J. Am. Ceram. Soc. 2007; **90**: 2698.
67. Bagayev S.N, Osipov V.V, Ivanov M.G, Solomonov V.I, Platonov V.V, Orlov A.N, Rasuleva A.V, Vatnik S.M. Fabrication and characteristics of neodymium-activated yttrium oxide optical ceramics. Opt. Mater. 2009; **31**: 740.
68. Mouzon J, Maitre A, Frisk L, Lehto N, Oden M. Fabrication of transparent yttria by HIP and the glass-encapsulation method. J. Euro. Ceram. Soc. 2009; **29**: 311.
69. Kim B.N, Hiraga K, Morita K, Yoshida H. Spark plasma sintering of transparent alumina. Scripta Materialia. 2007; **57:** 607.
70. Kim B.N, Hiraga K, Morita K, Yoshida H. Effects of heating rate on microstructure and transparency of spark-plasma-sintered alumina. J. Eur. Ceram. Soc. 2009; **29:** 323.
71. Suarez M, Fernandez A, Menendez J.L, Torrecillas R.Grain growth control and transparency in spark plasma sintered self-doped alumina materials. Scripta Materialia. 2009; **61**: 931.
72. Aman Y, Garnier V, Djurado E.Influence of green state processes on the sintering behaviour and the subsequent optical properties of spark plasma sintered alumina.J. Euro. Ceram. Soc. 2009; **29:** 3363.
73. Jiang D.T, Hilbert D.M, Tamburini U.A, Ng T., Land D, Mukherjee A.K.Optically Transparent Polycrystalline Al_2O_3 Produced by Spark Plasma Sintering. J. Am. Ceram. Soc. 2008; **91**: 151.

74. Chaim R, Shen Z, Nygren M. Transparent nanocrystalline MgO by rapid and low-temperature spark plasma sintering. J. Mater. Res. 2004; **19**: 2527.
75. Frage N, Cohen S, Meir S, Kalabukhov S, Dariel M.P. Spark plasma sintering (SPS) of transparent magnesium-aluminate spinel. J. Mater. Sci. 2007; **42**: 3272.
76. Wang C, Zhao Z. Transparent MgAl2O4 ceramic produced by spark plasma sintering, Scripta Materialia. 2009; **61**: 193.
77. Meir S, Kalabukhov S, Froumin N, Dariel M.P, Frage N. Synthesis and Densification of Transparent Magnesium Aluminate Spinel by SPS Processing. J. Am. Ceram. Soc. 2009; **92**: 358.
78. Morita K, Kim B.N, Hiraga K, Yoshida H. Fabrication of transparent MgAl2O4 spinel polycrystal by spark plasma sintering processing. Scripta Materialia. 2008; **58**: 1114.
79. Granger G. B, Benameur N, Guizard C, Nygren M. Inversion defects in $MgAl_2O_4$ elaborated by pressureless sintering, pressureless sintering plus hot isostatic pressing, and spark plasma sintering. Scripta Mater. 2009; **60**: 164.
80. Zhang G, Wang Y, Fu Z, Wang H., Wang W, Zhang J, Lee S.W, Niihara K. Translucent Mg-α-Sialon Ceramics Prepared by Spark Plasma Sintering. J. Eur. Ceram. Soc. 2009; **29**: 2705.
81. Chaim R., Kalina M., Shen J.Z. Transparent yttrium aluminum garnet (YAG) ceramics by spark plasma sintering. J. Euro. Ceram. Soc. 2007; **27**: 3331.
82. Mingsheng H, Jianbao L, Hong L, Gangfeng G, Long L. Fabrication of Transparent Polycrystalline Yttria Ceramics by Combination of SPS and HIP. J. Rare Earths 2006; **24**: 222.
83. Alaniz J.E, Gutierrez F.G.P, Aguilar G, Garay J.E. Optical properties of transparent nanocrystalline yttria stabilized zirconia J.E. Opt. Mater. 2009; **32**: 62.
84. Chaim R. Densification mechanisms in spark plasma sintering of nanocrystalline ceramics. Mater. Sci. Engg. A. 2007; **443**: 25.
85. Granger G. B, Guizard C. Spark plasma sintering of a commercially available granulated zirconia powder: I. Sintering path and hypotheses about the mechanism(s) controlling densification. Acta. Materialia. 2007; **55**: 3493.
86. Teng M.H. A computer program of master sintering curve model to accurately predict sintering results. Western pacific earth sciences. 2002; **2**:171.

87. Wang J, Raj R. Estimate of the activation energies for boundary diffusion from rate-controlled sintering of pure alumina, and alumina doped with zirconia or titania, J. Am. Ceram. Soc. 1990; **73**:1172.
88. Chu Y, Rahaman M.N, Jonghe L.C. De, Brook R.J. Effect of heating rate on sintering and coarsening. J. Am. Ceram. Soc. 1991; **74**: 1217.
89. Hansen J.D, Rusin R.P, Teng M-H, Johnson D.L. Combined-stage sintering model. J. Am. Ceram. Soc.1992; **75**:1129.
90. Su H, Johnson D.L. Master sintering curve: a practical approach to sintering. J. Am. Ceram. Soc. 1996; **79**: 3211.
91. Su H, Johnson D.L. A practical approach to sintering. Am. Ceram. Soc. Bull. 1997; **76**: 72.
92. DiAntonio C.B, Ewsuk K.G, Bencoe D. Extension of Master Sintering Curve Theory to Organic Decomposition. J. Am. Ceram. Soc. 2005; **88**: 2722.
93. Mandelson M. Average grain size in polycrystalline ceramics. J. Am. Ceram. Soc. 1992; **52**; 443.
94. Maeland D, Crina S, Ivar W, Alex C. Hoffmann. Sintering of 4YSZ (ZrO_2 + 4 mol% Y_2O_3) nano ceramics for SOFCs, their sintering and ionic conductivity. J. Euro. Ceram. Soc. 2009; **29**: 2537.
95. Shon I.J, Munir Z.A. Synthesis of $MoSi_{2-x}Nb$ and $MoSi_{2-y}ZrO_2$ composites by the field-activated combustion method. Mater. Sci. Eng. A. 1995; **202**: 256.
96. Tokita M. Development of Large-Size Ceramic/Metal Bulk FGM Fabricated by Spark Plasma Sintering. Mater. Sci. Forum. 1999; **83**: 308.
97. Chaim R. Superfast densification of nanocrystalline oxide powders by spark plasma sintering. J. Mater. Sci. 2006; **41**: 7862.
98. Risbud S.H, Shan C.H, Yamazaki K. Retention of nanostructure in aluminium oxide by very rapid sintering at 1150^{o}C. J. Mater. Res. 1993; **30**: 790
99. Wang X.Q, Xie Y.F, Guo H.L. Sintering of WC-Co powder with the nanocrystalline WC by spark plasma sintering. Rare Met. 2006; **25**:246
100. Omori M. Sintering, consolidation, reaction and crystal growth by the spark plasma system (SPS). Mater. Sci. Eng. A. 2000; **287**:183.
101. Demirsky D, Borodianska H, Grasso S, Sakka Y, Vasylkiv O. Microstructure evolution during field-assisted sintering of zirconia spheres. Scripta Materialia. 2011; **65**: 683.

102. Singhal C.S, Kendall K. High temperature solid oxide fuel cells: Fundamentals, design and application, Elsevier. 2003.
103. Frei J.M, Tamburini U.A, Munir Z. Current Effects on Neck Growth in the Sintering of Copper Spheres to Copper Plates by the Pulsed Electric Current Method. J. Appl. Phy. 2007; **101**: 11491.
104. Song X, Liu X, Zhang J. Neck Formation and Self-Adjusting Mechanism of Neck Growth of Conducting Powders in Spark Plasma Sintering. J. Am. Ceram. Soc. 2006; **89**: 494.
105. Granger G. B, Addad A, Fantozzi G, Bonnefont G, Guizard C, Vernat D. Spark Plasma Sintering of a commercially available granulated zirconia powder: comparison with hot pressing. Acta Materialia. 2010; **58**: 3390.
106. Granger G. B, Guizard C, Surble S, Baldinozzi G. Addad A. Spark plasma sintering of a commercially available granulated zirconia powder-II: Microstructure after sintering and ionic conductivity. Acta Materialia. 2008; **56**: 4658.
107. Gendre M, Maitre A, Trolliard G. A study of the densification mechanisms during spark plasma sintering (oxy) carbide powders. Acta Materialia. 2008; **58**: 2598.
108. Tamburini U. A, Garay J.E, Munir Z. A, Tacca A, Maglia F, Spinolo G. Spark plasma sintering and characterization of bulk nanostructured fully stabilized zirconia: Part I. Densification studies. J. Mater. Res. 2004; 19: 3255.

Chapter - IV

Electrical property Evaluation by Impedance Spectroscopy

4.0 Introduction

This chapter presents the attempts made to evaluate the ionic conductivity of zirconia samples densified to a minimum of 99 % of the theoretical density with diverse microstructures using different conventional sintering techniques such as Conventional Ramp and Hold Sintering (CRH), Two Stage Sintering (TSS) and non-conventional sintering techniques such as Microwave Sintering (MWS) and Spark Plasma Sintering (SPS) approaches. An attempt has also been made to correlate the ionic conductivity measured with the observed microstructures.

4.1 Impedance Spectroscopic technique

AC impedance spectroscopy is a valuable tool for studying both the bulk transport properties of a material and the electrochemical reactions on its surface [1-13]. Significance of the value of AC impedance spectroscopy derives from the effectiveness of the technique in isolating individual reaction/migration steps in a multi-step process. Typically, AC impedance experiments are carried out over a wide range of frequencies (several millihertz to several megahertz) and the interpretation of the resulting spectra is aided by analogy to equivalent circuits involving simple components such as resistors and capacitors. In general, such equivalent circuits are not unique and indeed there exists an infinite set of circuits that can represent any given impedance. It is common to select a physically conceivable circuit containing a minimal number of components and in a somewhat ad-hoc manner and a physical significance is assigned to the derived parameters. Often, a meaningful insight into material behavior can be gained from such analyses, which certainly explains the rise in popularity of impedance spectroscopy as a materials characterization tool. AC impedance analysis today regarded as one of the indispensable methods for evaluation of the cell performance and their components.

In the following section a simple one-one corresponding method is adopted to express the impedance of $Z(j\omega)$.

The AC response of any polycrystalline material and also of an electrolyte or electrochemical cell can be expressed in any of the four basic formulas [11, 12]. These are most conveniently expressed as:

$$\text{The complex impedance, } Z^* = Z' - iZ'' = R_s - j/\omega C_s \quad (4.1)$$

$$\text{The complex admittance, } Y^* = \frac{1}{Z^*} \quad (4.2)$$

$$\text{The complex permittivity, } \varepsilon^* = \varepsilon' - j\varepsilon'' \quad (4.3)$$

$$\text{The complex modulus, } M^* = (\varepsilon^*)^{-1} = M' + jM'' \quad (4.4)$$

Where, the subscripts p and **s** refer to the equivalent parallel and series circuit components respectively. These functions are separated into two groups, represents essentially parallel and series formulae. The two admittance functions are related as,

$Y^* = j\omega C_o \varepsilon^*$

Similarly the impedance functions are related as,

$M^* = j\omega C_o Z^*$,

Where, C_o is the vacuum capacitance of the cell.

Types of circuits in general are LCR, LR, LC and RC.

$$\text{Magnitude of impedance, } |Z| = \sqrt{(Z')^2 + (Z'')^2} = \sqrt{R^2 + (\omega L - \frac{1}{\omega C})^2} \quad (4.5)$$

where real (Z') and imaginary (Z'') parts of the impedance are determined by applying small sinusoidal voltage across the sample and measuring the amplitude and phase angle of the current in steady state condition.

$$\text{Specific Resistance of the material is } \rho = \frac{RA}{t} \quad (4.6)$$

$$\text{and Specific conductance is } \sigma = \frac{1}{\rho} = \frac{t}{RA} \quad (4.7)$$

where t is thickness of the electrolyte and A is the area of the electrolyte.

Every ceramic material is a combination of resistor or capacitor or resistor & capacitor. Combination of resistor and capacitor are parallel to each other and then it will result into a semicircle in the plots of real and imaginary parts of impedance (complex impedance plot). If the

centre of the semicircle lies on the real axis the capacitance effect will be seen, which indicates the uniform arrangement of grains in the material. If the centre of the semicircle lies below the real axis Constance Phase Element (CPE) should be taken at C, which indicates non uniform distribution of grains. Each semicircle is defined by single parallel RC circuit. Fig.4.1 shows the behavior of a polycrystalline material in terms of grain, grain boundary and electrode contributions by semicircular arcs [14,15].

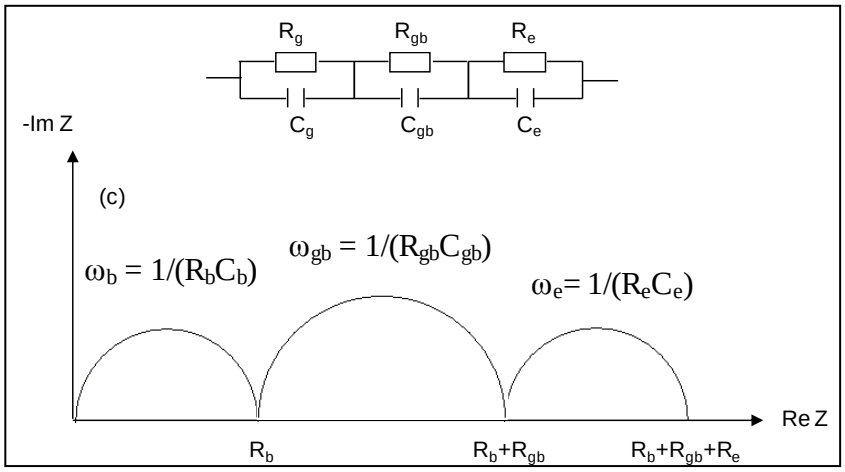

Fig.4.1 Complex impedance plot

Capacitance (C) value is considered where the complex plane impedance plot satisfies$2\pi f.RC = 1 = \omega\tau = 1$condition. This condition usually satisfies at the peak value of the semicircle. From the peak value capacitance can be evaluated.

The capacitance in the high frequency range will be in the order of $C = 10^{-12}\ to\ 10^{-9}$ F, which indicates grain contribution; $C = 10^{-10}\ to\ 10^{-8}$ F in the intermediate frequency range indicates grain boundary contribution, whereas at low frequency region $C = 10^{-6}\ to\ 10^{-3}$ F indicates electrode effect [16].

4.2 Sample Preparation

Sintered samples were ground and polished into discs of identical dimensions as shown in Table 4.1. The samples were screen printed on both sides with platinum paste to ensure good contact for the impedance measurements at high temperatures. Coated samples were examined under microscope to ensure the uniformity of coating and calcined at 850^{o}C for 30min in air to ensure

the binder removal and continuity. The samples were tested for their continuity of the coating surface using a multi-meter and further kept ready for impedance measurement.

Table 4.1 Details of the specimens subjected to impedance measurement

Sample Id	Sintering technique	Density (g/cc)	Theoretical Density (% TD)	Average grain size (µm)	Dimensions	
					Dia. (mm)	Thickness (mm)
1	CRH	5.867	99.44	4.67	11.39	0.705
2	TSS	5.865	99.40	2.64	11.15	0.702
3	MWS	5.850	99.15	3.70	11.21	0.705
4	SPS	5.870	99.50	1.16	10.42	0.702

4.3 Impedance Measurement Set-Up

An Impedance analyzer (Solartron SI1260, Ametek, Inc., Hampshire, UK) with hot stage facility is used for this study. Analyzer consists of sample holder, which is specially designed for screening of various SOFC components. The system is also provided with a split furnace which can be heated from RT to 1000°C. The furnace temperature is controlled by an Eurotherm controller, interfaced with the impedance analyzer. The entire system is computer controlled and the data acquisition and analysis is carried out using the SMART software. The analyzer is designed to measure various parameters such as, impedance (real and imaginary), admittance (real and imaginary), permittivity (real and imaginary), modulus (real and imaginary) and capacitance with at a frequency of 0.1 Hz to 10 MHz and at temperatures RT - 1000°C. The impedance measurement set-up is shown in Fig.4.2.

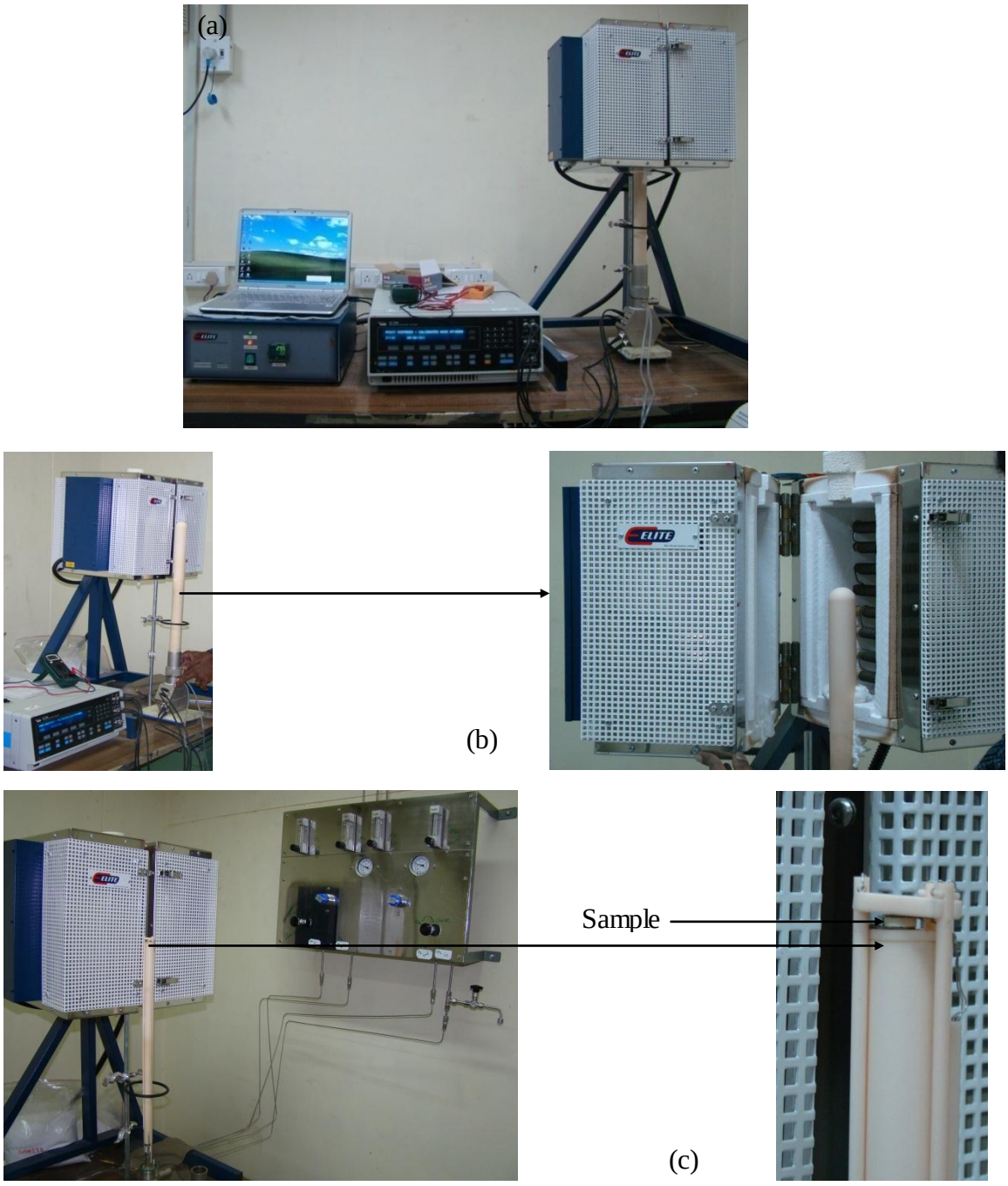

Fig.4.2 Impedance measurement set-up (Solartron SI1260, Ametek, Inc., Hampshire, UK) b) Furnace c) sample holder

4.4 Impedance measurements

Electrolyte coated with platinum paste on both sides and the sample is placed in the sample holder assembly are shown in Fig.4.3. Impedance was measured between 300°C and 800°C at 50°C increments with a computer aided data acquisition system using SMART software.

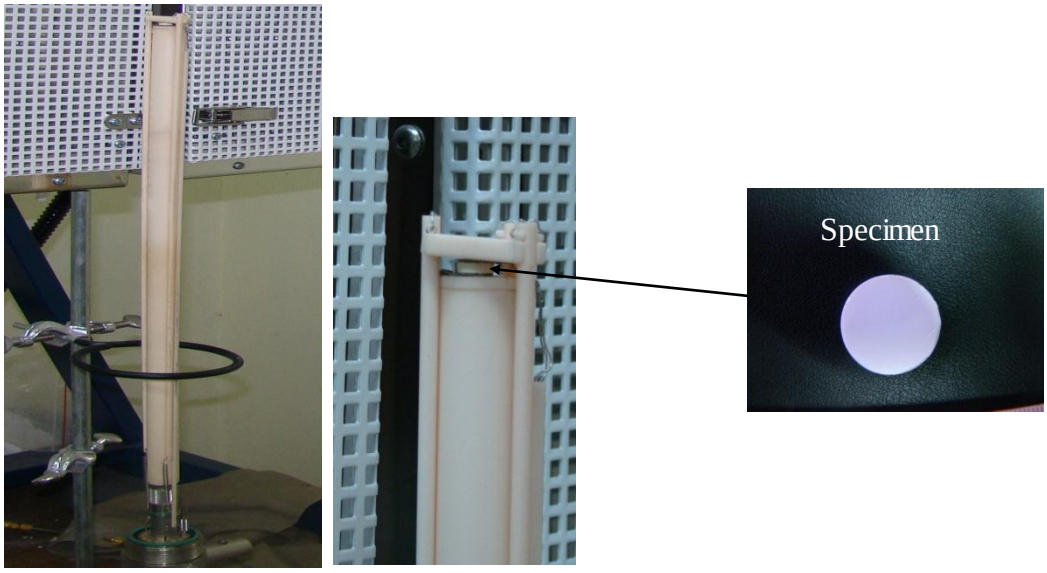

Fig.4.3 Sample holder assembly with sample

Impedance measurements were carried out in the frequency range varying from 0.1Hz to 10MHz and at applied AC amplitude of 100mV.Typical complex impedance plane plots(real part of impedance (Z′) vs. imaginary part of impedance (Z′′)), recorded at temperatures 300, 400, 600, 700 and 800°C for the CRH, TSS, MWS and SPS samples are shown in Fig.4.4(a-e).

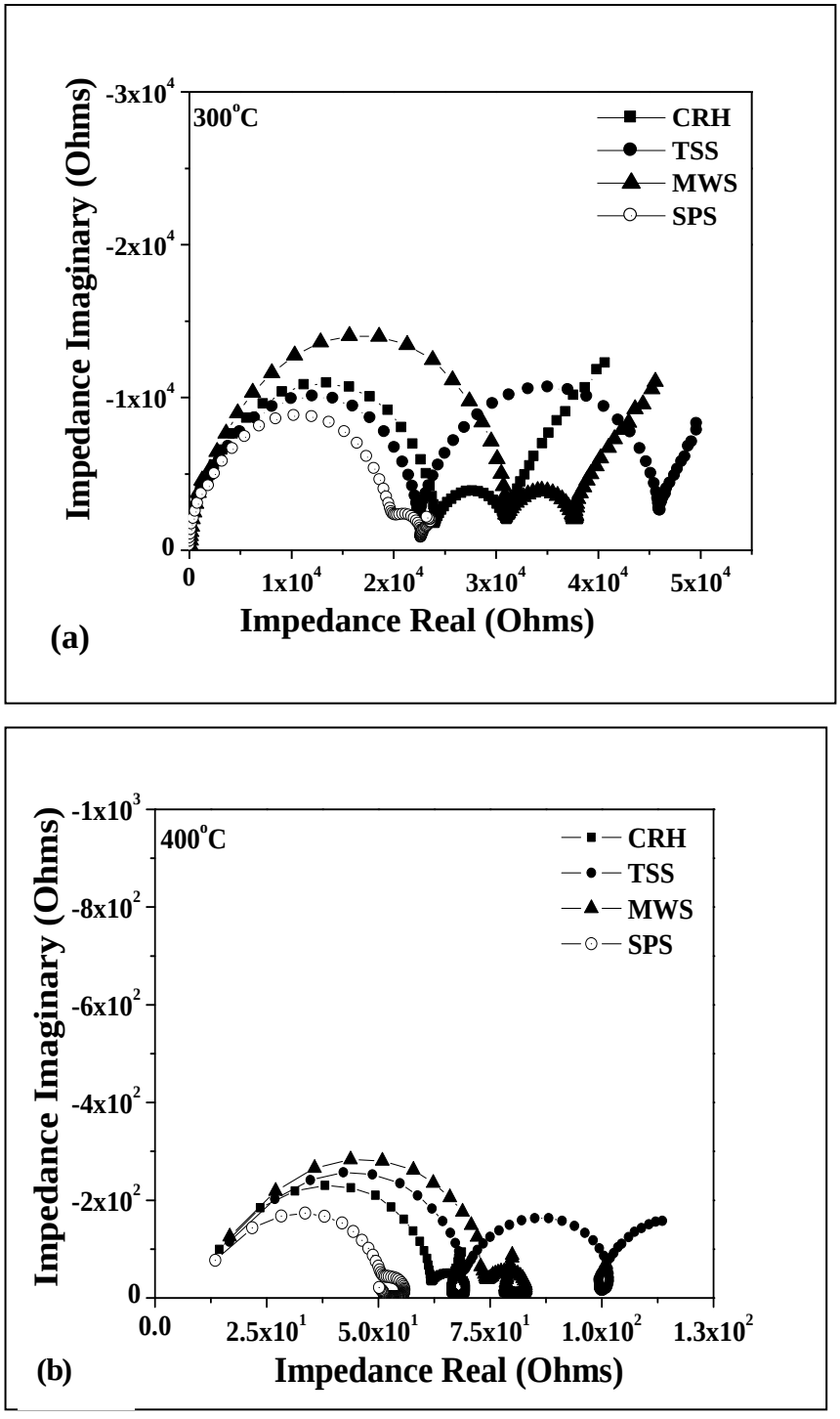

Fig. 4.4 (a-b)Complex impedance plane plots of CRH, TSS, MWS and SPS specimens at the temperature interval 300°C - 400°C

.

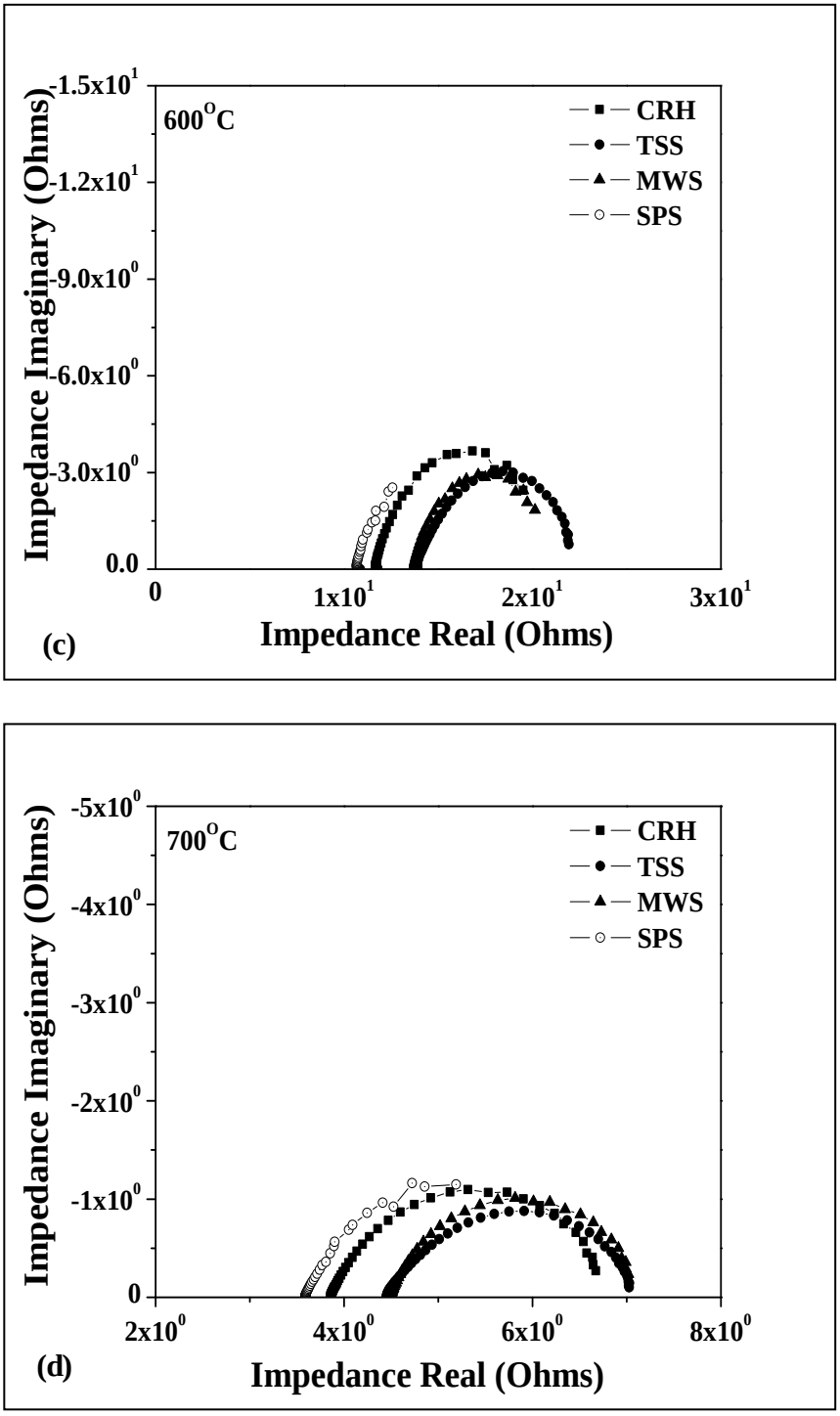

Fig. 4.4 (c-d)Complex impedance plane plots of CRH, TSS, MWS and SPS specimens at the temperature interval 600°C - 700°C

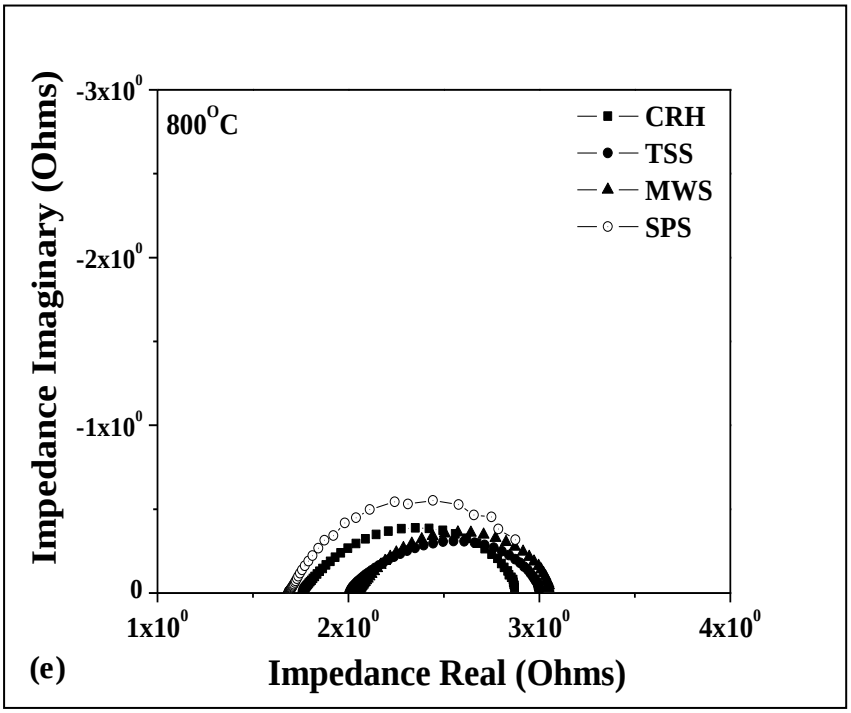

Fig.4.4(e)Complex impedance plane plots of CRH, TSS, MWS and SPS specimens at the temperature 800°C

The plots show semicircles for all the samples at all temperatures and the contribution of grain interior and grain boundaries can be distinguished clearly. The curve observed at low frequency region corresponds to electrolyte/electrode interface. A difference in diameter of the high and mid frequency semicircles are clearly observed for the samples processed via different sintering routes, indicating a different rate of oxygen ion/vacancy migration in the grain and grain boundary regions. At low temperatures (300°C) grain, grain boundary and electrode contributions are clearly separated in case of CRH, TSS, MWS and SPS samples. It is evident from the plots that specimens processed through CRH, MWS and SPS have exhibited lower grain boundary resistances than grain resistance.

Grain, grain boundary and total resistances of the samples were measured from Cole-Cole plots at different temperatures and the ionic conductivities of CRH,TSS, MWS and SPS samples were calculated using,

$$\sigma = \frac{1}{\rho} = \frac{t}{RA}$$

where σ is ionic conductivity, t is thickness of the electrolyte and A is the active surface area of the electrolyte. The data of ionic conductivities of the samples in the temperature region 300-800^{o}C are shown in Table 4.2

Table 4.2 Ionic conductivities of the specimens in the temperature range 300-800°C

Sp. Id	**Sintering technique**	**Density (g/cc)**	**Average grain size (μm)**	**Ionic Conductivity (S/cm)**				
				300° C	**400° C**	**600° C**	**700° C**	**800 ° C**
1	CRH	5.867	4.67	4.0×10^{-6}	1.4×10^{-4}	0.0015	0.036	0.094
2	TSS	5.865	2.64	1.0×10^{-6}	1.2×10^{-4}	0.0110	0.033	0.090
3	MWS	5.850	3.70	6.6×10^{-6}	1.9×10^{-4}	0.0010	0.029	0.088
4	SPS	5.870	1.16	7.0×10^{-5}	4.0×10^{-4}	0.0196	0.052	0.134

Highest ionic conductivity of 0.134 S/cm at 800^{o}C is observed for SPS sample sintered at 1325^{o}C with grain size of 1.16μm. The conductivity of SPS sample sintered at 1325^{o}C in the present study exhibited a relatively higher value in comparison to the 0.105 S/cm reported by Chen et al (2002) and 0.118 S/cm reported by Zha et al. (2003)in earlier studies [17, 18]. This relatively low ionic conductivity observed with the above reports can be attributed to the low density values (97.6%TD) though the finer grain sizes could be achieved. Dahl et al. [19] also reported relatively low ionic conductivity of spark plasma sintered 8YSZ around 0.082 S/cm at 900^{o}C even with the smaller average grain size of 210 nm in comparison to the presently reported value of 0.134 S/cm. The higher value obtained in the present study can be attributed to the high density of > 99 % of TD achieved through SPS sintering in comparison to the 96 % reported by the above study. Ionic conductivity of 8YSZ electrolyte sintered through all other sintering techniques such as CRH, TSS and MWS were found to be in the range of ~0.09 S/cm which is close to the conductivity of 8YSZ ceramics reported earlier [20, 21]. Further, Hesabi et al. [22] also reported ionic conductivity value of 0.132 S/cm at 900^{o}C for two step sintered specimens with average grain size of 0.9 μm and density of 98% TD. The present study demonstrates an ionic conductivity of 0.09S/cm for 8YSZ samples but at a relatively low

temperature of 800°C. It may be noted that though samples sintered by CRH, TSS, MWS could be sintered to > 99%TD in the present study the ionic conductivity values are lower because of the higher grain sizes which inherently occurs with high density values. Thus a combination optimum density and grain sizes will enhances the ionic conductivity values as revealed through the SPS studies.

Guo and Waser [23] reviewed several acceptor-doped zirconia and reported that the specific grain boundary conductivity increases as the grain size decreases into the nanocrystalline regime, while the grain core conductivity decreases slightly. Verkerk et al. [24] found increasing specific grain boundary conductivity with decreasing grain size in microcrystalline 8 mol% Y_2O_3- doped ZrO_2, but only at large grain sizes. The most dramatic result was that of Kosacki et al. [25], who showed a 1–2 order of magnitude increase in the total conductivity in spin-coated YSZ thin films with ~20 nm grain size versus a polycrystalline bulk sample with large grains (2.4 μm). Guo et al. [26-28] reported an analysis of the contributions of grain and grain boundaries to the total electrical conductivities of stabilized zirconia. The grain boundaries constituting the core (crystallographic mismatch zone) and space charge regions in stabilized zirconia impede ionic transport across them. The grain boundary resistivity is normally several orders of magnitude greater than the grain resistivity. The resistive grain boundaries have been linked to the impurities, particularly the siliceous phase, for a long time. But even in highly pure stabilized zirconia, the grain boundary resistivity was still found to be several orders of magnitude greater than the grain resistivity. It is also reported that the grain boundary resistivity can be correlated on the basis of space charges and depletion of oxygen vacancies in the vicinity of grain boundaries [28, 29].

Though an increased conductivity with decreased grain size was reported by several workers the grain-boundary conductivity is still lower than the bulk conductivity, even when the grain size is as small as in nm ranges [30]. In view of this the grain-boundary transport becomes especially important for nano-structured materials due to their high proportion of grain-boundary area. Thus, the benefits of small particle sizes in reducing processing temperatures must be balanced against increased grain-boundary resistance, particularly at lower operating temperatures.

Out of the four samples subjected to impedance analysis, SPS sample has shown low grain and grain boundary resistances as evidenced by high ionic conductivity values (Table 4.2 and Fig.4.4 (a)). The total resistivity of SPS sample sintered at 1325^{o}C (1.3x10$^{4}\Omega$-cm) as evidenced by the plot is significantly lower, when compared to TSS, CRH and MWS samples, where the values are in the order of 1-5 x10$^{5}\Omega$-cm. The impedance spectra indicate that the grain boundary resistivity is extremely small in SPS sample. It can be inferred that 8YSZ electrolyte prepared by spark plasma sintering process is favorable to improve electrical conductivity. Further with the increase of temperature, the grain and grain boundary resistivity decreased in all the samples tested under the present study. The TEM studies carried out in the earlier session revealed a clean grain boundary without any segregation due to the low sintering temperatures under the application of pressure. Further the interface patterns revealed the moiré fringes due to aligned dislocation densities, which are expected to increase the ionic conductivity. Hence it can be stated that the improved ionic conductivity observed with SPS samples can be not only attributed to the finer grain size and density values but also to the unique mechanisms that operative during SPS process.

4.5 Separation of Grain and Grain boundary Conductivities

As all the specimens are densified to >99 % of the theoretical density, the resistance offered by the grain boundary becomes critical and is determined by its area and the oxygen ion concentration. It is well known that the general grain conductivity is higher by two to three times than the grain boundary conductivity. Table 4.3 gives grain boundary conductivities of all the samples at 800^{o}C. Grain boundary conductivities are found to increase with temperature because the segregation at the grain boundary is low due to the low exposure temperature in case of TSS. Exposure to high temperature and dwell time at peak temperatures have clear effect on observed ionic conductivity at 800^{o}C. The CRH samples are exposed to 1525^{o}C for a period of 2h. However, in the case of TSS and MWS the dwell times are 5 and 10 minutes respectively at 1525^{o}C. The longer dwell times is expected to cause segregation of impurities. Accordingly the ionic conductivity at 800^{o}C is maximum for TSS sample followed by MWS and for CRH signifying the segregation effects. In the case of SPS samples, the temperatures are low and the dwell time is only 5 minutes which is responsible for no or minimum segregation leading to the highest ionic conductivity observed.

Table 4.3 Specific grain boundary conductivities of the specimens

Sp.Id	Sintering technique	Specific grain boundary conductivity (S/cm) at 800°C
1	CRH	3.6×10^{-4}
2	TSS	7.7×10^{-4}
3	MWS	5.4×10^{-4}
4	SPS	3.3×10^{-3}

4.6 Comparative ionic conductivity of SPS sample sintered at 1325°C and 1425°C

Based on the high ionic conductivity exhibited by the SPS sample an additional experiment was carried out by sintering of specimens at a high temperature of 1425°C intentionally growing the grain. Impedance measurements were carried out as described above and the sintering parameters along with the density and average grain sizes and the conductivity are given in Table 4.4. Cole-Cole plots of SPS samples sintered at 1325 and 1425°C are shown in Fig.4.5.

Table 4.4 Sintering parameters and results of the of SPS sintered 8 YSZ specimens

Sintering parameters	Density (g/cc)	% Theoretical density	Average grain Size (μm)	Total Ionic Conductivity (Scm^{-1}) at 800°C
1325°C/5min	5.870	99.50	1.16	0.134
1425°C/5min	5.870	99.50	8.80	0.103

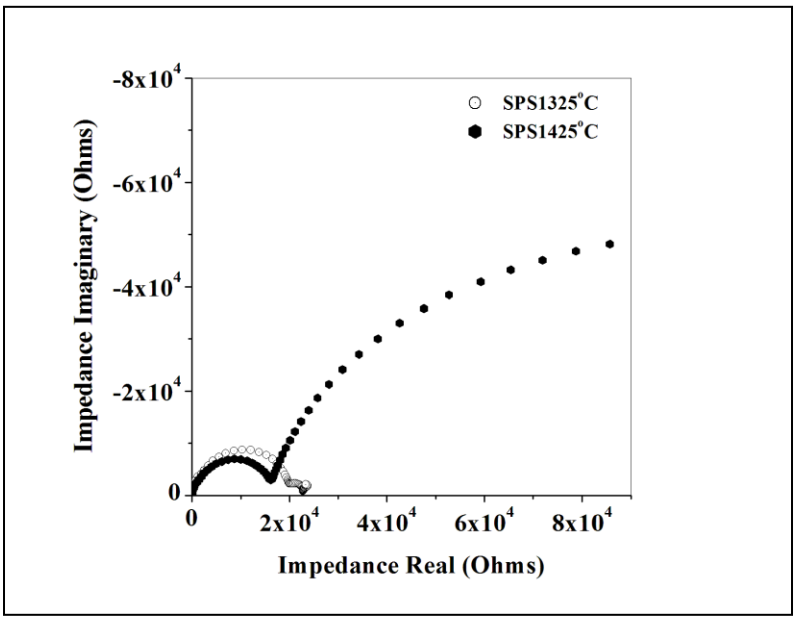

Fig. 4.5 Cole-Cole plots at 300°C of SPS sintered 8YSZ samples

At 300°C, the grain boundary resistivity of SPS sample sintered at 1325°C is $1.3x10^4\Omega$-cm, while the SPS sample sintered at 1425°C shown a resistivity of $6.11x10^5\Omega$-cm. Therefore, improvement of grain boundary ionic conductivity is very important for the development of SOFC electrolytes.

4.7 Estimation of blocking factor

Fig.4.6 shows the equivalent circuit for 8YSZ electrolyte which is composed of two parallel RC circuits, where the resistance R_g denotes the grain resistance and R_{gb}, grain boundary resistance. The corresponding capacitances of grain and grain boundary are C_g and C_{gb}.

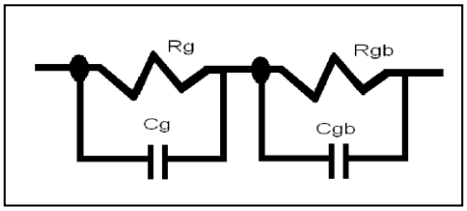

Fig.4.6 Equivalent circuit of 8 YSZ sample

The influence of the grain boundary conductivity in the total conductivity can be evaluated through the blocking factor (α_R), [21, 24] defined from the impedance diagram parameters as:

$$\alpha_R = R_{gb}/(R_g + R_{gb}) \quad (4.8)$$

where, R_g and R_{gb} are grain and grain boundary resistivity respectively. This factor gives the fraction of the electric carriers being blocked at the impermeable internal surfaces (grain boundary), under the measuring conditions, with respect to the total number of electric carriers in the sample. Table 4.5 shows the blocking factor at 800^{o}C for all the compositions. The lowest blocking factor was observed in SPS sample at 800^{o}C and also for all ranges of temperature. The assumption is that the observed blocking effect in stabilized zirconia results directly from the formation of blocked zones, where electric carriers are trapped and do not contribute to the transport of electric current. These results suggest that the SPS promotes grain boundary conduction and in turn the total conduction in 8YSZ [31].

Table 4.5Blocking factor (α_R) measured at 800^{o}C for 8YSZ samples sintered through different sintering methods

Sintering technique	**α_R at 800^{o}C**
CRH	0.38
TSS	0.33
MWS	0.32
SPS-1325	0.26
SPS-1425	0.29

The high bulk ionic conductivity of SPS sintered sample in the present study can be attributed to the decrease in grain and grain boundary resistances which is further supported by lower blocking factor (α) of 0.26-0.29 measured at 800^{o}C though the grain sizes have increased to 8.8μm almost two times in comparison to the CRH sample the ionic conductivities are close to the conventionally sintered samples. This indicates that the grain sizes when enhanced to the higher values (> 2.67μm) have minimum effect on ionic conductivity though a low blocking

factor is observed. Earlier studies attributed the lower grain boundary conductivity to the segregation of a blocking layer with space charges (for oxygen ion conduction) which decreases the oxygen ion conduction due to the reduced oxygen vacancy concentration at the grain boundary compared to that in the grain interior [32-34].

4.8 Estimation of activation Energies

The grain resistance (R_g), grain boundary resistance (R_{gb}) and total resistance were measured from the intersecting points of the semicircles on the real axis. Grain and grain boundary conductivities were calculated from the Cole-Cole plots at various temperatures for the CRH, TSS, MWS and SPS samples and plotted against the operating temperature regime as shown in Fig.4.7 (a-c).

The activation energy of conductivity is an important index to evaluate the electrical conductivity of electrolyte materials. The lower the activation energy, higher is the electrical conductivity. The activation energies of total bulk conductivity for various samples were calculated by fitting the data to the Arrhenius relation for thermally activated conduction which is given as,

$$\sigma = \frac{\sigma_0}{T} \exp(-E_A/kT) \tag{4.9}$$

where, E_a is the activation energy for conduction, T, the absolute temperature, k the Boltzmann's constant (k=1.23 x 10^{-23} J/sec)and σ_o the pre-exponential factor. The linear fit is applied for the conductivity data using least square fitting technique. The Arrhenius plots of the electrical conductivity with T are nearly linear for all the samples, which indicates that the relationship between ionic conductivity (σ) and temperature (T).

The activation energies were found to be lower (0.68 eV) for SPS, as expected, in comparison to 0.79eV, 0.99eV and 0.71eV for CRH, TSS and MWS samples respectively. Thus sintering methodology affects conductivity and activation energy.

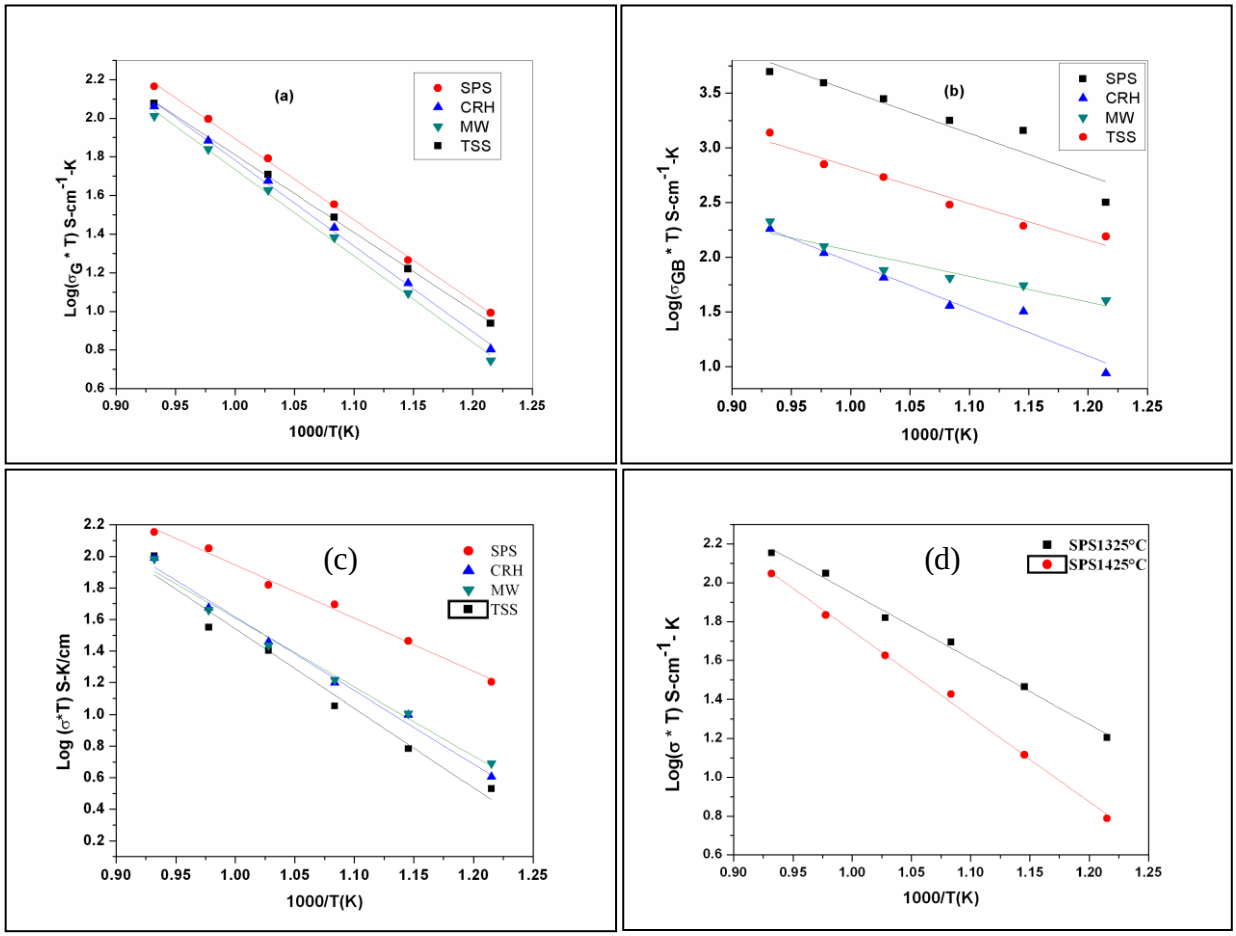

Fig.4.7 (a-c) Arrhenius plots for the grain, grain boundary and total conduction of 8YSZ samples of different sintering techniques (d) Arrhenius plots for 8YSZ sintered by SPS at 1325^{o}C and 1425^{o}C

---

1. **Studies on Ionic conductivity of Stabilized Zirconia Ceramics (8YSZ) densified through Conventional and Non-Conventional Sintering Methodologies.**
   Published in Ceramics International 37 (2011) 3557-3564.

2. **Ionic conductivity of 8 Y Stabilized Zirconia Ceramics Densified through Conventional and non-Conventional Sintering Methodologies.**
   Poster presentation, National Symposium on Energy Environment: Ceramics, Annual Technical Session of Indian Ceramic Society, 2011, Kolkata.

In order to study the effect of nanostructured sintered 8YSZ electrolyte produced out of ultrafine 8YSZ powder procured from MK nano (Refer Fig. 3.53(a), session 3.3.5.2 in Chapter III) were subjected to impedance analysis under identical condition as described above. The microstructure with an average grain size of 80nm and the typical Cole - Cole plot recorded at 325^{o}C are shown in Fig.4.8. The ionic conductivity values are estimated from the Cole - Cole plot and are presented in Table 4.6.

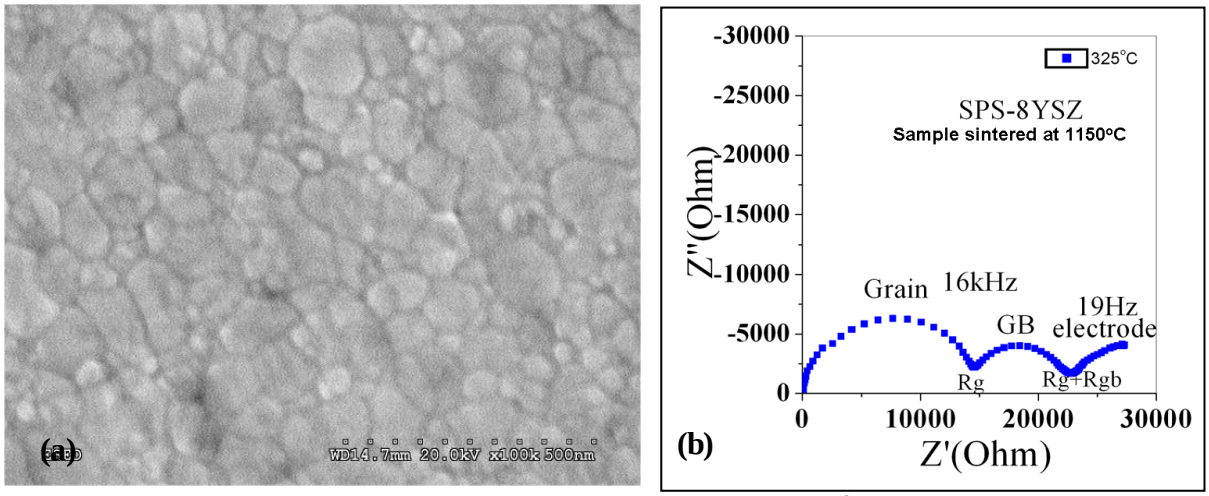

Fig. 4.8 (a) Micrograph of 8YSZ SPS sample sintered at 1050^{o}C and (b) Cole – Cole plot at 325^{o}C (MKnano powder)

Table 4.6Sintering parameters and results of the of SPS sintered 8YSZ specimens (MKnano)

Sintering parameters	Density (g/cc)	%Theoretical density	Average grain Size (nm)	Total Ionic Conductivity at 800° C(S/cm)
1050°C/5min	5.870	99.50	80	0.14

The ionic conductivity value of 0.14S/cm was observed with nanostructured sintered specimens against 0.134S/cm observed with specimens having grain sizes of 1.16µm (Refer Table 4.4). Though the 8YSZ samples could be sintered to 80nm the increase in ionic conductivity is only marginal, this may be due to the purity issues associated with the starting raw material.

---

1. **Effect of Nano Grain Size on the Ionic Conductivity of Spark Plasma Sintered 8YSZ Electrolyte. Published in International Journal of Hydrogen Energy 2011.**
2. **Microstructure and Ionic Conductivity Correlation of Nano-Structured 8 Y Zirconia Ceramics Sintered through Spark Plasma Sintering, Poster presentation, Annual Convention of Indian Ceramic Society, 2011, Agra.**

4.9 Fabrication of Single Cell

For the fabrication of the cell the SPS sintered samples of 8YSZ Tosoh 1.16µm grain size which have exhibited an ionic conductivity of 0.134S/cm in comparison to 0.09S/cm observed with other sintering techniques. The various anode and cathode materials and fabrication process are as follows.

4.9.1 Procurement of standard NiO- 8YSZ Anode Materials

Standard nickel oxide: zirconia anode powder procured from M/s. Nextech, USA is used as anode material in the present study. Specification of the powder as reported by the supplier is shown in Table 4.7.

Table 4.7 Specification of NiO- 8YSZ anode powder

Sr. No.	Property	Values
1	NiO	66wt%
2	8YSZ	34wt%

4.9.1.1 Sintering studies on nickel oxide: 8YSZ anode powder

In order to optimize the sintering schedule the compacts were prepared as per the flow chart depicted in Fig 4.9. The powder was granulated and then compacted using a die under a compaction pressure of 5tonne. The samples were characterized for their green densities and presented in Table 4.7. The samples were further sintered at four temperatures in a laboratory furnace at 1300, 1325, 1350 and 1380^{o}C. The sintered samples were characterized for their sintered density and porosity are also shown in Table 4.8.

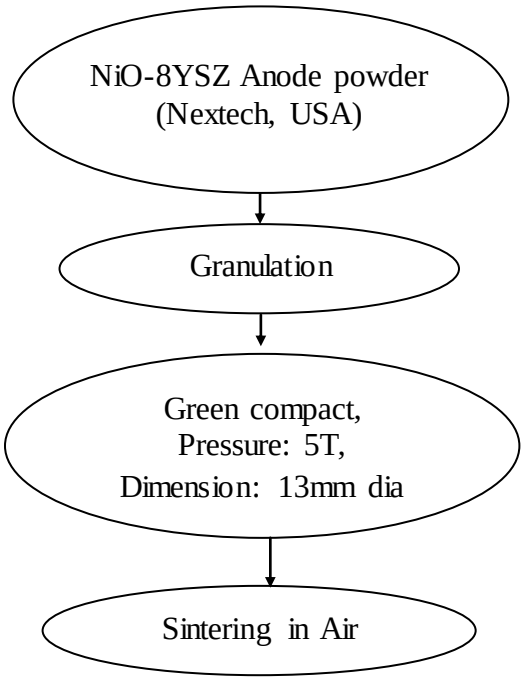

Fig.4.9 Process Flow chart for the processing of NiO-8YSZ Compacts

Table 4.8 Sintering studies of NiO-8YSZ anode

S. No	Compaction Pressure (tonne)	Green Density (g/cc)	Sintering Temperature (°C)	Sintered Density (g/cc)	Porosity (%)
1	5.0	4.22 (65.99%TD)	1300	5.14 (80% TD)	21.89
2	5.0	4.22 (65.99%TD)	1325	5.22 (81.24%TD)	21.38
3	5.0	4.22 (65.99%TD)	1350	5.40 (84.04%Td)	20.37
4	5.0	4.22 (65.99%TD)	1380	5.45 (84.82%TD)	13.07

4.9.1.2 Reduction of nickel oxide: 8YSZ Compacts

It is necessary to reduce the sintered NiO-8YSZ compacts to Ni- 8YSZ under hydrogen for the successful use as SOFC anode material. NiO-8YSZ compacts were sintered under flowing

hydrogen at 800°C for 1hr in a hydrogen sintering furnace. During the reduction, in addition to changes in the chemical composition to Ni-based cermet and the porosity of the anode samples changes as well as the specific volume of metallic Ni is significantly smaller than that of NiO. Radovic et al., [35] assuming that the decrease of the overall volume of anode samples after reduction is negligible, and then the following expression can be derived for the porosity of the anode sample after reduction, p, as a function of initial porosity before reduction, p_0:

$$p = p_0 + (1 - p_0).\bar{m}^0_{NiO} .\left[\frac{1}{\rho_{NiO}} - \frac{1}{\rho_{Ni}} + \frac{m_0}{m_{NiO}}.\frac{1}{\rho_{Ni}}\right] \quad (4.10)$$

where ρ_{Ni} and ρ_{NiO} are the density of Ni and density of NiO, respectively. $\bar{m}^0_{NiO}$ is the initial weight fraction of NiO in the NiO-YSZ composite. For the examined was $\bar{m}^0_{NiO} = 0.587$, for $\rho_{Ni} = 8.88\ g/cc$ and $\rho_{NiO} = 6.67 g/cc$ equation (1) yields:

$$p = 0.228 + 0.772 p_0 \quad (4.11)$$

Porosity values are calculated accordingly and along with the measured values by water immersion method by Archimedes principle are presented in Table 4.9. It is evident that measured porosity and calculated porosity are in good agreement indicating the complete reduction and formation of the cermet. In case of initial porosity of ~22% to ~38% after hydrogen reduction is reported to be suitable for increased catalytic activity. It is reported that in Ni/8YSZ cermet material, 8YSZ is an ionic conductor and Ni is an electronic conductor. In a simple diphase system the theory predicts the percolation threshold of ~30vol% of the higher conducting phase for the transition from dominant ionic conductivity to dominant electronic conductivity. This is generally true for the electronic conductivity of the composite Ni/8YSZcermet systems. Since the electronic conductivity of Ni is more than 5 orders of magnitude greater than that of 8YSZ under the fuel cell operating conditions, the electrical conductivity of a porous Ni-8YSZ cermet anode changes several orders of magnitude, usually from ~0.1 S/cm to the range of ~10^3, as the Ni to 8YSZvolume ratio varies across the percolation threshold, which depends on the morphology, particle size, and distribution of each phase: Ni, 8YSZ and pores. Dees et al. [36] studied the relationship between the electrical conductivity and the volume fraction of Ni in the Ni/8YSZ cermet measured at 1000°C and showed that the rapid rise in the electrical conductivity corresponds to a ~30vol% of Ni in the cermet.

Table 4.9 Density and porosity of Ni-8YSZ anode after reduction

S. No	Sintered Density of $NiO-ZrO_2$ (g/cc)	Initial Porosity (%)	After reduction in H_2 at 800°C	
			Measured Porosity (%)	Calculated Porosity (%)
1	5.14(80.00% TD)	21.89	37.83	39.69
2	5.22 (81.24%TD)	21.38	37.40	38.30
3	5.40 (84.04%TD)	20.37	35.70	38.80
4	5.45 (84.82%TD)	13.07	33.83	32.89

Microstructure of samples before and after reduction is carried out by SEM and is shown in Fig.4.10 along with pellets before and after reduction. It is evident that the microstructure complements with the density and porosity measurements.

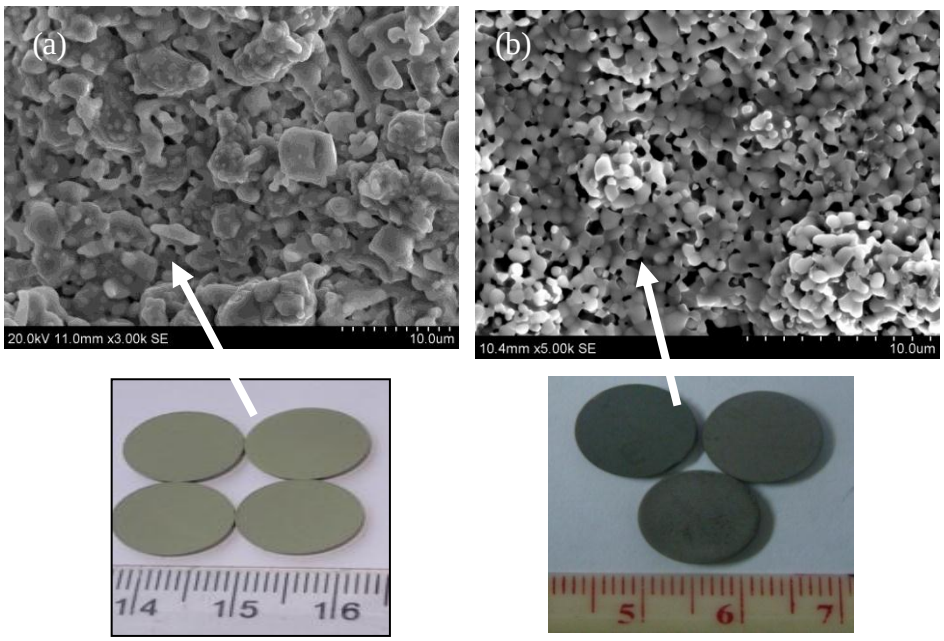

Fig. 4.10 (a) NiO – 8YSZ(sintered) and (b) Ni- 8YSZ pellets (H_2 reduced) and corresponding microstructures

4.9.2 Procurement of Standard Lanthanum Strontium Manganese Oxide Cathode Paste

Standard Lanthanum Strontium Manganese Oxide **(**LSM) paste, procured from M/s. Nextech, USA is used as cathode material in the present study. Specification of the powder reported by the supplier is shown in Table 4.10.

Table 4.10 Specifications of LSM cathode Paste

Sr. No.	Property	Value
1.	Composition	LSM: $(La_{0.80}Sr_{0.20})MnO_{3-\delta}$
2.	Crystal structure	Single Phase Perovskite
3.	Surface area	4-8m^2/g
4.	Particle size	0.3-0.6 microns
5.	Electrical conductivity	σ>200 S/cm @800°C
6.	Thermal expansion	10-11x 10^{-6}/°C

Cathode paste is ready to apply to the zirconia electrolyte by screen printing as per the standard procedures followed by sintering at 1300°C to form cathode suitable for SOFC applications as specified by the supplier.

4.9.3 NiO -8YSZ anode and LSM Cathode Coating on SPS Sintered Electrolyte

LSM paste / NiO - 8YSZ powder with above characteristics were subjected to coating by screen printing. Screen printing and subsequent firing method is a fairly simple method for depositing a green layer of ceramic paste on to the electrolyte and to produce electrodes with low polarization resistances [37].Subsequent to the screen printing, sintering steps are needed to densify the layers or to consolidate them to achieve good contact and bonding between the particles. Screen printing machine (Hongyan Industry Co. Ltd., China) was used in the present study is shown in Fig.4.11.

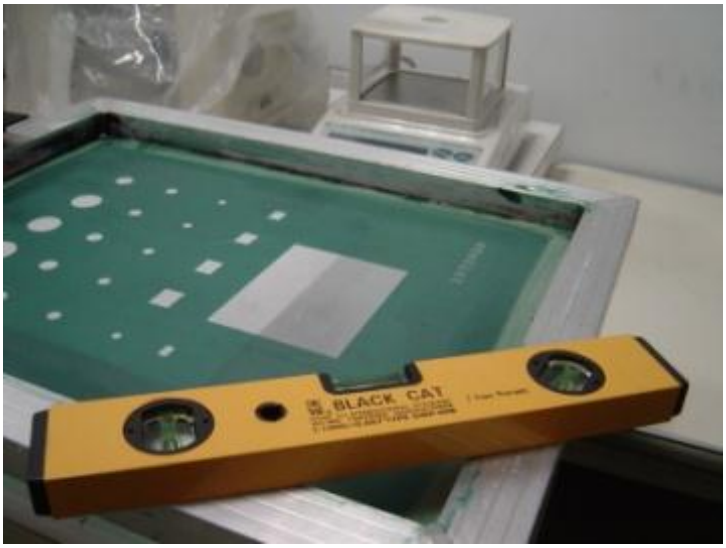

Fig.4.11 Screen printing unit

NiO - 8YSZ anode has made into a consistent paste using terpineol and methyl cellulose and screen printed on SPS sintered electrolytes and is fired at optimized temperature of 1350^{o}C for 2hours followed by the reduction in hydrogen at 800^{o}C.

NiO – 8YSZanode coated SPS sintered electrolytes are painted with platinum paste in the form of mesh and are fired at specified temperature of 900^{o}C for 1hr are shown in Fig. 4.12.

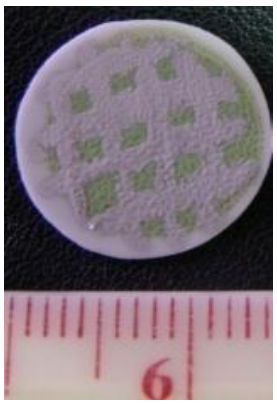

Fig.4.12 NiO – 8YSZ anode material screen printed on 8YSZ sintered electrolyte

SEM micrograph of the fractured cross section of the coated sample after reduction is shown inFig.4.13. It is evident that the microstructure component is porous as observed in the optimization studies (Fig.4.10).

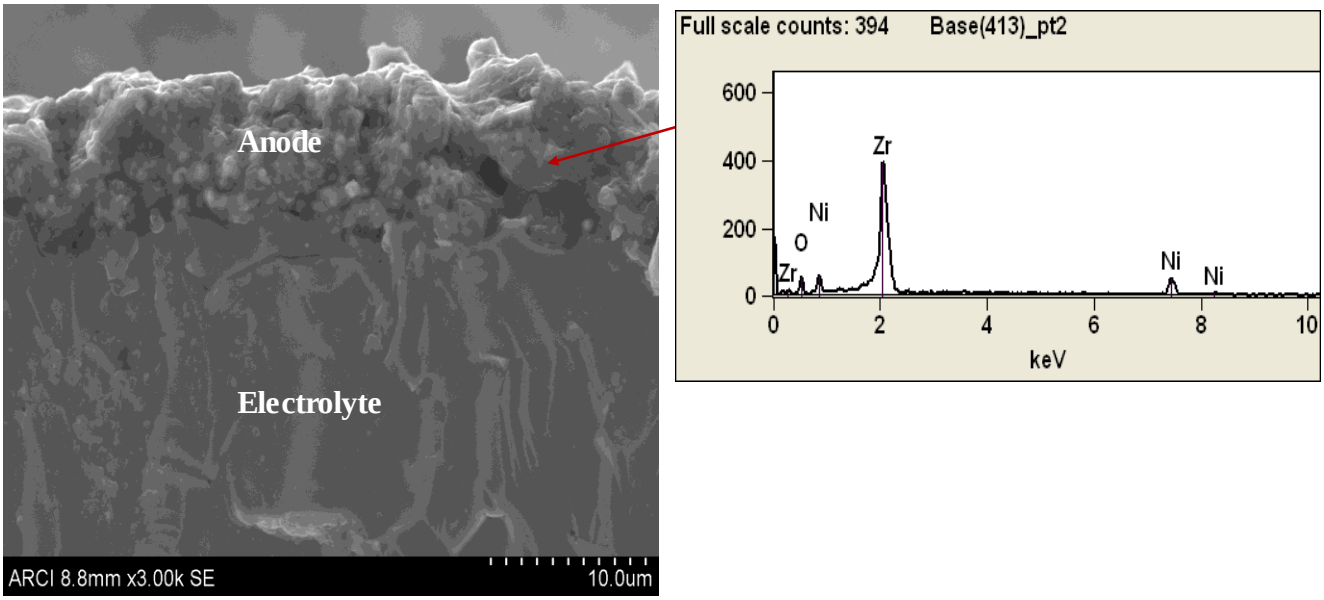

Fig.4.13Micrograph of cross section of the electrolyte with anode coating

Ready to apply LSM paste is screen printed on other side of the SPS sintered electrolytes one side coated with NiO-8YSZ (Fig 4.14(b)) and is fired at optimized temperature of 1300^{o}C for 2 hours to form the porous cathode coating. Microstructure of the coated sample after sintering is carried out by SEM analysis and is shown in Fig. 4.14(c) along with pellets.

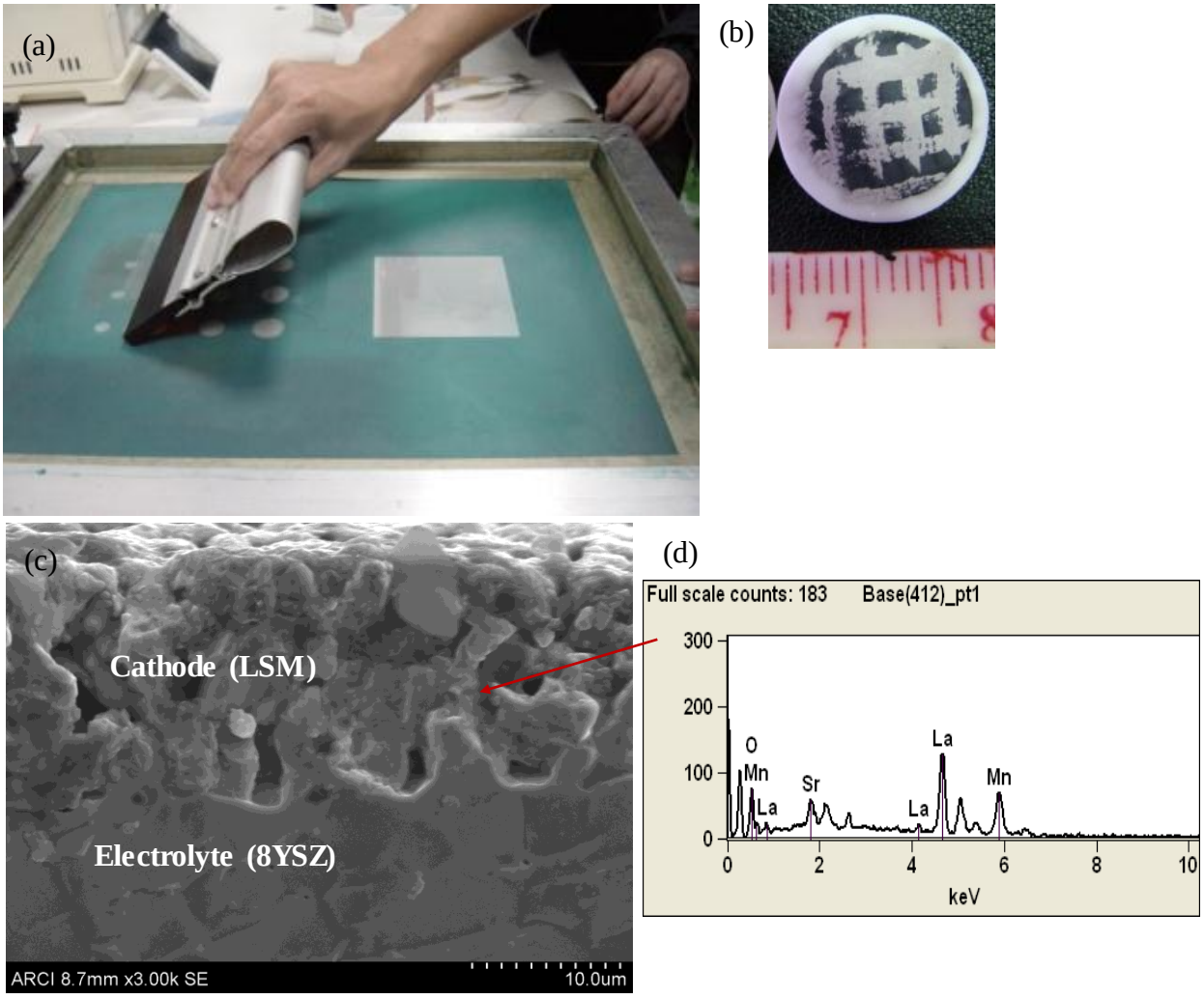

Fig. 4.14(a-d) Micrograph of cross section of the electrolyte with cathode coating along with coated pellet.

4.9.5 Single Cell Performance Test at IIT, Chennai

To evaluate the performance of an electrolyte supported solid oxide fuel cell, co-axial tube furnace (V.B. Ceramics, Chennai)was used. Figure 4.15 presents the schematic of the test facility at IIT, Chennai. Inside diameter of the outer tube is 8 mm and inner tube is 6 mm. Spring loaded fixtures were designed and fabricated for circular discs of 12mm diameter cells. In the present study a cell size of 12mm dia and 0.68 mm thickness have been used for cell performance testing. The test specimen is sandwiched between the two co-axial tubes, which are made of ceramic. Current collectors are used to collect the current by inserting the platinum wire in to the 8mm diameter tube from both the sides and platinum wires are joined to the cell from both sides with platinum paste. Test assembly is then enclosed in a programmable box type furnace for cell

testing up to 900^0C. The test facility allows a variety of gases in the fuel side, and air or oxygen in the oxidant side. Fuel gas, typically hydrogen, metered through a flow controller, is humidified with a water bubbler before entering the cell compartment. Fuel and oxidant gases are separately fed to the center of the anode and cathode sides and then distributed to the electrode surfaces along the flow channels. The temperature versus open circuit voltage measurements are carried out with the DC electronic load unit.

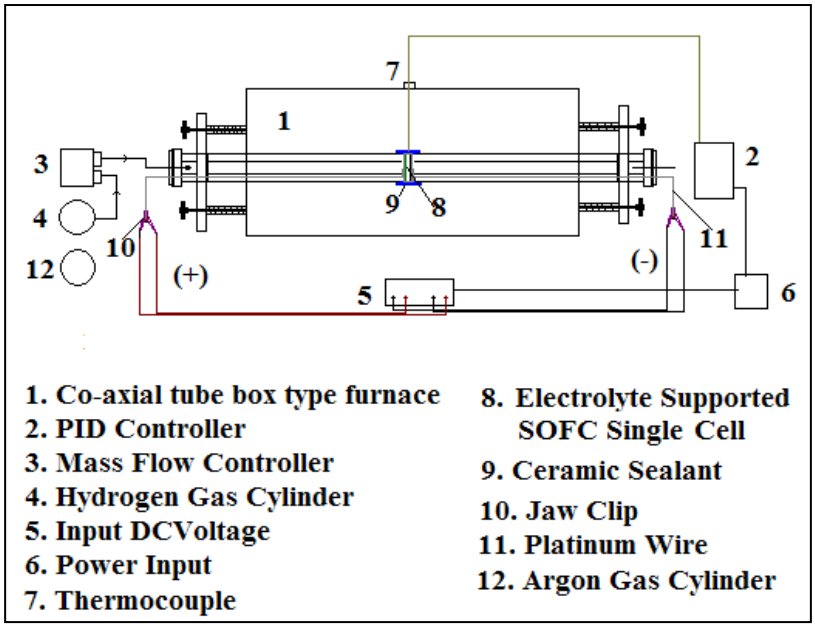

Fig.4.15 Schematic diagram of the SOFC performance test facility at IIT, Chennai

The performance of anode-supported SOFC was evaluated using the same test facility. The anode side of the cell was sealed with ceramic paste (Ceramabond 668, Aremco Products Inc., USA). Humidified hydrogen (3% H_2O) was fed to the anode chamber at a flow rate of 100 ml/min, while the cathode was exposed to ambient air. Platinum wire was used as current collector for both anode and cathode. Fig. 4.16 shows the variation in open circuit voltage with working temperature. At 500^oC the OCV is 0.65V and it is increased linearly with temperature and reached 0.985V at 800^oC, which is close to ideal OCV of the single cell. Power density of the cell could not be evaluated as the experiment was abandoned because of the leakage of the fuel observed with test facility.

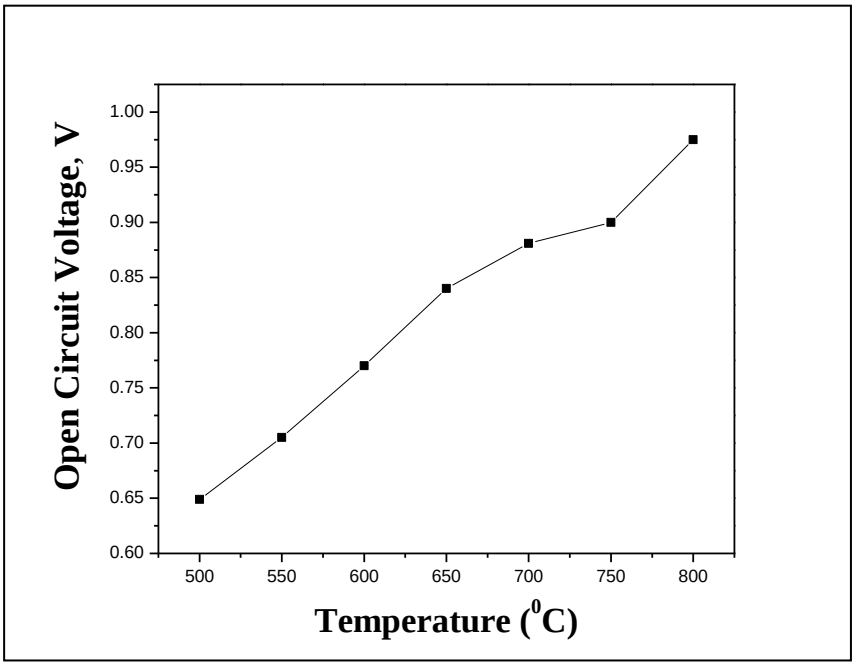

Fig.4.16 Effect of temperature on open circuit voltage for the single cell fabricated out of SPS sintered 8YSZ electrolyte

4.10 Summary and Conclusions

Out of the CRH, MWS, TSS and SPS samples subjected to impedance analysis, SPS sample has shown low grain and grain boundary resistances in all measured temperature regimes. SPS samples exhibited a high total ionic conductivity of 0.134 S/cm which was found to be higher than 0.09S/cm observed with CRH, TSS, and MWS samples. High ionic conductivity observed with SPS sintered samples can also be attributed to the highly aligned dislocation densities as revealed by moiré fringes through TEM analysis. Activation energy calculations were carried out and found to be in compliment with the observed ionic conductivity.

SPS samples exhibited the maximum specific grain boundary conductivity which is also revealed by the lowest blocking factor 0.26 in comparison to 0.38, 0.33 and 0.32 observed for CRH, TSS and MWS respectively.

SPS sintered samples were subjected to screen printing with anode and cathode material to form a single cell and the electrochemical performance evaluation have demonstrated an Open Circuit Voltage of 0.985V close to the ideal value.

4.11 References

1. Huang Q.A, Hui R, Wang B, Zhang J. A review of AC impedance modeling and validation in SOFC diagnosis. Electrochem. Acta. 2007; **52**: 8144.
2. Macdonald J.R. Impedance Spectroscopy—Emphasizing Solid Materials and Systems, John Wiley & Sons, New York, 1987.
3. Macdonald J.R. Impedance Spectroscopy—Theory Experiment and Application, John Wiley & Sons, New York, 2005.
4. Stoynov Z, Vladikova D, Differential Impedance Analysis, Marin Drinov Academic Publishing House, Sofia, Bulgaria, 2005.
5. Stoynov Z, Grafov B, Stoynova B.S, Elkin V, Electrochemical Impedance, Publishing House Nauka, Moscow, Russia, 1991.
6. Lasia A, Conwayin: B.E, Bockris J, White R. (Eds.), Electrochemical Impedance Spectroscopy and its Application-Modern Aspects of Electrochemistry, Kluwer Academic/Plenum Publishers, New York, 1999; **32**.
7. Gabrielli C, Identification of Electrochemical Processes by Frequency Response Analysis, Technical Report No004/83, Solartron, Farnborough, Hampshire, England, 1998.
8. Gabrielli C, Use and Application of Electrochemical Impedance Techniques, Technical Report Number 24, Solartron, Farnborough, Hampshire, England, 1997.
9. Huang K. Gas-diffusion process in a tubular cathode substrate of an SOFC. J. Electrochem. Soc. 2004; **151**: A716.
10. Huang K. Gas-diffusion process in a tubular cathode substrate of a SOFC - II: Identification of gas-diffusion process using AC impedance method. J. Electrochem. Soc. 2004; **151**: H117
11. Hodge I.M, Ingram M.D, West A.R. Impedance and modulus spectroscopy of polycrystalline Solid electrolytes. J. Electroanal.Chem.1976; **74**:125.
12. Macdonald J.R. Impedance spectroscopy and its use in analyzing steady state AC response of solid and liquid electrolytes. J. Electroanal. Chem. 1986; **225**: 25.
13. Macdonald J.R. Impedance spectroscopy fundamentals of solid materials, Chapel Hill, North Corolina, 1987.

14. Kleitz M, Bernard H, Fernandez E, Schouler E. Impedance spectroscopy and electrical resistance measurements on stabilized zirconia, in Advances in Ceramics, Vol. 3, Science and Technology of Zirconia, edited by Heuer A.H, Hobbs L.W. The American Ceramic Society, Columbus, OH, 1981:310.
15. Muccillo R. Impedance spectroscopy analysis of zirconia: 8mol% yttria solid electrolytes with graphite pore former. J. Mater. Res., 2009; **24**: 1780.
16. Li Q, Xia T, Liu X.D, Ma X.F, Menga J, Cao X.Q, Fast densification and electrical conductivity of yttria-stabilized zirconia nanoceramics. Mater. Sci. Engg. B. 2007; **138**:78.
17. Chen X.J, Khor K.A, Chan S.H, Yu L.G. Influence of microstructure on the ionic conductivity of yttria-stabilized zirconia electrolyte. Mater. Sci. Engg. A. 2002; **335**: 246.
18. Zha S, Xia C, Meng G. Effect of Gd(sm) doping on properties of ceria electrolyte for solid oxide fuel cells. J. Power Sour 2003; **115**: 44.
19. Dahl P, Kaus I, Zhao Z, Johnson M, Nygren M, Wiik K, Grande T, Einarsrud M.A. Densification and properties of zirconia prepared by three different sintering techniques. Ceram. Inter. 2007; **33**: 1603.
20. Minh N.Q. Ceramic Fuel Cells. J. Am. Ceram. Soc. 1993; **76**: 563.
21. Gerhardt R, Nowick A.S. Grain boundary effect in ceria doped with trivalent cations:I, electrical measuremenT. J. Am. Ceram. Soc. 1986; **69**: 641.
22. Hesabi Z.R, Mazaheri M, Ebadzadeh T. Enhanced electrical conductivity of ultrafine-grained $8Y_2O_3$ stabilized ZrO_2 produced by two step sintering technique. J. Alloys Compound. 2010; **494**: 362.
23. Guo X, Waser R. Electrical properties of the grain boundaries of oxygen ion conductors: acceptor-doped zirconia and ceria. Prog. Mater Sci. 2006; **51**:151.
24. Verkerk M.J, Middlehuis B.J, Burggraaf A.J. Effect of grain boundaries on the conductivity of high purity $ZrO_2 – Y_2O_3$ ceramics. Solid State Ionics. 1982; **6**: 159.
25. Kosacki I, Suzuki T, Petrovsky V, Anderson H.U. Electrical conductivity of nanocrystalline ceria and zirconia thin films. Solid State Ionics. 2000; **136–137**:1225.
26. Guo X, Ding Y. Grain boundary space charge effect in zirconia. Experimental evidence. J. Electrochem. Soc. 2004; **151**:1.

27. Guo X, Maier J. Grain boundary blocking effect in zirconia: A Schottky Barrier analysis. J. Electrochem. Soc. 2001; **148**: 121.
28. Guo X, Sigle W, Fleig J, Maier J. Role of space charge in the grain boundary blocking effect in doped zirconia. Solid State Ionics. 2002; **154–155**: 555.
29. Hui S(R), Roller J, Yick S, Zhang X, Petit C.D, Xie Y, Maric R, Ghosh D. A brief review of the ionic conductivity enhancement for selected oxide electrolytes. J. Power Sour. 2007; **172**: 493.
30. Durá O. J, Torre M. A. L, Vázquez L, Chaboy J , Boada R, Calzada A .R, Santamaria J. Leon C. Ionic conductivity of nanocrystalline yttria-stabilized zirconia: Grain boundary and size effects. Physical Review B. 2010; **81:** 184301
31. Chen X.J, Khor K.A, Chan S.H, Yu L.G. Preparation of yttria-stabilized zirconia electrolyte by spark-plasma sintering. Mater. Sci. Engg. A. 2003; **341**: 43.
32. Guo X. Physical origin of the intrinsic grain-boundary resistivity of stabilized-zirconia—Role of the space-charge layers. Solid State Ionics1995; **81**: 235.
33. Guo X. Solute segregations at the space-charge layers of stabilized zirconia: An opportunity for ameliorating conductivity. J. Eur. Ceram. Soc. 1996; **16**: 575.
34. Liu B, Zhang Y. LSGM sintered by spark plasma sintering (SPS) for intermediate temperature SOFC electrolyte. J. Alloys Compound. 2008; **458**: 383.
35. Radovic M, Curizio E.L. Mechanical properties of tape cast nickel-based anode materials for solid oxide fuel cells before and after reduction in hydrogen. Acta Materialia. 2004; **52**: 5747.
36. Dees D.W, Claar T.D, Easler T.E, Fee D.C, Mrazek F.C. Conductivity of porous Ni/ZrO_2-Y_2O_3 cermets. J. Electrochem. Soc.1987; **134**: 2141.
37. Wang J, Yan D, Pu J, Chi B, Lian L. Fabrication and performance evaluation of planar SOFC and large active reaction area. Int. J. Hydrogen Energy. 2011; **36**:7234.

****